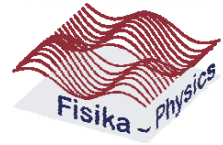


**Sol-gel synthesis and characterization of  $MA_2O_4$  (M = Zn or Mg)  
spinels doped, co-doped and triply doped nano-phosphors.**



by

**Motlounng Setumo Victor**  
**(MSc)**

*A thesis submitted in partial fulfilment of the requirements for the degree*

**Doctor of Philosophy (Ph.D.)**

in

**Physics**

in the

**Faculty of Natural and Agricultural Sciences**

at the

**University of the Free State (Qwaqwa Campus)**

Supervisor: Prof. B.F. Dejene (UFS Qwaqwa Campus)

Co-Supervisor: Prof. H.C. Swart (UFS Bloemfontein Campus)

Co-Supervisor: Prof. O.M. Ntwaeaborwa (UFS Bloemfontein Campus)

December 2014

## **Research/funding institutions**

The research described in this thesis was carried out at various institutions and they are as follows: The University of the Free State (QwaQwa and Bloemfontein Campuses), the Council for Scientific and Industrial Research (CSIR)–Pretoria, and the University of Cape Town (UCT)–Cape Town. The research project was financially supported by the National Research Foundation (NRF) Thuthuka bursary (UID: 87872)–South Africa and the Research funds of the University of the Free State. Special acknowledgement goes to National Research Foundation (NRF) Thuthuka programme for the award of the bursary.

## Declaration

I declare that “*Sol-gel synthesis and characterization of  $MAI_2O_4$  ( $M = Zn$  or  $Mg$ ) spinels doped, co-doped and triply doped nano-phosphor*” is my own work, that it has not been submitted for any degree or examination in any other university, and that all the sources I have used have been indicated and acknowledged by complete references.

Motlounq Setumo Victor

December 2014

Signature: .....

Date: .....

## Dedication

Dedicated to my father; the late Phutheho Smuts Motloun (1944 – 2009) and

To my lovely sister; the late Madiepetsane Mavis Motloun (Nanai) (1985 – 2014)

*“Robalang ka kgotso batshwane ba Sephophothwane, batho baha Setumo, batho baho tuma  
lebitso basa bonahale”*

## Acknowledgements

First and foremost, I would like to thank OUR FATHER IN HEAVEN, the  $\alpha$  and  $\omega$  for being with me all the way.

To my mother, Thobisile Rose Mbatha and my late father, Phutheho Smuts Motloug, for upbringing and for not giving up on me when I was heavily sick child during my early ages. If it wasn't because of your perseverance I would have not experience life.

My brothers, Tokiso, Goodman, Morwa, my sisters, Eunice and the late Mavis, my nephews, Pontsho and Mathapelo and my son-in-law *the naughty* Tshepo for their encouragement, endless love, support and for being on my side whenever I needed them. Without your support our family tree couldn't have established the Dr. Yes, I am the first one but I am confident that I am not the last one. To you, I owe to be the reliable role model of our son, daughters, grandchildren and so on.

To my main supervisor, Prof. B. F. Dejene, for introducing me "*by force*" in the field of phosphor materials fabrication and characterization. You have always been my inspiration. In fact, words aren't sufficient to describe my gratitude but at least you must know that; I thank you for believing in me and for guiding me since from the undergraduate degree. To you, in ten or so years, I would be very happy-man if I could think as quickly as you do now.

To my co-supervisors, Prof. H. C. Swart and Prof. O. M. Ntwaeaborwa, for their guidance, advice, criticism, encouragements and insight throughout the research. Keep on asking the question; *Why?* To your other future students. I am pretty sure that will teach them to explain the physics. To you, I owe the most unbelievable positive changes and growth in me.

To Prof R. E. Kroon for fruitful discussions on the results of some chapters. Your friendly criticism, discussion and help is appreciated. Most importantly, you are the reason why I am always striving for perfection in the courses I am presenting (FSK214, 232, 242 and 608) and my research work.

To the University of the Free State (UFS) Physics department, everybody is appreciated, from the gardeners to the Professors. You all are the reason why I feel at home here at UFS.

To the UFS top management office, for enforcing, encouraging and supporting its staff members to obtain at least PhD degree.

To my high school teacher, Mr K. Zengele, for his wonderful thoughts such as bringing the motivational days in action at my high school (Seotlong Agriculture and Hotel School). If it wasn't because of your ideas, most of us could have gave-up.

National Research Foundation (NRF) Thuthuka programme, for funding this research project. Yes! without proper funding, research is the impossible wish.

To my friends, listing you by your names will make another thesis if not two or three. I really appreciate your support and understanding why I could not go out with you sometimes “*especially on Fridays and weekends*”.

Lastly, but not least, I would also like to thank my dearest wife, Madiboneng Mkhwanazi (Khalos) for her trust and understanding why I couldn't be with her and our only daughter (Thandolwethu) most of the times during the course of this research “*especially at nights*”. To them, I owe my love and affection.

*“Love is the most powerful force in the universe that does not adhere to the laws of physics.”*

*~Msthpt4Eva*

## Abstract

The luminescent and structural properties of the  $MA_2O_4$  ( $M = Zn, Mg$ ) (which are thereafter referred as hosts) phosphors prepared by sol-gel methods at a relatively low temperature ( $\sim 80$  °C) are discussed. Zinc, magnesium and aluminium nitrates and citric acid were used as the starting materials for the hosts preparations. The prepared gels were dried in an oven and subsequently annealed in air either at  $800$  °C for an hour. In order to study the effects of the different dopants into the hosts matrix, the dopants concentration were varied. The host material was either singly doped or co-doped or triply doped. Furthermore, in order to study the effects of the catalyst content on the prepared powders, the optimum concentrations for the singly doped phosphors were prepared and the catalyst content was varied during synthesis.

Generally, the surface morphologies, surface topographies, crystal structure, photoluminescence (PL), Ultraviolet-visible (UV-Vis) properties were influenced by the dopant concentration and catalyst content. The incorporation of the foreign atoms seems to populate the hosts with more defects. For the  $ZnAl_2O_4: x\% Pb^{2+}$  samples, the Thermo gravimetric analysis (TGA) showed that the minimum annealing temperature required to obtain single phase  $ZnAl_2O_4$  is above  $400$  °C. Undoped and  $Pb^{2+}$ -doped  $ZnAl_2O_4$  nanoparticles exhibit the violet emission at slightly different positions, which suggests the possibilities that the luminescence centre can either be due to the defects level in the host or  $Pb^{2+}$  ions. The emission peaks at  $390$  and  $399$  nm are ascribed to the typical ultra-violet (UV) transitions  $^3P_{0,1} \rightarrow ^1S_0$  in  $Pb^{2+}$  ions.

On the study of  $ZnAl_2O_4: x\% Cr^{3+}$  ( $0 \leq x \leq 0.3$ ), Time-of-Flight Secondary Ion Mass Spectroscopy (TOF-SIMS) analysis confirmed the presence of all expected ions in the powder material. The results showed that  $Cr^{3+}$  can occupy multiple-sites in the host matrix. It was interesting to see, once again, that the PL results showed that the host and the  $Cr^{3+}$ -doped exhibit violet emission slightly at different peak positions, which suggests that the luminescence can originate from the host or  $Cr^{3+}$  ion. Emission from the host is attributed to the band-gap defects in the host material, while the emission from the  $Cr^{3+}$  is attributed to the  $^4T_1 \rightarrow ^4A_2$  transition. At the higher mol% there is an emission at  $692$  nm, which is attributed to the  $^2E \rightarrow ^4A_2$  transition in  $Cr^{3+}$ .

On the case-study of the co-doped  $ZnAl_2O_4: 0.1\% Ce^{3+}, x\% Eu^{3+}$  ( $0 \leq x \leq 2$  mol%), the results showed that the nanopowders microstructure consists of non-uniform sizes and the loss in

lattice fringes as the  $\text{Eu}^{3+}$  mol% increase suggest the increase in strain or disorder. The incorporation of the co-activator ( $\text{Eu}^{3+}$ ) at the higher mol% resulted in the radiative energy transfer from  $\text{Ce}^{3+} \rightarrow \text{Eu}^{3+}$ . The International Commission on Illumination (CIE) color coordinates show the shift from the blue to orange visible region as the  $\text{Eu}^{3+}$  concentration is increased.

From the triply doped  $\text{MgAl}_2\text{O}_4$ : 0.1%  $\text{Ce}^{3+}$ , 0.1%  $\text{Eu}^{2+}$ ,  $x\%$   $\text{Tb}^{3+}$  ( $0 \leq x \leq 2\%$ ) study, the PL results revealed the existence of the energy transfer from  $\text{Eu}^{2+} \rightarrow \text{Tb}^{3+} \rightarrow \text{Ce}^{3+}$ . CIE colour chromaticity showed that the colour can be tuned from bluish  $\rightarrow$  greenish by changing the  $\text{Tb}^{3+}$  mol% and the excitation wavelength.

In both studies of the effects of the catalyst content in  $\text{ZnAl}_2\text{O}_4$ :1.5%  $\text{Pb}^{2+}$  and  $\text{ZnAl}_2\text{O}_4$ :0.01%  $\text{Cr}^{3+}$ , the results showed that the increase in the catalyst content lead to the morphological evolution and transformation from small particles to rods-like-needles. In addition, at the higher catalyst content, the extra peak associated with the ZnO impurities are observed. The emission intensity was influenced by the catalyst content. The catalysts content does not affect the emission colour in the case of  $\text{ZnAl}_2\text{O}_4$ :1.25%  $\text{Pb}^{2+}$ . However, in the case of  $\text{ZnAl}_2\text{O}_4$ :0.01%  $\text{Cr}^{3+}$ , the results revealed the possibilities of tuning the emission colour by varying the catalyst content.

## **Keyword**

Sol-gel,  $\text{ZnAl}_2\text{O}_4$ ,  $\text{MgAl}_2\text{O}_4$ , doped and co-doped, ions, Vergard's law, catalyst content, energy transfer, life time, CIE.

## Acronyms and symbols

- Al : Aluminium
- BSE : Back-scattered electrons
- CA : Citric acid
- CB : Conduction band
- CIE : International Commission on Illumination
- CT : Charge transfer
- DL : Donor level
- e : Electron
- $E_g$  : Energy gap or band gap
- EDS : Energy dispersive spectroscopy
- ET : Energy transfer
- FTIR : Fourier-Transform infrared
- HR-TEM : High resolution Transmission electron microscopy
- IR : Infrared
- LC's : Luminescence centres
- LEDs : Light emitting diodes
- NRR : Non-radiative relaxation
- $V_o^*$  : Oxygen vacancies
- PL : Photoluminescence
- SEM : Scanning electron microscopy
- TOF-SIMS : Time-of-flight secondary ion mass spectrometry
- VB : Valance band
- UV : Ultra-violet
- UV-Vis : Ultraviolet-visible spectroscopy
- TGA : Thermogravimetric analysis
- TL : Thermoluminescence
- XRD : X-ray diffraction

## Table of Contents

Research/funding institutions.....	ii
Declaration.....	iii
Dedication.....	iv
Acknowledgements.....	v
Abstract.....	vii
Keyword.....	viii
Acronyms and symbols.....	ix
List of Figures.....	xiv
Chapter 1: Introduction.....	1
1.1 History and development of phosphors.....	1
1.2 Statement of the problem.....	4
1.3 Research objectives.....	4
1.4 Thesis layout.....	5
References.....	7
Chapter 2: Theoretical aspects.....	9
2.1 Introduction.....	9
2.2 Luminescence.....	9
2.2.1 Photoluminescence (PL).....	11
2.2.1.1 Intrinsic photoluminescence.....	12
2.2.1.2 Extrinsic photoluminescence.....	13
2.2.2 Thermoluminescence (TL).....	13
2.3 Defects states and doping.....	14
2.4 Vergard's law.....	16
2.5 Luminescence centres (LC's).....	17
2.6.1 Some LC's.....	18
2.6.1.1 ns <sup>2</sup> -type ions LC's.....	18
2.6.1.2 Transition metal ions LC's.....	19
2.6.1.3 Rare-earth ions LC's.....	19

2.6	Energy transfer (ET) .....	19
2.7	Concentration quenching .....	20
2.8	Crystal structure of $MAl_2O_4$ (M = Zn, Al).....	21
	References.....	22
Chapter 3: Synthesis and characterization techniques .....		24
3.1	Introduction.....	24
3.2	Synthesis techniques .....	24
3.3	Characterization techniques .....	25
3.3.1	X- ray diffraction (XRD) .....	25
3.3.2	Thermo gravimetric analysis (TGA).....	26
3.3.3	Fourier-transform infrared (FTIR).....	27
3.3.4	Scanning electron microscopy (SEM) and energy dispersive x-ray spectroscopy (EDXS) .	28
3.3.5	Transmission Electron Microscopy (TEM) .....	30
3.3.6	Time-of-Flight Secondary Ion Mass Spectroscopy (TOF-SIMS).....	30
3.3.7	Ultraviolet-visible (UV-Vis).....	31
3.3.8	Photoluminescence (PL).....	33
3.3.9	Thermoluminescence (TL).....	34
	References.....	35
Chapter 4: Effects of $Pb^{2+}$ ions concentration on the structure and PL intensity of $Pb^{2+}$ -doped $ZnAl_2O_4$ nanocrystals synthesized using sol-gel process.....		37
4.1	Introduction.....	37
4.2	Experimental .....	38
4.3	Results and discussion .....	38
4.3.1	TGA analysis .....	38
4.3.2	XRD .....	39
4.3.3	FTIR.....	41
4.3.4	SEM .....	42
4.3.5	PL analysis .....	43
4.4	Conclusion .....	45
	References.....	47

Chapter 5: Effects of Cr <sup>3+</sup> mol% on the structure and optical properties of the ZnAl <sub>2</sub> O <sub>4</sub> :Cr <sup>3+</sup> nanocrystals synthesized using sol-gel process.....	49
5.1 Introduction.....	49
5.2 Experimental.....	50
5.3 Results and discussion .....	51
5.3.1 XRD .....	51
5.3.2 TOF-SIMS .....	53
5.3.3 SEM and HR-TEM .....	55
5.3.4 UV-Vis.....	56
5.3.5 PL analysis.....	57
5.4 Conclusions.....	61
References.....	62
Chapter 6: Radiative energy transfer in ZnAl <sub>2</sub> O <sub>4</sub> :0.1% Ce <sup>3+</sup> , x% Eu <sup>3+</sup> nanophosphor synthesized by sol-gel process.....	64
6.1 Introduction.....	64
6.2 Experimental.....	66
6.3 Results and discussion .....	67
6.3.1 XRD .....	67
6.3.2 SEM and HR-TEM .....	71
6.3.3 PL analysis.....	73
6.4 Conclusion .....	81
References.....	82
Chapter 7: Colour tuning and energy transfer pathways in MgAl <sub>2</sub> O <sub>4</sub> triply doped with 0.1% Ce <sup>3+</sup> , 0.1% Eu <sup>2+</sup> , x% Tb <sup>3+</sup> (0 ≤ x ≤ 2%) nanocrystals synthesized using sol-gel process .....	85
7.1 Introduction.....	85
7.2 Experimental .....	87
7.3 Results and discussion .....	88
7.3.1 XRD .....	88
7.3.2 SEM.....	92
7.3.3 UV-Vis.....	93
7.3.4 PL analysis.....	96

7.4	Conclusion .....	102
	References.....	103
Chapter 8: Effects of Zn/Catalyst mole fraction on the Structure and Luminescence Properties of the un-doped and 1.5% Pb <sup>2+</sup> doped ZnAl <sub>2</sub> O <sub>4</sub> powders synthesized by citrate sol-gel method .....		
8.1	Introduction.....	105
8.2	Experimental.....	106
8.3	Results and discussion .....	108
8.3.1	XRD.....	108
8.3.2	EDS.....	112
8.3.3	SEM and TEM .....	112
8.3.4	PL analysis.....	114
8.4	Conclusion .....	119
	References.....	121
Chapter 9: Effects of catalyst/zinc mole fraction on ZnAl <sub>2</sub> O <sub>4</sub> :0.01% Cr <sup>3+</sup> nanocrystals synthesized using sol-gel process .....		
9.1	Introduction.....	123
9.2	Experimental.....	124
9.3	Results and discussion .....	125
9.3.1	Structure and morphology analysis.....	125
9.3.2	Optical properties.....	129
9.4	Conclusion .....	136
	References.....	137
Chapter 10: Summary and conclusion .....		
	Publications.....	142
	International conferences .....	142
	National conferences.....	143
	Biography.....	144

## List of Figures

<b>Figure 2.1.</b> Conversion of excitation energy in solids. ....	9
<b>Figure 2.2.</b> Energy band diagram of (a) phosphorescence and (b) fluorescence phosphors [5]. .....	10
<b>Figure 2.3.</b> Summarized point defects [27]. ....	5
<b>Figure 2.4.</b> Schematic drawing of various impurity levels in semiconductor [25]. ....	5
<b>Figure 2.5.</b> Configurational coordinate diagram [17]. ....	18
<b>Figure 2.6.</b> Crystal structure of the spinel $AB_2O_4$ (A = Zn or Mg and B = Al) [40]. ....	21
<b>Figure 3.1.</b> Basic components of an FTIR spectrometer [16]. ....	27
<b>Figure 3.2.</b> Schematic of an SEM .....	28
<b>Figure 3.3.</b> Schematic of UV-visible spectrophotometer [27]. ....	31
<b>Figure 3.4.</b> Schematic diagram of PL spectrometer [24]. ....	33
<b>Figure 4.1.</b> TGA curve of $ZnAl_2O_4$ gel obtained with the heating rate of 10 0C/min. ....	39
<b>Figure 4.2.</b> X-ray patterns of the (a) un-doped and $Pb^{2+}$ doped $ZnAl_2O_4$ phosphors and (b) analysis of (311) diffraction peak and (c) lattice spacing as a function of $Pb^{2+}$ mol%. ....	41
<b>Figure 4.3.</b> FTIR spectra of the undoped $ZnAl_2O_4$ (host). ....	42
<b>Figure 4.4.</b> SEM micrographs for the (a) $ZnAl_2O_4$ (host), (b) 1% $Pb^{2+}$ and (c) 5% $Pb^{2+}$ .....	43
<b>Figure 4.5.</b> (a) Excitation and emission spectra of the undoped and $Pb^{2+}$ -doped $ZnAl_2O_4$ at different $Pb^{2+}$ mol% (b) dependence of emission intensity as a function of excitation intensity (c) variation of emission intensity as a function of $Pb^{2+}$ mol%. ....	44
<b>Figure 4.6.</b> Energy levels diagram mechanism for the (a) $ZnAl_2O_4: Pb^{2+}$ emission at 399 nm, (b) undoped $ZnAl_2O_4$ emission at 395 nm and (c) $ZnAl_2O_4: Pb^{2+}$ emission at 390 nm. ....	45
<b>Figure 5.1.</b> (a) XRD patterns of $ZnAl_2O_4: x\% Cr^{3+}$ ( $0 \leq x \leq 0.3\%$ ) and (b) expanded version of XRD pattern for (311) peak.....	52
<b>Figure 5.2.</b> Lattice constant as a function of $x\% Cr^{3+}$ ions (insert: showing the ionic radius and increase and decrease in d spacing). ....	53
<b>Figure 5.3.</b> TOF-SIMS ion mapping images for $ZnAl_2O_4: 0.01\% Cr^{3+}$ mole fraction of 0.75 sample (a) $Zn^+$ (b) $Al^+$ (c) $Cr^+$ (d) three-colour overlay of positive ions and (d) $O^-$ .....	54
<b>Figure 5.4.</b> (a) Positive SIMS spectra of $ZnAl_2O_4: 0.01\% Cr^{3+}$ mole fraction of 0.75 showing Zn, Al, Cr peaks and (b) Negative SIMS spectra showing O peak. ....	54
<b>Figure 5.5.</b> SEM images for (a) Host, (b) 0.03% and (c) 0.3%.....	55

<b>Figure 5.6.</b> HR-TEM images for (a) Host, (b) 0.03% and (c) 0.3%.....	56
<b>Figure 5.7.</b> (a) The diffuse reflectance spectra of the $\text{ZnAl}_2\text{O}_4:x\% \text{Cr}^{3+}$ doped ( $0 \leq x \leq 0.3\%$ ) samples and (b) Estimate of the direct optical bandgap of the samples in (a) using Kubelka-Munk function.....	56
<b>Figure 5.8.</b> (a) Excitation and emission spectra of the series $\text{ZnAl}_2\text{O}_4: x\% \text{Cr}^{3+}$ ( $0 \leq x \leq 0.3\%$ ) and (b) deconvolution of $\text{ZnAl}_2\text{O}_4:0.3\% \text{Cr}^{3+}$ .....	57
<b>Figure 5.9.</b> $\text{Cr}^{3+}$ mol% as a function of emission intensity.....	58
<b>Figure 5.10.</b> The phosphor emission pathways mechanism for (a) $\text{ZnAl}_2\text{O}_4$ and (b) $\text{ZnAl}_2\text{O}_4:\text{Cr}^{3+}$ ion.....	60
<b>Figure 5.11.</b> CEI colour of the series $\text{ZnAl}_2\text{O}_4:x\% \text{Cr}^{3+}$ .....	61
<b>Figure 6.1.</b> Summarised scheme for sol-gel synthesis of un-doped, singly doped (with $\text{Ce}^{3+}$ and $\text{Eu}^{3+}$ ) and co-doped $\text{ZnAl}_2\text{O}_4$ .....	66
<b>Figure 6.2.</b> The XRD pattern for the (a) $\text{ZnAl}_2\text{O}_4$ and singly doped samples and (b) co-doped samples at the varying $\text{Eu}^{3+}$ mol%.....	69
<b>Figure 6.3.</b> Analysis of (311) peak for the host, singly doped and co-doped samples.....	69
<b>Figure 6.4.</b> (a) Full width at half maximum (FWHM) and strain as a function of $\text{Eu}^{3+}$ mol%. (b) Crystallites size as a function of $\text{Eu}^{3+}$ mol%.....	70
<b>Figure 6.5.</b> SEM images for (a) Host (b) $\text{ZnAl}_2\text{O}_4:0.1\% \text{Ce}^{3+}$ (c) $\text{ZnAl}_2\text{O}_4:0.1\% \text{Eu}^{3+}$ (d) $\text{ZnAl}_2\text{O}_4:0.1\% \text{Ce}^{3+}, 0.05\% \text{Eu}^{3+}$ (e) $\text{ZnAl}_2\text{O}_4:0.1\% \text{Ce}^{3+}, 0.7\% \text{Eu}^{3+}$ (f) $\text{ZnAl}_2\text{O}_4:0.1\% \text{Ce}^{3+}, 2\% \text{Eu}^{3+}$ .....	72
<b>Figure 6.6.</b> HR-TEM images for (a) Host (b) $\text{ZnAl}_2\text{O}_4:0.1\% \text{Ce}^{3+}$ (c) $\text{ZnAl}_2\text{O}_4:0.1\% \text{Eu}^{3+}$ (d) $\text{ZnAl}_2\text{O}_4:0.1\% \text{Ce}^{3+}, 0.05\% \text{Eu}^{3+}$ (e) $\text{ZnAl}_2\text{O}_4:0.1\% \text{Ce}^{3+}, 0.7\% \text{Eu}^{3+}$ (f) $\text{ZnAl}_2\text{O}_4:0.1\% \text{Ce}^{3+}, 2\% \text{Eu}^{3+}$ .....	72
<b>Figure 6.7.</b> (a) Excitation and emission spectra of the (a) undoped and singly doped (b) co-doped at varying $\text{Eu}^{3+}$ mol% (c) PL intensity as a function of $x\% \text{Eu}^{3+}$ for the violet emission at 396 nm (insert: emission intensity at 617nm as function of wavelength) and (d) PL emission intensity at 617 nm as function of $x\% \text{Eu}^{3+}$ mol%.....	74

<b>Figure 6.8.</b> The emission pathways for the (a) ZnAl <sub>2</sub> O <sub>4</sub> (host), (b) ZnAl <sub>2</sub> O <sub>4</sub> :0.1% Ce <sup>3+</sup> and (c) ZnAl <sub>2</sub> O <sub>4</sub> : 0.1% Eu <sup>3+</sup> .....	76
<b>Figure 6.9.</b> Schematic diagram of energy transfer mechanism from Ce <sup>3+</sup> → Eu <sup>3+</sup> in ZnAl <sub>2</sub> O <sub>4</sub> :0.1% Ce <sup>3+</sup> , x% Eu <sup>3+</sup> .....	77
<b>Figure 6.10</b> (a) Excitation and emission spectra and (b) emission pathways of the ZnAl <sub>2</sub> O <sub>4</sub> :0.1% Ce <sup>3+</sup> , 1.5% Eu <sup>3+</sup> .....	78
<b>Figure 6.11.</b> Glow curve of the UV-irradiated ZnAl <sub>2</sub> O <sub>4</sub> :0.1% Ce <sup>3+</sup> , 2% Eu <sup>3+</sup> nanopowder at a heating rate of 1 °C.s <sup>-1</sup> .....	79
<b>Figure 6.12.</b> CIE chromaticity co-ordinates for the host and singly doped samples.....	80
<b>Figure 7.1.</b> Summarised scheme for sol–gel synthesis of MgAl <sub>2</sub> O <sub>4</sub> : 0.1% Ce <sup>3+</sup> , 0.1% Eu <sup>2+</sup> , x% Tb <sup>3+</sup> .....	88
<b>Figure 7.2.</b> The XRD pattern for the (a) undoped and singly doped samples and (b) triply doped samples at the varying Tb <sup>3+</sup> mol%.....	89
<b>Figure 7.3.</b> (a) The analysis of (400) diffraction peak (b) dependence of lattice parameter on the dopant type (c) FWHM and crystallites size as function of Tb <sup>3+</sup> mol%.....	91
<b>Figure 7.4.</b> SEM images for (a) Host (b) 0.1% Ce <sup>3+</sup> doped (c) 0.1% Eu <sup>2+</sup> doped (d) 0.1% Tb <sup>3+</sup> doped (e) x = 0.7% and (f) x = 2%.....	91
<b>Figure 7.5.</b> HR-TEM images for (a) Host and (b) 0.1% Ce <sup>3+</sup> doped samples.....	92
<b>Figure 7.6.</b> (a) Diffuse reflectance spectra of the host and singly doped with 0.1% Ce <sup>3+</sup> , 0.1% Eu <sup>2+</sup> and 0.1% Tb <sup>3+</sup> samples. (b) Triply doped system at the varying Tb <sup>3+</sup> mol%. (c) Estimation of the direct optical bandgap of the host and (d) Triply doped system using Kubelka-Munkfunction.....	93
<b>Figure 7.7.</b> (a) Excitation and emission spectra of the (a) undoped and singly doped (b) emission spectra of the 0.1% Eu <sup>2+/3+</sup> doped in ZnAl <sub>2</sub> O <sub>4</sub> and MgAl <sub>2</sub> O <sub>4</sub> spinels (c) triply doped at varying Tb <sup>3+</sup> mol% and (d) PL intensity as a function of x% Tb <sup>3+</sup> for the violet emission (insert: normalized PL intensity as function of x% Tb <sup>3+</sup> ).....	94
<b>Figure 7.8.</b> PL intensity as function of x% Tb <sup>3+</sup> for the 546 nm emission (insert: magnified version of emission peak at 620 nm).....	95

<b>Figure 7.9.</b> Proposed energy levels scheme for emission from the (a) host (b) MgAl <sub>2</sub> O <sub>4</sub> :0.1% Eu <sup>2+</sup> (c) MgAl <sub>2</sub> O <sub>4</sub> :0.1% Ce <sup>3+</sup> and (d) MgAl <sub>2</sub> O <sub>4</sub> :0.1% Tb <sup>3+</sup> .....	97
<b>Figure 7.10.</b> Schematic diagram of energy transfer mechanism from Eu <sup>2+</sup> → Tb <sup>3+</sup> → Ce <sup>3+</sup> in MgAl <sub>2</sub> O <sub>4</sub> :0.1% Eu <sup>2+</sup> , 0.1% Ce <sup>3+</sup> , x% Tb <sup>3+</sup> .....	99
<b>Figure 7.11.</b> (a) Emission spectra of MgAl <sub>2</sub> O <sub>4</sub> :0.1% Eu <sup>2+</sup> ,0.1% Ce <sup>3+</sup> , 0.3% Tb <sup>3+</sup> excited by 225, 250, 260, 265 and 273 nm, (b) 546 nm emission peak intensity as a function of excitation wavelength (insert: 390 nm emission peak intensity as a function of excitation wavelength).....	100
<b>Figure 7.12.</b> (a) Decay curves of (a) MgAl <sub>2</sub> O <sub>4</sub> and singly doped MgAl <sub>2</sub> O <sub>4</sub> with 0.1% Eu <sup>2+</sup> ,0.1% Ce <sup>3+</sup> and 0.1% Tb <sup>3+</sup> (b) MgAl <sub>2</sub> O <sub>4</sub> : 0.1% Eu <sup>2+</sup> ,0.1% Ce <sup>3+</sup> , x% Tb <sup>3+</sup> at 0 ≤ x ≤ 2% and (c) MgAl <sub>2</sub> O <sub>4</sub> : 0.1% Eu <sup>2+</sup> ,0.1% Ce <sup>3+</sup> , 0.3% Tb <sup>3+</sup> at different excitation wavelength.....	101
<b>Figure 7.13.</b> CIE chromaticity co-ordinates for the (a) host, singly and triply doped samples (b) MgAl <sub>2</sub> O <sub>4</sub> : 0.1% Eu <sup>2+</sup> , 0.1% Ce <sup>3+</sup> , 0.3% Tb <sup>3+</sup> at different excitation wavelength.....	102
<b>Figure 8.1.</b> Summarised scheme for sol–gel synthesis of ZnAl <sub>2</sub> O <sub>4</sub> :1.5% Pb <sup>2+</sup> .....	107
<b>Figure 8.2.</b> (a) X-ray patterns of the un-doped and ZnAl <sub>2</sub> O <sub>4</sub> :1.5% Pb <sup>2+</sup> doped phosphors (b) deconvolution of the Zn/CA mole fraction is equal to 0.33.....	108
<b>Figure 8.3.</b> Analysis of (311) diffraction peak (a) shift and (b) intensity.....	110
<b>Figure 8.4.</b> Lattice spacing as a function of Zn/CA mole fraction.....	111
<b>Figure 8.5.</b> The raw EDS spectrum for various Zn/CA mole fraction (a) 1.3, (b) 0.33 and (c) 0.11 and (d) 0.33 (un-doped).....	111
<b>Figure 8.6.</b> SEM photographs of ZnAl <sub>2</sub> O <sub>4</sub> : 1.5% Pb <sup>2+</sup> powders annealed at 800 °C for various Zn/CA mole fraction (a) 1.3, (b) 0.33 and (c) 0.11 and (d) 0.33 (un-doped).....	113
<b>Figure 8.7.</b> TEM photographs of ZnAl <sub>2</sub> O <sub>4</sub> : 1.5% Pb <sup>2+</sup> powders annealed at 800 °C for various Zn/CA mole fraction (a) 1.3, (b) 0.33 and (c) 0.11 and (d) 0.33 (un-doped).....	114
<b>Figure 8.8.</b> (a) The excitation and emission spectra of the un-doped and 1.5% Pb <sup>2+</sup> doped ZnAl <sub>2</sub> O <sub>4</sub> nanophosphors for various Zn/CA mole fractions and (b) Deconvolution of 0.11 Zn/CA mole fraction.....	116
<b>Figure 8.9.</b> Emission intensity as a function of Zn/CA mole fractions (insert: normalized emission intensity).....	117

<b>Figure 8.10.</b> (a) Decay curves and (b) CIE chromaticity co-ordinates of the un-doped and 1.5% Pb <sup>2+</sup> -doped ZnAl <sub>2</sub> O <sub>4</sub> nanopowders at the varying Zn/CA mole fraction (star indicates the un-doped sample).....	118
<b>Figure 8.11.</b> Glow curve of the UV-irradiated ZnAl <sub>2</sub> O <sub>4</sub> : 1.5% Pb <sup>2+</sup> nanopowder for Zn/CA mole fraction is 0.083 at a heating rate of 1 °C.s <sup>-1</sup> .....	119
<b>Figure 9.1.</b> X-ray patterns of the (a) un-doped, 0.01% Cr <sup>3+</sup> -doped catalysed and non-catalyzed ZnAl <sub>2</sub> O <sub>4</sub> phosphors. (b) The analysis of the (311) peak shifts. (c) XRD intensity as a function of mole fraction and (d) Crystallites sizes as a function of mole fraction.....	127
<b>Figure 9.2.</b> SEM images of the ZnAl <sub>2</sub> O <sub>4</sub> :0.01% Cr <sup>3+</sup> powders annealed at 800 °C using various catalyst/Zn mole fractions (a) 0 (non-catalysed), (b) 0.38 and (c) 3.0.....	128
<b>Figure 9.3.</b> Schematic diagram for morphological evolution of ZnAl <sub>2</sub> O <sub>4</sub> :0.01% Cr <sup>3+</sup> nanoparticles.....	129
<b>Figure 9.4.</b> (a) The reflectance spectra of the un-doped and 0.01% Cr <sup>3+</sup> doped ZnAl <sub>2</sub> O <sub>4</sub> samples at the varying catalyst/Zn mole fraction (b) Plot of $\frac{F(R_{\infty})}{R_{\infty}}$ versus photon energy to determine the band gap energy of the nano-powder samples.....	130
<b>Figure 9.5.</b> (a) Excitation and emission spectra of the un-doped and 0.01% Cr <sup>3+</sup> -doped ZnAl <sub>2</sub> O <sub>4</sub> at different catalyst/Zn mole fractions (b) Comparison of the un-doped and 0.01% Cr <sup>3+</sup> -doped ZnAl <sub>2</sub> O <sub>4</sub> samples. (c) Normalized emission intensity versus wavelength (d) PL intensity as a function of catalyst/Zn mole fractions.....	132
<b>Figure 9.6.</b> The proposed absorption and emission mechanism in (a) un-doped and (b) 0.01% Cr <sup>3+</sup> ZnAl <sub>2</sub> O <sub>4</sub> prepared by the sol-gel technique.....	134
<b>Figure 9.7.</b> (a) The decay curves and (b) natural logarithm as a function of time for the un-doped and 0.01% Cr <sup>3+</sup> -doped ZnAl <sub>2</sub> O <sub>4</sub> nanopowders at the varying catalyst/Zn mole fraction.....	134
<b>Figure 9.8.</b> CEI colour tuning by varying the catalyst/Zn mole fraction as indicated.....	135



# Chapter 1: Introduction

*“Physicists are made of atoms. A physicist is an attempt by an atom to understand itself.”*

*~ Michio Kaku*

## 1.1 History and development of phosphors

As far as humanity is concerned, the historical perspectives of phosphors can be traced by looking back to the story concerning the Chinese scholar and government official, Ch'e Yin or Hsien Yin, who lived in the Tsin Dynasty (a. d. 264-419) and died about (a. d. 399). His bibliography in the history of Tsin Dynasty describes him as poor but diligent student who could not afford to buy oil, and, because of his poverty collected fireflies and used them to pursue his studies in the evening [1]. The Japanese artist, Ka-no Tan-yu (1602-1650) prepared the phosphorescent paint from seashells and these paintings remained visible at night when different colours were mixed with a special kind of pearl shell [1,2]. It is very interesting to learn that the credit for preparing phosphors for the first time should be credited to the Japanese [2].

The shoemaker and alchemist, Vincentinus Casciarolo of Bologna, Italy, reported the next important contribution in 1602, when discovering a heavy crystalline stone with a gloss at the foot of a volcano [1-3]. This stone emitted red light in the dark after exposure to sunlight and it was later called *“Bolognian stone”*. With the knowledge known today, the famous Bolognian stone appears to have been barite sulphate ( $\text{BaSO}_4$ ), which is a host for phosphor materials. In 1640, Fortunius Licetus explained the causes of the afterglow behaviour of this stone as the characteristic of the impurities presents in the stone [1].

Apart from the above findings, many other findings were reported from many places in Europe, and these light-emitting stones were called ***phosphors***, from Greek root meaning *“light bearer”* [2]. The term *phosphor* has been used since the Middle Ages to designate materials that glow in the dark after exposure to light [3]. A phosphor is composed of a host lattice and one or more activators in amounts from parts per million to a few mole percent. Either the host or activator can determine the luminescent properties of a phosphor [4]. The

phosphors are usually in the form of powders but in some cases, in thin films. In this study, attention is mainly focused to the nano-scaled phosphor particles in the powder form.

From scientific research point of view, phosphor materials has long history going back more than 130 years. The ZnS phosphor prepared accidentally by a French chemists, Théodore Sidot, in 1866 seems to have marked the beginning of scientific research and synthesis of phosphors [2]. After this and for many decades, zinc sulphide (ZnS) doped with copper (and later co-doped with cobalt) was the most famous and widely used persistent phosphor [5-7]. It was used in many commercial products including watch dials, luminous paints and glow-in-the-dark toys even though their brightness and lifetime was low for practical purposes [7]. In order to tackle this problem, other researchers [7,8] tried to enhance the phosphorescence of these phosphors by adding radioisotopes such as tritium and promethium, but this could not materialize due to safety and environmental concerns since these isotopes are radioactive [8].

In August 1996, Matsuzawa et al. [9] published an article on the  $\text{SrAl}_2\text{O}_4: 1\% \text{Eu}^{2+}, 2\% \text{Dy}^{3+}$  or  $1\% \text{Nd}^{3+}$  where they reported that the introduction of  $\text{Dy}^{3+}$  or  $\text{Nd}^{3+}$  as an auxiliary activator gave rise to the intense phosphorescence with the very bright and long afterglow material that lasted for several hours. In the same year (and independently), Takasaki et al. [10] reported similar results. Note that these 1996 discoveries [9,10] are both from the Japanese and are regarded as the beginning of a renewed search for different and better persistent luminescence materials [7,9,10]. It is quite interesting, indeed, to recognize that the research of phosphor material have a long history with Japanese.

Ever since Matsuzawa et al. [9] the research have been concentrated on the aluminates type of phosphor and it took few years before other types of compounds came into consideration. As far as this study is concern, the focus is particularly drawn in the following alkaline earth or/and transition metal doped aluminates:  $\text{MAl}_2\text{O}_4$  ( $\text{M} = \text{Zn}, \text{Mg}$ ). Spinel oxides have attracted much attention around the world due to the large range of interesting electrical, magnetic and optical properties [11].  $\text{ZnAl}_2\text{O}_4$  is widely used as high-temperature material, ceramic, catalyst, catalyst support, optical coating for spacecrafts and emerging as one of the best wide band gap compound semiconductor ( $E_g = 3.8 \text{ eV}$ ) for UV optoelectronic applications [11]. On the other hand,  $\text{MgAl}_2\text{O}_4$  has a wide range of applications in a great number of industrial areas, particularly as an insulating material in a fusion reactor, refractory material in ceramic industry and humidity sensor [12].

Spinel such as  $\text{ZnAl}_2\text{O}_4$  and  $\text{MgAl}_2\text{O}_4$  (shown in figure 2.6), have previously shown to be suitable host lattice for different foreign atoms [13]. The foreign atoms can either be singly, co-doped or even triply doped in these host lattices. For example, Lakshminarayana et al. [14] showed that the energy transfer from  $\text{Tb}^{3+} \rightarrow \text{Mn}^{2+}$  occurs dominantly upon 350 nm excitation. Moreover, they also showed that the interionic distance and charge transfer probability between both species depend on crystallization conditions and that enables control of the energy transfer process and, hence, tenability of the colour of photo emission by simultaneous emission from  $\text{Tb}^{3+}$  and  $\text{Mn}^{2+}$  centers. Qai et al. [15] have shown that the  $\text{MgAl}_2\text{O}_4$  can be co-doped with transition metal ions for the possible application in white LEDs. In their report [15], they successfully showed that  $\text{Mn}^{2+}$  ions have a strong sensitization effect on a  $\text{Cr}^{3+}$  ion. The enhancement of the  $\text{Cr}^{3+}$  emission intensity and the  $\text{Mn}^{2+}$  intensity quenching was attributed to the energy transfer from  $\text{Mn}^{2+} \rightarrow \text{Cr}^{3+}$  ion by means of reabsorption of  $\text{Mn}^{2+}$  photons.

Many fabrication methods for the phosphor material synthesis such as solid state reaction [16], co-precipitation [17], hydrothermal [18], combustion [19] and sol-gel [20] have been developed.

As an alternative, in this work, the sol-gel method [20] (discussed in chapter 3 section 3.2) was adopted to synthesize the  $\text{MAl}_2\text{O}_4$  ( $\text{M} = \text{Zn}, \text{Mg}$ ) and all of the samples were synthesized at a very low temperature ( $\sim 80^\circ\text{C}$ ). The influence of  $\text{Pb}^{2+}$  and  $\text{Cr}^{3+}$  mol% on the structural, morphology and optical properties of  $\text{ZnAl}_2\text{O}_4$  nanophosphors were investigated. The possibility of tuning the emission colour from bluish to reddish by increasing the  $\text{Eu}^{3+}$  mol% in the 0.1%  $\text{Ce}^{3+}$ , x%  $\text{Eu}^{3+}$  co-doped  $\text{ZnAl}_2\text{O}_4$  is reported. The proposed energy transfer mechanism from  $\text{Ce}^{3+} \rightarrow \text{Eu}^{3+}$  have been discussed. The photoluminescence characteristics of turning the emission colour of the triply doped  $\text{MgAl}_2\text{O}_4$ : 0.1%  $\text{Ce}^{3+}$ , 0.1%  $\text{Eu}^{2+}$ , x%  $\text{Tb}^{3+}$  phosphor from greenish-to-bluish by varying the x%  $\text{Tb}^{3+}$  at ( $0 \leq x \leq 2\%$ ) and the excitation wavelength was investigated. The proposed energy transfer mechanism from  $\text{Eu}^{2+} \rightarrow \text{Tb}^{3+} \rightarrow \text{Ce}^{3+}$  is presented. Furthermore, the effects of citric acid (CA) content in the  $\text{ZnAl}_2\text{O}_4$  doped with 1.25%  $\text{Pb}^{2+}$  and 0.01%  $\text{Cr}^{3+}$  is investigated. The corresponding luminescence mechanisms or pathways in all studies have been discussed in details. The main aim of these study is to fabricate phosphor material that can be used for light emitting devices such as light-emitting diodes (LEDs).

## 1.2 Statement of the problem

Many researchers have studied the luminescence behaviour of the rare earths and transition metals in various hosts and most of these studies focus more on the well-known luminescing dopants such as  $\text{Mn}^{2+}$ ,  $\text{Eu}^{2+}$ ,  $\text{Tb}^{3+}$ ,  $\text{Er}^{3+}$ ,  $\text{Yb}^{3+}$  and so on [21]. However, there are scarce works reported on sol-gel synthesis of  $\text{ZnAl}_2\text{O}_4$  and  $\text{MgAl}_2\text{O}_4$  doped, co-doped and triply doped with  $\text{Pb}^{2+}$ ,  $\text{Cr}^{3+}$ ,  $\text{Eu}^{3+}$ ,  $\text{Ce}^{3+}$  in literature to date. The effects of non-popular dopant ion such as  $\text{Pb}^{2+}$  in these hosts, to the best of our knowledge, have not been attempted. Furthermore, there have been few reports on the triply doping these hosts material in the literature to date. Thus, it is urgently necessary to study and report on these matters. One of the main challenges faced by the industries fabricating the LED's is the phosphor materials that have a long lifetime of the emission light. Thus, in this study, the co-doping and triple doping of the hosts is proposed in order to increase the life-span of the emission light.

Many other, synthesis techniques as mentioned in chapter 3 (section 3.2) has been developed to fabricate the phosphor materials and the reasons why sol-gel was chosen are also outline. As far as the sol-gel technique is concern, one of the fundamental ingredients during synthesis is a catalyst. Catalytic experiments are well known to produce the products at the lower activation energy compared to the non-catalytic reactions. Thus, catalysis plays a prominent role in the chemical industry and societies. For example, the majority of chemicals and fuels produced in the chemical industry have been produced using one or more catalysts [22]. Without any doubt, it is therefore clear that catalysis plays a prominent role in society today and will be a critical technology for advancing our life. On the other hand, researchers in the green and sustainable chemistry are focusing on the development of economic and eco-friendly methodologies that are free from the use of any catalyst, reagent, promoter or surfactant in aqueous media [23]. Hitherto, there has been rare studies undertaken to report on the effects of catalysing and non-catalysing the chemical reaction during sol-gel synthesis. Accordingly and amongst others, this study is devoted to investigate the effects of the catalyst content during the synthesis of these phosphor materials. This research work is expected to contribute to the new body of knowledge in the research, development of new phosphor materials, white light emitting devices and green energy technology.

## 1.3 Research objectives

Nano-science and technology (NS&T) are widely seen as having huge potential to bring benefits to many areas of Research and Development (R&D) and application, and are

attracting rapidly increasing investment from Governments agencies and business around the world. Recently, South African (SA) Government showed their obligation to nanotechnology development with the commencement of the national nanotechnology strategy [24]. The SA Nanotechnology Strategy (SANS) [24] addresses the anticipated opportunities from this new wave of technology. In line with our constitutional mandate as the custodian of innovation, the Ministry of Science and Technology seeks to ensure that SA is ready to optimally use nanotechnology to enhance the global competitiveness and sustainable economic growth. Nanotechnology promises more for less – smaller, cheaper, lighter and faster devices with greater functionality. Indeed, there is a bright future in nanotechnology. Amongst others, one of the main objectives of SANS [24] is to support long-term nanoscience research that will lead to the fundamental understanding of the design, synthesis, characterization, modelling and fabrication of nanomaterials. Furthermore, the SANS [24] addresses the need to share the information on the physics affecting atomic and molecular interactions. It is with these concepts that this study aligns itself to the SANS. In this study the focus is drawn particularly on the  $\text{ZnAl}_2\text{O}_4$  and  $\text{MgAl}_2\text{O}_4$  nanophosphors with the following main objectives:

- ✓ To investigate the effects of  $\text{Pb}^{2+}$  ions concentration on the structure and PL intensity of Pb-doped  $\text{ZnAl}_2\text{O}_4$  nanocrystals;
- ✓ To investigate the effects of  $\text{Cr}^{3+}$  mol% on the structure and optical properties of the  $\text{ZnAl}_2\text{O}_4:\text{Cr}^{3+}$  nanocrystals;
- ✓ To investigate the influence of co-doping  $\text{ZnAl}_2\text{O}_4$  with 0.1%  $\text{Ce}^{3+}$ , x%  $\text{Eu}^{3+}$  on the structure and optical properties;
- ✓ To investigate the effects of triply doping the  $\text{MgAl}_2\text{O}_4$  nanocrystals with 0.1%  $\text{Ce}^{3+}$ , 0.1%  $\text{Eu}^{2+}$ , x%  $\text{Tb}^{3+}$  on the structure and optical properties;
- ✓ To investigate effects of catalyst content on both the un-doped, 1.25%  $\text{Pb}^{2+}$  and 0.01%  $\text{Cr}^{3+}$  doped  $\text{ZnAl}_2\text{O}_4$  nanocrystals and
- ✓ To investigate the emission mechanisms or pathway in each case mentioned above.

#### 1.4 Thesis layout

This thesis is organised in three major parts; namely theory (Chapters 2-3), effects of doping, co-doping and triply doping (Chapters 4-7) and effects of catalyst content (Chapters 8-9). Note that the references are presented at the end of each Chapter.

Chapter 2 provides the theoretical aspects of luminescence and an overview of luminescence mechanism and their fundamental properties are outlined. The crystal structures of  $\text{ZnAl}_2\text{O}_4$

and  $\text{MgAl}_2\text{O}_4$  are also presented. Chapter 3 presents a brief description of the experimental techniques used to synthesize the aluminate phosphors. As a results, the sol-gel technique is discussed in detail. Detailed information on the principle and operation of the experimental techniques used to investigate the luminescence and the structure of the phosphors are presented.

Chapter 4 consists of the results obtained through varying the  $\text{Pb}^{2+}$  mol% in  $\text{Pb}^{2+}$  doped  $\text{ZnAl}_2\text{O}_4$ . Chapter 5 consists of the results obtained when  $\text{Cr}^{3+}$  mol% was varied in  $\text{ZnAl}_2\text{O}_4$ . Chapter 6 comprises the results obtained when the  $\text{Eu}^{3+}$  mol% was varied in the co-doped  $\text{ZnAl}_2\text{O}_4$ : 0.1%  $\text{Ce}^{3+}$ , x%  $\text{Eu}^{3+}$ . Chapter 7 covers the results obtained when the  $\text{Tb}^{3+}$  mol% was varied in the triply doped  $\text{MgAl}_2\text{O}_4$ : 0.1%  $\text{Ce}^{3+}$ , 0.1%  $\text{Eu}^{2+}$ , x%  $\text{Tb}^{3+}$  nanocrystals.

Chapter 8 discusses the results obtained when the catalyst content was varied in the un-doped and 1.5%  $\text{Pb}^{2+}$  doped  $\text{ZnAl}_2\text{O}_4$ . Chapter 9 presents the results obtained when the catalyst content was varied in 0.01%  $\text{Cr}^{3+}$  doped  $\text{ZnAl}_2\text{O}_4$  nanocrystals.

Lastly but not least, Chapter 10 presents the thesis summary and conclusions. The recommendations, suggestions for future work and publications resulting from this work are also given in this Chapter. Biography is presented at the end of this thesis.

## References

1. E. N. Harvey, A History of Luminescence from the Earliest Times until 1900; American Philosophical Society: Philadelphia, PA, USA, 1957.
2. W. M. Yen, S. Shionoya, H. Yamamoto, Phosphor handbook second edition; Taylor & Francis Group, LLC, USA, 2006.
3. B. Valeur, M. N. B. Santos, J. Chem. Educ. **88** (2011) 731.
4. J. C. Whitaker, The Electronics Hand Book second edition, CRC Press, USA, 1996.
5. H. C. Swart, J. S. Sebastian, T. A. Trottier, S. L. Jones, P. H. Holloway, J. Vac. Sci. Technol. A **14** (1996) 1697.
6. H. C. Swart, T. A. Trottier, J. S. Sebastian, S. L. Jones, P. H. Holloway, J. Appl. Phys. **83** (1998) 4578.
7. K. Van den Eeckhout, P. F. Smet, D. Poelman, Materials **3** (2010) 2536.
8. B. M. Mothudi, PhD thesis, University of the Free State (2009) 2.
9. T. Matsuzawa, Y. Aoki, N. Takeuchi, Y. A. Murayama, J. Electrochem. Soc. **143** (1996) 2670.
10. H. Takasaki, S. Tanabe, T. Hanada, J. Ceram. Soc. **104** (1996) 322.
11. K. Kumar, K. Ramamoorthy, P. M. Koinkar, R. Chandramohan, K. Sankaranarayanan, Journal of Crystal Growth **289** (2006) 405.
12. A. Laobuthee, N. Koonsaeng, B. Ksapabutr, M. Panapoy, C. Veranitisagul, International Journal of Materials & Structural Reliability **3** (2005) 95.
13. V. Singh, R. P. S. Chakradhar, J. L. Rao, D-K. Kim, J. Lumin. **128** (2008) 394.
14. G. Lakshminarayana, L. Wondraczek Journal of Solid State Chemistry **184** (2011) 1931.
15. Q. Sai, C. Xia, H. Rao, X. Xu, G. Zhou, P. Xu, J. Lumin. **131** (2011) 2359.
16. F. L. Yuan, P. Hu, C. L. Yin, S. L. Huang, J. L. Li, J. Mater. Chem. **13** (2003) 634.
17. J. T. Keller, D. K. Agrawal, H. A. McKinstry, Adv. Ceram. Mater **3** (1998) 420.
18. Z. Chen, E. Shi, Y. Zheng, W. Li, N. Wu, W. Zhong, Mater Lett. **56** (2002) 601.
19. A. K. Adak, A. Pathak, P. Pramanik, J. Mater Sci. Lett. **17** (1998) 559.
20. Y. Wu, J. Du, K. Choy, L. L. Hench, J. Guo, Thin Solid Films **472** (2005) 150.
21. D. Zhang, C. Wang, Y. Liu, Q. Shi, W. Wang, Y. Zhai, J. Lumin. **132** (2012) 1529.

22. D. Duzenli, PhD thesis submitted at The Graduate School of Natural and Applied Science, Middle East Technical University, 2010.
23. R. G. Chary, G. R. Reddy, Y. S. S. Ganesh, K. V. Prasad, A. Raghunadh, T. Krishna, S. Mukherjee, M. Pal, *Adv. Synth. Catal.* **356** (2014) 160.
24. Department of Science and Technology (Republic of South Africa) The national nanotechnology strategy ISBN 0-621-36395-2.

## Chapter 2: Theoretical aspects

*“It doesn’t matter how beautiful your theory is, it doesn’t matter how smart you are. If it doesn’t agree with experiment, it’s wrong.”*

*~ Richard Feynman*

### 2.1 Introduction

In this chapter, the theoretical aspects such as; luminescence, defects states and doping, Vegard’s law, luminescence centers, energy transfer, luminescence quenching and crystal structure of  $\text{MAI}_2\text{O}_4$  ( $M = \text{Zn}, \text{Al}$ ) are discussed.

### 2.2 Luminescence

When a solid absorbs photons or charged particles, as illustrated in figure 2.1, a number of energy conversion processes are possible. For instance, the solid materials can be excited by irradiating them with higher to lower energies ranging from X-ray to visible light, respectively. Amongst other processes, after the absorption of the excitation energy, one of the conversion process that can take place is luminescence. The term, luminescence, is defined as a phenomenon in which the electronic state of a substance is excited by some kind of external energy such as X-ray, electrons and UV (see figure 2.1) and the excitation energy is given off or emitted as light [1,2].

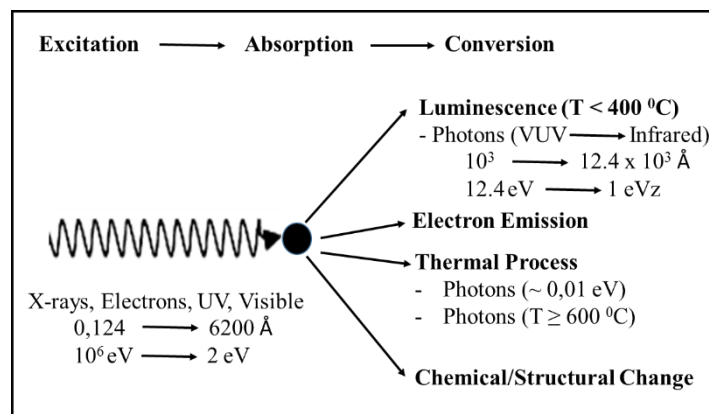


**Figure 2.1.** Conversion of excitation energy in solids.

The word luminescence, which includes both the fluorescence and phosphorescence, was first used by Eilhardt Wiedemann, a German physicist in 1888. The word originated from the Latin word *lumen*, which means light. Phosphorescence is a luminescence process whereby the light emission from a substance continues for few seconds, minutes or hours after the exciting radiation has ceased, while fluorescence is a process in which emission stops suddenly after radiations have ceased [2,3]. Yen et al. [4] distinguished fluorescence and phosphorescence by whether the transition to emit light is allowed or forbidden by spin selection rules. The light emission due to an allowed singlet-singlet transition is called fluorescence, while that due to a forbidden transition which usually shows long afterglow is called phosphorescence [4]. As shown in figure 2.2, it is important to note that; in the phosphorescence process, the excited electrons and holes in the conduction (CB) and valence (VB) bands of a phosphor can often be captured by impurity centers or crystal defects before they reach emitting centers, which eventually prolongs the decay time of phosphorescence. These centers or defects are called the traps [5]. On the other hand, in fluorescence there are no traps (see figure 2.2) but many luminescent centers, as a results, that is why the fluorescence materials are imperceptible short after-glow.

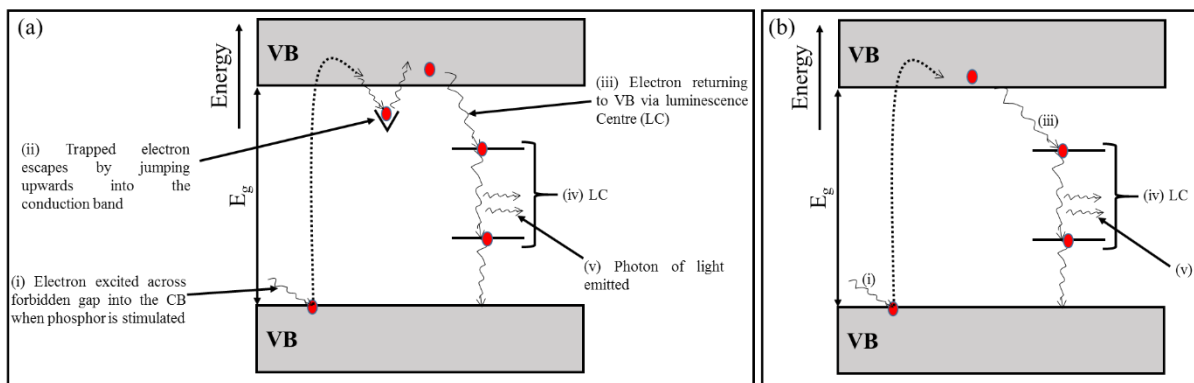


**Figure 2.2.** Energy band diagram of (a) phosphorescence and (b) fluorescence phosphors [5].

Class of materials or substances which emits characteristic luminescence are called **phosphors**. As stated in section 1.1 that phosphors consist of a host lattice which constitutes the bulk of the phosphor and one or more activators [1,7]. Emission of light by the phosphor strongly dependent upon the nature of the emitting substance. Either the host or activator/s, or

both in some cases, can determine the characteristic luminescence properties of a phosphor [1-3].

There are many processes by which electrons can be excited in luminescent materials. These includes bioluminescence (generated by a living organism), chemiluminescence (caused by chemical or electrochemical reactions), crystalloluminescence (produced during crystallization), electroluminescence (generates light in response to an electric current passing through some material), cathodoluminescence (electron beam impacts on a luminescent material such as a phosphor), mechanoluminescence (resulting from any mechanical action on a solid), **photoluminescence** (caused by moving electrons to energetically higher levels through the absorption of photons), radioluminescence (generated when some materials are exposed to ionizing radiation like  $\alpha$ ,  $\beta$  or  $\gamma$  rays), sonoluminescence (emission of short bursts of light from imploding bubbles in a liquid when excited by sound) and **thermoluminescence** (phenomenon that certain crystalline materials emit light when heated) [8].

This study, is mainly focused on photoluminescence (PL) and thermoluminescence (TL) for a fundamental understanding of the prepared phosphors. Therefore, only these two processes will be discussed in details.

### 2.2.1 Photoluminescence (PL)

As it was stated in section 2.1 that the PL in solids is a process in which the solids are excited by a photon (electromagnetic radiation) and the final process is an electronic transition between two energy levels,  $E_1$  and  $E_2$  and ( $E_2 > E_1$ ), with the emission or released of radiation of wavelength  $\lambda_0$  and the energy difference between ( $E_2 - E_1$ ) also known as the band gap ( $E_g$ ) is given by [9]:

$$E_g = E_2 - E_1 = \frac{hc}{\lambda_0} \quad (2.1)$$

where  $h$  and  $c$  are the Plank's constant and speed of light, respectively. In PL spectra, emission peaks are observed at a lower energy than the absorption energy. The difference in energy between the PL emission and the absorption is called the Stokes shift [10]. PL emission in solids such as inorganic insulators and semiconductors is classified in terms of the nature of

the electronic transitions producing it. The process is divided into two major types, namely intrinsic and extrinsic photoluminescence [5], and they are discussed in the following sections.

### 2.2.1.1 Intrinsic photoluminescence

In the intrinsic process, the PL results from the inherent defects (see section 2.3) present in the crystal structure [11]. Thus, this type of PL does not involve impurity atoms. There are several factors that may influence intrinsic PL such as non-stoichiometry (a state of a material (semiconductor) not having exactly the correct elemental proportion) and structural imperfections (owing to poor ordering, radiation damage, or shock damage). There are three kinds of intrinsic PL, which are; band-to-band, exciton and cross-luminescence.

In semiconductors, an electron-hole pair is created when an electron leaves the VB and enters the CB due to excitation. Band-to-band results from the recombination of an electron in the CB with a hole in the VB and can only be observed in a very pure crystals at relatively high temperatures [12]. An exciton is a bound state of an electron and an electron hole which are attracted to each other by the electrostatic Coulomb force. It is an electrically neutral quasiparticle that exists in insulators, semiconductors and in some liquids. The exciton is regarded as an elementary excitation of condensed matter that can transport energy without transporting net electric charge [9,13]. It may be bound or moving in a crystal conveying energy. Luminescence may result from the recombination of the electron and the hole. Excitons have a natural physical separation that varies from semiconductor to semiconductor [14]. This average separation distance is termed Exciton Bohr Radius (EBR), which is mathematically defined by the following equation [14]:

$$a_B = \frac{\hbar^2 \varepsilon}{e^2} \left[ \frac{1}{m_e} + \frac{1}{m_h} \right] \quad (2.2)$$

Where  $\varepsilon$  is the dielectric constant,  $\hbar$  is the reduced Planck's constant,  $e$  is the electronic charge, and  $m_e$  and  $m_h$  are the electron and hole effective masses, respectively.

In the bulk semiconductor the dimensions of the crystals are much larger than the EBR, allowing the exciton to extend to its natural limit. The energy levels of a bulk semiconductor are very close together, and are referred as continuum states, such that there is almost no energy difference between them. Since the band gap of the bulk semiconductor is fixed, the transitions result in fixed emission frequencies [15]. However, if the crystal sizes of a

semiconductor are comparable or small enough that they approach the size of the materials bulk EBR, then the continuum states are broken down into discrete states having small and finite separation between energy levels. As a result, this results in a large effective band gap and according to equation 2.1, this means lower wavelength leading to an optical transition which is blue-shifted from that of bulk materials [15,16].

Cross-luminescence is produced by the recombination of an electron in the VB with a hole in the outermost core band. It can only take place when the energy difference between the top of the VB and that of the outermost core band is smaller than the band gap energy; otherwise, an Auger process occurs. Examples of the compounds for which this phenomena has been observed are BaF, CsCl, CsBr, KF, KMgF<sub>3</sub>, KCaF<sub>3</sub> and K<sub>2</sub>YF<sub>5</sub> [14,17].

#### 2.2.1.2 Extrinsic photoluminescence

In extrinsic process, the PL results from the intentionally incorporated impurities in the crystal structure. As it was stated in section 1.1 and 2.2 that these intentionally incorporated impurities are called activators and the materials exhibiting the luminescence in this way are called phosphors. In this case, defects and activators with energy levels in the band gap provide additional energy levels for excitation and relaxation processes [18]. Thus, both the defects and activators (see section 2.3) are responsible for the luminescence. Extrinsic photoluminescence can be divided into two categories; namely localized and delocalized. In the localized luminescence excitation and emission processes are confined to a localized luminescence center, that is; the host lattice does not contribute to luminescence process [12,14]. In the delocalized luminescence the electrons and holes participate in the luminescence process (free electron in the CB and free holes in the VB). It is important to mention that most of the observed types of luminescence that have practical applications belong to this category [14,18].

#### 2.2.2 Thermoluminescence (TL)

TL is a luminescence phenomenon of an insulator or semiconductor which can be observed when the solid is thermally stimulated [19]. From this explanation and the one stated in section 2.2, it is important to note that TL should not be confused with the light spontaneously emitted from a substance when it is heated to incandescence. For an example, at higher temperatures, in excess of 200 °C, a solid emits (infra) red radiation of which the

intensity increases with increasing temperature. This is thermal or black body radiation. TL, however, is the thermally stimulated emission of light following the previous absorption of energy from excitation radiation [19] as shown in figure 2.1. This is possible due to the fact that a material may contain defects (see section 2.3) that can trap electrons and holes as illustrated in figure 2.2 (a). If the temperature of the system is increased by heating the material, the trapped electrons and holes may obtain enough energy to become free, and then they can recombine. If the recombination is radiative, a photon is emitted and the process is called TL [20]. Based on this description there are three essential ingredients necessary for the production of TL and they are as follows: Firstly, the material must be an insulator or a semiconductor. Secondly, the material must have at some time absorbed energy during exposure to ionising radiation. Thirdly, the luminescence emission is triggered by heating the material [19]. A thermoluminescent material is thus a material that during exposure to ionising radiation absorbs some energy, which is stored in the traps. It can be seen that the presence of traps is essential for the TL production. When considering figure 2.2 (a) and (b) it can be concluded that the TL phenomena is expected to be more pronounced in phosphorescence material, while no TL is expected to arise from the fluorescence material since there are no traps present.

A curve of luminescence intensity versus temperature is called a glow curve. Amongst others, TL glow curves can be analysed to extract information on the various parameters such as the trapping process, traps depth, trapping and re-trapping rates. Glow peaks at lower temperatures corresponds to shallower traps (e.g. donor level, which will be explained in section 2.3) and they are more sensitive to fading [19-21]. Thus, glow peaks at the higher temperatures corresponds to the deep traps. Many methods such as first-order kinetics [22], second-order kinetics [23] and general-order kinetics [24] are the most popular used methods to analyse the TL data.

### 2.3 Defects states and doping

In section 2.2.1.1 and 2.2.1.2 it has already been mentioned that the PL process is induced by defects within the material. Defects are structural imperfection on the crystal, which are classified according to the way in which they are incorporated into the crystal lattice. There are three classification of defects in crystalline solids and they are namely; planar defects (grain boundaries: interfaces between two single crystal regions of different orientation tend to be loosely bound), line defects (dislocations) and point defects (self-interstitial (extra

atom), vacancy (missing atom), substitution (impurity atom in a lattice) and interstitial (impurity atom not in regular lattice site)) [25,26]. The point defects are summarized in figure 2.3.

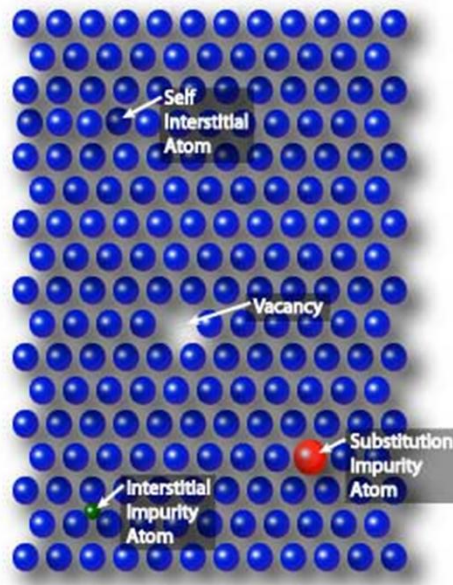


**Figure 2.3.** Summarized point defects [27].

In practice, most of these defects are induced by incorporating or adding foreign atoms (also known as doping) into the host material crystal lattice. Figure 2.4 illustrates the fact that the defects presents extra donor, acceptor, traps and recombination centers levels in the semiconductor material.

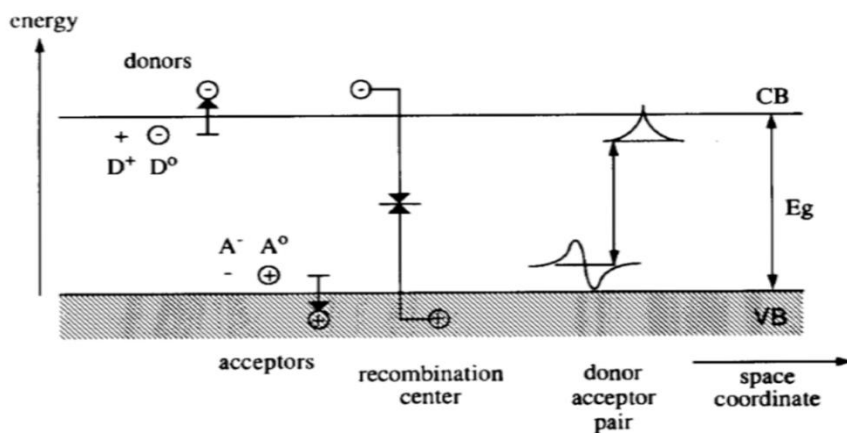


**Figure 2.4.** Schematic drawing of various impurity levels in semiconductor [25].

As shown in figure 2.4, a donor has an energy level just below the CB and can easily give an electron to CB via thermal ionization. As discussed in section 2.2.2, the donor glow peaks must be observed at the lower temperature region in the glow curve [21,25]. Donor is presented by the following equation [25]:



Donor can be formed by substitutional atoms situated in the periodic table one column to the right of the atom which they replace. Furthermore, they can be formed by interstitial which have a weak bound electron such as H, Li or Na in a II-VI compounds [25].

An acceptor shown in figure 2.4 can easily accommodate an electron from the VB, i.e. by a hole on it via the following reaction or equation [25]:



Acceptor may be formed by substitutional atom which has one electron less than the one which they replace. Thus, the impurities are often found in the periodic table to the left of the atom they replace. Based on section 2.2.2, it is clear that the shallow donor (acceptor) can be considered as a positively (negatively) charged centre to which an electron (hole) is bound by Coulomb interaction [25].

#### 2.4 Vegard's law

This law has been used extensively in mineralogy, metallurgy and materials science for the past several decades. It states that the crystallographic parameters of a continuous substitutional solid solution vary linearly with concentration at constant temperature when the nature of the bonding is similar in the constituent phases. It is understood in context that the substituting atoms (see figure 2.3) are statistically distributed. The lattice parameter is controlled by the relative size of the atoms or species exchanged. The approximation is valid for ideal solutions when the lattice parameters of the pure components differ by less than 5 % [28]. The simplest mathematical expression for Vegard's law for a binary solid solution A-B is [28]:

$$a = a_A^0(1 - X) + a_B^0(X) \quad (2.4)$$

where  $X = X_B$  is the mole fraction of component B and  $a_A^0$  and  $a_B^0$  are respectively the lattice parameters of pure components A and B. Although the law was postulated on empirical evidence, several cases of both positive and negative deviations from this law have been documented. For instance, Córdoba et al. [29] have shown that for the silicon-rich and germanium-rich compositions, a positive and negative deviation from Vegard's model was observed, respectively, producing an S-shaped variation of lattice parameters with composition. In their results [29] the presence of secondary phases or unreacted elements, which could account for the deviation between the presumed composition of the solid solution and the estimated composition according to Vegard's law, was not detected.

### 2.5 Luminescence centres (LC's)

A variety of defects and dopants (discussed in section 2.3) giving rise or responsible for the luminescence in semiconductors and insulating materials are normally referred as the LC's. LC's includes the rare earth ions, transition metal ions, excitons, donor-acceptor pairs, and ions with a  $d^{10}$  or  $s^2$  (angular momentum  $l = 2$  or  $0$ , respectively) electronic configuration state. The resultant luminescence can either comprise of the sharp or broad-band emission lines [30,31]. Sharp emission lines usually shown by most of the rare earth ions arise from purely electronic transitions and the effect of the environment is felt mainly through their effects on the lifetimes of the states. The broad emission bands arise from the interaction between the electronic system of the luminescent centre and the vibrations of the atoms or ions, which surround it. This is due to the simultaneous transitions of both electronic and vibrational systems [30]. Furthermore, the broad band spectra are observed when the character of the chemical bonding in the ground and excited states differs considerably. This process goes hand in hand with a change in equilibrium distance between the emitting ion and its immediate environment and it is commonly explained with the configuration coordinate diagram shown in figure 2.5 [17].

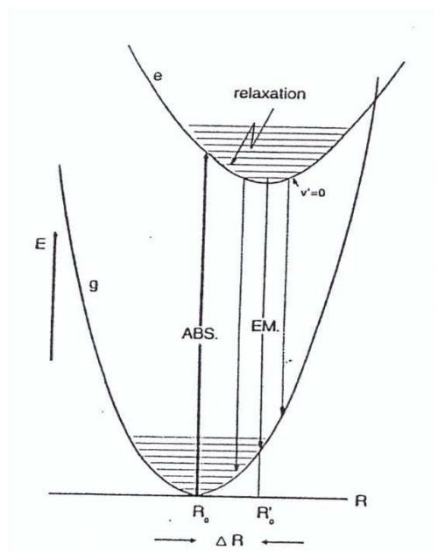


**Figure 2.5.** Configurational coordinate diagram [17].

As shown in figure 2.5, g and e represents the ground and excited states or levels, respectively. The mechanism can be explain as follows; after the phosphor material has been excited by the external radiation as shown in figure 2.1, an absorption ( $g \rightarrow e$ ) occurs and brings the centre in a high vibrational level of the excited state. Subsequently, the centre relaxes first to the lowest vibrational level  $v' = 0$  of the excited state by giving up the excess energy to the surroundings. From the lowest vibrational level, the emission ( $e \rightarrow g$ ) occurs in a broad band. The parabola offset is denoted by  $\Delta R$ . The energy difference between the maximum of the lowest excitation band and that of the emission band is called Stokes shift (see section 2.2.1) [17].

### 2.6.1 Some LC's

Although there are many LC's, in this study the focus is drawn more into the centres such as  $ns^2$ -type, transition metals and rare-earth ions. Each of these LC's are therefore discussed in the following sub-sections.

#### 2.6.1.1 $ns^2$ -type ions LC's

Ions with the electronic configuration  $ns^2$  for the ground state and  $nsnp$  for the first excited state ( $n = 4, 5, 6$ ) are called  $ns^2$ -type ions. Amongst others, these ions includes  $In^+$ ,  $Pb^{2+}$ ,  $Bi^{3+}$  and  $Tl^+$ . As for powder phosphors, excitation and emission spectra of  $Sn^{2+}$ ,  $Sb^{3+}$ ,  $Tl^+$ ,  $Pb^{2+}$ , and  $Bi^{3+}$  ions introduced into various oxygen-dominated host lattices have been extensively

studied [2]. As far as the current study is concern, only  $\text{Pb}^{2+}$  ion doping into the  $\text{ZnAl}_2\text{O}_4$  is discussed in chapter 4 and 9. The energy level diagrams and emission pathways are also discussed in chapter 4.

#### 2.6.1.2 Transition metal ions LC's

The electronic configuration in transition metal ions consists of optically active unfilled outer 3d shells. The unfilled shells cause the ions to present quite unique features [32]. The 3d transition metal ions utilized in commercial powder phosphors have three electrons (in the case of  $\text{Cr}^{3+}$  and  $\text{Mn}^{4+}$ ) or five electrons ( $\text{Mn}^{2+}$  and  $\text{Fe}^{3+}$ ) occupying the outermost 3d electron orbitals of the ions [2]. This study specifically focuses on  $\text{Cr}^{3+}$  ion. In chapter 5 and 9 we respectively report on the effects of  $\text{Cr}^{3+}$  mol% and the citric acid/Zn mole fraction on the  $\text{ZnAl}_2\text{O}_4$  (host). The energy levels and emissions pathways of  $\text{Cr}^{3+}$  ion as a LC's and impurity on the  $\text{ZnAl}_2\text{O}_4$  (host) crystal lattice are explained in details in chapter 5 and 9.

#### 2.6.1.3 Rare-earth ions LC's

The rare-earth elements usually comprise 17 elements consisting of the 15 lanthanides from La (atomic number 57) to Lu (atomic number 71), of Sc (atomic number 21), and of Y (atomic number 39). Their 4f orbital lies inside the ion and is shielded by the filled  $5s^2$  and  $5p^6$  orbitals [2,17]. The rare earth ions, either in their divalent or trivalent charge states, form a very important class of luminescence activators in phosphors and single crystals [33]. In this work, the following rare-earth metal ions;  $\text{Ce}^{3+}$ ,  $\text{Eu}^{3+}$ ,  $\text{Eu}^{2+}$  and  $\text{Tb}^{3+}$  and their energy levels as well as the emission pathways are discussed in details (see chapter 6 and 7). Chapter 6 focuses on the doubly doped  $\text{ZnAl}_2\text{O}_4$ : 0.1% Ce, x%  $\text{Eu}^{3+}$  system, while chapter 7 is focused on the triply doped  $\text{ZnAl}_2\text{O}_4$ : 0.1%  $\text{Ce}^{3+}$ , 0.1%  $\text{Eu}^{2+}$ , x%  $\text{Tb}^{3+}$  system.

### 2.6 Energy transfer (ET)

The process of ET in phosphors is the excitation between two or more luminescent centres referred to as the sensitizer (energy donor) and the activator (energy acceptor) [17]. The ions involved can either be identical or of different species (e.g. it can be the rare-earth and transition metal ions). The excitation residing in an ion can migrate to another identical ion that is in the ground state as a result of resonant ET when they are located close to each other. The ET between different ion species can also take place when they have closely matched energy levels. The ET results either in the luminescence enhancement or quenching [17,32].

In a situation of the ET process involving two luminescent centres (D and A) separated by distance R, and requires a certain interaction between these centres. The interaction can be an exchange interaction, radiation reabsorption or multipole-multipole interaction [34]. In general, the ET process can be explained by two phenomena, namely Dexter exchange and Förster resonance. In both phenomena, the energy transfer occurs by the nonradiative energy transfer mechanism. In the Dexter exchange mechanism, the donor and acceptor orbitals must overlap with each other. In the Förster resonance process the energy from the donor is transferred to the acceptor through a long range coulombic interaction, typically a dipole-dipole interaction or more generally multipole interaction [35].

Besides the energy transfer arising from the interaction between ions, the process can also occur from a host crystal to activators leading to host-excited luminescence [33]. As far as this study is concern, energy transfer was evaluated between non-identical rare-earth LC's and these is presented in chapter 6 and 7 for the double and triple doped systems, respectively.

## 2.7 Concentration quenching

Concentration quenching of luminescence is the reduction in the emission of a phosphor when the activator or co-activator concentration surpasses a certain critical value [36]. For an example, in this study, the critical value refers to the 1.5%  $\text{Pb}^{2+}$  and 0.01%  $\text{Cr}^{3+}$  in singly doped  $\text{ZnAl}_2\text{O}_4$  as shown in figure 4.5 and 5.9. This effects is shown to arise at the higher activators concentrations, that is; some fraction of the activators change to be the killers (are caused by incidental impurities (contamination) and inherent lattice defects that reduce the luminescence intensity of a phosphor) due to the local field disturbance [5,37]. In summary, the origin of this effect is thought to be caused by one of the following aspects [36]:

- ✓ Cross-relaxation (process in which the excited ion transfers only part of its energy to another ion) between the activators results in the loss of excitation energy from the emitting state. Thus, the emission colour of a phosphor can change with the increase in activator concentration when the concentration quenching is due to cross-relaxation occurs on a particular level among several emitting levels.
- ✓ Increased activator concentration facilitates migration of excitation energy to remote killers.
- ✓ The pairing or coagulation of activator ions converts them into quenching centres.

## 2.8 Crystal structure of $MAl_2O_4$ ( $M = Zn, Al$ )

$MgAl_2O_4$  and  $ZnAl_2O_4$  have the spinel structure as shown in figure 2.5, belonging to the cubic space group  $Fd\bar{3}m$ . Spinel represent an important class of chemically and thermally stable crystalline materials [35,38]. The general formula of spinel is  $AB_2O_4$  (where  $A = Zn^{2+}$  or  $Mg^{2+}$  and  $B = Al^{3+}$ ), the unit cell formula of spinel is expressed as  $A_8B_{16}O_{32}$ . The 32 oxygen ions form a face-centred cubic lattice, providing 64 tetrahedral sites and 32 octahedral sites. In normal spinel the divalent A cations are located in one-eighth of the tetrahedral sites and the trivalent B cations occupy one-half of the octahedral sites [35]. Note that the  $AB_2O_4$  spinels can also crystallize in the “normal” or “inverse” spinel structures. The occupation or substitution (see figure 2.3) of these two sites is decided by various factors, such as ionic size, cationic charge (see chapter 5 in case of  $Cr^{3+}$ ), electron distribution and electronic state. The situation in which the substitution of  $Mg^{2+}$  at an  $Al^{3+}$  site and the substitution of  $Al^{3+}$  at an  $Mg^{2+}$  site is elaborated in chapter 6.

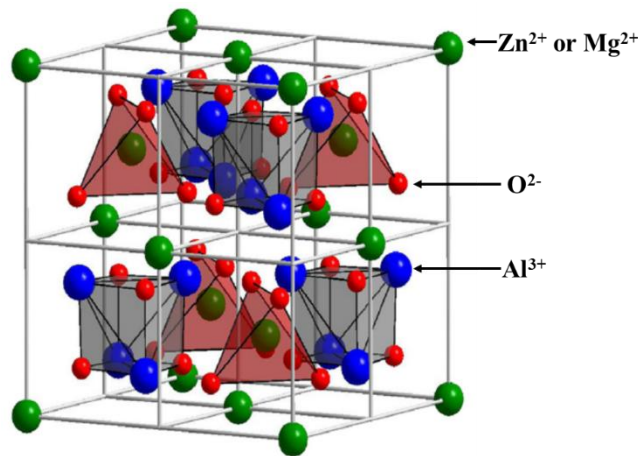


**Figure 2.6.** Crystal structure of the spinel  $AB_2O_4$  ( $A = Zn$  or  $Mg$  and  $B = Al$ ) [40].

## References

1. J. A. DeLuca, *Journal of Chemical Education* **57** (1980) 541.
2. W. M. Yen, S. Shionoya, H. Yamamoto, *Phosphor handbook second edition*; Taylor & Francis Group, LLC, USA, 2006.
3. T. Matsuzawa, Y. Aoki, N. Takeuchi, Y.A Murayama, *J. Electrochem. Soc.* **143** (1996) 2670.
4. W. M. Yen, S. Shionoya, *Fundamentals of phosphors*, CRC Press, USA, 2007.
5. S. Shionoya, W.M. Yen, *Phosphors Handbook*, CRC Press, USA, 1998.
6. J. Ball, A. D. Moore *Essential physics for radiographers*, Blackwell Publishing, First edition, Oxford, 1979.
7. J. C. Whitaker, *The Electronics Hand Book second edition*, CRC Press, USA, 1996.
8. [http://www.tf.uni-kiel.de/matwis/amat/admat\\_en/kap\\_5/advanced/t5\\_2\\_4.html](http://www.tf.uni-kiel.de/matwis/amat/admat_en/kap_5/advanced/t5_2_4.html) (taken on 18/11/2014).
9. J. Wilson, J. Hawkes, *Optoelectronics an introduction*, Prentice Hall Europe, London New York, 1998.
10. K. N. Shinde, S. J. Dhoble, H. C. Swart, K. Park, *Phosphate Phosphors for Solid-State Lighting*, Springer-Verlag, Berlin, 2012.
11. S. Boggs, D. Krinsley, *Application of Cathodoluminescence imaging to the study of sedimentary rocks*, Cambridge University Press, England, 2006.
12. D. R. Vij, *Luminescence of Solids*, Plenum Press, New York, 1998.
13. W. Y. Liang, *Phys. Educ.* **5** (1970) 226.
14. M. S. Dlamini, PhD thesis, University of the Free State, 2008.
15. H. Yang, PhD dissertation, University of Florida, Florida, 2003.
16. H. Tang, G. Xu, L. Weng, L. Pan, L. Wang, *Acta Materialia* **52** (2004) 1489.
17. G. Blasse, B. C. Grabmier, *Luminescent Marerials*, Springer, Verlag Berlin Heidelberg, 1994.
18. R. D. Blackledge, *Forensic analysis on the cutting edge*, John Willey & Sons Publications, USA, 2007.
19. A. J. J. Bos, *Radiation Measurements* **41** (2007) S45.
20. R. Xie, Y. Q. Li, N. Hirosaki, H. Yamamoto, *Nitride Phosphors and Solid-State Lighting*, Taylor and Francis, New York, 2011.

21. S. Basun, G. F. Imbusch, D. D. Jia, W. M. Yen, *J. Lum.* **104** (2003) 283.
22. J. T. Randall, M. H. F. Wilkins, *Proc. R. Soc. London A* **184** (1945) 366.
23. G. F. J. Garlick, A. F. Gibson, *Proc. Phys. Soc.* **60** (1948) 574.
24. C. E. May, J. A. Partridge, *J. Chem. Phys.* **40** (1964) 1401.
25. C. F. Klingshirn, *Semiconductor Optics*, Springer, Berlin, 1995.
26. <http://www.uccs.edu/~tchriste/courses/PHYS549/549lectures/defects.html> (taken on 04/12/2014).
27. <http://www.authorstream.com/Presentation/ganeshbilla-1254468-defects-in-crystals/> (taken on 04/12/2014).
28. K. T. Jacob, S. Raj, L. Rannesh, Department of Materials Engineering, Indian Institute of Science, Bangalore, India  
<http://core.kmi.open.ac.uk/download/pdf/11613418.pdf> (taken 08/12/2014)
29. J. M. Córdoba, E. Chicardi, M. A. Avilés, F. J. Gotor, *Intermetallics* **19** (2011) 1688.
30. W. Martienssen, H. Warlimont, *Handbook of Condensed Matter and Data Materials*, Springer, USA, 2005.
31. C. R Ronda, *Luminescence from Theory to Applications*, Willy-VCH, Germany, 2008.
32. B. D. Bem, PhD thesis, University of the Free State, 2010.
33. L. A. Riseberg, H. W. Moos, *Phys. Rev.* **174** (2) (1968) 429.
34. L. Jiang, C. Chang, D. Mao, C. Feng, *Materials Science and Engineering B* **103** (2003) 273.
35. W. A. I. Tabaza, PhD thesis, University of the Free State, 2014.
36. E. Nakazawa, *Fundamentals of Luminescence*. CRC Press: New York, 2007.
37. M. Garcia-Hipolito, R. Martinez, O. Alvarez-Fregoso, E. Martinez, C. Falcony, *J. Lumin.* **93** (2001) 13.
38. G. Lakshminarayana, L. Wondraczek, *J. Solid State Chemistry* **184** (2011) 1931.

## Chapter 3: Synthesis and characterization techniques

*“Mathematical physics is in the first place physics and it could not exist without experimental investigation.”*

*~ Peter Debye*

### 3.1 Introduction

In this chapter a brief description of the doped  $\text{MAl}_2\text{O}_4$  ( $\text{M} = \text{Zn}$  or  $\text{Mg}$ ) powder samples synthesis method; the sol-gel and characterization techniques used, which are: XRD, TGA, FTIR, SEM and EDXS, TEM, TOF-SIMS, UV-Vis, PL and TL are discussed.

### 3.2 Synthesis techniques

The growth of nanoscience and nanotechnology in the last decade has been made possible by the success in the synthesis of nanomaterials. The synthesis of the nanomaterials includes control of size, shape and structure of the materials [1]. Numerous methods of preparation of these nanomaterials such as solid state reaction [2], co-precipitation [3], hydrothermal [4], combustion [5] and sol-gel [6] have been developed. For the purpose of this study, sol-gel method was used to synthesize the powder samples and the steps followed are illustrated in figures 6.1, 7.1 and 8.1.

From the historical point of view, the earliest sol-gel derived material was reported by M. Ebelmen in 1845 at the Manufacture de Ceramiques de Servres in France [7]. The potential of the sol-gel method was rediscovered in the 1980's due to its usefulness during the synthesis of various materials of practical importance such as optical glasses and solid state laser materials [8]. Since then the method has received considerable attention and has been extensively investigated by the researchers around the world.

Sol-gel method is one of the traditional wet chemical techniques which occurs in liquid solution of organometallic and salt precursors for producing metal oxide nanoparticles through chemical processes such as hydrolysis, gelation, followed by drying, and finally thermal treatment. In general, the method can be defined as the preparation of ceramic materials by preparation of sol, gelation of sol and removal of solvent [7,9]. A sol differs

from a solution in that a solution is a single-phase system, while a sol is defined as colloidal particles suspended in a liquid solvent from which a gel can be formed. A sol can be stabilized by peptization, i.e. the addition of peptizing agents (e.g.  $\text{HNO}_3$ ) which form an electrically charged layer around each particle; electrostatic repulsion then prevents the particles to aggregate. Under suitable chemical and thermal conditions, the particles in some sols can be made to react or interact electrostatically so that they form a continuous, three dimensional network of connected particles called gel. A gel network consists of submicrometre pores and a polymeric chain whose average length is of the order of microns [8,10]. The gels are usually dried at room or lower temperatures, which is subsequently annealed at higher temperature to form powders.

In sol-gel processing, the most popular precursors are metal alkoxides because they react readily with water. Other precursors may be organic salts which can be dissolved in alcohols for an example. The chemistry processes involved in sol-gel method have been reviewed in detail by Brinker et al. [11]. In comparison with other synthesis techniques, the advantages of sol-gel methods, amongst others, include the following:

- ✓ the formation products of high purity and homogeneity;
- ✓ opens a possibility of incorporating variety of foreign atoms in a host matrix, which is one of the basis of the synthesis of nanophosphors;
- ✓ lower reaction temperature;
- ✓ the particle size of the final product can be easily controlled;
- ✓ requires considerably less equipment;
- ✓ structures of different shapes can easily be fabricated; and
- ✓ can be adapted to other techniques such as spray coating, roll coating,

As far as this study is concern, the details of the synthesis procedure followed are presented in experimental section of each chapter.

### 3.3 Characterization techniques

#### 3.3.1 X- ray diffraction (XRD)

XRD is a versatile analytical non-destructive technique used to investigate structural properties of solid materials, which include ceramics, metals, electronic materials, organics and polymers. These material may be powders, multilayer thin films, fibers and polymers. Depending on the desired measurements, these solid materials may be in different forms such

as powders, multilayer thin films, fibers, sheets or irregular. XRD is used for identifying major constituents, degree of crystallinity in a mixture of amorphous and crystalline substances and is also an effective tool for determining the phase, purity, crystallite sizes and lattice constant [12,13].

XRD consist of three basic elements, which are: an X-ray tube, a sample holder, and an X-ray detector. The X-rays are produced in a cathode ray tube by heating a filament to produce electrons. When the voltage is applied, the electrons will accelerate towards the target material (the target materials that are usually used are Cu, Fe, Mo and Cr). When electrons have sufficient energy to dislodge the inner shell electrons of the target material, characteristic X-ray spectra will be produced. These X-ray spectra consist of several components and the most common are  $K_{\alpha}$  and  $K_{\beta}$  [14]. The x-ray spectra generated by this technique provide a structural fingerprint of the unknown material and can easily be distinguished by comparison with reference data. Usually electronic databases such as the International Centre for Diffraction Data (ICDD) are used for this comparison [12]. In XRD spectroscopy the intensity of the diffracted x-rays is measured as a function of diffraction angle  $2\theta$  and the specimen's orientation. The x-ray diffractometer used in this study is Bruker AXS Discover diffractometer with  $\text{CuK}\alpha$  ( $1.5418\text{\AA}$ ) radiation).

### 3.3.2 Thermo gravimetric analysis (TGA)

TGA is a method of thermal analysis in which changes in physical and chemical properties of materials are measured as a function of increasing temperature (with constant heating rate), or as a function of time (with constant temperature and/or constant mass loss). TGA can provide information about physical phenomena, such as second-order phase transitions, including vaporization, sublimation, absorption, adsorption, and desorption. In addition, the technique can also provide information about chemical phenomena including chemisorptions, desolvation (especially dehydration), decomposition, and solid-gas reactions (e.g., oxidation or reduction) [15].

TGA relies on a high degree of precision in three measurements: mass change, temperature, and temperature change. Therefore, the basic instrumental requirements for TGA are a precision balance with a pan loaded with the sample, and a programmable furnace. The furnace can be programmed either for a constant heating rate, or for heating to acquire a constant mass loss with time. The sample is placed in a small, electrically heated furnace equipped with a thermocouple to monitor accurate measurements of the temperature by

comparing its voltage output with that of the voltage-versus-temperature table stored in the computer's memory. A reference sample may be placed on another balance in a separate chamber. The atmosphere in the sample chamber may be purged with an inert gas to prevent oxidation or other undesired reactions [15].

In this study, the TGA was done using a Perkin Elmer TGA7 in the temperature range of 20 - 580 °C at a heating rate of 10 °C/min under an air flux. Approximately 80 mg of the ZnAl<sub>2</sub>O<sub>4</sub> gel was placed in open alumina pan and heated from 25 °C to ~ 590 °C. A typical TGA curve of the ZnAl<sub>2</sub>O<sub>4</sub> nano-powders is shown in figure 4.1 and the changes taking place are explained in details in section 4.3.1.

### 3.3.3 Fourier-transform infrared (FTIR)

FTIR spectroscopy is based on the idea of the interference of radiation between two beams to yield an *interferogram*. The latter is a signal produced as a function of the change of path length between the two beams. The two domains of distance and frequency are interconvertible by the mathematical method of *Fourier-transformation* [16]. In infrared spectroscopy, IR radiation is passed through a sample. Some of the infrared radiation is absorbed by the sample and some of it is passed through (transmitted). The resulting spectrum represents the molecular absorption and transmission, creating a molecular fingerprint of the sample. Like a fingerprint no two unique molecular structures produce the same infrared spectrum. This makes infrared spectroscopy useful for several types of analysis such as; identifying unknown materials, determining the quality or consistency of a sample and to determine the amount of components in a mixture [17].



**Figure 3.1.** Basic components of an FTIR spectrometer [16].

The basic components of an FTIR spectrometer are illustrated in figure 3.1. The IR radiation emerging from the source is passed through an interferometer to the sample before reaching a detector. Upon amplification of the signal, in which high-frequency contributions have been eliminated by a filter, the data are converted to digital form by an analog-to-digital converter and transferred to the computer for Fourier-transformation [16]. The FTIR spectroscopy used

in this study is Perkin Elmer Spectrum 100 FTIR spectrometer. The typical spectra for the  $\text{ZnAl}_2\text{O}_4$  gel and powder samples are shown in figure 4.3 and the bands therein are explained in section 4.3.3.

### 3.3.4 Scanning electron microscopy (SEM) and energy dispersive x-ray spectroscopy (EDXS)

SEM is a type of electron microscope that produces images of a sample by scanning it with a focused beam of electrons. During SEM measurements, the electrons interact with atoms in the sample, producing various signals that can be detected and that contain information about the sample's surface topography and composition. The electron beam is generally scanned across the sample and the beam's position is combined with the detected signal to produce an image [18,19]. Figure 3.2 shows schematic diagram of an SEM.

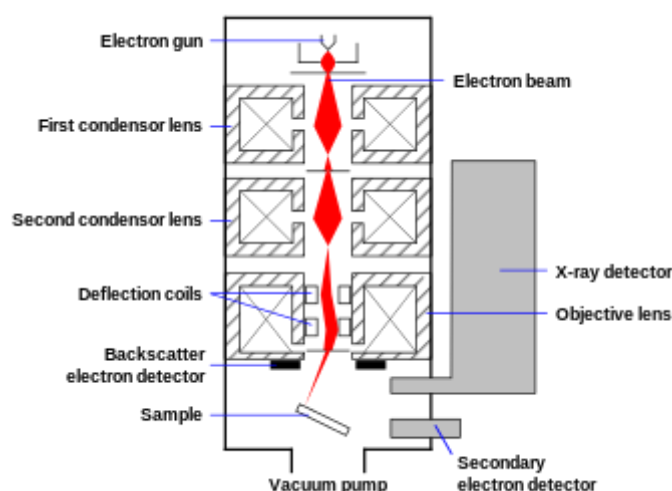


**Figure 3.2.** Schematic of an SEM

The electron beam is emitted from electron gun and accelerated towards to the surface of the sample. The electron beam generally has energies that range from a few keV to 50 keV. The beam is collimated by electromagnetic condenser lenses, focused by an objective lens, and then scanned across the surface of the sample by electromagnetic deflection coils. A metal sample is conductive and requires no preparation before being studied. Non-metallic samples such as ceramics need to be prepared with a thin conductive coating such as Au to prevent charging [20]. The coating process is done by using a sputter coater.

The types of signals produced by a SEM include secondary electrons (SE), back-scattered electrons (BSE), characteristic X-rays, light (cathodoluminescence) (CL), specimen current and transmitted electrons. Secondary electron detectors are standard equipment in all SEMs, but it is rare that a single machine would have detectors for all possible signals. The signals result from interactions of the electron beam with atoms at or near the surface of the sample. The primary imaging method is by collecting secondary electrons that are released by the sample. The electrons are detected by a scintillation material that produces flashes of light from the electrons. The light flashes are then detected and amplified by a photomultiplier tube. By correlating the sample scan position with the resulting signal, an image can be formed that is strikingly similar to what would be seen through an optical microscope [18,20].

Beside the emitted electrons, BSE are also produced by the interaction of electrons with the sample. BSE are beam electrons that are reflected from the sample by elastic scattering. BSE are often used in analytical SEM along with the spectra made from the characteristic X-rays (are emitted when the electron beam removes an inner shell electron from the sample, causing a higher-energy electron to fill the shell and release energy), because the intensity of the BSE signal is strongly related to the atomic number ( $Z$ ) of the specimen. BSE images on the SEM coupled with an x-ray analyzer such as the energy dispersive x-ray spectrometer (EDXS) can provide information about the distribution of different elements in the sample [18,21]. Although SEM is one of the most important technique used to characterize the materials morphology on the nanometre and nowadays even on the atomic scale, it is however, noted that one has to be to be aware of some limiting aspects such as [22]:

- ✓ All specimens are in high vacuum and probably have another shape in a liquid or gel-like surrounding.
- ✓ The images reveal only a small fragment of the whole sample raising the possibility that the region analyzed may not be characteristic of the whole sample.
- ✓ The high energy electron beam incident on the sample may probably change it.

In this study, the surface morphology and elemental composition of the phosphor powders were investigated using a Shimadzu Superscan SSX-550 electron microscope (SEM) coupled with an energy dispersive x-ray spectroscope (EDS). The typical SEM images and EDS spectra are presented and explained in chapter 4-9 and figure 8.5, respectively.

### 3.3.5 Transmission Electron Microscopy (TEM)

In TEM, the thin solid or diluted sample can be analyzed by bombarding the sample with a focused beam of electrons under high vacuum [23]. The focused electron beam in TEM can be used to produce images and to determine the crystallographic and morphological information of the material, including the particle shape and size distribution in the sample. TEM requires an ultra high vacuum and the accelerating voltage is considerably higher than in an SEM, typically 100-400 kV. Powder samples to be measured by TEM are often ground and then dispersed in ethanol. A drop is then placed onto an amorphous support film on a circular metal grid generally copper). The specimen must be no more than a few hundred nanometres in thickness (less than 200 nm) [24].

Owing to its high resolution, TEM is in principle appropriate for providing topographic data in the nanometer range. In addition to the high resolution, TEM provides the advantage that not only the sample surface, but also the interior, e.g., the arrangement of the layers, is visualized due to the contrasts in the material [25].

In this study the images of nano-phosphor particles were obtained using a JEOL JEM 2100 containing a LaB<sub>6</sub> filament. Typical TEM images are illustrated in figure 6.6 and 8.7 and are discussed in sections 6.3.2 and 8.3.3, respectively.

### 3.3.6 Time-of-Flight Secondary Ion Mass Spectroscopy (TOF-SIMS)

TOF-SIMS is a surface-sensitive analytical method that uses a pulsed ion beam (Cs or microfocused Ga) to remove molecules from the very outermost surface of the sample. The particles are removed from atomic monolayers on the surface (secondary ions). These particles are then accelerated into a “flight tube” and their mass is determined by measuring the exact time at which they reach the detector (i.e. time-of-flight). Three operational modes are available using ToF-SIMS: surface spectroscopy, surface imaging and depth profiling [26].

ToF-SIMS uses a focused, pulsed particle beam (typically Cs or Ga) to dislodge chemical species on a materials surface. Particles produced closer to the site of impact tend to be dissociated ions (positive or negative). Secondary particles generated farther from the impact site tend to be molecular compounds, typically fragments of much larger organic macromolecules. The particles are then accelerated into a flight path on their way towards a detector. Because it is possible to measure the “time-of-flight” of the particles from the time

of impact to detector on a scale of nano-seconds, it is possible to produce a mass resolution as fine as 0.00x atomic mass units (i.e. one part in a thousand of the mass of a proton). Under typical operating conditions, the results of TOF-SIMS analysis include [12]:

- ✓ a mass spectrum that surveys all atomic masses over a range of 0-10,000 amu,
- ✓ the rastered beam produces maps of any mass of interest on a sub-micron scale, and
- ✓ depth profiles are produced by removal of surface layers by sputtering under the ion beam.

In this study the TOF-SIMS were performed using the Iontof SIMS<sup>5</sup>. Typical elementary mapping and mass spectrum are presented in figure 5.3 and 5.4, respectively.

### 3.3.7 Ultraviolet-visible (UV-Vis)

UV-Vis refers to absorption or reflectance spectroscopy in the ultraviolet-visible spectral region. This means it uses light in the visible and adjacent (near-UV and near-infrared [NIR]) ranges. This technique is based on the reflection of light in the ultraviolet (10–420 nm), visible (420–700 nm) and near-infrared (700–2500 nm) regions by a powder sample [27].

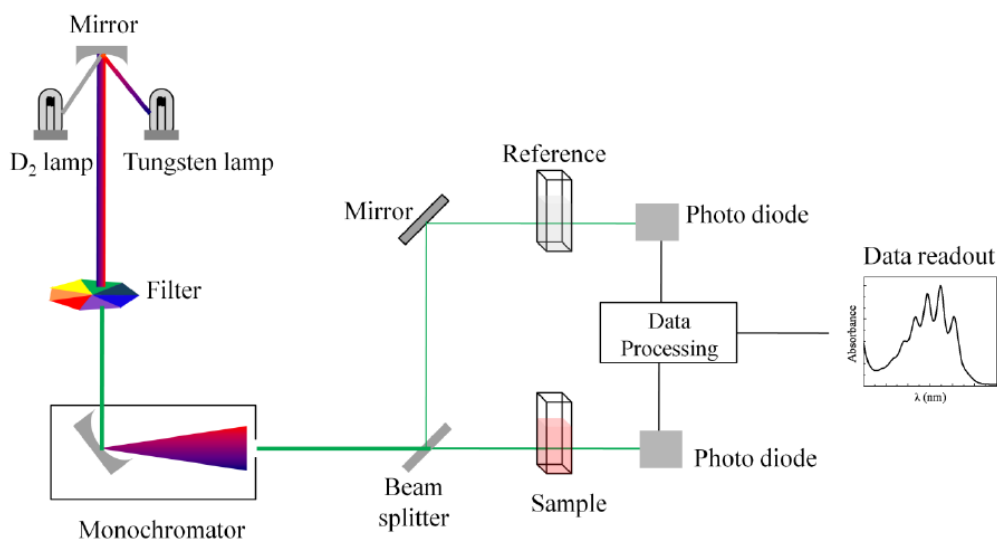


**Figure 3.3.** Schematic of UV-visible spectrophotometer [27].

The basic parts of a spectrophotometer are a light source, a holder for the sample, a diffraction grating in a monochromator or a prism to separate the different wavelengths of light, and a detector as shown in figure 3.3. The radiation source is usually a deuterium discharge lamp for UV measurements and a tungsten-halogen lamp for visible measurements. The detector converts a light signal into an electrical signal and is typically a photodiode or photomultiplier tube (PMT). Single photodiode detectors and photomultiplier tubes are used with scanning monochromators, which filter the light so that only light of a single wavelength reaches the detector at one time. First a background scan is recorded without the sample present, and then the light passing through the sample ( $I$ ) is compared to a reference beam ( $I_0$ ) to obtain the ratio  $I/I_0$  which does not depend on changes of the incident light intensity and is called the transmittance [24,27]:

$$T = \frac{I}{I_0} \quad (3.1)$$

In a diffuse reflectance spectrum, the ratio of the lights scattered from a ( $> 2-3$  mm) thick layer of sample and an ideal non-absorbing reference sample is measured as a function of the wavelength  $\lambda$  (i.e.  $F_{SKM}(R_\infty)$  vs  $\lambda$  in nm). The relation between the diffuse reflectance of the sample ( $R_\infty$ ), absorption (K) and scattering (S) coefficients are related by the Schuster–Kubelka–Munk (SKM) remission function [28]:

$$F_{SKM} = \frac{(1 - R_\infty)^2}{2R_\infty} = \frac{K}{S} \quad (3.2)$$

The SKM remission function relates the experimentally determined diffuse reflectance of a thick sample to  $K$  and  $S$ . At constant  $S$ ,  $F_{SKM}(R_\infty)$  is directly proportional to  $K$  and a plot of  $F_{SKM}(R_\infty)$  vs concentration of absorbing species should be a straight line passing through the origin. The remission function also depends strongly on particle size for weak absorbers but not for strong absorbers which absorb almost all the incident photons. Although the technique have been extensively used to study materials, it is however has limitations due to the difficulty in interpreting the large bandwidths and specular reflectance often observed in the spectra [28].

In this study the diffuse reflectance spectra were recorded using a Lambda 950 UV–Vis spectrophotometer with an integrating sphere using spectralon as a reflectance standard. Typical spectrums for  $ZnAl_2O_4$  and  $MgAl_2O_4$  are shown in figure 5.7 and 7.5, respectively.

### 3.3.8 Photoluminescence (PL)

PL spectroscopy is a contactless, non-destructive method to probe the electronic structure of materials. As discussed in chapter 2 (section 2.2) that when a radiation (e.g. light) of sufficient energy is illuminated a material, photons are absorbed and excitations are created. In this technique, a sample is excited by photons (generally in the UV range) and the excess energy released by the sample through the emission of light is detected and recorded for different modes, i.e. excitation and emission [24,29].

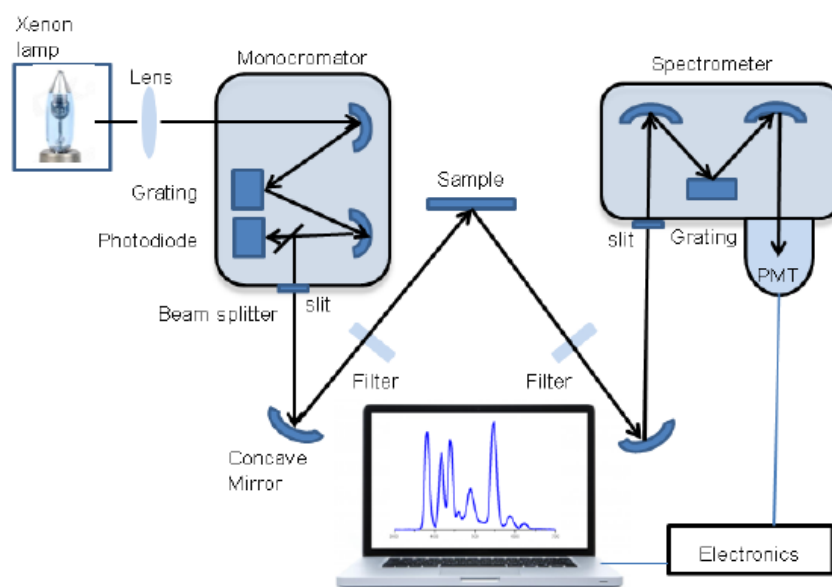


**Figure 3.4.** Schematic diagram of PL spectrometer [24].

The schematic diagram of general basic equipment for PL is shown in figure 3.4. This instrument has a source (exciting light) of white light from a xenon lamp which is collected by an elliptical mirror and directed to the entrance slit of a monochromator. Xenon lamps are useful because of their high intensity at all wavelengths ranging upward from 250 nm. The slits of the monochromator determine the amount of monochromatic light that is used to illuminate the sample. The emitted light is analysed with a spectrometer and detected with a photomultiplier tube (PMT). The output of the PMT signal is amplified and recorded [24].

In this study, PL spectra were recorded at room temperature using a Hitachi F-7000 fluorescence spectrophotometer and all measurements were recorded using the phosphorescence mode. Typical spectrums are presented and discussed in details in chapters 4 - 9.

### 3.3.9 Thermoluminescence (TL)

TL is a sensitive technique for studying defects and defect concentrations in insulators. TL spectra provide important information on the nature of both intrinsic and extrinsic defects, and on their spatial relationships within crystals, by allowing both temperature-dispersive separation of different traps (defects) and wavelength-dispersive separation of radiative recombination centres. TL records metastable defects, dispersed throughout the bulk of the material, with charge states within the band gap [30]. TL measurements are relatively simple to make. An irradiated sample is placed on a heater strip, in an inert atmosphere or under vacuum, the temperature is then raised at a constant rate (e.g.  $10^{\circ}\text{C}\cdot\text{min}^{-1}$ ) and the emitted light is detected by a photomultiplier tube with either current or photon counting electronics. In principle, different depth traps release charge at different temperatures so that the TL signal gives a temperature-dispersive measure of the trap population [30].

In this study, TL analyses were done above room temperature by using Nucleonix 1009I TL reader. Typical TL spectrum for  $\text{ZnAl}_2\text{O}_4: 1.5\% \text{Pb}^{2+}$  nanopowder is illustrated in figure 8.11.

## References

1. Y. Gogotsi, *Nanomaterials Handbook, Materials Science at the Nanoscale*, Routledge Publishers, USA, 2006.
2. N. J. Van de Laag, S. G. Snel, P. C. M. M. Magusin, G. de With, *J. Eur. Ceram. Soc.* **4 (8)** (2004) 2417.
3. F. L. Yuan, P. Hu, C. L. Yin, S. L. Huang, J. L. Li, *J. Mater. Chem.* **13** (2003) 634.
4. Z. Chen, E. Shi, Y. Zheng, W. Li, N. Wu, W. Zhong, *Mater. Lett.* **56** (2002) 601.
5. A. K. Adak, A. Pathak, P. Pramanik, *J. Mater. Sci. Lett.* **17** (1998) 559.
6. M. Nikl, A. Novoselov, E. Mihokova, K. Polak, M. Dusek, B. McClune, A. Yoshikawa, T. Fukuda, *J. Phys. Condens. Mat.* **17** (2005) 3367.
7. S. M. Attia, J. Wang, G. Wu, J. Shen, J. Ma, *J. Mater. Sci. Technol.* **18** (2002) 211.
8. W. M. Yen, M. J. Weber, *Inorganic Phosphors*, Routledge Publishers, USA, 2004.
9. T. Aitasalo, J. Hölsä, J. Jungner, H. Lastusaari, M. Niittykoski, J. Parkkinen, M. Valtonen, *R. Opt. Mater.* **26** (2004) 113.
10. S. Elliot, *The Physics and Chemistry of Solids*, John Willey and Sons, New York, 1998, pp 28
11. C. J. Brinker, G. W. Scherer, *Sol-Gel Science: The Physics and Chemistry of Sol-Gel Processing*, Academic Press, San Diego, 1990. ISBN 0121349705
12. G. Cao, *Nanostructures and Nanomaterials: Synthesis, Properties & Applications*, 6<sup>th</sup> edition, London, 2004.
13. B. D. Cullity, S. R. Stock, *Elements of X-Ray Diffraction*. 3rd Edition, Prentice-Hall Inc. New Jersey, 2001.
14. B. M. Mothudi, PhD thesis, University of the Free State, 2009.
15. [http://en.wikipedia.org/wiki/Thermogravimetric\\_analysis](http://en.wikipedia.org/wiki/Thermogravimetric_analysis) (taken 02/01/2015)
16. B. Stuart, *Infrared Spectroscopy: Fundamentals and Applications*, John Wiley & Sons, 2004. ISBNs: 0-470-85427-8
17. <http://mmrc.caltech.edu/FTIR/FTIRintro.pdf> (taken 02/01/2015)
18. [http://en.wikipedia.org/wiki/Scanning\\_electron\\_microscope](http://en.wikipedia.org/wiki/Scanning_electron_microscope) (taken 02/01/2015)
19. D. K. Schroder, *Semiconductor Material and Device Characterization, 3rd Ed.*, John Wiley & Sons (Hoboken) 2006.

20. R. F. Egerton, *Physical Principles of Electron Microscopy: An Introduction to TEM, SEM, and AEM*, Springer Media (New York, 2005).
21. B. G. Yacobi, D. B. Holt, L. L. Kazmerski, *Microanalysis of Solids*. New York, Plenum Press, 1994.
22. J. I. Goldstein, *Scanning Electron Microscopy and X-ray Microanalysis*. Plenum Press, New York, 1981.
23. M. Kuno, *Introduction to Nanoscience and Nanotechnology: A Workbook*, Notre Dame, 2005.
24. W. A. I. Tabaza, PhD thesis, University of the Free State, 2014.
25. M. Kohler, W. Fritzsche, *Nanotechnology, An Introduction Nanostructuring Techniques*, Wiley-VCH, 2003.
26. [http://serc.carleton.edu/research\\_education/geochemsheets/techniques/ToFSIMS.html](http://serc.carleton.edu/research_education/geochemsheets/techniques/ToFSIMS.html) (taken 02/01/2015)
27. [http://en.wikipedia.org/wiki/Ultraviolet%E2%80%93visible\\_spectroscopy](http://en.wikipedia.org/wiki/Ultraviolet%E2%80%93visible_spectroscopy) (taken 02/01/2015)
28. G. Ranga Rao, H. Ranjan Sahu, *Proc. Indian Acad. Sci. (Chem. Sci)*, **113** (2001) 651.
29. [http://www.nrel.gov/pv/measurements/photoluminescence\\_spectroscopy.html](http://www.nrel.gov/pv/measurements/photoluminescence_spectroscopy.html) (taken 02/01/2015)
30. [http://rruff.info/doclib/MinMag/Volume\\_57/57-387-217.pdf](http://rruff.info/doclib/MinMag/Volume_57/57-387-217.pdf) (taken 02/01/2015)

## Chapter 4: Effects of $\text{Pb}^{2+}$ ions concentration on the structure and PL intensity of $\text{Pb}^{2+}$ -doped $\text{ZnAl}_2\text{O}_4$ nanocrystals synthesized using sol-gel process

*“There is no such thing as failure. There are only results.”*

*~ Anthony Robbins*

### 4.1 Introduction

Doped and undoped semiconductor nanoparticles have received major interest in the scientific community because of their unique and superior properties, such as size-dependent optical properties [1].  $\text{ZnAl}_2\text{O}_4$  is one of the wide-band gap ( $\sim 3.8$  eV) semiconductors being considered for the photoelectronic devices, UV-transparent conductor, sensor, and dielectric material [2-4].  $\text{ZnAl}_2\text{O}_4$  have the chemical formula  $\text{AB}_2\text{O}_4$ , where A is  $\text{Zn}^{2+}$  ion that occupies a tetrahedral and B represent  $\text{Al}^{3+}$  ion which occupies octahedral sites of a cubic crystal [5].  $\text{ZnAl}_2\text{O}_4$  and other spinels are known to be suitable host lattice for various dopants or activator atoms [6,7]. For instance, there have been several reports on the rare earth and transition metal ions doped  $\text{ZnAl}_2\text{O}_4$  phosphor, and most of these studies focus more on the well-known luminescing dopants such as  $\text{Mn}^{2+}$ ,  $\text{Eu}^{2+}$ ,  $\text{Tb}^{3+}$ , etc. [3]. Apart from the rare earths and transition metal, a group of so called heavy  $ns^2$  metal ions such as  $\text{Tl}^+$ ,  $\text{Pb}^{2+}$  and  $\text{Bi}^{3+}$  luminescing dopants have been studied in a considerable number of hosts [8,9]. In particular, the luminescence of the  $\text{Pb}^{2+}$  ion is quite diverse and strongly depends on the environmental condition of  $\text{Pb}^{2+}$  in a host lattice [10,11]. The nature of  $\text{Pb}^{2+}$  ion luminescence in complex oxides usually consists of emission bands in the UV and visible ranges [12]. The UV emission is ascribed to the  $^3\text{P}_{0,1,2} \rightarrow ^1\text{S}_0$  transition in the  $\text{Pb}^{2+}$  monomer center. While the visible emission is ascribed to emission from the D-level, which is believed to originate from a charge transfer transition [10,13]. Many fabrication methods of  $\text{ZnAl}_2\text{O}_4$  phosphor such as solid state reaction [14], co-precipitation [15], hydrothermal [16], combustion [17] and sol-gel [18] have been developed. As an alternative, in this work, we have adopted the sol-gel method [18], which is known to be a low-temperature technique, in order to obtain a low cost green phosphor for use in applications such as x-ray imaging device, low pressure lamps, and

S.V. Motlounge et al. / J. Sol-Gel Sci. Technol. **70** (2014) 422-427.

high-energy physics [18]. In view of these, this paper, reports on the sol-gel synthesis of undoped and  $\text{Pb}^{2+}$ -doped  $\text{ZnAl}_2\text{O}_4$  at a very low temperature ( $\sim 80\text{ }^\circ\text{C}$ ). The effects of  $\text{Pb}^{2+}$  content at a range of 0 - 5 mol% on the structural and luminescence properties were investigated with the aim of fabricating UV down-conversion phosphor materials that can be used in different types of light emitting devices.

## 4.2 Experimental

The undoped and  $\text{Pb}^{2+}$ -doped  $\text{ZnAl}_2\text{O}_4$  nanocrystals were synthesized using a well-known sol-gel technique [18].  $\text{Zn}(\text{NO}_3)_2 \cdot 6\text{H}_2\text{O}$  (98%),  $\text{Al}(\text{NO}_3)_3 \cdot 9\text{H}_2\text{O}$  (98.5%) and Citric acid,  $\text{C}_8\text{H}_8\text{O}_7 \cdot \text{H}_2\text{O}$  (99%) were dissolved in deionized water. The sols stoichiometric molar ratio of Zn:Al was 2:1. Specified amounts of  $\text{Pb}(\text{NO}_3)_2$  was added in the solution to dope with different mol% of  $\text{Pb}^{2+}$  ions. The  $\text{Pb}^{2+}$  content was varied at the range of 0 - 5 mol%. In all samples, the heating temperature was kept below  $80\text{ }^\circ\text{C}$  while constantly stirring on a magnetic stirrer until the transparent gels of the mixed metal citrates were formed. The gels were dried at room temperature for two days and then in an oven kept at a temperature of  $145\text{ }^\circ\text{C}$ . The white dried gels were ground into fine powders and were subsequently annealed at  $800\text{ }^\circ\text{C}$  in a furnace for an hour. The samples were then taken for the characterization. Thermogravimetric analysis was carried out using a Perkin Elmer TGA7 in the temperature range of  $20 - 580\text{ }^\circ\text{C}$  at a heating rate of  $10\text{ }^\circ\text{C}/\text{min}$  under an air flux. The stretching mode frequencies were determined using a Perkin Elmer Spectrum 100 FTIR spectrometer. The crystal structure of the samples was characterized by X-ray powder diffraction (Bruker AXS Discover diffractometer) with  $\text{CuK}\alpha$  ( $1.5418\text{ \AA}$ ) radiation). The surface morphology of the phosphor powders was analyzed using a Shimadzu Superscan ZU SSX-550 scanning electron microscope (SEM). Photoluminescent spectra were recorded at room temperature using a Hitachi F-7000 fluorescence spectrophotometer.

## 4.3 Results and discussion

### 4.3.1 TGA analysis

Figure 4.1 shows the thermal decomposition of the as prepared  $\text{ZnAl}_2\text{O}_4$  (host) gel. Several thermal features take place during the heating of the gel. As anticipated the variation of the mass of the compound with temperature indicates slow weight loss up to  $80\text{ }^\circ\text{C}$  due to the

release of interlayer water [4,19]. An event at around 150-200 °C, is attributed to the expulsion of hydrated water [4,19,20]. The last event at around 300-400 °C is attributed to the elimination of organic compounds and starting of crystallization process and the formation of single phase ZnAl<sub>2</sub>O<sub>4</sub> [4,19].

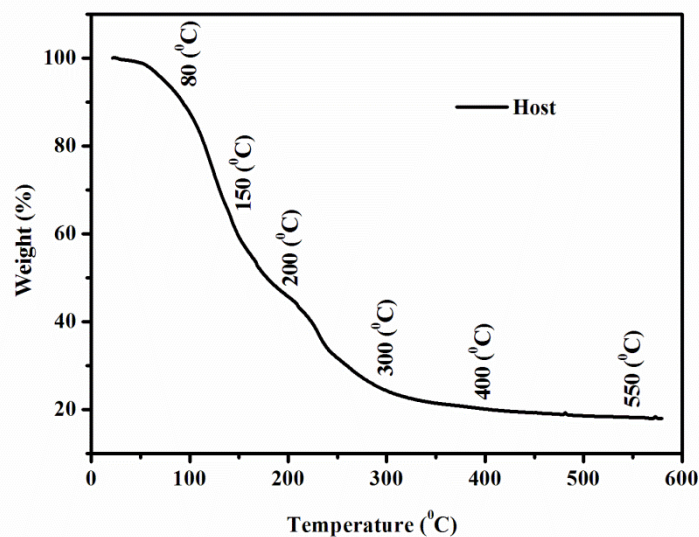


**Figure 4.1.** TGA curve of ZnAl<sub>2</sub>O<sub>4</sub> gel obtained with the heating rate of 10 °C/min.

These results suggest that the minimum annealing temperature to start obtaining cubic phase ZnAl<sub>2</sub>O<sub>4</sub> signature is 400 °C with high chances of forming other oxides impurities such as ZnO and Al<sub>2</sub>O<sub>3</sub>. Thus, the annealing temperature must be higher than 400 °C to completely eradicate impurities and enhances the crystallinity of the single phase ZnAl<sub>2</sub>O<sub>4</sub>. TGA results are consistent with what is observed in the XRD and FTIR analysis.

#### 4.3.2 XRD

The crystallinity of the powder samples prepared by sol-gel method was determined by means of XRD. To reveal the structural properties of the un-doped and Pb<sup>2+</sup>doped ZnAl<sub>2</sub>O<sub>4</sub>, the XRD patterns are presented in figure 4.2. The XRD pattern is consistent with the standard data for the cubic ZnAl<sub>2</sub>O<sub>4</sub> spinel phase (JCDPS: 82-1043). The results clearly reveal that highly crystalline cubic ZnAl<sub>2</sub>O<sub>4</sub> single phase can be obtained after annealing at 800 °C. This is supported by the fact that there were no extra peaks of impurities related to ZnO or Al<sub>2</sub>O<sub>3</sub>.

The same phases without impurities were observed for all  $\text{Pb}^{2+}$  doped samples at the range of 0 - 5 mol%. Thus, it is highly believed that the  $\text{Pb}^{2+}$  ions were fully incorporated into the host matrix. The results suggest that varying the mol% of  $\text{Pb}^{2+}$  ions does not affect the crystal structure of the phosphor. The average crystallites sizes were estimated by using the Scherrer formula [21], using the most intense peak, and were found to be 22, 29, 21, 30 and 22 nm for the 0%, 0.25%, 1%, 3% and 5%  $\text{Pb}^{2+}$  ions, respectively. Furthermore, when considering the most intense diffraction peak (311) shown in figure 4.2 (b), it can be seen that there is a peak shift to the higher angle and decrease in diffraction intensity with an increase in  $\text{Pb}^{2+}$  mol% concentration. This relationship in our results is consistent with what has been reported by Hou et al. [22] in the study of electrical and optical properties of Al doped ZnO and  $\text{ZnAl}_2\text{O}_4$ . The average lattice spacing was estimated to be 0.24 nm, which corresponds with (311) lattice spacing of the  $\text{ZnAl}_2\text{O}_4$  reported by Zawadzki et al. [23]. As expected, shifting to the higher angle is attributed to the decrease in the lattice spacing as the  $\text{Pb}^{2+}$  ions are incorporated into the  $\text{ZnAl}_2\text{O}_4$  matrix (see figure 4.2 (c)). This is due to the substitution of  $\text{Zn}^{2+}$  (ionic radius 0.74 Å) [22] with bigger  $\text{Pb}^{2+}$  (ionic radius 1.01 ~ 1.40 Å) [24] ions. In general, it is assumed that when a cation is replaced by other larger, the result is an expansion of the lattice and therefore both the interplanar d-spacing increases and the  $2\theta$  is shifted to lower angle. So, the mechanism of  $\text{Pb}^{2+}$ -doped  $\text{ZnAl}_2\text{O}_4$  solid solution formation must be different. May be it could include anionic vacancy formation.

Lubarda et al. [25] observed similar results deviating from Vegard's law when replacing Au atoms (1.5939 Å) with Ag atoms (1.5969 Å) in the Ag-Au alloy. The variation of the lattice spacing of the (311) diffraction peak, shows (in figure 4.2 (c)) the parabolic behaviour relationship to the  $\text{Pb}^{2+}$  mol%. The decrease in lattice spacing in our study is, therefore, attributed to the shrinkage of the  $\text{Pb}^{2+}$  outer electron shell due to its electronic interactions with more neighbouring  $\text{Zn}^{2+}$  ions, which makes it smaller than the  $\text{Zn}^{2+}$  ion [25]. As the  $\text{Pb}^{2+}$  mol% is increased further, the shrinkage is expected to be less pronounced (due to the additional  $\text{Pb}^{2+}$  ions), as a results, the lattice spacing is expected to recover or increase and this serves as a motivation why there is an increase in lattice spacing at 5%  $\text{Pb}^{2+}$ . These can also be a relevant reason why Lubarda et al. [25] observed high increase in lattice spacing at higher mol% of the Ag. Lubarda et al. [25] results and our results suggest that for some materials, at a low mol% of the dopant, the Vegard's law is not favoured. Thus, it is concluded that there is an optimum mol% required for the Vegard's law to occur. The second order polynomial fit in figure 4.2 (c) shows that the 3.4%  $\text{Pb}^{2+}$  is an optimum for our

results to behave as expected by Vergard's law. The decrease of the (311) diffraction peak intensity as the  $\text{Pb}^{2+}$  mol% is increased can be explained to be due to the replacement of smaller with bigger atoms, which destroys the crystal quality. The destruction of crystal quality is expected to be more pronounced as bigger foreign atoms are incorporated and this is supported by our findings in figure 4.2 (b). It is therefore concluded that the  $\text{Pb}^{2+}$  mol% influences the particle size growth, the lattice spacing and crystal quality.

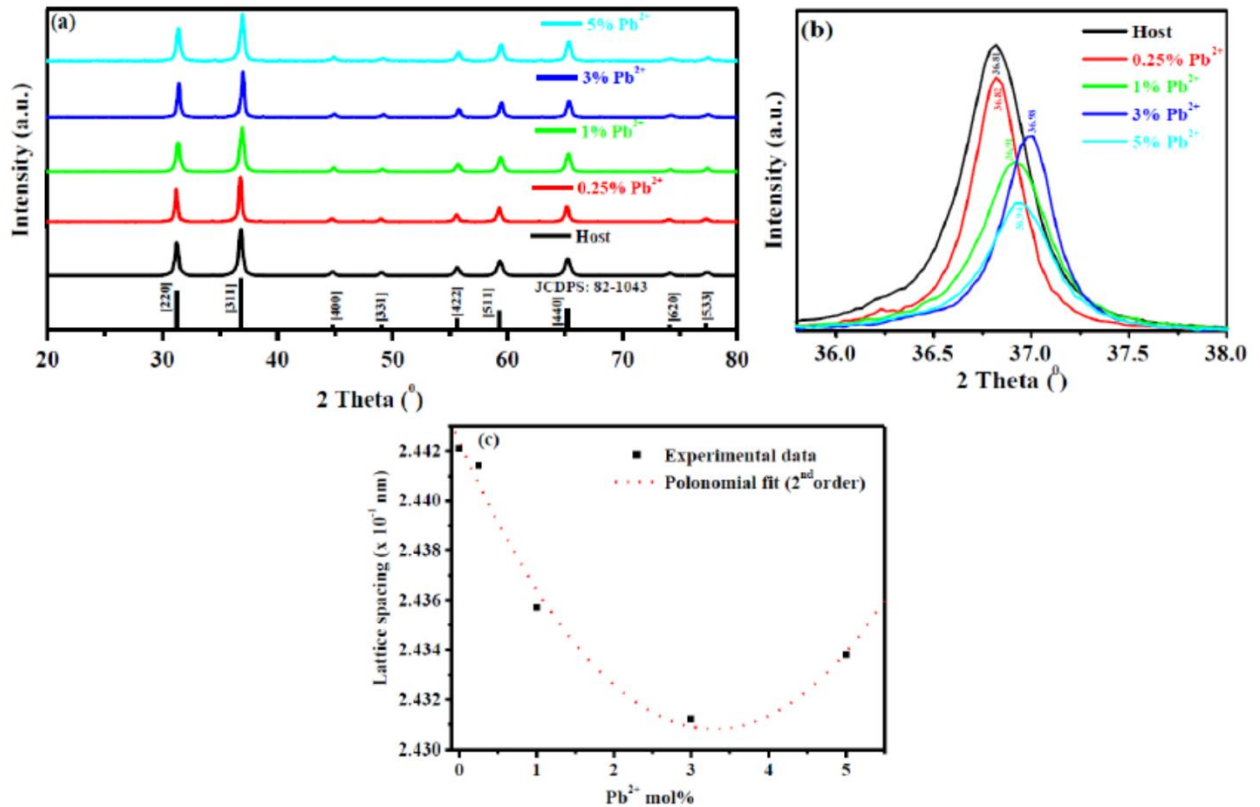


**Figure 4.2.** X-ray patterns of the (a) un-doped and  $\text{Pb}^{2+}$  doped  $\text{ZnAl}_2\text{O}_4$  phosphors and (b) analysis of (311) diffraction peak and (c) lattice spacing as a function of  $\text{Pb}^{2+}$  mol%.

#### 4.3.3 FTIR

Figure 4.3 shows the FTIR spectra of the un-doped  $\text{ZnAl}_2\text{O}_4$  gel and annealed powder at 800 °C powder. The band at  $682\text{ cm}^{-1}$  is assign to the stretching vibration of tetrahedral and octahedral bonds in the spinel [4,26,20]. The IR spectra of the gel indicate the presence of nitrates groups at  $805$ ,  $897$  and  $1052\text{ cm}^{-1}$ . The bands at  $1330 - 1628\text{ cm}^{-1}$  can be attributed to the OH group in the metal alkoxides present in the gel [20,27]. The wide absorption band centred at  $2965 - 3520\text{ cm}^{-1}$  corresponds to OH group, which is contributed by the water content present in the gel. As far as the annealed sample is concern, the shallow band

observed at  $3581\text{ cm}^{-1}$  is assigned to O–H stretching vibration [28]. The band at  $2337\text{ cm}^{-1}$  is attributed to the presence of O–O bonds in the crystal lattice, which is treated as a feature of spinel structured crystallites. Finally, a small band at  $1545\text{ cm}^{-1}$  is attributed to the amide bonds [29]. In comparing the gel and the annealed powder, it can be seen that the number of bands decreases when the samples were annealed at  $800\text{ }^{\circ}\text{C}$ , suggesting that the annealing temperature destroys most of the bonds, which suggests the formation of the single phase  $\text{ZnAl}_2\text{O}_4$  as shown by the XRD results.

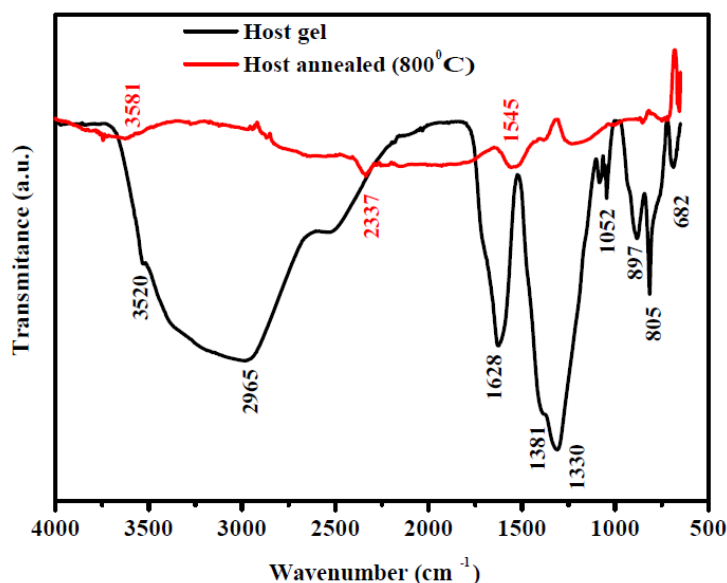


**Figure 4.3.** FTIR spectra of the undoped  $\text{ZnAl}_2\text{O}_4$  (host).

#### 4.3.4 SEM

The surface morphologies of the samples annealed at  $800\text{ }^{\circ}\text{C}$  for the undoped, 1%  $\text{Pb}^{2+}$  and 5%  $\text{Pb}^{2+}$ -doped  $\text{ZnAl}_2\text{O}_4$  are shown on SEM micrographs in figure 4.4 (a), (b) and (c), respectively. The undoped powder composed of small spherical and chunk granular particles dispersed all over the surface. The 1%  $\text{Pb}^{2+}$ -doped sample shows rough particle agglomerates with voids distributed in the matrix. It is, therefore, proposed that the rough particle agglomerates with voids might lead to easy escape routes to the emitted light with the consequent increase in the light output. The 5%  $\text{Pb}^{2+}$ -doped sample shows the particle-to-particle separation and more grain boundaries-like-porous structures distribution on the surface.

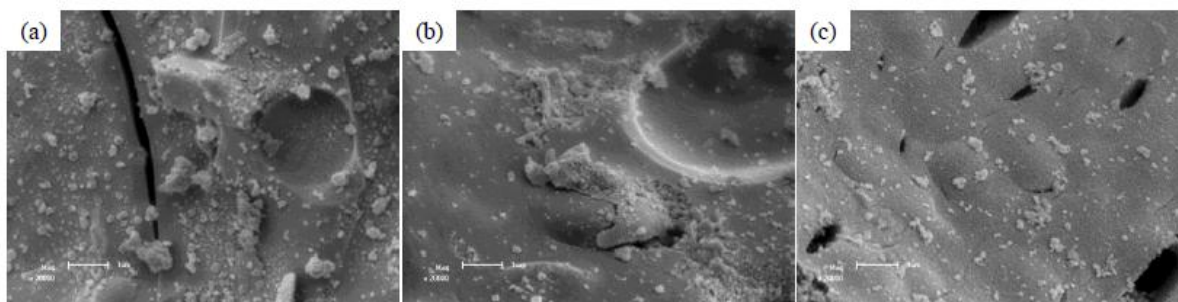


**Figure 4.4.** SEM micrographs for the (a) ZnAl<sub>2</sub>O<sub>4</sub> (host), (b) 1% Pb<sup>2+</sup> and (c) 5% Pb<sup>2+</sup>.

#### 4.3.5 PL analysis

Figure 4.5 (a) shows the PL excitation and emission spectra. It was observed that the main peaks of excitation when monitoring the UV emission at 395 nm are at 285 and 332 nm. Both absorption bands are attributed to the host absorption [26]. The emission spectra reveal that both undoped and Pb<sup>2+</sup>-doped ZnAl<sub>2</sub>O<sub>4</sub> powders exhibit UV emission peaks at slightly different positions 390, 395 and 399 nm. Note that within the investigated range of 0 - 5 mol%, the 1% Pb<sup>2+</sup> had the highest emission intensity. The emission intensity as a function of Pb<sup>2+</sup> mol% is presented in figure 4.5 (b). The Gaussian fit suggests that the optimum dopant concentration of these nanoparticles must be at 1.5% Pb<sup>2+</sup>. Above this optimum concentration, the concentration quenching effect on the emission intensity is observed. Similar quenching in luminescence intensity has been observed in TiO<sub>2</sub> doped with In- and Ce- by Tang et al. [30] and for TiO<sub>2</sub> doped with Pb- by Rahman et al. [31]. Thus, it is strongly believed that doping at higher Pb<sup>2+</sup> mol% introduces new defect sites that enhance non-radiative recombination of the excited electrons. Furthermore, the small shift in peak position indicates that the UV emission can be from either the host or Pb<sup>2+</sup> ions. The emission from the host at 395 nm is ascribed to be due to the intrinsic intrabandgap defects, such as oxygen vacancies ( $V_O^*$ ) [4,26] as shown in figure 4.6 (b). Da Silva et al. [4] suggested that these defects provide donor levels near the conduction band edge of the oxide.

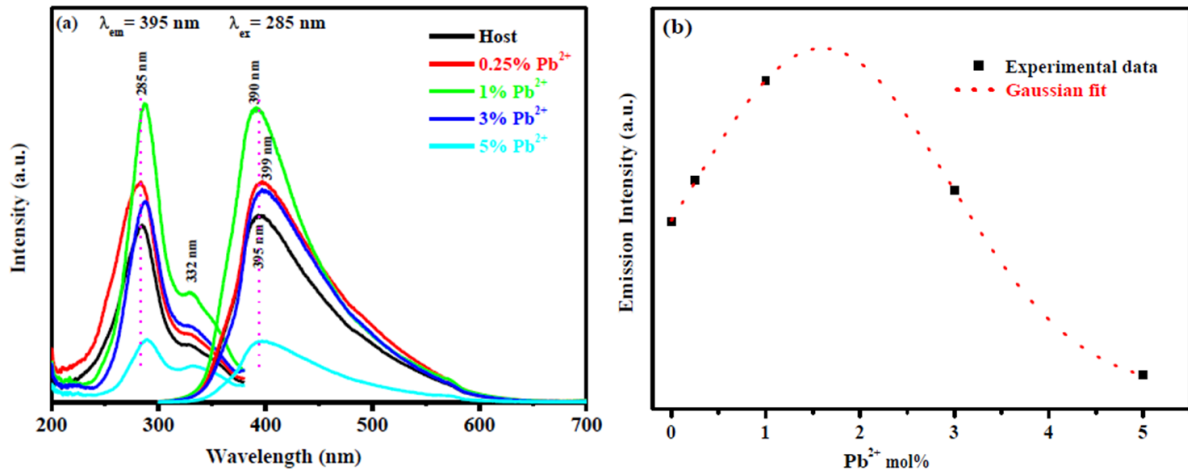


**Figure 4.5.** (a) Excitation and emission spectra of the undoped and  $\text{Pb}^{2+}$ -doped  $\text{ZnAl}_2\text{O}_4$  at different  $\text{Pb}^{2+}$  mol% (b) dependence of emission intensity as a function of excitation intensity (c) variation of emission intensity as a function of  $\text{Pb}^{2+}$  mol%.

The luminescence mechanism taking place for all emission arising from the undoped and  $\text{Pb}^{2+}$ -doped  $\text{ZnAl}_2\text{O}_4$  are illustrated in figure 4.6. The electrons in the ground state are excited to the conduction band after the excitation of 285 nm. As far as the host emission is concerned, the excited electrons are de-excited by non-radiative relaxation (NRR) and trapped on the defect states ( $V_0^*$ ), and then de-excited to the valence band by radiative decay. The incorporation of  $\text{Pb}^{2+}$  into the  $\text{ZnAl}_2\text{O}_4$  matrix can be interpreted as a development of more new trapping centers [1]. For the emission from the  $\text{Pb}^{2+}$ , it is proposed here that the mechanism is exactly similar to that one of the host emission but the difference is the trapping centers. As shown in figure 4.5 (a), the emission from the  $\text{Pb}^{2+}$  doped  $\text{ZnAl}_2\text{O}_4$  are slightly at different positions, which are at 390 and 399 nm. These shifts of the emissions peaks towards the shorter and higher wavelength suggest that the emission must be from different transitions in  $\text{Pb}^{2+}$  ion. Mehnaoui et al. [32] made an attempt to identify the pure electronic transitions between the ground and the excited levels of  $\text{Pb}^{2+}$  ion. In their study [32], they were successful to show that  $\text{Pb}^{2+}$  ions can occupy two different sites in the apatite and that leads to the probabilities of having two distinct emissions from the lower  $^3\text{P}_1 \rightarrow ^1\text{S}_0$  and higher  $^3\text{P}_0 \rightarrow ^1\text{S}_0$  energy transitions, which are associated to the  $\text{Pb}^{2+}$  ion. It is therefore, reasonable to draw-up the conclusion that these two emission bands from this report must originate from slightly different energy levels transitions from  $\text{Pb}^{2+}$  ion as shown in figure 4.6 (a) and (c). The emission at the higher wavelength (lower energy), 399 nm, is assign to be

from the  $^3P_0 \rightarrow ^1S_0$  transition [12,32], which must be within the host bandgap with possibilities of NRR and radiative decay. Finally, the emission from the lower wavelength, 390 nm, (higher energy) is attributed to the  $^3P_1 \rightarrow ^1S_0$  transition induced by  $Pb^{2+}$  ion. In this case, because of the bandgap energy ( $\sim 3.18$  eV), it is proposed that some of the  $Pb^{2+}$  energy levels are trapped within the conduction band of the host (since the host band gap is 3.14 eV see figure 4.6 (b)). Thus, it is concluded that the  $Pb^{2+}$  doping results in the modification of the bandgap energy and defects levels within the host matrix. As anticipated, the emission from the  $Pb^{2+}$  energy level trapped within the conduction band has the maximum intensity as shown in figure 4.5 (a). Note that the lifetime and afterglow spectrum were not gathered and therefore they are not discussed in this report.

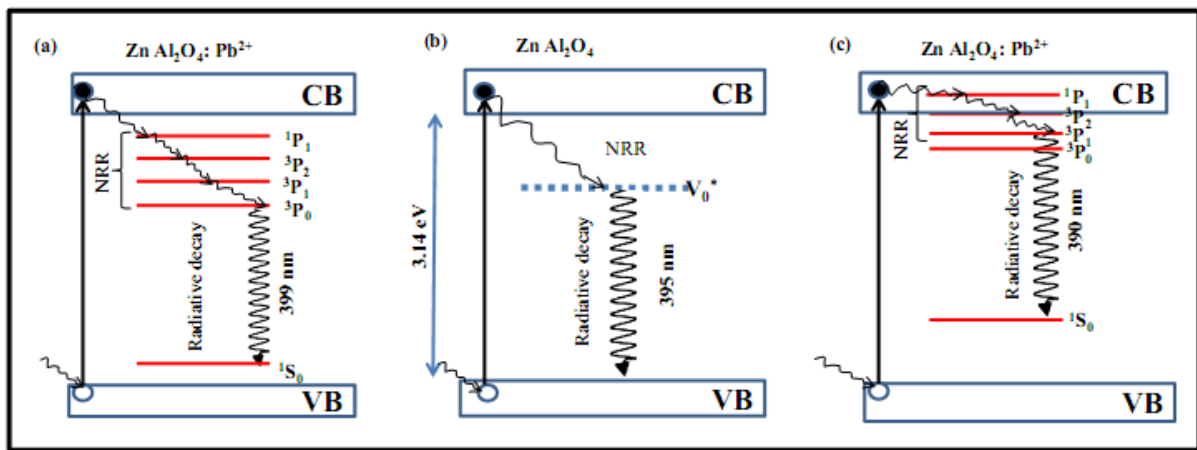


**Figure 4.6.** Energy levels diagram mechanism for the (a)  $ZnAl_2O_4: Pb^{2+}$  emission at 399 nm, (b) undoped  $ZnAl_2O_4$  emission at 395 nm and (c)  $ZnAl_2O_4: Pb^{2+}$  emission at 390 nm.

#### 4.4 Conclusion

The X-ray diffraction data revealed that the annealed samples consist of highly crystalline cubic  $ZnAl_2O_4$ . Varying the mol% of  $Pb^{2+}$  ions does not affect the crystal structure of the phosphor. The shifting of the 311 reflection in to the higher angle is attributed to the decrease in the lattice spacing. The results also suggest that the good particle agglomeration and voids leads to an easy escape routes to the emitted light with the consequent of enhancing the luminescence of a phosphor. The PL results demonstrated that undoped and  $Pb^{2+}$  impurities activated  $ZnAl_2O_4$  emits at slightly different UV positions. It is concluded that the emission can be from either the host or  $Pb^{2+}$  ions. The incorporation of  $Pb^{2+}$  ions influences the defects levels position and bandgap energy. At the higher  $Pb^{2+}$  mol%, the luminescence quenching

behaviour occurs due to the introduction of more new defect sites that enhance non-radiative recombination of the excited electrons.

## References

1. P. Borse, W. Vogel, S. Kulkarni, *J. Colloid Interface Sci.* **293** (2006) 437.
2. O. Ehlert, A. Osvet, M. Batentschuk, A. Winnacker, T. Nann, *J. Phys. Chem. B* **110** (2006) 23175.
3. D. Zhang, C. Wang, Y. Liu, Q. Shi, W. Wang, Y. Zhai, *J. Lumin.* **132** (2012) 1529.
4. A. A. Da Silva, A. Goncalves, M. R. Davolos, *J. Sol-Gel Sci. Technol.* **49** (2009) 101.
5. V. Ciupina, I. Carazeanu, G. Prodan, *J. Optoelectron Adv. Mater* **6** (2004) 1317.
6. V. Singh, R. P. S. Chakradhar, J. Rao, D. K. Kim, *J. Lumin.* **128** (2008) 394.
7. G. Lakshminarayana, L. Wondraczek, *J. Solid State Chem.* **184** (2011) 1931.
8. M. Nikl, A. Novoselov, E. Mihokova, K. Polak, M. Dusek, B. McClune, A. Yoshikawa, T. Fukuda, *J. Phys. Condens. Matter* **17** (2005) 3367.
9. A. A. Seltur, A. M. Srivastava, *Opt. Mater* **29** (2006) 410.
10. H. F. Folkerts, M. A. Hamstra, G. Blasse, *Chem. Phys. Letters* **246** (1995) 135.
11. Q. Sun, J. Wang, J. Shi, *J. Solid State Chem.* **183** (2010) 1174.
12. Y. Zorenko, V. Gorbenko, T. Voznyak, T. Zorenko, *Phys. Stat. Sol. B* **245** (2008) 1618.
13. A. A. Bol, A. Meijerink, *Phys. Chem.* **3** (2001) 2105.
14. J. T. Keller, D. K. Agrawal, H. A. McKinstry, *Adv. Ceram. Mater* **3** (1998) 420.
15. Y. L. Yuan, P. Hu, C. L. Yin, S. L. Huang, J. L. Li, *J. Mater Chem.* **13** (2003) 634.
16. Z. Chen, E. Shi, Y. Zheng, W. Li, N. Wu, W. Zhong, *Mater Lett.* **56** (2002) 601.
17. A. K. Adak, A. Pathak, P. Pramanik, *J. Mater Sci. Lett.* **17** (1998) 559.
18. Y. Wu, J. Du, K. Choy, L. L. Hench, J. Guo, *Thin Solid Films* **472** (2005) 150.
19. M. A. Valenzuela, P. Bosch, G. Aguilar-Rios, A. Montoya, I. Schifter, *J. Sol-Gel Sci. Techno.* **18** (1997) 110.
20. E. M. A. Jamal, D. S. Kumar, M. R. Anantharaman, *Bull Mater Sci.* **34** (2011) 251.
21. B. D. Cullity, 1956 *Elements of X-ray Diffraction* (2nd Ed) Addison Wesley 285 (1978).
22. Q. Hou, F. Meng, J. Sun, *Nanoscale Research Letters* **8** (2013) 144.
23. M. Zawadzki, *Solid State Sci.* **8** (2006) 14.
24. S. B. Chen, Y. B. Ma, L. Chen, K. Xian, *Geochemical Journal* **44** (2010) 233.
25. V. A. Lumbarda, *Mechanics of Materials* **35** (2003) 53.
26. A. A. Da Silva, A. Goncalves, M. R. Davolos, S. H. Santagneli, *J. Nanosci Nanotechnol.* **8** (2008) 5690.

27. W. X. Kuang, Y. N. Fan, K. W. Yao, Y. Chen, *J. Solid State Chem.* **140** (1998) 354.
28. A. K. Bajpai, S. Likhitar, *Bull Mater Sci.* **36** (2001) 15.
29. Y. Zhou, M. L. Bruening, D. E. Bergbreiter, R. M. Crooks, M. Wells, *J. Am. Chem. Soc.* **118** (1996) 3773.
30. H. Tang, H. Berger, P. E. Schmid, F. Levy, G. Burri, *Solid State Commun.* **87** (1993) 847.
31. M. M. Rahman, K. M. Krishna, T. Soga, T. Jimbo, M. Umeno, *J. Phys. Chem. Solid* **60** (1999) 201.
32. M. Mehnaoui, R. Ternane, G. Panczer, M. Trabelsi-Ayadi, G. Boulon, *J. Phys.: Condens. Matter* **20** (2008) 275227.

## Chapter 5: Effects of Cr<sup>3+</sup> mol% on the structure and optical properties of the ZnAl<sub>2</sub>O<sub>4</sub>:Cr<sup>3+</sup> nanocrystals synthesized using sol-gel process

*“Nothing in life is to be feared, it is only to be understood. Now is the time to understand more, so that we fear less.”*

*~ Marie Curie*

### 5.1 Introduction

Spinel type oxides like zinc aluminate ZnAl<sub>2</sub>O<sub>4</sub> present very attractive applications such as high temperature material, optical coating and catalysts or supports in many catalytic reactions due to its high thermal stability, low surface acidity and hydrophobicity properties [1-3]. ZnAl<sub>2</sub>O<sub>4</sub> is a well-known wide-band gap semiconductor ( $E_g \sim 3.8$  eV), which occurs naturally as the mineral commonly called gahnite [3,4]. It has the chemical formula of AB<sub>2</sub>O<sub>4</sub>, where A stands for metal cation that occupies a tetrahedral site and B represents Al which occupies the octahedral sites of a cubic packed crystal structure that belongs to the space group *Fd3m* [3,4]. These sites occupation or substitution depends on various factors such as ionic size, cationic charge, electron distribution and electronic states. Gahnite and other spinels are known to be suitable host lattice for various dopants or foreign atoms [3,5,6]. Many foreign atoms have been successfully incorporated into different host matrices and the luminescence property of the resulting phosphors has been shown to strongly depend on the particle size, crystal structure, and uniform distribution of activators in the host lattice [3,5]. To mention a few, Cheng et al. [7] fabricated mesoporous ZnAl<sub>2</sub>O<sub>4</sub>: Eu<sup>3+</sup> spinel nanorods using a simple homogeneous co-precipitation combined with the surfactant assembly method. Their results showed that the predominance and the strongly inhomogeneous broadening of the typical electric-dipole fluorescence emission (<sup>5</sup>D<sub>0</sub> → <sup>7</sup>F<sub>2</sub>) behaviour of Eu<sup>3+</sup> can be well observed in the optical spectra due to the rather disordered surroundings in the ZnAl<sub>2</sub>O<sub>4</sub> spinel nanolattice. The green emitting ZnAl<sub>2</sub>O<sub>4</sub>: Mn<sup>2+</sup> phosphor have also been developed by Singh et al. [3] and their findings suggested that the green emission at 511 nm is due to the <sup>4</sup>T<sub>1</sub> → <sup>6</sup>A<sub>1</sub> transition in the Mn<sup>2+</sup> ion. Apart from Mn<sup>2+</sup>, the other interesting transition metal ion for ZnAl<sub>2</sub>O<sub>4</sub> doping is Cr<sup>3+</sup>. Cr<sup>3+</sup> ion gives either pink or

S.V. Motlounq et al. / J. Ceramics International **41** (2015) 6776-6783.

green emission in coloured pigments depending on the strength of the  $\text{ZnAl}_2\text{O}_4$  crystal field [8]. Dong et al. [9] report has shown that the difference in crystal field strength value gives a good explanation of the spectroscopic and decay evolution between  $\text{ZnAl}_2\text{O}_4$ : x%  $\text{Cr}^{3+}$  and  $\text{MgAl}_2\text{O}_4$ : x%  $\text{Cr}^{3+}$  nanofibers.  $\text{Cr}^{3+}$  doped spinels are stable at high temperatures thus they can be used in ceramic applications [8,10]. For the fabrication point of view, many methods such as the solid state reaction [6], co-precipitation method [8], hydrothermal [10], combustion [5] and sol-gel [1] have been applied to prepare  $\text{ZnAl}_2\text{O}_4$  powders. Compared to the traditional techniques, sol-gel route is a versatile and attractive technique for the fabrication of nanocrystalline powders due to its advantage of producing pure and ultrafine powders at a very low temperature [11].

Although the  $\text{ZnAl}_2\text{O}_4$ : x%  $\text{Cr}^{3+}$  phosphor synthesis by the single-nozzle electrospinning technique has been reported in the literature [8], in this work we report on the sol gel synthesis of  $\text{ZnAl}_2\text{O}_4$ : x%  $\text{Cr}^{3+}$  at low temperature ( $\sim 80$  °C). Based on the current study results, we have recently reported [12] the effects of catalyst/Zn mole fraction on  $\text{ZnAl}_2\text{O}_4$ :0.01%  $\text{Cr}^{3+}$  nanocrystals synthesized using sol-gel process. The influences of  $\text{Cr}^{3+}$  mol% on the structural, morphology and optical properties of undoped and Cr-doped  $\text{ZnAl}_2\text{O}_4$  nanophosphors were investigated. The phosphor energy-level diagram and emission pathways mechanism is also presented. The main goal is to develop phosphor material that can be used for blue and red light emitting devices such as light-emitting diodes (LEDs).

## 5.2 Experimental

$\text{ZnAl}_2\text{O}_4$  was prepared by dissolving  $\text{Zn}(\text{NO}_3)_2 \cdot 6\text{H}_2\text{O}$  (98%) and  $\text{Al}(\text{NO}_3)_3 \cdot 9\text{H}_2\text{O}$  (98.5%) in deionized water. The molar ratio of Zn:Al was 1:2. Citric acid,  $\text{C}_8\text{H}_8\text{O}_7 \cdot \text{H}_2\text{O}$  (99%), was used as a catalyst. The molar ratio of Zn:catalyst was 1:3 and specified amounts of  $\text{Cr}(\text{H}_2\text{O})_6(\text{NO}_3)_3 \cdot 3\text{H}_2\text{O}$  (98%) were added to dope with  $\text{Cr}^{3+}$  ions. The mol% of  $\text{Cr}^{3+}$  was varied between  $0 \leq x \leq 0.3\%$ . All solutions were heated below 80 °C with constant stirring on a magnetic stirrer until gelation following the chemical reaction. The gels were dried at a temperature of 130 °C in an oven for powders synthesis. The powders samples were ground and subsequently annealed at 800 °C for an hour. The crystal structure of the samples was characterized by powder X-ray diffraction (Bruker AXS Discover diffractometer) with  $\text{CuK}\alpha$  (1.5418 Å) radiation). The surface morphology and elemental composition of the phosphor powder were investigated using a Shimadzu Superscan ZU SSX-550 electron microscope (SEM) coupled with an electron diffraction spectroscopy (EDS). High-Resolution

Transmission Electron microscopy (HR-TEM) was performed with a JEOL JEM 2100 containing a LaB<sub>6</sub> filament. TOF-SIMS measurements were performed using the Iontof SIMS<sup>5</sup>. A pulsed 30 kV Bi<sup>+</sup> primary ion beam, pulsed at 100 μs and operated at 1 pA, was used to acquire chemical images of the phosphor in both the positive and the negative polarities. The powder sample was sputtered on an area of 300 x 300 μm at the sputtering time of 26.21 s/scan. The elemental mapping was rastered over an area of 100 x 100 μm on the surface. The surface images were recorded with a resolution of 512 x 512 pixels. The measurements were performed in a chamber maintained at the base pressure of 9.4 x 10<sup>-9</sup> mbar. Photoluminescent (PL) spectra were recorded at room temperature using a Hitachi F-7000 fluorescence spectrophotometer.

### 5.3 Results and discussion

#### 5.3.1 XRD

The XRD patterns of the series ZnAl<sub>2</sub>O<sub>4</sub>: x% Cr<sup>3+</sup> (0 ≤ x ≤ 0.3%) are shown in figure 5.1 (a). XRD patterns obtained for all Cr<sup>3+</sup> doped ZnAl<sub>2</sub>O<sub>4</sub> samples were indexed according to the standard data provided by the International Center for Diffraction Data (JCDPS: 82-1043) for the cubic ZnAl<sub>2</sub>O<sub>4</sub> spinel phase. The peaks were indexed as (220), (311), (400), (331), (422), (511), (440), (620) and (533) diffraction lines. As the Cr<sup>3+</sup> concentration was increased no extra diffraction peak related to the Al<sub>2</sub>O<sub>3</sub> and ZnO impurities were detected in the patterns which consequently confirm the single phase of the prepared powder samples. From figure 5.1 (a), it can be seen that the (311) diffraction peak is the highest intense peak amongst other peaks. It is clearly observed in the expanded version of the spectra in figure 5.1 (b) that the peak shifts to the lower angle value for all ZnAl<sub>2</sub>O<sub>4</sub>:x% Cr<sup>3+</sup> samples, which indicates that the lattice parameters are slightly larger than those of undoped ZnAl<sub>2</sub>O<sub>4</sub> [13]. The results suggest that the Cr<sup>3+</sup> ions were successfully incorporated into the ZnAl<sub>2</sub>O<sub>4</sub> crystal lattice. Evaluating from the Virgard's law point of view [14], and comparing the atomic radius of Cr<sup>3+</sup> (0.63 Å) with Zn<sup>2+</sup> (0.74 Å) [7] and Al<sup>3+</sup> ions (0.53 Å) [10] this observation suggests that Cr<sup>3+</sup> ions likely to substitute Al<sup>3+</sup> atoms at the octahedral sites. In addition, the change in (311) diffraction peak intensity as shown in figure 5.1 (b) is attributed to the change in the degree of crystalline quality [15]. Compared to the host, the decrease of the (311) peak intensity as the Cr<sup>3+</sup> mol% is increased is linked to the destruction of the crystalline quality, while an increase in (311) peak intensity is linked to the enhancement of the crystals growth of

ZnAl<sub>2</sub>O<sub>4</sub>. Thus, the Cr<sup>3+</sup> mol% influences the crystallinity of the ZnAl<sub>2</sub>O<sub>4</sub>. The crystallites sizes were estimated by Scherrer's equation [16] using the most intense peak (311) and they were found to be 24, 22, 23, 24, 23, 23 nm for x = 0, 0.01, 0.03, 0.05, 0.1 and 0.3 mol%, respectively.

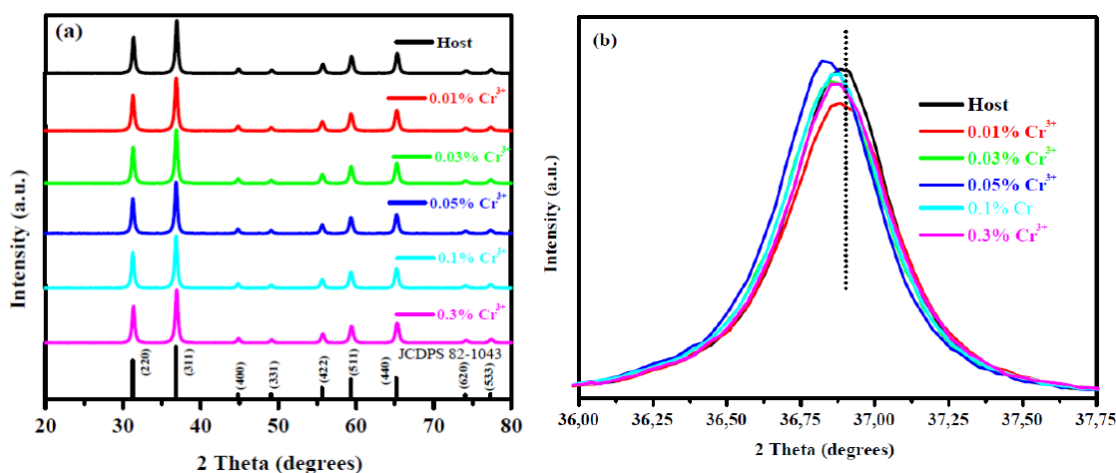


**Figure 5.1.** (a) XRD patterns of ZnAl<sub>2</sub>O<sub>4</sub>: x% Cr<sup>3+</sup> (0 ≤ x ≤ 0.3%) and (b) expanded version of XRD pattern for (311) peak.

Lattice spacing as a function of the Cr<sup>3+</sup> concentration shows the Gaussian-type behaviour as presented in figure 5.2. As mentioned above, at the lower mol%, the increase in lattice spacing is attributed to the substitution of Al<sup>3+</sup> by the Cr<sup>3+</sup> ion at the octahedral sites as shown on the inset in figure 5.2. However, as the Cr<sup>3+</sup> mol% was increased further, the increase in lattice spacing reached a critical point at  $0.065 \pm 0.002\%$  Cr<sup>3+</sup> and then started to decrease as the Cr<sup>3+</sup> mol% was increased further. It is important to note that we have observed similar kind of behaviour departing from the Vegard's law in our recent results [17] and the references therein. Our previous results [17] have indicated that for some materials such as ZnAl<sub>2</sub>O<sub>4</sub>, the Vegard's law can be obeyed and disobeyed but that depends on the dopant concentration. In the current results, it is concluded that the decrease in lattice spacing above the critical point was certainly due to the substitution of the Zn<sup>2+</sup> by the Cr<sup>3+</sup> ions as well (see insert in figure 5.2). Therefore, in such cases the Cr<sup>3+</sup> ions occupies the tetrahedral site in the host matrix. Without any doubt this results suggest that, depending on the mol%, Cr<sup>3+</sup> ions can occupy either the octahedral or tetrahedral sites in the ZnAl<sub>2</sub>O<sub>4</sub> host matrix, which is in good agreement with Dong et al. [9] results. Their results [9] showed that the luminescence

properties of  $\text{Cr}^{3+}$  ions depend strongly on their coordination, crystal field and lattice imperfections. For an example, when  $\text{Cr}^{3+}$  ions occupy sites with strong or intermediate crystal field, the lowest excited state is the  ${}^2\text{E}_g$  level, which will be responsible for the narrow band phosphorescence with a characteristic lifetime of tens of ms. While in the case where  $\text{Cr}^{3+}$  ions lie at sites with weak crystal field, the lowest excited state will be the  ${}^4\text{T}_{2g}$  level, which will be responsible for the broad band fluorescence with a characteristic lifetime of tens of ms [9]. Different  $\text{Cr}^{3+}$  environment or locations in the host matrix is anticipated to have dissimilar crystal field strength and, as a results, diverse emission on the PL results are expected [8,9]. The average lattice spacing was estimated to be 0.243 nm, which corresponds with the (311) lattice spacing of the  $\text{ZnAl}_2\text{O}_4$  reported in our recent results [17] and by Zawadzki et al. [18].

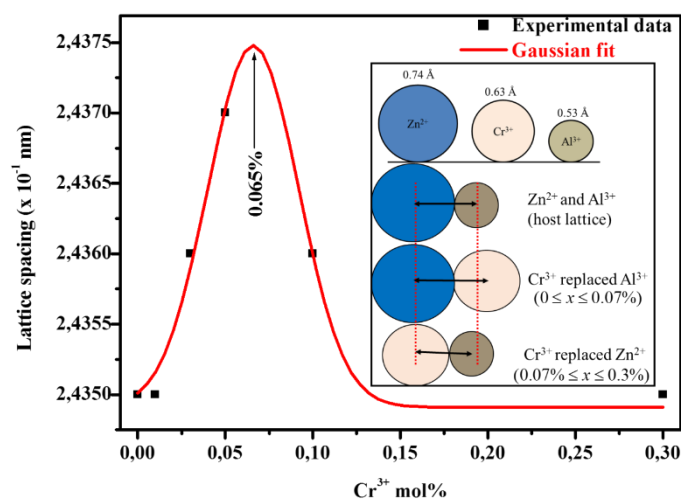


**Figure 5.2.** Lattice constant as a function of  $x\%$   $\text{Cr}^{3+}$  ions (insert: showing the ionic radius and increase and decrease in d spacing).

### 5.3.2 TOF-SIMS

To further investigate the ionic composition, presence of dopant and homogeneity of doping in the  $\text{ZnAl}_2\text{O}_4$  host crystal lattice, TOF-SIMS analysis was performed on a catalyst/Zn mole fraction equal to 0.75 sample. Figure 5.3 shows the surface images of the sample after 60 scans. Note that only elements of interest (e.g. Zn, Al, Cr and O) are shown. Figure 5.3 (a) – (c) shows the positive ions mapping while figure 5.3 (d) illustrates the overlay of  $\text{Zn}^+$ ,  $\text{Al}^+$

and  $\text{Cr}^+$ , wherein each particle is clearly observed. It can evidently be seen in figure 5.3 (d) that the dopant ( $\text{Cr}^{3+}$  ions) are homogeneously distributed in the host matrix. Figure 5.3 (e) illustrates the  $\text{O}^-$ , which confirms the presence of oxygen in the powder sample. This result indicates that the  $\text{Cr}^{3+}$  could be successfully doped very uniformly in the  $\text{ZnAl}_2\text{O}_4$  nanoparticles using the sol-gel method. Furthermore, the mass spectra of the sample was acquired and it is illustrated in figure 5.4 (a) and (b) for both negative and positive polarity mode, respectively. All the signals of the expected elements were detected. Thus, the prepared powder samples were cubic  $\text{ZnAl}_2\text{O}_4:0.01\% \text{Cr}^{3+}$  as it was confirmed by the XRD results.

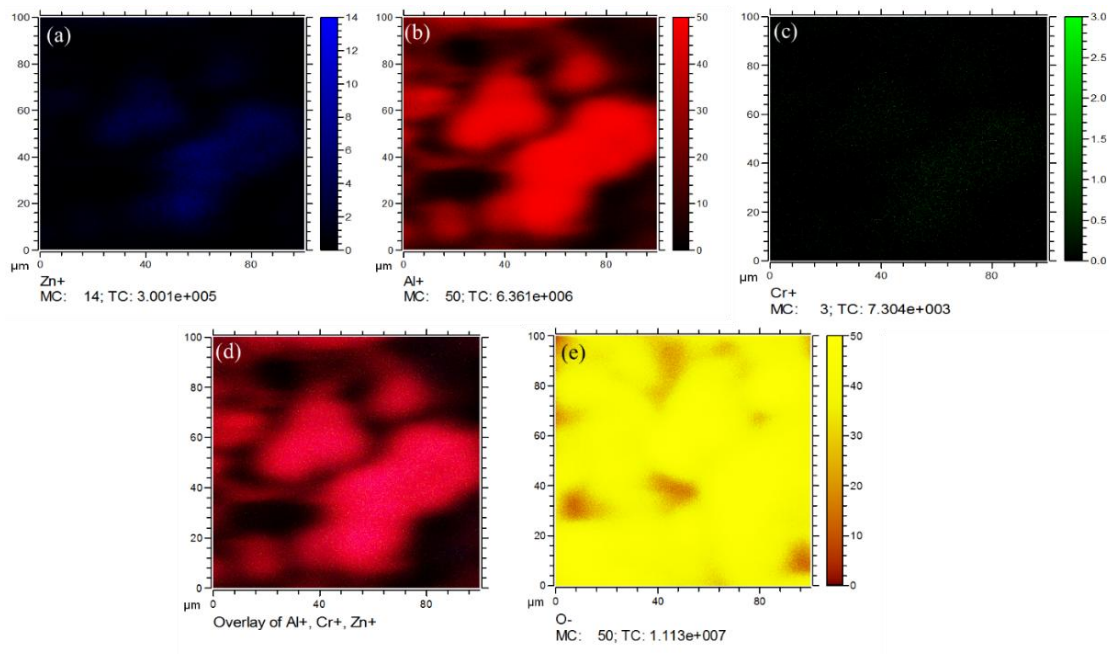


**Figure 5.3.** TOF-SIMS ion mapping images for  $\text{ZnAl}_2\text{O}_4: 0.01\% \text{Cr}^{3+}$  mole fraction of 0.75 sample (a)  $\text{Zn}^+$  (b)  $\text{Al}^+$  (c)  $\text{Cr}^+$  (d) three-colour overlay of positive ions and (e)  $\text{O}^-$ .

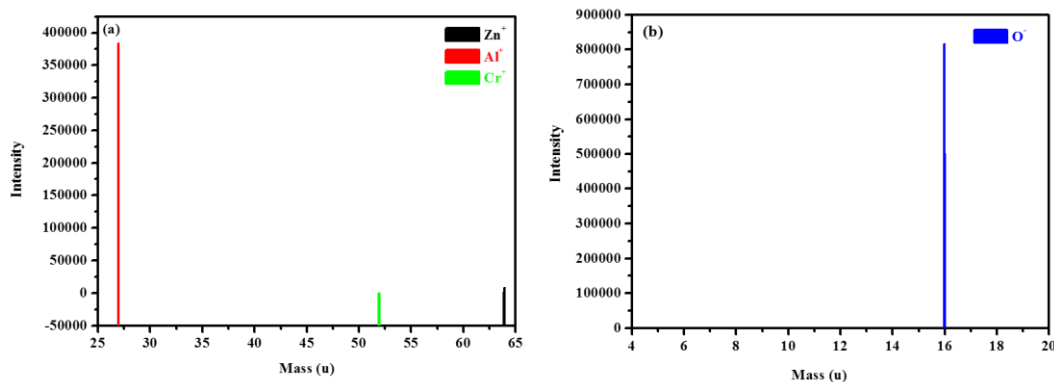


**Figure 5.4.** (a) Positive SIMS spectra of  $\text{ZnAl}_2\text{O}_4: 0.01\% \text{Cr}^{3+}$  mole fraction of 0.75 showing Zn, Al, Cr peaks and (b) Negative SIMS spectra showing O peak.

### 5.3.3 SEM and HR-TEM

The SEM images of the host and x% Cr<sup>3+</sup> doped samples are shown in figure 5.5. The undoped ZnAl<sub>2</sub>O<sub>4</sub> (host) consisting of the plate-like morphology with irregular particles sizes distribution all over the surface as shown in figure 5.5 (a). High degree of pores and little grain boundaries are also observed for the undoped sample. When the ZnAl<sub>2</sub>O<sub>4</sub> was doped with 0.03% Cr<sup>3+</sup> ions, as shown in figure 5.5 (b), cups and plate-like morphology as well as the pores seems to be less pronounced. Finally, as the dopant mol% was increase to the maximum, the cups and plate-like morphology has vanishing and more grain boundaries with more particle distribution were observed. Thus, the Cr<sup>3+</sup> ions mol% influences the morphology of the phosphor.

Furthermore, the prepared powders microstructure was characterised by HR-TEM shown in figure 5.6, which evidently reveal that the powders consists of nanoparticles. By inspection, from figure 5.6 (a) – (c), their average sizes appears to be ranging from 20 -25 nm, which agrees very well with the calculated crystallites sizes on XRD results. Figure 5.6 (a) presents the TEM image for the host and in the magnified vision, indicated by the red square, it can be seen that there are lattice fringe spacing observed. As the host is doped at the lower and higher mol% (see figure 5.6 (b) and (c), respectively) the cubic-like-structures, indicated by red cycles, are observed, which is yet again in good agreement with the cubic structure of ZnAl<sub>2</sub>O<sub>4</sub> (JCDPS: 82-1043) reported in the XRD results. Thus, it is evident that the TEM and XRD results supports each other.

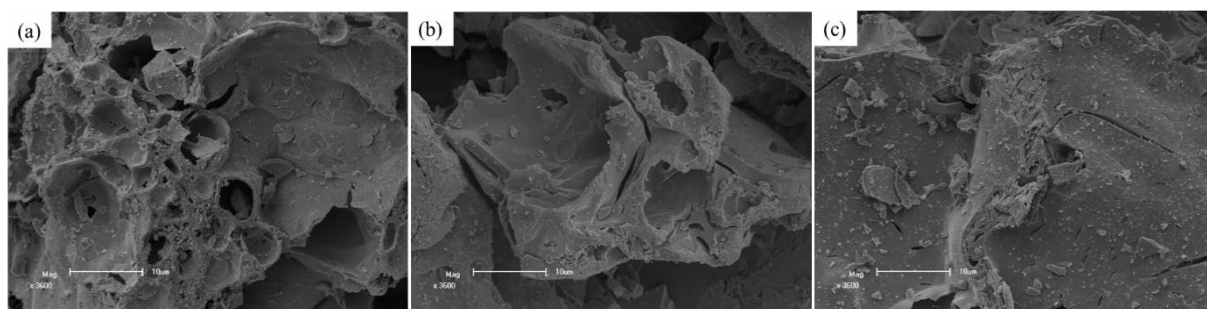


**Figure 5.5.** SEM images for (a) Host, (b) 0.03% and (c) 0.3%

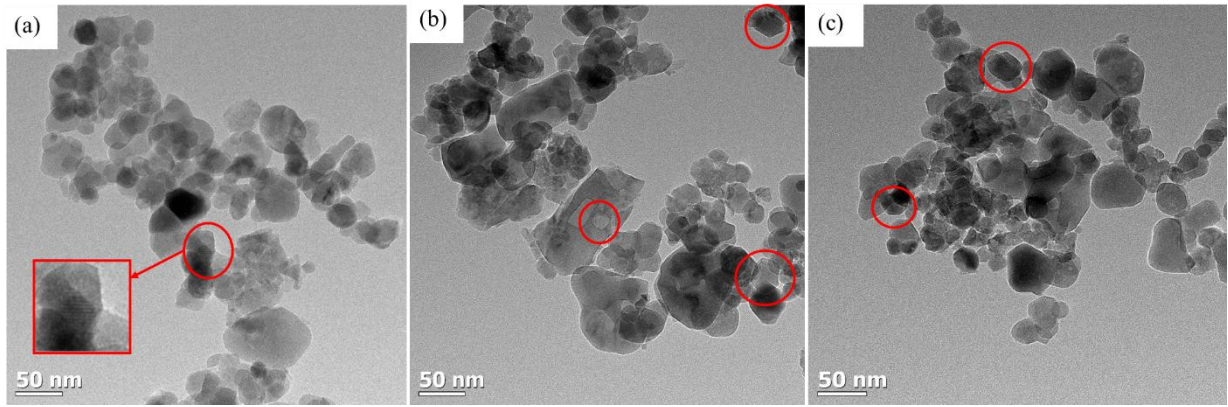


**Figure 5.6.** HR-TEM images for (a) Host, (b) 0.03% and (c) 0.3%

### 5.3.4 UV-Vis

UV-Vis diffuse reflection spectroscopy was used to study the absorption characteristics of the host and the effects of  $\text{Cr}^{3+}$  ions. The spectra in figure 5.7 (a) revealed that there are two absorption bands observed at 283 and 383 nm. Clearly, it can be seen that both the absorption band at 283 and 383 nm originates from the host material [17]. The band with a maximum at 283 nm is attributed to the band-to-band transition of the  $\text{AlO}_6$  anion grouping in  $\text{ZnAl}_2\text{O}_4$ , [7] while the other band at 383 nm might arise from the defects absorption within the host material.

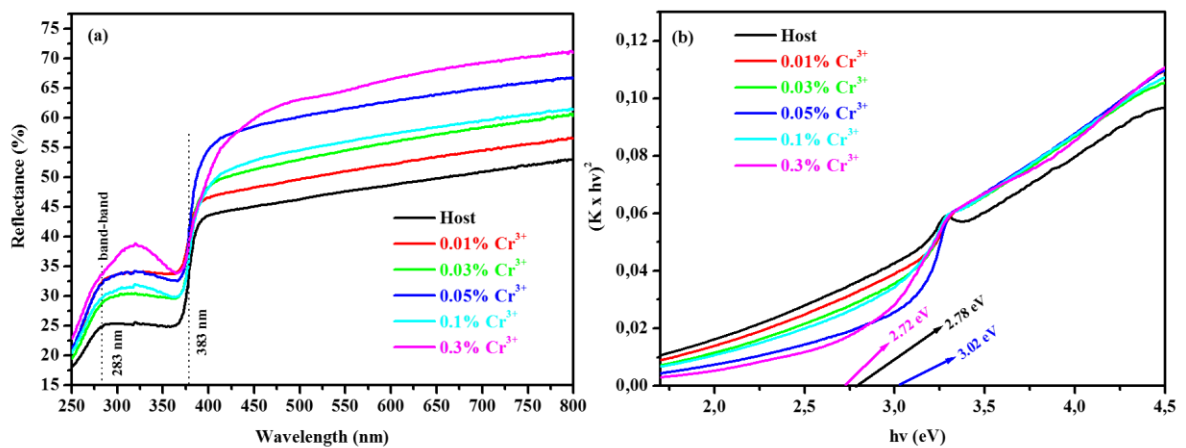


**Figure 5.7.** (a) The diffuse reflectance spectra of the  $\text{ZnAl}_2\text{O}_4:x\% \text{Cr}^{3+}$  doped ( $0 \leq x \leq 0.3\%$ ) samples and (b) Estimate of the direct optical bandgap of the samples in (a) using Kubelka-Munk function.

The Kubelka–Munk function  $K = (1 - R)^2/(2R)$  was used to transform the reflectance to the values proportional to absorbance, and the Tauc plot of  $(K \times hv)^n$  against  $hv$  (with  $n = 2$ , which is appropriate for a direct bandgap material such as  $ZnAl_2O_4$ ) is given in figure 5.7 (b) for all samples [21]. The results indicates that the bandgap of the host depends on the  $Cr^{3+}$  mol%, which suggest that the optical bandgap of  $ZnAl_2O_4$  can be engineered or tuned between 2.72 - 3.02 eV by varying x%  $Cr^{3+}$  at the range of ( $0 \leq x \leq 0.3\%$ ).

### 5.3.5 PL analysis

The PL excitation and emission spectra of the series  $ZnAl_2O_4: x\% Cr^{3+}$  ( $0 \leq x \leq 0.3\%$ ) is shown in figure 5.8 (a). The main peaks of excitation when monitoring the emission at 396 nm are at 283 and 336 nm. Both absorption bands are attributed to arise from the host material as discussed in UV-Vis results [7]. As shown in figure 5.10, both absorption bands are specifically attributed to the band-to-band and defects in the host, respectively. The emission spectra reveal that all powder samples exhibit a violet emission. Emission peak at 396 nm is ascribed to the intrinsic intraband gap defects, such as oxygen vacancies ( $V_o^*$ ) [11,19]. Da Silva et al. [11] suggested that these defects provide donor levels (DL), near the conduction band edge of the oxide as shown in figure 5.10 (a).

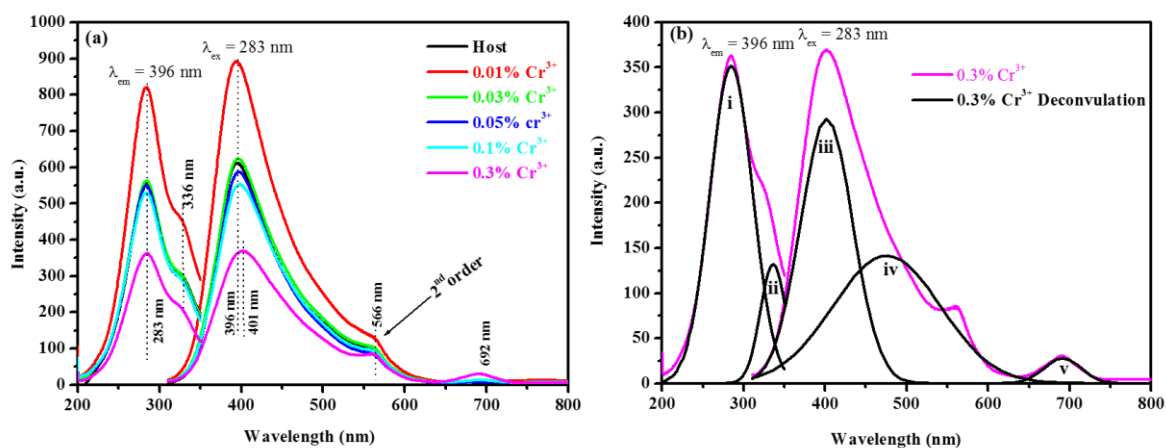


**Figure 5.8.** (a) Excitation and emission spectra of the series  $ZnAl_2O_4: x\% Cr^{3+}$  ( $0 \leq x \leq 0.3\%$ ) and (b) deconvolution of  $ZnAl_2O_4:0.3\% Cr^{3+}$ .

However, at the higher mol% (e.g. 0.3%  $Cr^{3+}$ ), the emission slightly shifts to the higher wavelength (401 nm) suggesting that the emission is originating from both contribution of the host and  $Cr^{3+}$  ion (see figure 5.10 (b)). Emission originating from the  $Cr^{3+}$  ion is attributed to

arise from the  ${}^4T_1 \rightarrow {}^4A_2$  transition [10] as illustrated in figure 5.10 (b). In addition, at 0.3%  $Cr^{3+}$ , an extra peak at 692 nm is observed (see figure 5.8 (a)). Certainly, that peak is also originating from the  $Cr^{3+}$  ion and is assigned to so-called R lines (as described in ref [20]) of the  ${}^2E \rightarrow {}^4A_2$  transition in  $Cr^{3+}$  ion (see figure 5.10 (b)). These results confirms the XRD that the  $Cr^{3+}$  ions are indeed occupying multiple sites in  $ZnAl_2O_4$ , as previously suggested by Chary et al. [22] Finally, the emission peak at 566 nm is assigned to either the second order emission or  ${}^4T_2 \rightarrow {}^4A_2$  transition from  $Cr^{3+}$  [10] as shown in figure 5.8 and 5.10 (b). It can also be due to the host as it was reported by Da Silva et al. [11]. We emphasize and infer that the 566 nm peak is due to the second order emission based on the following arguments. When considering the host sample in figure 5.8 (a), the existence of 566 nm serves as the good reason to not assign it to the  $Cr^{3+}$  ion ( ${}^4T_2 \rightarrow {}^4A_2$ ) transition as shown in figure 5.10 (b). Furthermore, since there is no peak shift in all samples for the 566 nm in figure 5.8 (a), it is reasonable to attribute it to the second order emission. Deconvolution of  $ZnAl_2O_4:0.3\% Cr^{3+}$  sample is presented in figure 5.8 (b). The peaks labelled (i), (ii), (iii), (iv) and (v) corresponds to the 283, 336, 401, 566 and 692 nm, respectively.

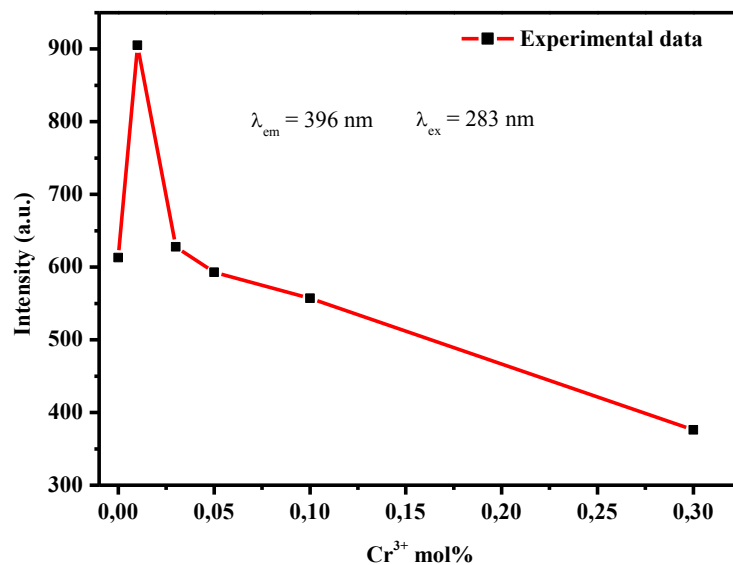


**Figure 5.9.**  $Cr^{3+}$  mol% as a function of emission intensity.

It is evident that the emission intensity strongly depends on the  $Cr^{3+}$  doping mol%. For the host (undoped) sample, the emission intensity is weak because there are not sufficient

luminescence centers. However, when increasing  $\text{Cr}^{3+}$  mol%, the emission intensity increases, and reaches the maximal value at 0.01 %  $\text{Cr}^{3+}$  as shown in figure 5.9. Note that although the synthesis techniques from this report (sol-gel) and Dong et al. [9] (single-nozzle electrospinning) differs, it is surprising and interesting to establish that  $\text{ZnAl}_2\text{O}_4:0.01\% \text{Cr}^{3+}$  is the optimal doping concentration. Hence, our results confirm previous results reported by Dong et al. [9]. When the  $\text{Cr}^{3+}$  mol% is increased further than 0.01 %  $\text{Cr}^{3+}$ , the luminescence intensity starts to reduce and that is attributed to the well-known concentration quenching, which occurs due to the decrease in Cr–Cr distance [23]. Thus, an increase in  $\text{Cr}^{3+}$  mol% modifies the defects levels and local environment of the emission centers [24]. Liu et al. [23] reported similar observation on the study of the effects of Cr content on the Cr-doped alpha- $\text{Al}_2\text{O}_3$  powders. In addition, their results [23] showed that the luminescence properties of the samples are also dependent on the morphology. The concentration quenching is mainly caused by the non-radiative energy transfer, which occurs as a result of an exchange interaction (EI), radiation reabsorption, or a multipole–multipole interaction (M-MI) [25]. According to Blasse [26], the critical energy transfer distance ( $R_c$ ) between the neighbouring donors (activators) and acceptors (quenching site) can be expressed by the following relation:

$$R_c = 2 \left( \frac{3V}{4\pi X_c N} \right)^{\frac{1}{3}} \quad (5.1)$$

where  $V$  is the volume of the unit cell,  $X_c$  is the critical concentration of the activator ion and  $N$  is the number of host cations ( $\text{Zn}^{2+}$ ) in the unit cell [25]. In the present host material ( $\text{ZnAl}_2\text{O}_4$ ) and assuming the normal spinel [3], the value of  $N$  is taken as 8,  $V = 526.7 \text{ \AA}^3$  and the critical concentration of  $\text{Cr}^{3+}$  in the  $\text{ZnAl}_2\text{O}_4$  (host) is  $X_c = 0.01$ . Therefore, the  $R_c$  of  $\text{Cr}^{3+}$  ions is determined to be  $23 \text{ \AA}^3$ . Liu et al. [23] obtained the  $R_c$  value of  $24 \text{ \AA}^3$ , which is very close to the value reported in this study.

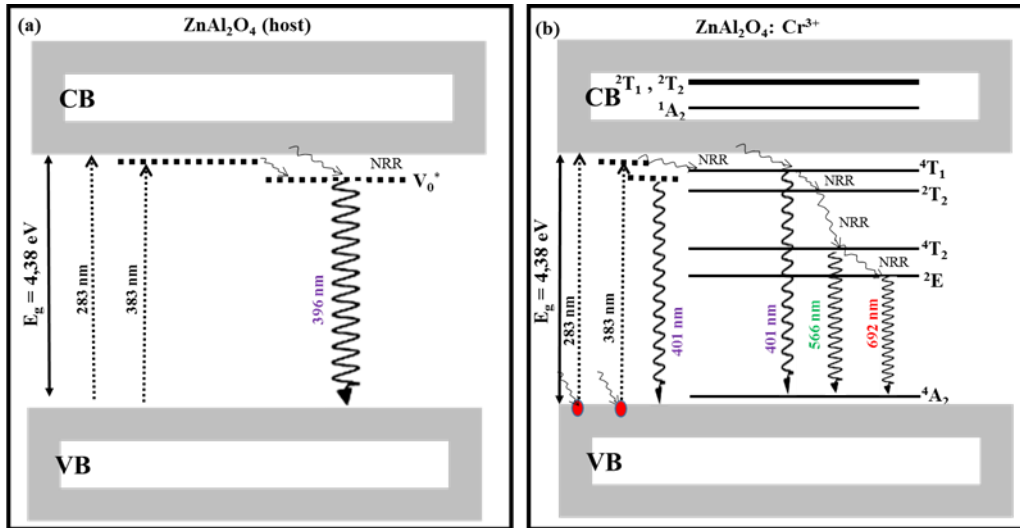


**Figure 5.10.** The phosphor emission pathways mechanism for (a)  $\text{ZnAl}_2\text{O}_4$  and (b)  $\text{ZnAl}_2\text{O}_4:\text{Cr}^{3+}$  ion.

The phosphor emission pathways mechanism taking place for all emission arising from the series  $\text{ZnAl}_2\text{O}_4:x\% \text{Cr}^{3+}$  ( $0 \leq x \leq 0.3\%$ ) are illustrated in figure 5.10. As far as the host is concern, the luminescence mechanism can be explained as follows; after the excitation of 283 nm, the electrons in the valence band (VB) are excited to conduction band (CB) and then the excited electrons are de-excited by NRR and trapped on the defect states ( $V_0^*$ ), and then de-excited to the valence band by radiative decay (see figure 5.10 (a)). The excitation peak at 336 nm is also shown in figure 5.8 (a) and (b). In this case, we propose that the excited electrons are getting trapped in the defect state due to less excitation energy. In contrast, the incorporation of  $\text{Cr}^{3+}$  into the  $\text{ZnAl}_2\text{O}_4$  matrix can be interpreted as a development of more new trapping centers [27]. The emission mechanism for the  $\text{Cr}^{3+}$  ion is exactly similar to that one of the host emission but the difference is the trapping centers. As shown in figure 5.10 (b), the emission from the  $\text{Cr}^{3+}$  ion can arise from different energy levels of  $\text{Cr}^{3+}$  ion to its ground state.

Figure 5.11 represent the chromaticity co-ordinates of all the series  $\text{ZnAl}_2\text{O}_4:x\% \text{Cr}^{3+}$  ( $0 \leq x \leq 0.3\%$ ) determined using the CIE Coordinate Calculator software [28]. The software also shows the position of the co-ordinates in the chromaticity diagram and the expected colour of the material. As shown in figure 5.11 that all the samples exhibit the violet emission. Hence, it is concluded that the emission colour can be tuned by varying the  $\text{Cr}^{3+}$  mol%.

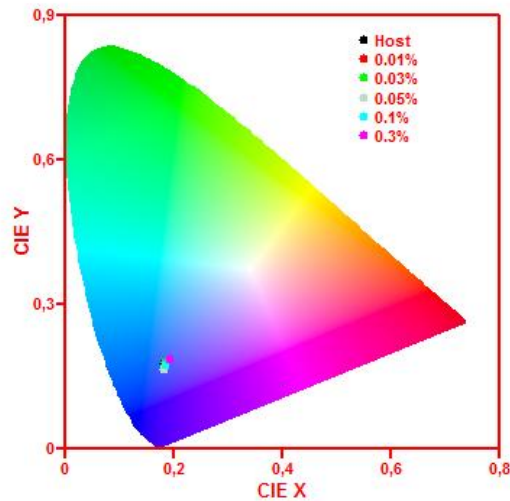


**Figure 5.11.** CIE colour of the series  $\text{ZnAl}_2\text{O}_4:x\% \text{Cr}^{3+}$  ( $0 \leq x \leq 0.3\%$ ).

#### 5.4 Conclusions

The violet emitting  $\text{ZnAl}_2\text{O}_4:x\% \text{Cr}^{3+}$  phosphors were successfully prepared by sol-gel technique. The X-ray diffraction data revealed that all samples consist of highly crystalline cubic  $\text{ZnAl}_2\text{O}_4$ . Varying the mol% of  $\text{Cr}^{3+}$  ions affects the crystallinity of the phosphor.  $\text{Cr}^{3+}$  ions can occupy both the octahedral and tetrahedral sites in  $\text{ZnAl}_2\text{O}_4$  host matrix. TOF-SIMS analysis revealed the presence of all as-designed elements including Cr. Varying  $\text{Cr}^{3+}$  influences the morphology of the phosphor. UV-Vis results showed that the band gap of the phosphor can be engineered or tuned. The PL results demonstrated that the violet emission can be due to the host or  $\text{Cr}^{3+}$  ions. The results also proved that at the higher  $\text{Cr}^{3+}$  mol%, the dopant can occupy multi-sites in the host material. The incorporation of  $\text{Cr}^{3+}$  ions added extra defects within the host. The critical energy transfer distance of  $\text{Cr}^{3+}$  in  $\text{ZnAl}_2\text{O}_4$  host is calculated to be 23 Å. CIE colour coordinate showed no significant shifts on the violet emission colour.

## References

1. M. Tsai, Y. Chen, P. Tsai, Y. Wang, *Thin Solid Films* **518** (2010) e9.
2. M. Zawadzki, W. Staszak, F. E. Lo´pez-Sua´ rez, M. J. Illa´n-Go´mez, A. Bueno-Lo´pez, *Applied Catalysis A: General* **371** (2009) 92.
3. V. Singh, R. P. S. Chakradhar, J. L. Rao, D. K. Kim, *J. Lumin.* **128** (2008) 394.
4. E. M. A. Jamal, D. S. Kumar, M. R. Anantharaman, *Bull. Mater. Sci.* **34** (2011) 251.
5. G. Lakshminarayana, L. Wondraczek, *J. Solid State Chem.* **184** (2011) 1931.
6. K. G. Tshabalala, S. Cho, J. K. Park, S. Pitale, I. M. Nagpure, R. E. Kroon, H. C. Swart, O. M. Ntwaeaborwa, *Journal of Alloys and Compounds* **509** (2011) 10115.
7. B. Cheng, S. Qu, H. Zhou, Z. Wang, *Nanotechnology* **17** (2006) 2982.
8. Cz. Koepke, K. Wisniewski, M. Grinberg, G. H. Beall, *Spectrochimica Acta Part A* **54** (1998) 1725.
9. G. Dong, X. Xiao, M. Peng, Z. Ma, S. Ye, D. Chen, H. Qin, G. Deng, Q. Liang, J. Qiu, *RSC Adv.* **2** (2012) 2773.
10. I. Miron, I. Grozescu, *Optoelectron Adv. Mat.* **6** (2012) 673.
11. A. A. Da Silva, A. de Souza Goncalves, M. R. Davolos, *J. Sol-Gel. Sci. Technol.* **49** (2009) 101.
12. S.V. Motlounge, B. F. Dejene, H. C. Swart, O. M. Ntwaeaborwa, *Mater. Res. Express* **1** (2014) 045029.
13. L. F. Koao, B. F. Dejene, R. E. Kroon, H. C. Swart, *J. Lumin.* **147** (2014) 85.
14. V. A. Lubarda, *Mechanics of Materials* **35** (2003) 53.
15. Q. Hou, F. Meng, J. Sun, *Nano Res. Lett.* **8** (2013) 144.
16. B. D. Cullity, *1956 Elements of X-ray Diffraction (2nd Ed)* Addison Wesley 285 (1978).
17. S.V. Motlounge, B. F. Dejene, H. C. Swart, O. M. Ntwaeaborwa, *J. Sol-gel Sci. technol.* **70** (2014) 422.
18. M. Zawadzki, *Solid State Sci.* **8** (2006) 14.
19. A. A. Da Silva, A. Goncalves, M. R. Davolos, S. H. Santagneli, *J. Nanosci. Nanotechnol.* **8** (2008) 5690.
20. D. Jia, L. A. Lewis, X-j. Wang, *Electrochem. Solid-State Lett.* **13** (4) (2010) J32.
21. M. Casalboni, A. Luci, U. M. Grassano, B. V. Mill, A. A. Kaminskii, *Phys. Rev. B* **49** (1994) 3781.

22. R. G. Chary, G. R. Reddy, Y. S. S. Ganesh, K. V. Prasad, A. Raghunadh, T. Krishna, S. Mukherjee, M. Pal, *Adv. Synth. Catal.* **356** (2014) 160.
23. D. Liu, *Ceramics International* **39** (2013) 4765.
24. D. Gao, H. Zheng, X. Zhang, W. Gao, Y. Tian, J. Li, M. Cui, *Nanotechnology* **22** (2011) 175702 (5pp).
25. G. R. Dillip, B. Ramesh, C. M. Reddy, K. Mallikarjuna, O. Ravi, S. J. Dhoble, S. W. Joo, B. Deva Prasad Raju, *Journal of Alloys and Compounds* **615** (2014) 719.
26. G. Blasse, *J. Solid State Chem.* **62** (1986) 207.
27. P. Borse, W. Vogel and S Kulkarni, *J. Colloid Interface Sci.* **293** (2006) 437.
28. <http://www.mathworks.com/matlabcentral/fileexchange/29620-cie-coordinate-calculator> (accessed 21.10.2012).

## Chapter 6: Radiative energy transfer in $\text{ZnAl}_2\text{O}_4:0.1\% \text{Ce}^{3+}$ , $x\% \text{Eu}^{3+}$ nanophosphor synthesized by sol-gel process

*“It is wrong to think that the task of physics is to find out how nature is. Physics concerns what we say about nature.”*

*~ Neils Bohr*

### 6.1 Introduction

In recent years, much effort has been devoted to the research of doped nanostructured materials. This kind of nanomaterials exhibits unusual physical and chemical properties in comparison with their bulk materials, such as size-dependent variation of the band gap energy [1]. Furthermore, the impurity states in a doped semiconductor nanocrystal can play a special role in affecting the electronic energy structures and transition probabilities. As a result of confinement effects on the energy states and scattering rates, and therefore, the unusual physical behaviours are expected to emerge in semiconductor nanocrystals when their sizes are reduced to sizes comparable to some characteristic lengths, such as the electronic de Broglie wavelength, effective Bohr radius around the impurity centers, exciton radius, etc. [2]. A typical example of such material is  $\text{ZnAl}_2\text{O}_4$ , which is a well-known wide-band gap ( $E_g \sim 3.8 \text{ eV}$ ) semiconductor, with a spinel structure [3]. In the normal spinel structure presented by the chemical formula  $\text{AB}_2\text{O}_4$ , the A site is tetrahedrally coordinated by oxygen, while the B site is octahedrally coordinated by oxygen. The spinel structure has the oxygen anions in face-centered-cubic (fcc) close packing [3,4]. The unit cell contains 32 oxygen anions, 16 octahedral cations, and 8 tetrahedral cations. Studies [3,5] have shown that these sites occupation or substitution depend on various factors such as ionic size, cationic charge, electron distribution and electronic states.  $\text{ZnAl}_2\text{O}_4$  has been extensively studied by many researchers as a phosphor host material for applications such as in thin film electroluminescent displays, mechano-optical stress sensors, and stress imaging devices because of its moderate conductivity, high thermal and chemical stability, and good optical and catalytic properties [3,6]. Spinel structures such as  $\text{ZnAl}_2\text{O}_4$  are known to be suitable host lattices for various dopants or activator ions for the preparation of phosphor materials [3,5]. The luminescence properties of the singly doped trivalent rare-earth ( $\text{RE}^{3+}$ ) ions such as  $\text{Sm}^{3+}$  [7], S.V. Motloun et al. / Physica B (2015) accepted (DOI: 10.1016/j.physb.2015.04.007).

Ce<sup>3+</sup> [8] and Eu<sup>3+</sup> [9,10] in ZnAl<sub>2</sub>O<sub>4</sub> (host) nanoparticles have been reported in literature. Martinez-Sanchez et al. [7], showed that the cathodoluminescence (CL) emission spectra for the ZnAl<sub>2</sub>O<sub>4</sub>: Sm<sup>3+</sup> consists of the broad bands localized at 564, 602, 644, and 703 nm, which are associated with <sup>4</sup>G<sub>5/2</sub> → <sup>6</sup>H<sub>5/2</sub>, <sup>4</sup>G<sub>5/2</sub> → <sup>6</sup>H<sub>7/2</sub>, <sup>4</sup>G<sub>5/2</sub> → <sup>6</sup>H<sub>9/2</sub>, and <sup>4</sup>G<sub>5/2</sub> → <sup>6</sup>H<sub>11/2</sub> transitions in the Sm<sup>3+</sup> ions, respectively. Furthermore, they [7] showed that the concentration quenching of the CL occurred at about 4.26% of the activator (Sm<sup>3+</sup>) ions. In the case of Ce<sup>3+</sup> doped phosphors, the reports [8,11] have shown that the Ce<sup>3+</sup> doped phosphor exhibit the broad emission band near ultraviolet (UV) region, which is associated with 5d → 4f transitions of Ce<sup>3+</sup> ion. However, it is noted from [11] that the broad band luminescence near UV region strongly depend on the host lattice. Moreover, Le Toquin et al. [12] have reported unfamiliar red emission from 5d (e<sub>g</sub>) → 4f<sup>1</sup> transition in Ce<sup>3+</sup> doped CaSiN<sub>2</sub>. The existence of this unusual red emission from Ce<sup>3+</sup> ion is due to the successful adjustment of the crystal field splitting by lowering the lowest 5d level in order to decrease the 5d-5f energy gap, which shifts the phosphor emission towards higher wavelengths [12]. Ce<sup>3+</sup> activated host materials have received great attention because of their practical applications in thermoluminescence lighting and scintillators [11]. For the Eu<sup>3+</sup> doped ZnAl<sub>2</sub>O<sub>4</sub>, the reports [9,10] have shown that there are series of resolvable bands peaking at 570–720 nm, which were assigned to the characteristic transitions of Eu<sup>3+</sup> (4f<sub>6</sub> configuration) 4f - 4f from <sup>5</sup>D<sub>0</sub> → <sup>7</sup>F<sub>*j*</sub> (*j* = 0, 1, 2, 3, 4). In addition, the results in [9,10] also showed that among the <sup>5</sup>D<sub>0</sub> → <sup>7</sup>F<sub>*j*</sub> transitions, the <sup>5</sup>D<sub>0</sub> → <sup>7</sup>F<sub>1</sub> band at 590 nm occurs by means of the magnetic dipole transition and hardly changes with the crystal field strength around the Eu<sup>3+</sup> ion, while the <sup>5</sup>D<sub>0</sub> → <sup>7</sup>F<sub>2</sub> band at 617 nm takes place through force electric dipole (FED) transition of the 4f shell and is highly sensitive to structural changes and environmental effects in the vicinity of the Eu<sup>3+</sup> ion [9,10]. Phosphor materials doped with Eu<sup>3+</sup> ions exhibit higher absorption coefficient and excellent luminescence efficiency [13]. Apart from the singly doped phosphors with Ce<sup>3+</sup> and Eu<sup>3+</sup>, phosphors co-doped with Ce<sup>3+</sup> and Eu<sup>3+</sup> ions are normally used to produce the blue and red emissions, respectively [14]. In the study of Ce<sup>3+</sup> and Eu<sup>3+</sup> ions co-doped Na<sub>3</sub>Gd(PO<sub>4</sub>)<sub>2</sub> phosphor, Chengaiah et al. [11] showed the existence of energy transfer from Eu<sup>3+</sup> → Ce<sup>3+</sup> ions. Furthermore, their results [11] showed the possibility of tuning the luminescent colours of the Na<sub>3</sub>Gd(PO<sub>4</sub>)<sub>2</sub>: Ce<sup>3+</sup>; Eu<sup>3+</sup> phosphors from reddish to bluish by increasing the Ce<sup>3+</sup> ions concentration.

Inspired by the Chengaiah et al. [11] results, in this study we have chosen ZnAl<sub>2</sub>O<sub>4</sub> as our host matrix. A series of ZnAl<sub>2</sub>O<sub>4</sub>:0.1% Ce<sup>3+</sup>, x% Eu<sup>3+</sup> (0 ≤ x ≤ 2) phosphors was synthesized

by the sol-gel technique and their luminescent characteristics were investigated. In contrast with Chengaiah findings, we report on the possibility of tuning the emission colour from bluish to reddish by increasing the  $\text{Eu}^{3+}$  mol%. The proposed energy transfer mechanism from  $\text{Ce}^{3+} \rightarrow \text{Eu}^{3+}$  and the emission pathways have been discussed in details. This study and Chengaiah et al. [11] results confirmed that the energy transfer pathway or direction in the  $\text{Ce}^{3+}$  and  $\text{Eu}^{3+}$  co-doped systems can be controlled to favour  $\text{Ce}^{3+} \rightarrow \text{Eu}^{3+}$  or  $\text{Eu}^{3+} \rightarrow \text{Ce}^{3+}$ . The principal idea of this work was to fabricate or produce the phosphor material, which could be used in plasma display panels (PDPs) and light emitting diodes (LEDs).

## 6.2 Experimental

The  $\text{ZnAl}_2\text{O}_4$  (host), singly doped (with 0.1%  $\text{Ce}^{3+}$  or 0.1%  $\text{Eu}^{3+}$ ) and co-doped with 0.1%  $\text{Ce}^{3+}$ ,  $x\%$   $\text{Eu}^{3+}$  ( $0 \leq x \leq 2$ )  $\text{ZnAl}_2\text{O}_4$  nanocrystals were synthesized using a well-known sol-gel technique [15]. The experimental steps followed are summarized in figure 6.1.  $\text{Zn}(\text{NO}_3)_2 \cdot 6\text{H}_2\text{O}$  (98%) and  $\text{Al}(\text{NO}_3)_3 \cdot 9\text{H}_2\text{O}$  (98.5%) were dissolved in deionized water. The sols stoichiometric molar ratio of Zn:Al was 2:1. The weighed raw materials  $\text{Ce}(\text{NO}_3)_3 \cdot 6\text{H}_2\text{O}$  (99.9%) and  $\text{Eu}(\text{NO}_3)_3 \cdot 5\text{H}_2\text{O}$  (99.9%) were added in separate beakers of the solution to single dope with 0.1%  $\text{Ce}^{3+}$  and 0.1%  $\text{Eu}^{3+}$  ions. Similar procedure was followed for the co-doping and the mol% of  $\text{Ce}^{3+}$  ions was kept constant at 0.1%, while the molar concentrations of  $\text{Eu}^{3+}$  ions were varied at ( $0 \leq x \leq 2$ ) mol%. Citric acid,  $\text{C}_6\text{H}_8\text{O}_7 \cdot \text{H}_2\text{O}$  (99%), was used as a catalyst and the Zn:catalyst molar ratio was kept constant at 1:0.75 for all samples. The heating temperature was kept at  $\sim 80^\circ\text{C}$  while constantly stirring on a magnetic stirrer until gels were formed. The gels were dried in an oven kept at a temperature of  $130^\circ\text{C}$ . The dried gels were ground into fine powders and were subsequently annealed at  $800^\circ\text{C}$  in a furnace for an hour.

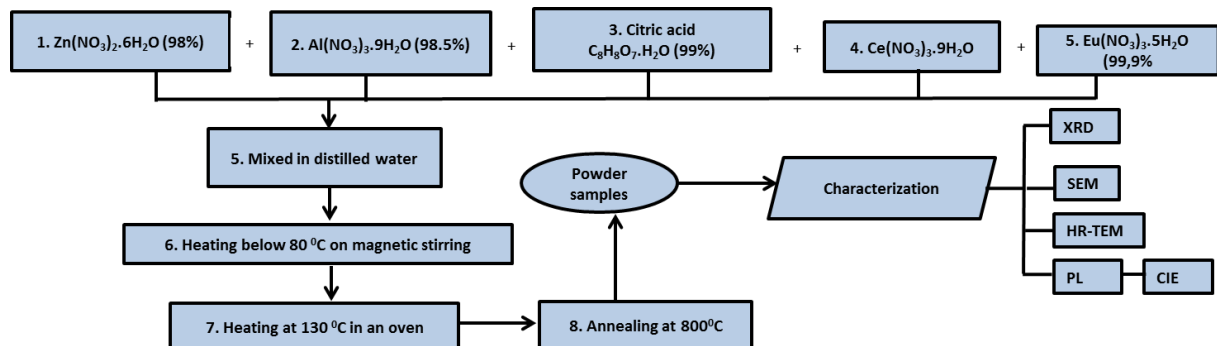


**Figure 6.1.** Summarised scheme for sol-gel synthesis of un-doped, singly doped (with  $\text{Ce}^{3+}$  and  $\text{Eu}^{3+}$ ) and co-doped  $\text{ZnAl}_2\text{O}_4$ .

The crystal structure and phase composition of the samples was characterized by powder X-ray diffraction (XRD) (Bruker AXS D8 Advance diffractometer) with  $\text{CuK}\alpha$  ( $1.5418\text{\AA}$ ) radiation. The surface morphology of the phosphor powder was investigated using a Shimadzu Superscan ZU SSX-550 electron microscope (SEM). High-Resolution Transmission Electron microscopy (HR-TEM) was performed with a JEOL JEM 2100 containing a  $\text{LaB}_6$  filament. Room temperature photoluminescence (PL) measurements were done using a Hitachi F-7000 fluorescence spectrophotometer.

## 6.3 Results and discussion

### 6.3.1 XRD

To examine the crystal structure of the  $\text{ZnAl}_2\text{O}_4$  (host), singly doped and co-doped samples, we carried out XRD analysis on all samples and their patterns are shown in figure 6.1 (a) and (b), respectively. It can be seen that the prepared materials are fully crystalline and the diffraction patterns corresponds to those of the standard patterns of cubic  $\text{ZnAl}_2\text{O}_4$  spinel (JCPDS, No. 82-1043). The average lattice spacing calculated from the most intense peak (311) was estimated to be  $8.07\text{ \AA}$ , which corresponds to the lattice spacing of the  $\text{ZnAl}_2\text{O}_4$  reported by Zawadzki et al. [16]. The peak ratios intensities of all prepared powders and that of standard were found to be precisely the same. No other reflection traces due to the impurities phases were detected in all samples, which confirm that the prepared powders were in the single phase. Figure 6.3 presents the analysis of the (311) diffraction peaks for the host, singly doped and co-doped samples. It is noted that the incorporation of foreign atoms into the host matrix influences the diffraction intensity. For instance, it can be seen that doping with  $\text{Ce}^{3+}$  enhances the crystallinity, while doping and co-doping the host with  $\text{Eu}^{3+}$  ions decreased the diffraction intensity, which suggest the destruction of the crystalline quality during the growth of  $\text{ZnAl}_2\text{O}_4$  nanocrystals [17]. The decrease in crystallinity with the incorporation of the rare earth ions has been explained by Barros et al. [10] to be due to high disorder these ions produce in the host lattice matrix in response to the ionic radius mismatch between the rare earth ions and  $\text{Zn}^{2+}$  or  $\text{Al}^{3+}$  ions.

Furthermore, when comparing the host to the singly doped and co-doped samples in figure 6.3, it is evidently observed that there is a peak shift to the lower diffraction angle. This shift to the lower angle indicates that the lattice parameters are slightly larger than those of un-

doped  $\text{ZnAl}_2\text{O}_4$  [18], which can also be verified by the values obtained in table 6.1. An increase in lattice parameter can be interpreted as follows; when the smaller ionic radius  $\text{Zn}^{2+}$  (0.74 Å) or  $\text{Al}^{3+}$  (0.53 Å) [17] are substituted by the bigger ionic radius  $\text{Ce}^{3+}$  (1.03 Å) and  $\text{Eu}^{3+}$  (0.95 Å) [19], the unit-cell volume is expected to expand. Therefore, this serves as a proof that the foreign atoms (namely  $\text{Ce}^{3+}$  and  $\text{Eu}^{3+}$ ) have successfully been incorporated into the  $\text{ZnAl}_2\text{O}_4$  crystal structure [9]. In addition, the results suggests that for the ( $\text{ZnAl}_2\text{O}_4$  singly doped and co-doped with  $\text{Ce}^{3+}$  and  $\text{Eu}^{3+}$  ions) systems, the Vegard's law [20] is obeyed. It is important to note that for the singly doped samples, there is no change in lattice parameter values shown in table 6.1 and that is attributed to the similarities in size for both  $\text{Ce}^{3+}$  and  $\text{Eu}^{3+}$  ions. Note that in some systems, Vergard's law may be violated. For an example, we have recently [21] shown that in  $\text{ZnAl}_2\text{O}_4:\text{Pb}^{2+}$  system, the Vergard's law can be disobeyed at the lower  $\text{Pb}^{2+}$  (ionic radius 1.01 ~ 1.40 Å) mol% and that was attributed to the shrinkage of the  $\text{Pb}^{2+}$  outer electron shell due to its electronic interactions with more neighbouring  $\text{Zn}^{2+}$  ions, which suppresses or makes it smaller than the  $\text{Zn}^{2+}$  ion [21].

**Table 6.1.** Sample identification and corresponding FWHM, crystallites size, strain, decay times, energy transfer efficiency and CIE colour coordinates.

Sample	FWHM (rad) x $10^{-3}$	Crystallites size (nm)	Strain (%)	a (Å)	Dislocation density ( $\text{nm}^{-2}$ ) x $10^{-3}$	CIE
Host	6.68	22.0	2.00	8.073	2.09	(0.179,0.165)
0.1% $\text{Ce}^{3+}$	6.61	22.1	1.98	8.076	2.05	(0.185,0.186)
0.1% $\text{Eu}^{3+}$	6.84	21.4	2.05	8.076	2.19	(0.199,0.195)
x = 0.05	7.19	20.3	2.16	8.083	2.42	(0.193,0.193)
x = 0.3	7.17	20.4	2.15	8.086	2.41	(0.252,0.232)
x = 0.5	7.25	20.2	2.18	8.086	2.46	(0.305,0.266)
x = 0.7	7.64	19.1	2.30	8.086	2.74	(0.348,0.288)
x = 0.9	7.75	19.0	2.32	8.079	2.81	(0.394,0.310)
x = 1.5	8.11	18.0	2.43	8.079	3.08	(0.497,0.355)
x = 2.0	8.48	17.2	2.55	8.089	3.37	(0.507,0.358)

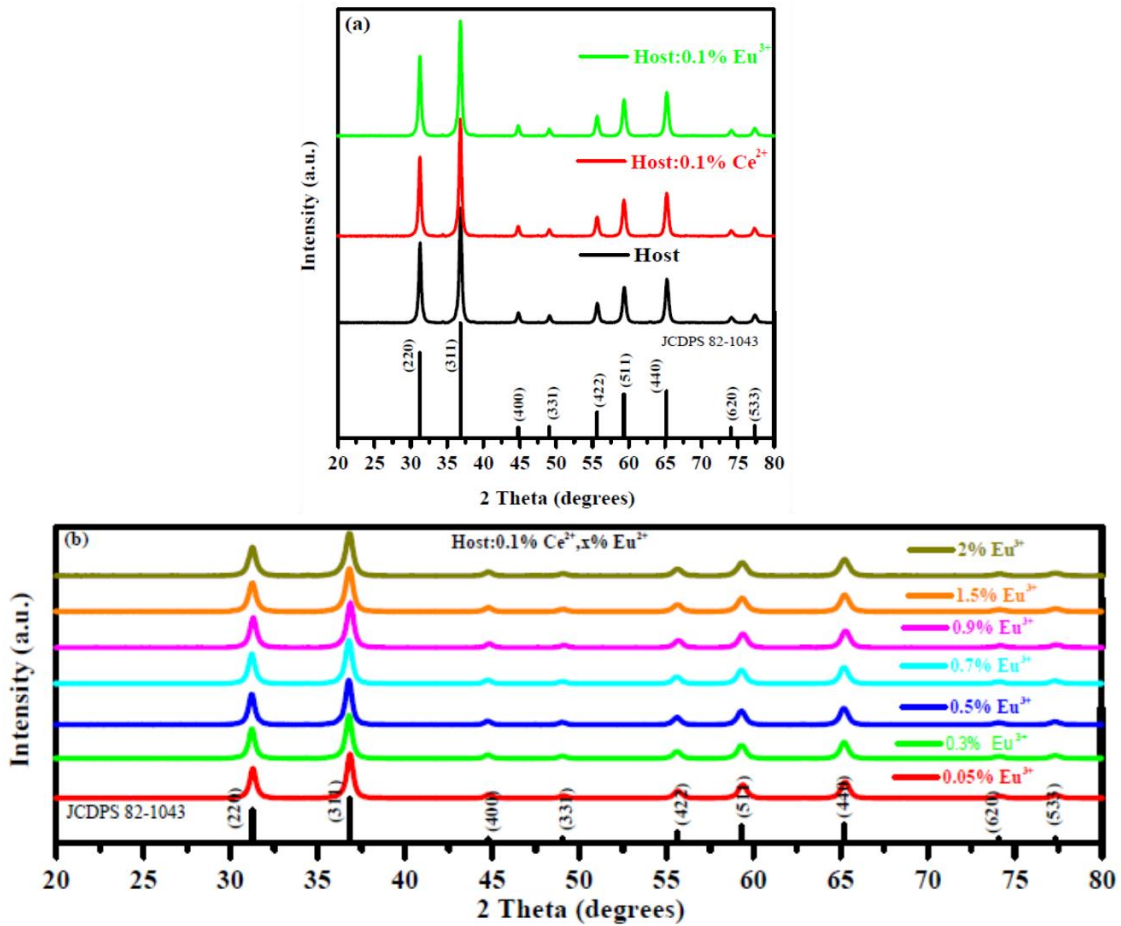


**Figure 6.2.** The XRD pattern for the (a)  $\text{ZnAl}_2\text{O}_4$  and singly doped samples and (b) co-doped samples at the varying  $\text{Eu}^{3+}$  mol%.

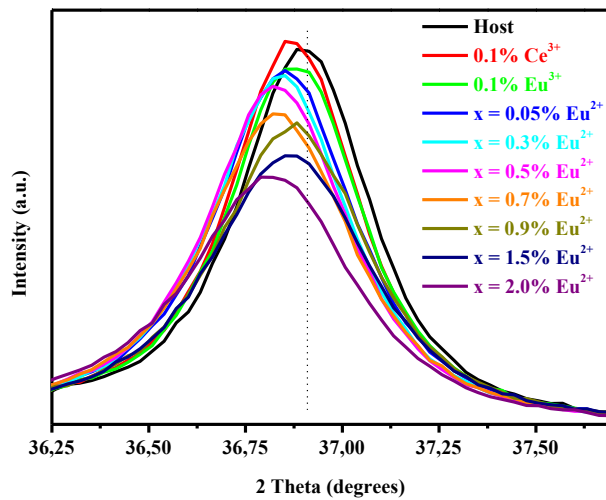


**Figure 6.3.** Analysis of (311) peak for the host, singly doped and co-doped samples.

Generally, when comparing the host and the co-doped samples, the Gaussian fits of the Full Width at Half Maximum (FWHM) in figure 6.3 is observed to increase with the  $\text{Eu}^{3+}$  mol% as shown in table 6.1. Figure 6.4 (a) illustrates both the FWHM (black scale) and strain (red scale) as a function of co-dopant ( $\text{Eu}^{3+}$ ) mol%. In table 6.1 and figure 6.4 (a) the FWHM increases as the  $\text{Eu}^{3+}$  doping concentration increases. This could be caused by a decrease in crystallites sizes, but it could be caused by increasing strain or disorder due to the increasing amount of co-dopant ( $\text{Eu}^{3+}$ ) while the crystallites size remains constant. The average crystallites sizes were calculated from the (311) diffraction peak broadening by using the Scherer equation [22]. The strain broadening, calculated from Williamson and Hall method [23], as a function of  $\text{Eu}^{3+}$  mol% showed the linear increase behaviour (see figure 6.4 (a)). These results suggest that the inclusion of more bigger foreign atoms such as  $\text{Ce}^{3+}$  and  $\text{Eu}^{3+}$  into the crystal structure of  $\text{ZnAl}_2\text{O}_4$  results in an increase in strain and as a consequence more structural dislocations density. The dislocation density as function of  $\text{Eu}^{3+}$  mol% showed a linear relationship as shown on the insert of figure 6.4 (b), which suggests that doping with  $\text{Eu}^{3+}$  at the higher concentration increases the defects population in the host crystal structure. The dislocation density was calculated using the relation as presented in Som et al. [24] report. In summary, our results show that an increase in strain is accompanied by the decrease in crystallites sizes. Similar kind of relationship to our results has been previously observed by Paiva-Santos et al. [25] on the study of Mn doped  $\text{SnO}_2$  system. Furthermore in their results [25] they showed that the inclusion of Mn into  $\text{SnO}_2$  at the higher mol% increases the segregation of Mn in the  $\text{SnO}_2$  surface.

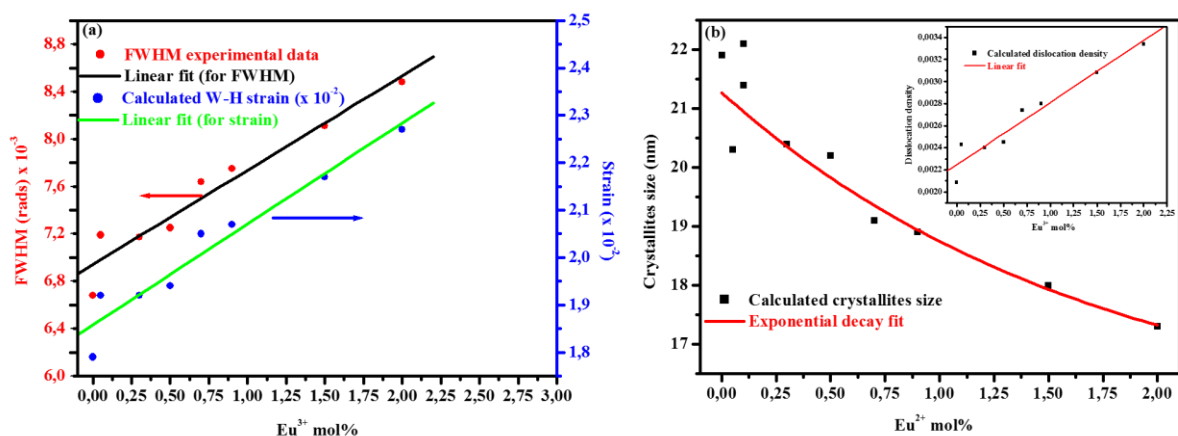


**Figure 6.4.** (a) Full width at half maximum (FWHM) and strain as a function of  $\text{Eu}^{3+}$  mol%. (b) Crystallites size as a function of  $\text{Eu}^{3+}$  mol%.

### 6.3.2 SEM and HR-TEM

The morphological aspect of the selected nanopowder samples was examined by SEM, as shown in figure 6.5. The host or un-doped sample is shown in figure 6.5 (a), the micrographs reveal that the morphology consists of irregular crystallite sizes, pores and grain boundaries distributed over the surface. Single doping the host with 0.1%  $\text{Ce}^{3+}$  seems to enhance particles agglomeration (see figure 6.5 (b)) and the pores morphology as in figure 6.5 (a) is observed. On the other hand, when doping with  $\text{Eu}^{3+}$  (see figure 6.5 (c)), the morphology reveals similar traits to the host sample presented in figure 6.5 (a) with additional irregular plates-like-structure morphology. Co-doping the host at the lower and intermediate  $\text{Eu}^{3+}$  mol% as shown in figure 6.5 (d) and (e) appears to resemble the morphological combination of the samples shown in figure 6.5 (a)-(c). At the higher co-dopant mol% as shown in figure 6.5 (f), similar morphology as discussed in figure 6.5 (c) with additional bigger plate-like-morphology is observed.

The prepared nanopowders microstructure was further characterised by HR-TEM shown in figure 6.6, which also revealed that the material consists of non-uniform sizes. It can be seen that the clear lattice fringe spacing is observed in the host or un-doped sample shown by the red square in figure 6.6 (a). As the host is singly doped and co-doped it is clearly observed (see the red ellipses and their magnified versions) that the visibility of the lattice fringes is lost compared to the host sample. The loss in lattice fringes suggest the increase in strain or disorder (see figure 6.4 (a)), which result in decrease on the crystalline quality as the foreign atoms are incorporated on the host crystal lattice. Considering the decrease in (311) diffraction intensity as shown on the XRD results presented in figure 6.3, it is evident that the TEM and XRD results are in good agreement with each other. Thus, taking the average lattice parameter values presented in table 6.1, the average d spacing as shown in figure 6.6 (a) is predicted to be 0.24 nm. Note that similar microstructure to our results have been previously reported in literature [9,16]. In addition, it is reasonable to estimate the average crystallite size from TEM image for the host as shown in figure 6.6 (a) to be around 23 nm, which also agrees very well with calculated crystallites size from the XRD results. The consistency in agreement between XRD and TEM results confirms the nanocrystalline nature of the prepared powder samples.

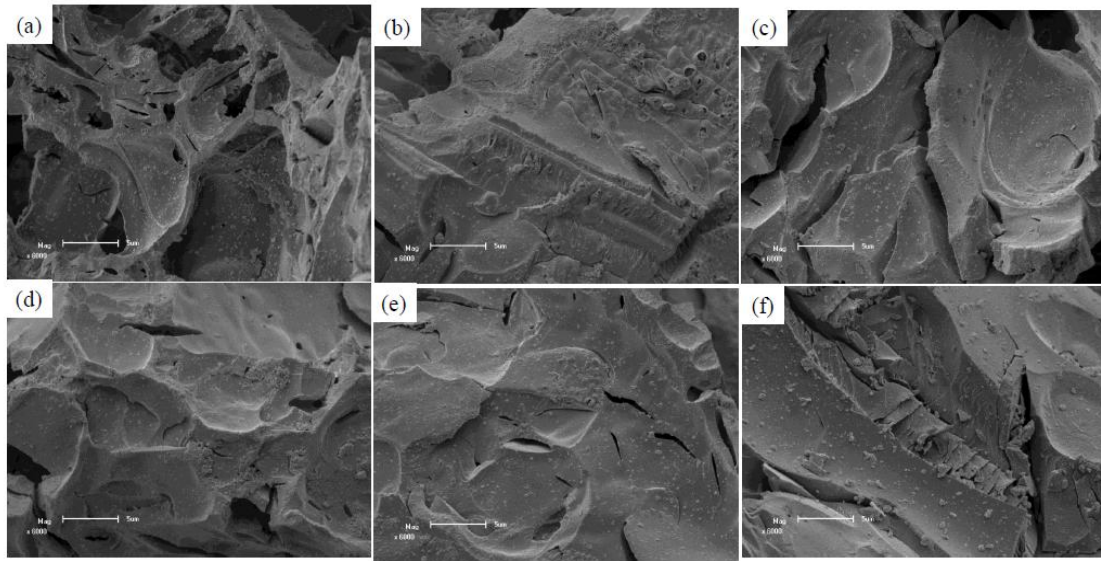


**Figure 6.5.** SEM images for (a) Host (b)  $\text{ZnAl}_2\text{O}_4:0.1\% \text{Ce}^{3+}$  (c)  $\text{ZnAl}_2\text{O}_4:0.1\% \text{Eu}^{3+}$  (d)  $\text{ZnAl}_2\text{O}_4:0.1\% \text{Ce}^{3+}, 0.05\% \text{Eu}^{3+}$  (e)  $\text{ZnAl}_2\text{O}_4:0.1\% \text{Ce}^{3+}, 0.7\% \text{Eu}^{3+}$  (f)  $\text{ZnAl}_2\text{O}_4:0.1\% \text{Ce}^{3+}, 2\% \text{Eu}^{3+}$ .

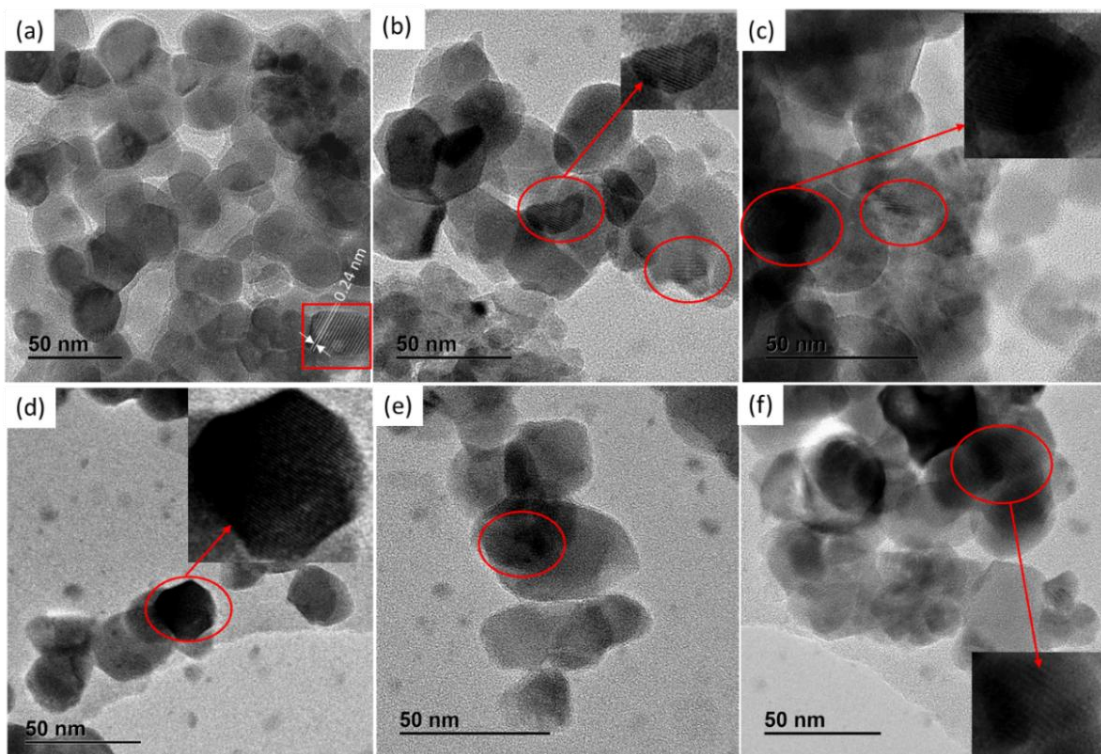


**Figure 6.6.** HR-TEM images for (a) Host (b)  $\text{ZnAl}_2\text{O}_4:0.1\% \text{Ce}^{3+}$  (c)  $\text{ZnAl}_2\text{O}_4:0.1\% \text{Eu}^{3+}$  (d)  $\text{ZnAl}_2\text{O}_4:0.1\% \text{Ce}^{3+}, 0.05\% \text{Eu}^{3+}$  (e)  $\text{ZnAl}_2\text{O}_4:0.1\% \text{Ce}^{3+}, 0.7\% \text{Eu}^{3+}$  (f)  $\text{ZnAl}_2\text{O}_4:0.1\% \text{Ce}^{3+}, 2\% \text{Eu}^{3+}$ .

### 6.3.3 PL analysis

The room-temperature PL excitation and emission spectra of the un-doped, single doped and co-doped  $\text{ZnAl}_2\text{O}_4$  spinels are illustrated in figure 6.7 (a) and (b), respectively. When monitoring the emission at 396 nm, the excitation spectra in figure 6.7 (a) and (b) indicate that there are two ultraviolet (UV) absorption bands located at 284 and 330 nm. Since there is no evidence of the peak shift in both absorption bands they must certainly be originating from the host material absorption. The absorption band with a maximum at 284 nm is attributed to the band-to-band transition of  $\text{AlO}_6$  anion grouping in  $\text{ZnAl}_2\text{O}_4$  [9] as shown in figure 6.8 (a). According to the Cheng et al. [9] and the references therein, the other absorption band at around 330 nm arises from the charge-transfer transition from coordination anions ( $\text{O}^{2-}$ ) to the rare-earth ions (e.g.  $\text{Eu}^{3+}$ ). Our results indicate that the Cheng et al. [9] idea is questionable and must be re-examined because even for the un-doped sample the 330 nm absorption band is still present. Thus, in this study, we emphasise that the absorption band at 330 nm originates from the host material, which might probably be arising from the defects absorption as shown in figure 6.8 (a)-(c). To examine and reveal the origin of different emissions in the co-doped samples it is very important to test the host and singly doped sample as shown in figure 6.7 (a). The emission spectra reveal that all powder samples exhibit violet emission. The emission band at 396 nm should originate from the host material and it is credited to the intrinsic intra-band gap defects, such as oxygen vacancies ( $\text{V}_\text{o}^*$ ) [26,27] as shown in Fig. 8 (a). Da Silva et al. [26,27] suggested that these defects provide donor levels near the conduction band edge of the oxide.

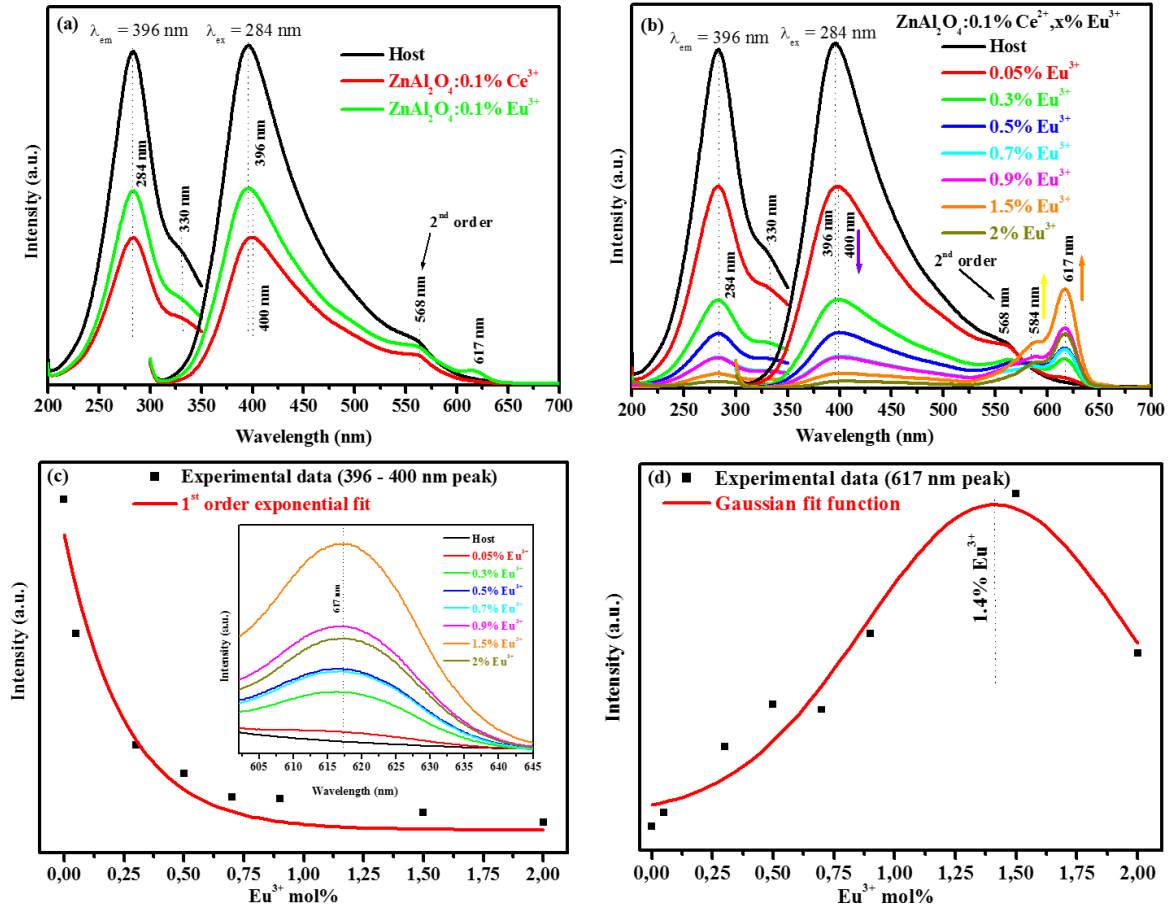


**Figure 6.7.** (a) Excitation and emission spectra of the (a) undoped and singly doped (b) co-doped at varying Eu<sup>3+</sup> mol% (c) PL intensity as a function of x% Eu<sup>3+</sup> for the violet emission at 396 nm (insert: emission intensity at 617 nm as function of wavelength) and (d) PL emission intensity at 617 nm as function of x% Eu<sup>3+</sup> mol%.

When considering the sample doped with 0.1% Ce<sup>3+</sup>, it can be noticed that there is a slight peak shift to the higher wavelength (e.g. from 396 to 400 nm), which signifies that the emission is from the Ce<sup>3+</sup> ion. As shown in figure 6.8 (b), the violet emission at 400 nm is attributed to the  $5d \rightarrow {}^2F_{7/2}$  transition in Ce<sup>3+</sup> ion [28]. One might consider the emission at 400 nm to be due to the mixture of Ce<sup>3+</sup> and host material emissions. However, from our recent results [21] in ZnAl<sub>2</sub>O<sub>4</sub>:Pb<sup>2+</sup>, we have shown that the emissions originating from different transitions are expected to have different emissions wavelengths regardless of how close they might be, for an example, we have shown that slightly different emission peak position at 390, 395 and 399 nm in ZnAl<sub>2</sub>O<sub>4</sub>: Pb<sup>2+</sup> are due to the  ${}^3P_1 \rightarrow {}^1S_0$ , host and  ${}^3P_0 \rightarrow {}^1S_0$  transitions, respectively. The emission band at 568 nm in figure 6.7 (a) and (b) is attributed to the second detection of the excitation light wavelength 284 nm. This can be

motivated by the fact that there is no peak shift in all samples for the 568 nm emission. The emission peak at 617 nm is certainly from the  $\text{Eu}^{3+}$  ion, which can be attributed to the  ${}^5\text{D}_0 \rightarrow {}^7\text{F}_2$  transition [11] (see figure 6.8 (c)). figure 6.7 (b) presents the comparison of the host and the co-doped samples. The new emerging emission peak at 584 nm is attributed to the well-known orange emission from  ${}^5\text{D}_0 \rightarrow {}^7\text{F}_1$  transition in  $\text{Eu}^{3+}$  ion [11] (see figure 6.8 (c)). As described by Hu et al. [29], the weaker emission at 584 nm is ascribed to the  $\text{Eu}^{3+}$  magnetic dipole transition  ${}^5\text{D}_0 \rightarrow {}^7\text{F}_1$ , which is insensitive to the site symmetry, while the emission peak at 617 nm (magnified version is an inset in figure 6.7 (c)) is assigned to the  $\text{Eu}^{3+}$  electric dipole transition of  ${}^5\text{D}_0 \rightarrow {}^7\text{F}_2$ , induced by the lack of inversion symmetry at the  $\text{Eu}^{3+}$  site in  $\text{ZnAl}_2\text{O}_4$  singly doped with 0.1%  $\text{Eu}^{3+}$  and co-doped with 0.1%  $\text{Ce}^{3+}$ , x%  $\text{Eu}^{3+}$  and the break of parity selection rules, and is much stronger than that of the  ${}^5\text{D}_0 \rightarrow {}^7\text{F}_1$  transition. All other peaks in figure 6.7 (b) have similar origins as in figure 6.7 (a).

The luminescence mechanisms for all emissions arising from the un-doped, singly doped and co-doped  $\text{ZnAl}_2\text{O}_4$  are illustrated in figure 6.8 (a) – (c). The absorption and emission mechanism can be explained as follows; the electrons in the host valence band (VB) are excited to the conduction band (CB) after the excitation of 284 nm. Most of the studies, for an example, Singh et al. [3] have reported the band gap of  $\text{ZnAl}_2\text{O}_4$  to be  $\sim 3.8$  eV, which does not corresponds to the 4.4 eV (284 nm) from our results. However, it is also important to consider the possible band gap value of  $\sim 4.3$  eV reported by Dixit et al. [30]. In their results it is stated that the band gap have been overestimated. Most interesting, they also stated that they anticipate the future experimental work to confirm their results. Thus, our results are confirming the Dixit et al. [30] results. For the host emission, the excited electrons are de-excited by non-radiative relaxation (NRR) and trapped on the defect states (denoted by  $\text{V}_0^*$  in figure 6.8 (a)), and then de-excited to the VB by radiative decay. Single and co-doping the host with  $\text{Ce}^{3+}$  and  $\text{Eu}^{3+}$  ions can be interpreted as a development of extra more new trapping centres [31]. The mechanism for the singly doped and co-doped is exactly similar to that one of the host emission but the difference is the trapping centres, which are  $\text{Ce}^{3+}$  or  $\text{Eu}^{3+}$  ions in the singly doped and both for the co-doped samples.

The reason why we have attribute the emission from the europium ion to be from  $\text{Eu}^{3+}$  not  $\text{Eu}^{2+}$  is based on the fact that  $\text{Eu}^{2+}$  ions have a broad emission band while  $\text{Eu}^{3+}$  ions emit discrete narrow lines. These differences have been explained by Xia et al. [32] as follows: The electronic structure of  $\text{Eu}^{2+}$  is  $[\text{Xe}]4f^75d^0$  while it is  $[\text{Xe}]4f^6$  for  $\text{Eu}^{3+}$ . Thus, the allowed  $4f^75d^0 \rightarrow 4f^75d^1$  transition of  $\text{Eu}^{2+}$  would occur when it is excited. Furthermore, the emission

of  $\text{Eu}^{2+}$  is significantly affected by the surrounding environment of the structure and finally causes the broadband emission since the 5d orbital is naked. However, the energy levels of  $\text{Eu}^{3+}$  ions arise from its  $4f^n$  configuration, so that the  $f \rightarrow f$  transitions of  $\text{Eu}^{3+}$  typically have atomic-like sharp peaks owing to the shielding effect of 4f electrons.

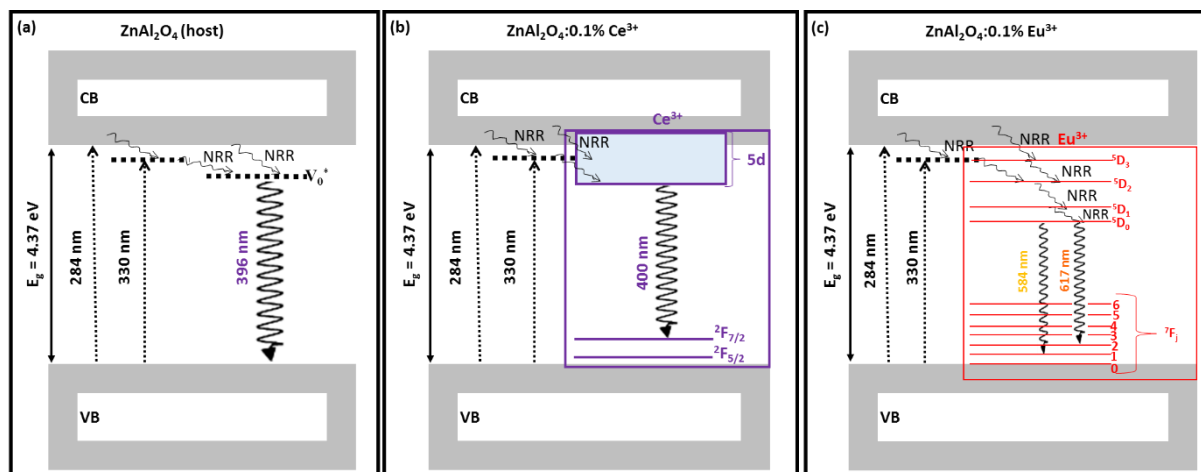


**Figure 6.8.** The emission pathways for the (a)  $\text{ZnAl}_2\text{O}_4$  (host), (b)  $\text{ZnAl}_2\text{O}_4:0.1\% \text{Ce}^{3+}$  and (c)  $\text{ZnAl}_2\text{O}_4:0.1\% \text{Eu}^{3+}$ .

The violet emission intensity at 396 – 400 and 617 nm as a function of  $\text{Eu}^{3+}$  mol% is presented in figure 6.7 (c) and (d), respectively. The emission at 396 – 400 nm shows an exponential decay behaviour, which is however not attributed to the concentration quenching effect [32]. Orange emission peak at 617 nm as a function of  $\text{Eu}^{3+}$  mol% is shown in figure 6.7 (d), which shows a Gaussian fit kind of behaviour. It is important to mention that the emission at 584 nm gave similar kind of behaviour as 617 nm peak. Within the investigated range of 0 - 2 %  $\text{Eu}^{3+}$ , the 1.5%  $\text{Eu}^{3+}$  had the highest emission intensity. However, in figure 6.7 (d) the Gaussian fit suggests that 1.4%  $\text{Eu}^{3+}$  is the optimum dopant concentration for the emission at 617 nm in the  $\text{ZnAl}_2\text{O}_4:0.1\% \text{Ce}^{3+}$ , x%  $\text{Eu}^{3+}$  co-doped system and above this optimum concentration, the concentration quenching effect on the emission intensity is observed. Thus, Gaussian fit clearly reveals the existence of both well-known luminescence enhancement and quenching phenomena as the co-dopant mol% is increased. Luminescence enhancement is attributed to the modification of the defect levels or local environment of the dopant ions [33], which is evidently favouring the lower  $\text{Eu}^{3+}$  mol%. Luminescence quenching is attributed to the new defect sites that enhance non-radiative recombination (NRR) of the excited electrons [34], which favours the higher  $\text{Eu}^{3+}$  mol%. Thus, it is reasonable to come to the following conclusion, that doping at higher  $\text{Eu}^{3+}$  concentration introduces new defect sites that enhanced NRR recombination of the excited electrons.

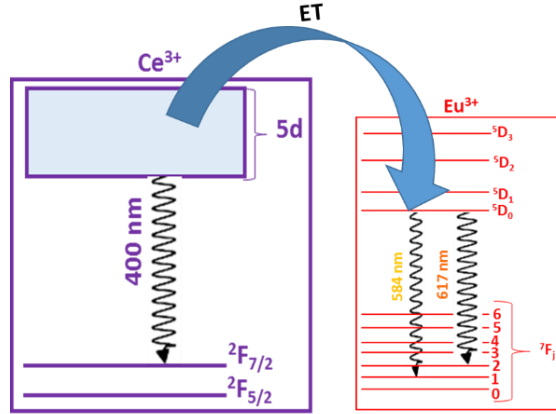


**Figure 6.9.** Schematic diagram of energy transfer mechanism from  $\text{Ce}^{3+} \rightarrow \text{Eu}^{3+}$  in  $\text{ZnAl}_2\text{O}_4:0.1\% \text{Ce}^{3+}, x\% \text{Eu}^{3+}$ .

The comparison of the 400, 584 and 617 nm emissions peaks trends as shown by the arrows in figure 6.7 (b) clearly confirms the existence of energy transfer. For an example, it is observed that the emission from  $\text{Ce}^{3+}$  at 400 nm decreases with an increase in the  $\text{Eu}^{3+}$  mol%. On the other hand, the emissions peaks from  $\text{Eu}^{3+}$  at 584 and 617 nm increases with an increase in  $\text{Eu}^{3+}$  mol%. Such decrease in  $\text{Ce}^{3+}$  emission peak and increase in  $\text{Eu}^{3+}$  peaks trends confirms the energy transfer from  $\text{Ce}^{3+} \rightarrow \text{Eu}^{3+}$  ion as shown in figure 6.9. Chengaiah et al. [11] reported the energy transfer from  $\text{Eu}^{3+} \rightarrow \text{Ce}^{3+}$  (note the order) in  $\text{Eu}^{3+}/\text{Ce}^{3+}$  co-doped  $\text{Na}_3\text{Gd}(\text{PO}_4)_2$  as the  $\text{Ce}^{3+}$  concentration was increased. Unlike in the Chengaiah et al. [11] report, our results have revealed the energy transfer to be in the following order  $\text{Ce}^{3+} \rightarrow \text{Eu}^{3+}$ . The reason why there is this difference in the energy transfer order or pathways in Chengaiah et al. [11] and our results is credited to the co-dopant ion (e.g.  $\text{Ce}^{3+}$  was varied in Chengaiah et al. [11] and  $\text{Eu}^{3+}$  was varied in our results). Based on Chengaiah et al. [11] and our results, we therefore conclude that the energy transfer order or pathways can be tuned to favour  $\text{Eu}^{3+} \rightarrow \text{Ce}^{3+}$  or  $\text{Ce}^{3+} \rightarrow \text{Eu}^{3+}$  in the  $\text{Eu}^{3+}/\text{Ce}^{3+}$  co-doped phosphor materials. This situation also occurs in  $\text{Tb}^{3+}/\text{Ce}^{3+}$  co-doped systems where energy transfer can occur from  $\text{Tb}^{3+}$  to  $\text{Ce}^{3+}$  (e.g. in  $\text{Y}_{3-x-y}\text{Tb}_y\text{Gd}_x\text{Al}_5\text{O}_{12}$  ( $x=0.65, y=0.575$ ) doped with  $\text{Ce}^{3+}$  [35]) or from  $\text{Ce}^{3+}$  to  $\text{Tb}^{3+}$  (e.g. in  $\text{LaF}_3$  [36]).

To further examine whether the energy transfer from  $\text{Ce}^{3+} \rightarrow \text{Eu}^{3+}$  is radiative or non-radiative, possible excitations peaks were monitored for the emission at 617 nm as shown in figure 6.10 (a). Evidently the excitation spectra show that there are two absorption bands located at 265 and 396 nm. The absorption band with a maximum at 265 nm is attributed to

the band-to-band transition in a host material ( $\text{ZnAl}_2\text{O}_4$ ) [9], while the absorption band at 396 nm is confidently attributed to be due to the defects level from the  $\text{Eu}^{3+}$  ion impurities. The emission spectra in figure 6.10 (a) reveal that there are four emission bands located at 586, 617, 657 and 704 nm. The emission peak at 586 nm is attributed to the  ${}^5\text{D}_0 \rightarrow {}^7\text{F}_1$  transition in  $\text{Eu}^{3+}$  ion [11] as shown in figure 6.10 (b). Thus, 586 nm emission peak shown in figure 6.10 (b) originates from the same transition as the emission peak at 584 nm as shown in figure 6.8 (c) and figure 6.9. The emission peak at 617 nm is assigned to  ${}^5\text{D}_0 \rightarrow {}^7\text{F}_2$  transition as shown in figure 6.8 (c). Finally, the emissions at 657 and 704 nm are attributed to the  ${}^5\text{D}_0 \rightarrow {}^7\text{F}_3$  and  ${}^5\text{D}_0 \rightarrow {}^7\text{F}_4$  transitions in  $\text{Eu}^{3+}$  ion [11], respectively. Note that in figure 6.7 (b) there were no emissions at 657 and 704 nm due to the fact that the  $\text{Eu}^{3+}$  electrons in the ground state ( ${}^7\text{F}_0$ ) were not excited at 284 nm as shown in figure 6.8 (c). Therefore, we conclude that when exciting at 284 nm, the light which is emitted from the sample at 396 or 400 nm is re-absorbed by another emission centre (which is  $\text{Eu}^{3+}$ ) in the host material via radiation re-absorption process. These results, have evidently confirmed that there is radiative energy transfer from  $\text{Ce}^{3+} \rightarrow \text{Eu}^{3+}$  in  $\text{ZnAl}_2\text{O}_4:0.1\% \text{Ce}^{3+}, x\% \text{Eu}^{3+}$  as shown in figure 6.9.

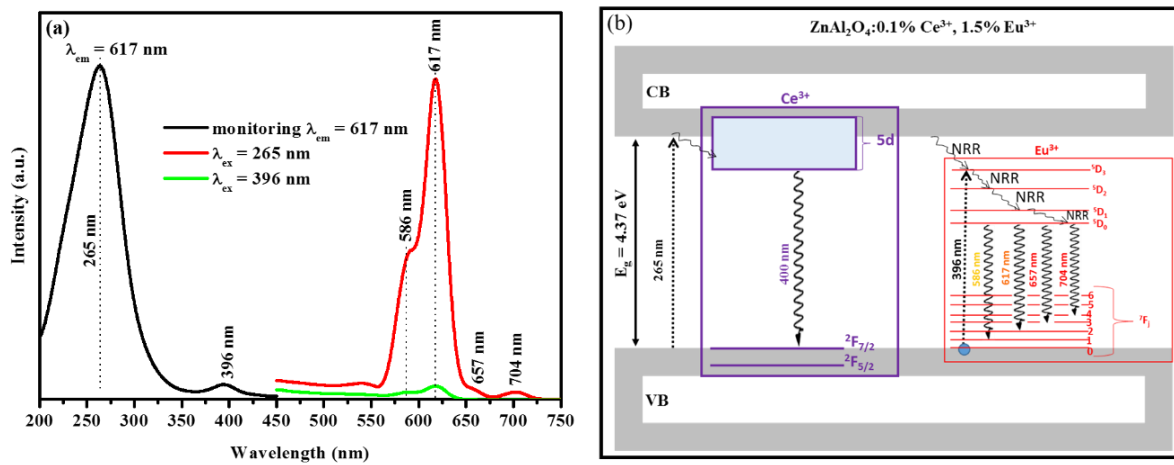


**Figure 6.10** (a) Excitation and emission spectra and (b) emission pathways of the  $\text{ZnAl}_2\text{O}_4:0.1\% \text{Ce}^{3+}, 1.5\% \text{Eu}^{3+}$ .

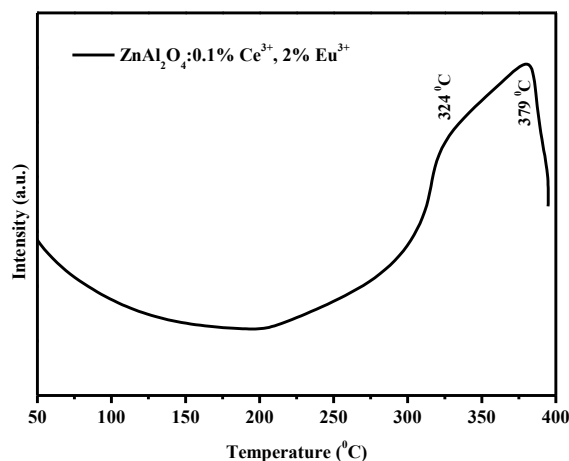


**Figure 6.11** Glow curve of the UV-irradiated  $\text{ZnAl}_2\text{O}_4:0.1\% \text{Ce}^{3+}, 2\% \text{Eu}^{3+}$  nanopowder at a heating rate of  $1^\circ\text{C}\cdot\text{s}^{-1}$ .

In order to examine the presence of defects on the prepared powders, a sample with the highest co-doping concentration,  $\text{ZnAl}_2\text{O}_4:0.1\% \text{Ce}^{3+}, 2\% \text{Eu}^{3+}$ , was analysed for the thermo stimulated luminescence (TSL). As shown in figure 6.11 that the TSL glow curves exhibits two distinct peaks at around 324 and 379 °C. It is noted that the high temperature peak is found to be more intense than the lower temperature peak, which suggest deep traps. In our previous results [37] on  $\text{ZnAl}_2\text{O}_4:1.5\% \text{Pb}^{2+}$ , we observed a similar kind of behaviour to these results. In comparison with the current results a glow curve at 160 °C in [37] is not observed in this results. In addition, it is known that each and every peak on the TSL glow curve represent one type of trap present in the lattice [38,39]. From [38,39] it is known that in  $\text{ZnAl}_2\text{O}_4$ , the most probable centres which can be observed are the  $\text{V}_0^*$  (as stated in PL results) centres (a hole trapped at a cation vacancy) and F centres (an electron trapped at an anion vacancy). In addition to this, it is known that the cation disorder and non-stoichiometry of aluminates like  $\text{ZnAl}_2\text{O}_4$  provide a large number of lattice defects, which may serve as trapping centres. Therefore, it is with these reasons that the origin of the PL emission is attributed to defect emission.

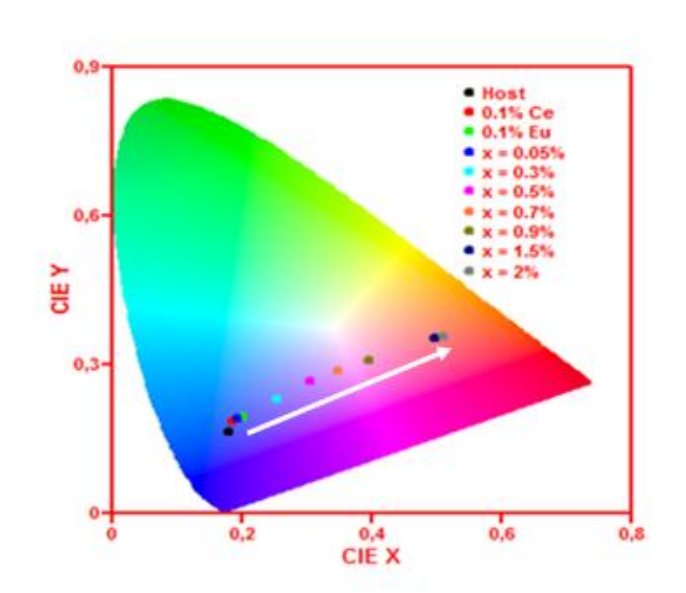


**Figure 6.12.** CIE chromaticity co-ordinates for the host and singly doped samples.

In order to examine the possible application of the prepared phosphors, the International Commission on Illumination (CIE) chromaticity coordinates are calculated. The chromaticity coordinates for the prepared phosphors were estimated from the emission spectra, excited by 284 nm. The corresponding chromaticity coordinates ( $x$ ,  $y$ ) are presented in Table 1 and the CIE chromaticity diagram is shown in Fig. 12. As shown in Fig. 12 the luminescent colour of the prepared phosphors were changed from bluish to reddish with the increase of  $\text{Eu}^{3+}$  concentration, which is the reverse of the Chengaiah et al. [11] results. Thus, the results of Chengaiah et al. [11] and our results have evidently showed that the emission colour and energy transfer in  $\text{Ce}^{3+}/\text{Eu}^{3+}$  co-doped phosphors can be tuned in any direction required and that depends on the co-dopant being varied. From the practical application point of view, we propose that the fabricated phosphor materials might be considered for the possible application such as in PDPs and field emission displays (FEDs) since in these devices the noble gas discharge (e.g. Xe/Ne discharge) emitting UV-rays and electrons are used [40]. In addition to this and for the host material to qualify to be used in PDPs, it should possess good UV and VUV excited luminescence [41]. Amongst other requirements that the host material should possess are: (1) high physical and chemical stability and (2) the host should provide metal ions that match well with RE ions so that they can easily be substituted [42]. With these traits, we propose that the prepared material could be potentially applied in PDPs.

#### 6.4 Conclusion

A series of un-doped, singly  $\text{Ce}^{3+}$  or  $\text{Eu}^{3+}$  doped and co-doped  $\text{ZnAl}_2\text{O}_4$  phosphors was successfully prepared by a sol-gel technique. XRD analysis confirmed that all of the nanopowders consisted of the single phase cubic spinel structure. The XRD peak widths, lattice strain, crystallite size, degree of crystallinity and lattice fringes were influenced by the type of the dopant and co-doping. PL results confirmed the existence of the radiative energy transfer from  $\text{Ce}^{3+} \rightarrow \text{Eu}^{3+}$ . CIE colour chromaticity showed that the colour can be tuned from bluish to reddish by changing the  $\text{Eu}^{3+}$  concentration.

## References

1. W. Q. Peng, G. W. Cong, S. C. Qu, Z. G. Wang, *Opt. Mat.* **29** (2006) 313.
2. Y. L. Soo, Z. H. Ming, S. W. Huang, Y. H. Kao, R. N. Bhargava, D. Gallagher, *Phys. Rev. B* **50** (1994) 7602.
3. V. Singh, R. P. S. Chakradhar, J. L. Rao, D-K. Kim, *J. Lumin.* **128** (2008) 394.
4. S. K. Sampath, J. F. Cordaro, *J. Am. Ceram. Soc.* **81** (1998) 649.
5. G. Lakshminarayana, L. Wondraczek, *J. Solid State Chem.* **184** (2011) 1931.
6. X. Wang, M. Zhang, Hui Ding, H. Li, Z. Sun, *J. Alloys Compd.* **509** (2011) 6317.
7. E. Martinez-Sanchez, M. Garcia-Hipolito, J. Guzman, F. Ramos-Brito, J. Santoyo-Salazar, R. Martinez-Martinez, O. Alvarez-Fregoso, M. I. Ramos-Cortes, J. J. Mendez-Delgado, C. Falcony, *Phys. Stat. Sol. (a)* **202**, No. 1, (2005) 102.
8. K. G. Tshabalala, I. M. Nagpure, H. C. Swart, O. M. Ntwaeaborwa, S. -H. Cho and J. -K. Park, *J. Vac. Sci. Technol. B* **30** (3) (2012) 031401.
9. B. Cheng, S. Qu, H. Zhou, Z. Wang, *Nanotechnology* **17** (2006) 2982.
10. B. S. Barros, P. S. Melo, R. H. G. A. Kiminami, A. C. F. M. Costa, G. F. de Sa', S. Alves Jr, *J. Mater Sci.* **41** (2006) 4744.
11. T. Chengaiah, C. K. Jayasankar, L. R. Moorthy, *Physica B* **431** (2013) 137.
12. R. Le Toquin, A. K. Cheetham, *Chem. Phys. Lett.* **423** (2006) 352.
13. Y. Wang, T. Endo, L. He, C. Wu, *Journal of Crystal Growth* **268** (2004) 568.
14. R. Ternane, G. Panzer, M.Th. Cohen-Adad, C. Goutaudier, G. Boulon, N. Kbir-Ariguib, M. Trabelsi-Ayedi, *Opt. Mater.* **16** (2001) 291.
15. Y. Wu, J. Du, K. Choy, L. L. Hench, J. Guo, *Thin Solid Films* **472** (2005) 150.
16. M. Zawadzki, *Solid State Sci.* **8** (2006) 14.
17. Q. Hou, F. Meng, J. Sun, *Nano Res. Lett.* **8** (2013) 144.
18. L. F. Koao, F. B. Dejene, R. E. Kroon, H. C. Swart, *J. Lumin.* **147** (2014) 85.
19. D. J. Robbins, B. Cockayne, J. L. Glasper, B. Lent, *J. Electrochem. Soc.: Solid-state Sci. Technol.* **126** (1979) 1221.
20. V. A. Lumbarda, *Mech. Mater* **35** (2003) 53.
21. S. V. Motloun, F. B. Dejene, H. C. Swart, O. M. Ntwaeaborwa, *J. Sol-Gel Sci. Technol.* **70** (2014) 422.
22. R. E. Kroon, *S. Afr. J. Sci.* **109** (2013) (5/6) Art. #a0019.

23. B. S. Ravikumar, H. Nagabhushana, S. C. Sharma, B. M. Nagabhushana, *Spectrochimica Acta Part A: Molecular and Biomolecular Spectroscopy* **122** (2014) 489.
24. S. Som, S. K. Sharma and S. P. Lochab, *Mater. Res. Bull.* **48** (2013) 844.
25. C. O. Paiva-Santos, H. Gouveia, W. C. Las, J. A. Varela, *Materials Structure* **6** (1999) 111.
26. A. A. Da Silva, A. de Souza Goncalves, M. R. Davolos, *J. Sol-Gel. Sci. Technol.* **49** (2009) 101.
27. A. A. Da Silva, A. Goncalves, M. R. Davolos, S. H. Santagneli, *J. Nanosci. Nanotechnol.* **8** (2008) 5690.
28. Z. Fang, R. Cao, F. Zhang, Z. Ma, G. Dong, J. Qiu, *J. Mater. Chem. C* **2** (2014) 2204.
29. Y. Hu, W. Zhuang, H. Ye, D. Wang, S. Zhang, X. Huang, *J. Alloys Compd.* **390** (2005) 226.
30. H. Dixit, N. Tandon, S. Cottenier, R. Saniz, D. Lamoen, B. Partoens, V. Van Speybroeck, M. Waroquier, *New Journal of Physics* **13** (2011) 063002.
31. P. H. Borse, W. Vogel, S. K. Kulkarni, *J. Colloid Interface Sci.* **293** (2005) 437.
32. Z. Xia, J. Zhuang, H. Liu, I. Liao, *J. Phys. D: Appl. Phys.* **45** (2012) 015302 (7pp).
33. D. Gao, H. Zheng, X. Zhang, W. Gao, Y. Tian, J. Li and M. Cui, *Nanotechnology* **22** (2011) 175702 (5pp).
34. H. Tang, H. Berger, P. E. Schmid, F. Levy, G. Burri, *Solid State Commun.* **87** (1993) 847.
35. R. Turos-Matysiak, W. Gryk, M. Grinberg, Y.S. Lin, R.S. Liu, *Rad. Meas.* **42** (2007) 755.
36. R. E. Kroon, H. C. Swart, O. M. Ntwaeaborwa, H. A. A. Seed Ahmed, *Physica B* **439** (2014) 83.
37. S. V. Motloun, F. B. Dejene, H. C. Swart, O. M. Ntwaeaborwa, *J. Lumin.* (2015) accepted for publication (DOI 10.1016/j.jlumin.2015.02.027).
38. V. Singh, S. Watanabe, T. K. Gundu Rao, J. F. D. Chubaci, I. Ledoux-Rak, H-Y. Kwak, *Appl. Phys. B* **98** (2010) 165.
39. K. K. Satapathy, F. Khan, *International Journal of Chemical Sciences and Applications* **3** (2012) 366.
40. T. Justel, J-C. Krupa, D. U Wiechert, *J. Lumin.* **93** (2001) 179.

41. Z. Wang, Y. Li, X. Liu, X. Wei, Y. Chen, F. Zhou, Y. Wang, *Mater. Res. Bull.* **59** (2014) 295.

## **Chapter 7: Colour tuning and energy transfer pathways in MgAl<sub>2</sub>O<sub>4</sub> triply doped with 0.1% Ce<sup>3+</sup>, 0.1% Eu<sup>2+</sup>, x% Tb<sup>3+</sup> (0 ≤ x ≤ 2%) nanocrystals synthesized using sol-gel process**

*“If you can’t explain it simply, you don’t understand it well enough.”*

*~ Albert Einstein*

### 7.1 Introduction

Many aluminate materials have been extensively studied as phosphors for the next generation of display and lighting devices. Among them, magnesium aluminate (MgAl<sub>2</sub>O<sub>4</sub>) spinel crystals have received a great deal of attention due to its mechanical strength, chemically stable, and its outstanding dielectric and optical properties [1]. MgAl<sub>2</sub>O<sub>4</sub> can crystallize in the “normal” or “inverse” spinel structures. The MgAl<sub>2</sub>O<sub>4</sub> spinel crystal structure may be described as a cubic closest-packed array of oxygen ions, with a lattice parameter of 8.08 Å and it belongs to a space group Fd3m [2,3]. Eight molecules form its unit cell, in which there are 64 tetrahedral symmetry and 32 octahedral ones. In the case of a “normal” spinel structure, the Mg<sup>2+</sup> and Al<sup>3+</sup> ions are located in tetrahedral and octahedral sites, respectively [3]. Other reports [4,5] have shown that the presence of high concentration of intrinsic defects in the MgAl<sub>2</sub>O<sub>4</sub> (host) are due to the large number of cations disorder. For an example, the substitution of Mg<sup>2+</sup> at an Al<sup>3+</sup> site induces a hole trap; in contrast, the substitution of Al<sup>3+</sup> at an Mg<sup>2+</sup> site induces an electron trap [4,5]. Oxygen vacancies may also serve as F center-like electron traps [5]. Izumi et al. [6] report showed that MgAl<sub>2</sub>O<sub>4</sub> can easily be singly doped by transition metal ions such as Ti, V, Cr, Mn, Co, and Ni. When these transition metal ions are singly doped in MgAl<sub>2</sub>O<sub>4</sub> crystals, the strong emission bands in the visible region are observed under excitation at the band-to-band transitions. Qai et al. [7] have shown that the MgAl<sub>2</sub>O<sub>4</sub> can be co-doped with these transition metal ions for the possible application in white LEDs. In their report [7], they successfully showed that Mn<sup>2+</sup> ions have a strong sensitization effect on a Cr<sup>3+</sup> ion. The enhancement of the Cr<sup>3+</sup> emission intensity as the Mn<sup>2+</sup> intensity quenching was attributed to the energy transfer from Mn<sup>2+</sup> → Cr<sup>3+</sup> ion by means of reabsorption of Mn<sup>2+</sup> photons. Furthermore, this compound have also been shown to be a

S.V. Motloung et al. / J. Lumin. (2015) revised article submitted.

good host material for the rare earth metal ions such as  $\text{Ce}^{3+}$ ,<sup>4</sup>  $\text{Eu}^{3+}$ ,<sup>1</sup>  $\text{Tb}^{3+}$ .<sup>3</sup> Raja et al. results [4] showed that the green emission (at 520 nm) long afterglow of 1 hour for the un-doped  $\text{MgAl}_2\text{O}_4$  samples can greatly be enhanced to more than 10 hours when doping with  $\text{Ce}^{3+}$  ions. This was explained to be due to the increase in the trapped electrons and holes population induced by the incorporation of  $\text{Ce}^{3+}$  ion. Singh et al. [1] showed that when doping  $\text{MgAl}_2\text{O}_4$  with  $\text{Eu}^{3+}$ , a strong red-light emitting phosphor can be fabricated. The emission at 611 nm was attributed to the  $^5\text{D}_0 \rightarrow ^7\text{F}_2$  transition of  $\text{Eu}^{3+}$  ions. Raja et al. [3] results revealed that when doping  $\text{MgAl}_2\text{O}_4$  with  $\text{Tb}^{3+}$  ions, the emission spectrum consists of several emissions bands located at 380, 415, 440, 490, 545, 580 and 620 nm. All of these bands were found to originate from the following transitions in the  $\text{Tb}^{3+}$  ion:  $^5\text{D}_3 \rightarrow ^7\text{F}_6$ ,  $^5\text{D}_3 \rightarrow ^7\text{F}_5$ ,  $^5\text{D}_3 \rightarrow ^7\text{F}_4$ ,  $^5\text{D}_4 \rightarrow ^7\text{F}_6$ ,  $^5\text{D}_4 \rightarrow ^7\text{F}_5$ ,  $^5\text{D}_4 \rightarrow ^7\text{F}_4$  and  $^5\text{D}_4 \rightarrow ^7\text{F}_3$ , respectively. In addition to singly doped systems,  $\text{MgAl}_2\text{O}_4$  have also been co-doped or co-activated with rare earth ions. For an example, Singh et al. [8] report revealed that in the  $\text{Er}^{3+}$  and  $\text{Yb}^{3+}$  co-doped  $\text{MgAl}_2\text{O}_4$  system, the increase in photoluminescence (PL) and thermally stimulated luminescence (TSL) of the  $\text{Er}^{3+}$  indicates an efficient energy transfer from  $\text{Yb}^{3+} \rightarrow \text{Er}^{3+}$ . It is also possible to co-dope  $\text{MgAl}_2\text{O}_4$  with different metal ions from different metal groups (e.g. transition, rare earth or even alkali metal). Saha et al. [9] report indicated that  $\text{Li}^+$  co-doping in  $\text{MgAl}_2\text{O}_4:\text{Eu}^{3+}$  significantly improves luminescence intensity along with good crystallinity. Furthermore, the charge compensation due to the addition of  $\text{Li}^+$  co-activator in  $\text{MgAl}_2\text{O}_4:\text{Eu}^{3+}$  lattice led to the two fold enhancement of PL intensity. Most interesting, researchers have also attempted the triple doping of foreign ions into different host matrix. To mention a few,  $\text{Y}_2\text{SiO}_5:\text{Ce}^{3+}, \text{Tb}^{3+}, \text{Eu}^{3+}$ ,<sup>10</sup>  $\text{LaF}_3:\text{Tm}^{3+}, \text{Tb}^{3+}, \text{Eu}^{3+}$ ,<sup>11</sup>  $\text{Ca}_3\text{Bi}(\text{PO}_4)_3:\text{Eu}^{3+}, \text{Tb}^{3+}, \text{Tm}^{3+}$ ,<sup>12</sup>  $\text{CaO-B}_2\text{O}_3\text{-SiO}_2:\text{Ce}^{3+}, \text{Tb}^{3+}, \text{Eu}^{3+}$ , [13] phosphors have been successfully fabricated. Generally, the reports on the lanthanides and alkali earth metal ions incorporation into the host lattice demonstrated that the emission intensity and emission colour of the host can be tuned. In most co-doped and triple doped studies, the results showed that the energy transfer is likely to occur, which plays an important role in the luminescence of the phosphor material [7,10,13].

Currently, the production of high-quality phosphors for white-light-emitting applications is a hot topic in the phosphor material synthesis research around the world due to the important goals such as; for the light-emitting diodes (LEDs) in the market and possible applications in households [11,13]. Single phosphors directly yielding white emission are advantageous in comparison to a mixture of individual red, green, and blue phosphors as these are hampered

by reabsorption of the blue light [11]. Keeping the above advantages in mind, and inspired by the possibility of fabricating the white light phosphor by simply triple doping the host material with ions such as  $\text{Ce}^{3+}$ ,  $\text{Tb}^{3+}$  and  $\text{Eu}^{3+}$ ,<sup>13</sup> we chose  $\text{MgAl}_2\text{O}_4$  as a host matrix for our work. Even though several investigations based on rare-earth and transition metal ions singly-doped and doubly-doped on the  $\text{MgAl}_2\text{O}_4$  host are available in literature to date, it is to the best of our knowledge that studies based on the triply doped  $\text{MgAl}_2\text{O}_4$  phosphors have not yet been attempted. Thus, this study is most probably the first one to investigate  $\text{MgAl}_2\text{O}_4$  triply doped nanophosphor prepared using the sol-gel technique. In this paper, we report our recent investigation results on the photoluminescence characteristics of turning the emission colour of  $\text{MgAl}_2\text{O}_4$ : 0.1%  $\text{Ce}^{3+}$ , 0.1%  $\text{Eu}^{2+}$ , x%  $\text{Tb}^{3+}$  phosphor from greenish-to-bluish by varying the x%  $\text{Tb}^{3+}$  at ( $0 \leq x \leq 2\%$ ) and the excitation wavelength. The proposed energy transfer mechanism from  $\text{Eu}^{2+} \rightarrow \text{Tb}^{3+} \rightarrow \text{Ce}^{3+}$  and emission pathways are presented. In addition, structural, morphological and optical studies were also performed and discussed. The original idea was to synthesize or produce the white-light-emitting phosphor for the possible application in LEDs.

## 7.2 Experimental

The triple doped  $\text{MgAl}_2\text{O}_4$ :0.1%  $\text{Ce}^{3+}$ , 0.1%  $\text{Eu}^{2+}$ , x%  $\text{Tb}^{3+}$  nanoparticles were synthesized using a well-known sol-gel technique [14], which is summarized in figure 7.1.  $\text{Mg}(\text{NO}_3)_2 \cdot 6\text{H}_2\text{O}$  (98%),  $\text{Al}(\text{NO}_3)_3 \cdot 9\text{H}_2\text{O}$  (98.5%) and citric acid (CA)  $\text{C}_8\text{H}_8\text{O}_7 \cdot \text{H}_2\text{O}$  (99%) were dissolved in deionized water. The sols stoichiometric molar ratio of Mg:Al was 1:2. The weighed raw materials  $\text{Ce}(\text{NO}_3)_3 \cdot 6\text{H}_2\text{O}$  (99.9%),  $\text{Eu}(\text{NO}_3)_3 \cdot 5\text{H}_2\text{O}$  (99.9%) and  $\text{Tb}(\text{NO}_3)_3 \cdot 6\text{H}_2\text{O}$  (99.9%) were added in separate beakers of the solution to single dope with 0.1%  $\text{Ce}^{3+}$ , 0.1%  $\text{Eu}^{2+}$  and 0.1%  $\text{Tb}^{3+}$  ions. Similar procedure was followed for the triple doping. The mol% of both  $\text{Ce}^{3+}$  and  $\text{Eu}^{2+}$  ions were kept constant at 0.1% each, while the molar concentrations of  $\text{Tb}^{3+}$  ions were varied at  $0 \leq x \leq 2$  mol%. These dopant ions were chosen because they may possibly result in the white-light emission at the appropriate mol% combination [13]. Mg:CA molar ratio was kept constant at 1:0.75 for all samples. The temperature was kept at  $\sim 80$  °C while constantly stirring using a magnetic stirrer until the solution forms gels. The gels were dried in an oven at 130 °C, and ground to get powders. The powder samples were subsequently fired at 800 °C in a furnace for an hour.

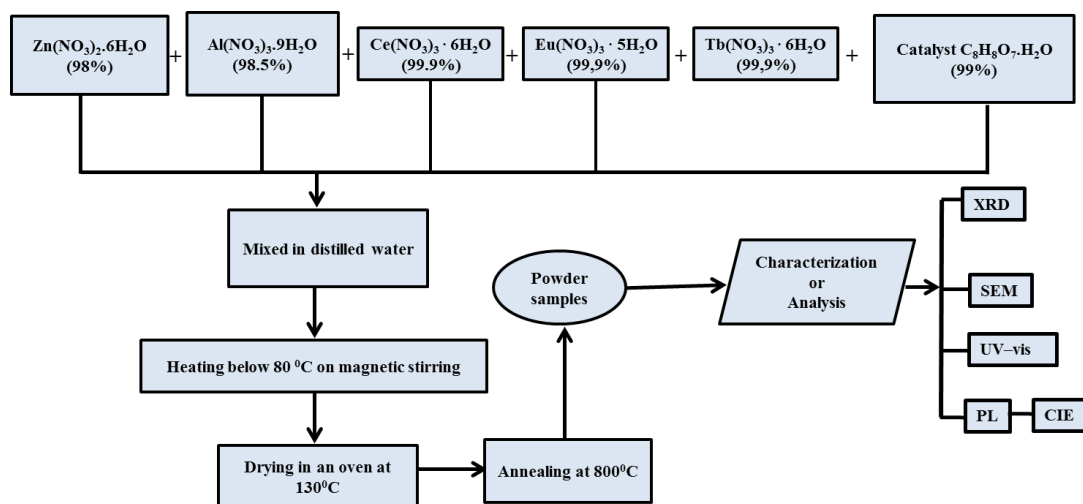


**Figure 7.1.** Summarised scheme for sol–gel synthesis of  $\text{MgAl}_2\text{O}_4$ : 0.1%  $\text{Ce}^{3+}$ , 0.1%  $\text{Eu}^{2+}$ , x%  $\text{Tb}^{3+}$ .

The crystal structure and phase composition of the samples was characterized by powder X-ray diffraction (XRD) (Bruker AXS Discover diffractometer) with  $\text{CuK}\alpha$  ( $1.5418\text{\AA}$ ) radiation). The surface morphology of the phosphor powder was investigated using a Shimadzu Superscan ZU SSX-550 electron microscope (SEM). High resolution transmission electron microscopy (HR-TEM) was performed with a JEOL JEM 2100 containing a  $\text{LaB}_6$  filament. Diffuse reflectance spectra were recorded using a Lambda 950 UV–Vis spectrophotometer with an integrating sphere using spectralon as a reflectance standard. Room temperature photoluminescence (PL) measurements were done using a Hitachi F-7000 fluorescence spectrophotometer.

## 7.3 Results and discussion

### 7.3.1 XRD

XRD patterns of the  $\text{MgAl}_2\text{O}_4$  (host), singly doped and triply doped samples are shown in figure 7.2 (a) and (b), respectively. The XRD pattern of the pure cubic structure for undoped and doped  $\text{MgAl}_2\text{O}_4$  is essentially the same as that of the literature (cubic spinel Fd3m JCDPS card 75-1797). No other peaks of possible intermediate products such as  $\text{Al}_2\text{O}_3$  and  $\text{MgO}$  were detected in the patterns which consequently confirm the single phase of the prepared powder samples. Figure 7.3 (a) shows the analysis of the Gaussian fits of the (400) diffraction peak. Compared to the host, evidently there is a slight shifting to the lower angle

as the dopant is changed and the mol% of  $\text{Tb}^{3+}$  is varied. Shifting of diffraction angles to the lower side indicates that the lattice parameters are slightly larger than those of undoped  $\text{MgAl}_2\text{O}_4$  [15]. As an example, the column bar in figure 7.3 (b) shows the lattice parameter dependence on the dopant type for the undoped and single doped samples. These phenomena can be explained in terms of the larger dopants radius  $\text{Ce}^{3+}$  (1.01 Å) [10],  $\text{Eu}^{2+}$  (1.25 Å) [16],  $\text{Tb}^{3+}$  (0.92 Å) [10] substituting the smaller  $\text{Mg}^{2+}$  (0.72 Å) [9] ion. Note that for the  $\text{Ce}^{3+}$  and  $\text{Eu}^{2+}$  ions singly doped into the  $\text{MgAl}_2\text{O}_4$  matrix results in the expansion of the unit-cell volume of the  $\text{MgAl}_2\text{O}_4$  nanocrystals. Therefore, the Virgard's law [17] is obeyed when singly doping  $\text{MgAl}_2\text{O}_4$  with 0.1%  $\text{Ce}^{3+}$  and 0.1%  $\text{Eu}^{2+}$  ions. However, in the case of 0.1 %  $\text{Tb}^{3+}$  ions doped sample, no change in lattice parameter is observed (see figure 7.2 (b) and Table 7.1), which confirms the deviation from the Virgard's law [17]. Apart from Lumbarda et al. [17] report, we [18] have recently reported similar kind of behaviour in  $\text{ZnAl}_2\text{O}_4$ : x%  $\text{Pb}^{2+}$ . Thus, no change in lattice spacing for the 0.1%  $\text{Tb}^{3+}$  ions singly doped sample (as shown on the insert of figure 7.3 (b) and Table 7.1) is therefore, attributed to the shrinkage of the  $\text{Tb}^{3+}$  outer electron shell due to its electronic interactions with more neighbouring  $\text{Mg}^{2+}$  ions, which makes it equal to the  $\text{Zn}^{2+}$  ion [17]. These results indicate that the dopants ions were well incorporated into the host matrix [15].

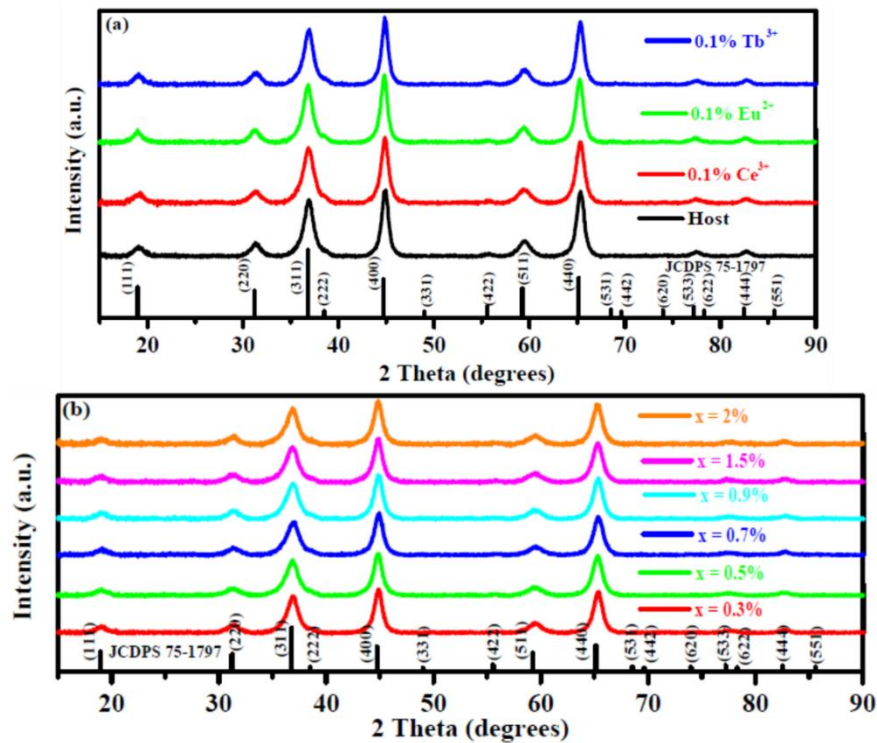


**Figure 7.2.** The XRD pattern for the (a) undoped and singly doped samples and (b) triply doped samples at the varying  $\text{Tb}^{3+}$  mol%.

Furthermore, figure 7.3 (a) shows that the (400) diffraction peak intensity is influenced by the dopant type and the variation in  $\text{Tb}^{3+}$  mol%, which is attributed to the change in the degree of crystalline quality. Generally, the decrease of the (400) peak intensity as the  $\text{Tb}^{3+}$  mol% is increased can be explained as the destruction of the crystalline quality during the growth of  $\text{MgAl}_2\text{O}_4$  crystals [19]. The dopant type is also shown to influence the degree of crystallization. For an example, doping with 0.1%  $\text{Ce}^{3+}$  and 0.1%  $\text{Eu}^{2+}$  seems to slightly destroy the crystalline growth, while doping with 0.1%  $\text{Tb}^{3+}$  enhances the crystals growth of  $\text{MgAl}_2\text{O}_4$ . Thus, the  $\text{Tb}^{3+}$  mol% and dopant type influences the crystallinity of the  $\text{MgAl}_2\text{O}_4$ .

**Table 7.1.** Sample identification and corresponding unit cell parameter of  $\text{MgAl}_2\text{O}_4$ : 0.1%  $\text{Ce}^{3+}$ , 0.1%  $\text{Eu}^{2+}$ , x%  $\text{Tb}^{3+}$  calculated by the Rietveld method and crystallites sizes obtained from Scherrer equation.

Sample ID	FWHM (rads)	Crystallites size (nm)	a (Å)	$\tau$ (ms)	CIE coordinates (x;y)
Host	0.695	12.4	6.692	576.8	(0.163;0.103)
0.1% $\text{Ce}^{3+}$	0.766	11.2	6.696	536.8	(0.181;0.119)
0.1% $\text{Eu}^{2+}$	0.706	12.2	6.696	537.4	(0.161;0.103)
0.1% $\text{Tb}^{3+}$	0.689	12.5	6.692	576.5	(0.169;0.132)
x = 0.3%	0.739	11.6	6.702	545.4	(0.195;0.214)
x = 0.5%	0.773	11.1	6.699	520.0	(0.239;0.358)
x = 0.7%	0.794	10.8	6.696	519.9	(0.245;0.397)
x = 0.9%	0.785	10.9	6.699	521.9	(0.244;0.407)
x = 1.5%	0.807	10.7	6.706	523.0	(0.250;0.456)
x = 2.0%	0.792	10.9	6.696	520.3	(0.249;0.474)
$\lambda_{\text{ex}} = 225$ nm	0.739	11.6	6.702	512.8	(0.251;0.489)
$\lambda_{\text{ex}} = 250$ nm	0.739	11.6	6.702	518.0	(0.230;0.346)
$\lambda_{\text{ex}} = 260$ nm	0.739	11.6	6.702	542.7	(0.210;0.264)
$\lambda_{\text{ex}} = 265$ nm	0.739	11.6	6.702	542.6	(0.202;0.238)
$\lambda_{\text{ex}} = 273$ nm	0.739	11.6	6.702	545.4	(0.195;0.214)

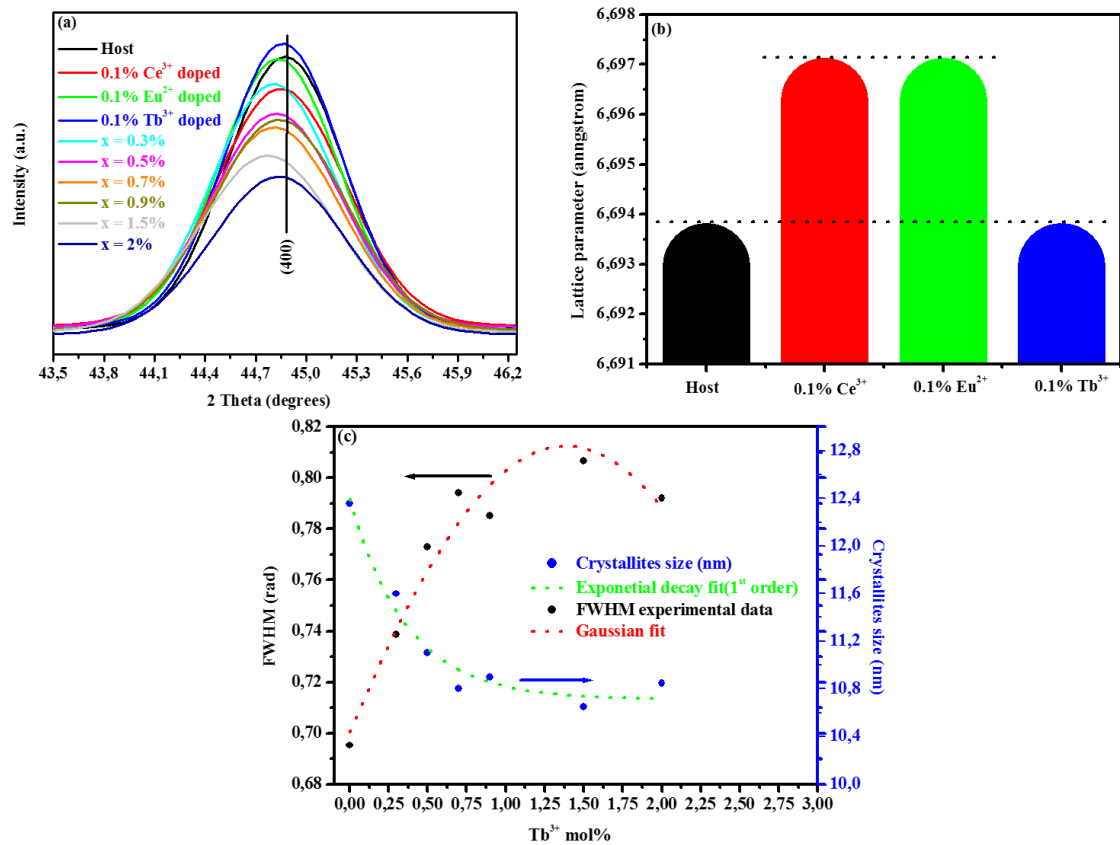


**Figure 7.3.** (a) The analysis of (400) diffraction peak (b) dependence of lattice parameter on the dopant type (c) FWHM and crystallites size as function of Tb<sup>3+</sup> mol%.

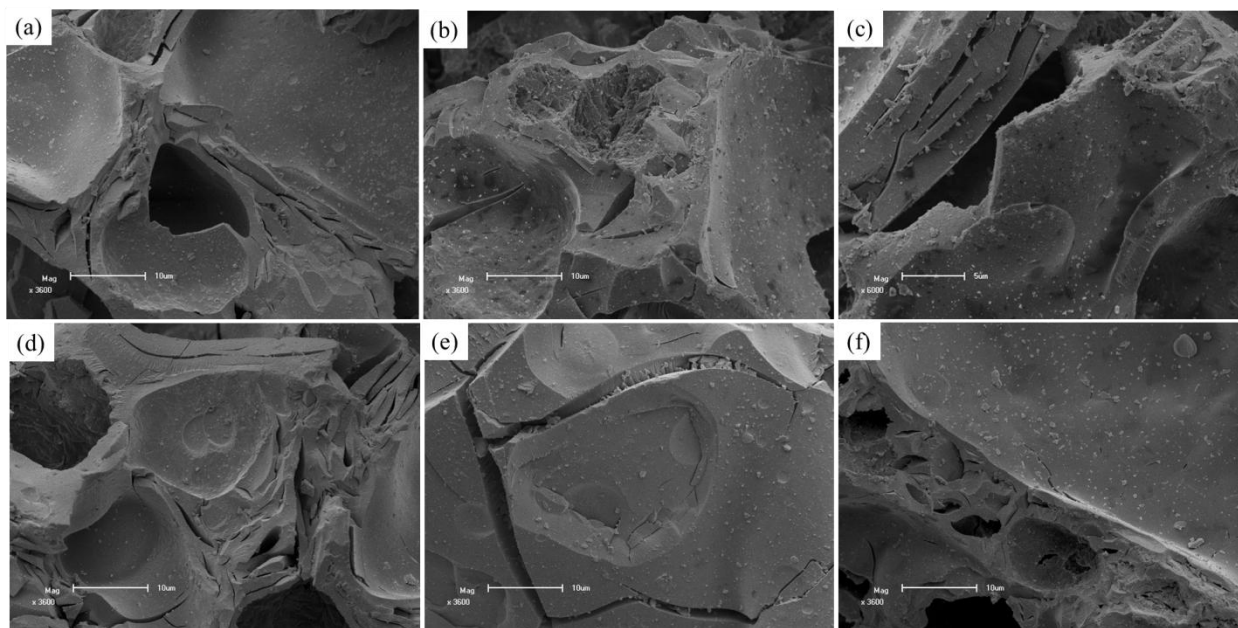


**Figure 7.4.** SEM images for (a) Host (b) 0.1% Ce<sup>3+</sup> doped (c) 0.1% Eu<sup>2+</sup> doped (d) 0.1% Tb<sup>3+</sup> doped (e) x = 0.7% and (f) x = 2%.

### 7.3.2 SEM

The SEM images of the host, singly doped and triply doped samples are shown in figure 7.4. As it can be observed that all specimens exhibited a multimodal grain size distribution. Figure 7.4 (a) illustrates the undoped (host) sample, which shows the distribution of different particle sizes with small particle agglomeration. Furthermore, the surface morphology consists of grain boundaries and plate-like structures over the surface. Single doping with 0.1%  $\text{Ce}^{3+}$  and 0.1%  $\text{Eu}^{2+}$  (shown in figure 7.4 (b) and (c)) illustrates similar morphology as the undoped sample with high degree of non-uniform pores and small particles distributed on the surface, which has been observed previously in  $\text{MgAl}_2\text{O}_4: \text{Eu}^{3+}$  phosphor synthesized by combustion method in Singh et al. [1] report. Single doping with 0.1%  $\text{Tb}^{3+}$  seems to decrease the degree of voids (see figure 7.4 (d)) compared to the 0.1 %  $\text{Ce}^{3+}$  and 0.1%  $\text{Eu}^{2+}$  single doped systems. Furthermore, when single doping with 0.1%  $\text{Tb}^{3+}$ , similar morphology as in figure 7.4 (a) with less degree of plate-like structure is observed suggesting that 0.1%  $\text{Tb}^{3+}$  influence the morphology of the host. Triple doping of the host at  $x = 0.7\%$  shown in figure 4 (e) illustrates similar morphology to the one shown in figure 7.4 (a) and (d). As the  $\text{Tb}^{3+}$  mol% is changed to  $x = 2\%$  (see figure 7.4 (f)), the plate-like morphology observed in figure 7.4 (a), (b) and (d) appears to be diminishing. This results shows that the dopant type and the  $\text{Tb}^{3+}$  mol% influences the powders morphologies.

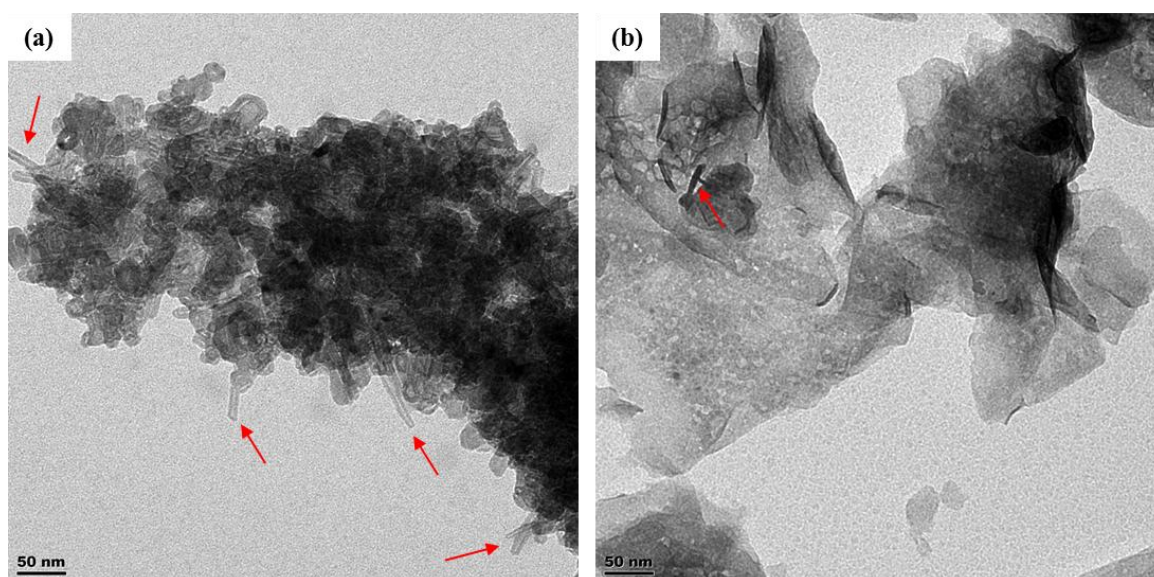


**Figure 7.5.** HR-TEM images for (a) Host and (b) 0.1%  $\text{Ce}^{3+}$  doped samples.

Furthermore, the microstructure of the host and the 0.1%  $\text{Ce}^{3+}$  doped samples were characterized by the HR-TEM as shown in figure 7.5 (a) and (b), respectively. The images revealed that the crystallites sizes are in the nanoscale range (i.e. below 20 nm) as predicted by the XRD results presented in table 7.1. In addition, the non-uniform rods structures, shown by the red arrows, were observed for both samples.

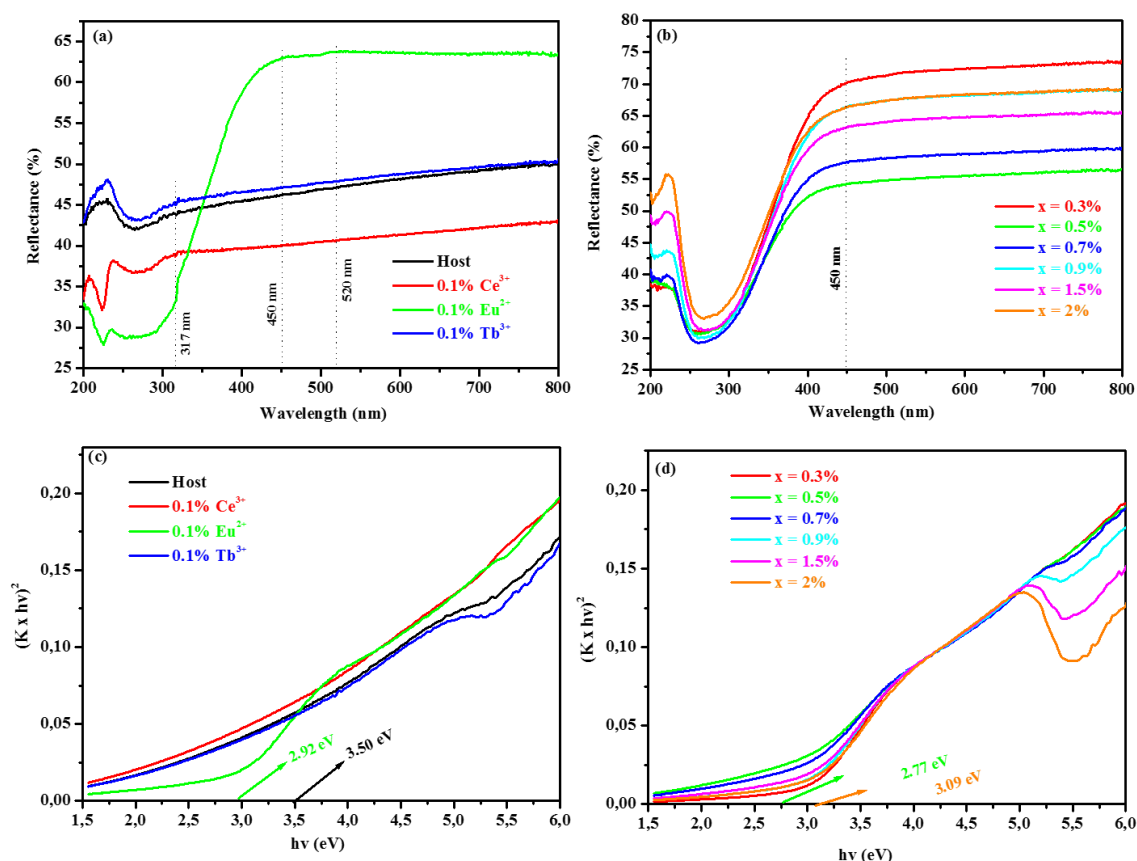


**Figure 7.6.** (a) Diffuse reflectance spectra of the host and singly doped with 0.1%  $\text{Ce}^{3+}$ , 0.1%  $\text{Eu}^{2+}$  and 0.1%  $\text{Tb}^{3+}$  samples. (b) Triply doped system at the varying  $\text{Tb}^{3+}$  mol%. (c) Estimation of the direct optical bandgap of the host and (d) Triply doped system using Kubelka-Munk function.

### 7.3.3 UV-Vis

UV-Vis diffuse reflection spectroscopy was used to study the absorption characteristics of the host and the effects of each dopant (0.1%  $\text{Ce}^{3+}$ , 0.1%  $\text{Eu}^{2+}$ , 0.1%  $\text{Tb}^{3+}$ ) in the singly and triply doped systems. Figure 7.6 (a) compares the UV-Vis spectra of the host and singly doped specimens with different dopants ions type (i.e. 0.1%  $\text{Ce}^{3+}$ , 0.1%  $\text{Eu}^{2+}$  and 0.1%  $\text{Tb}^{3+}$ ). The

absorption band at 317 nm in figure 7.6 (a) is attributed to be due to the charge transfer excitation from  $O^{2-}$  ( $2p$ )<sup>6</sup> electron into the conduction band in the host ( $MgAl_2O_4$ ) material [22,23]. When considering the 0.1%  $Eu^{2+}$  doped sample in figure 7.6 (a), it can be noticed that both of the absorption bands at 427 and 520 nm are originating from the  $Eu^{2+}$  ion and they are attributed to the  $4f \rightarrow 5d$  transition [24]. Similarly, the absorption band at the triple doped systems at 427 nm shown in figure 7.6 (b) is attributed to the  $4f \rightarrow 5d$  transition in  $Eu^{2+}$  ion.

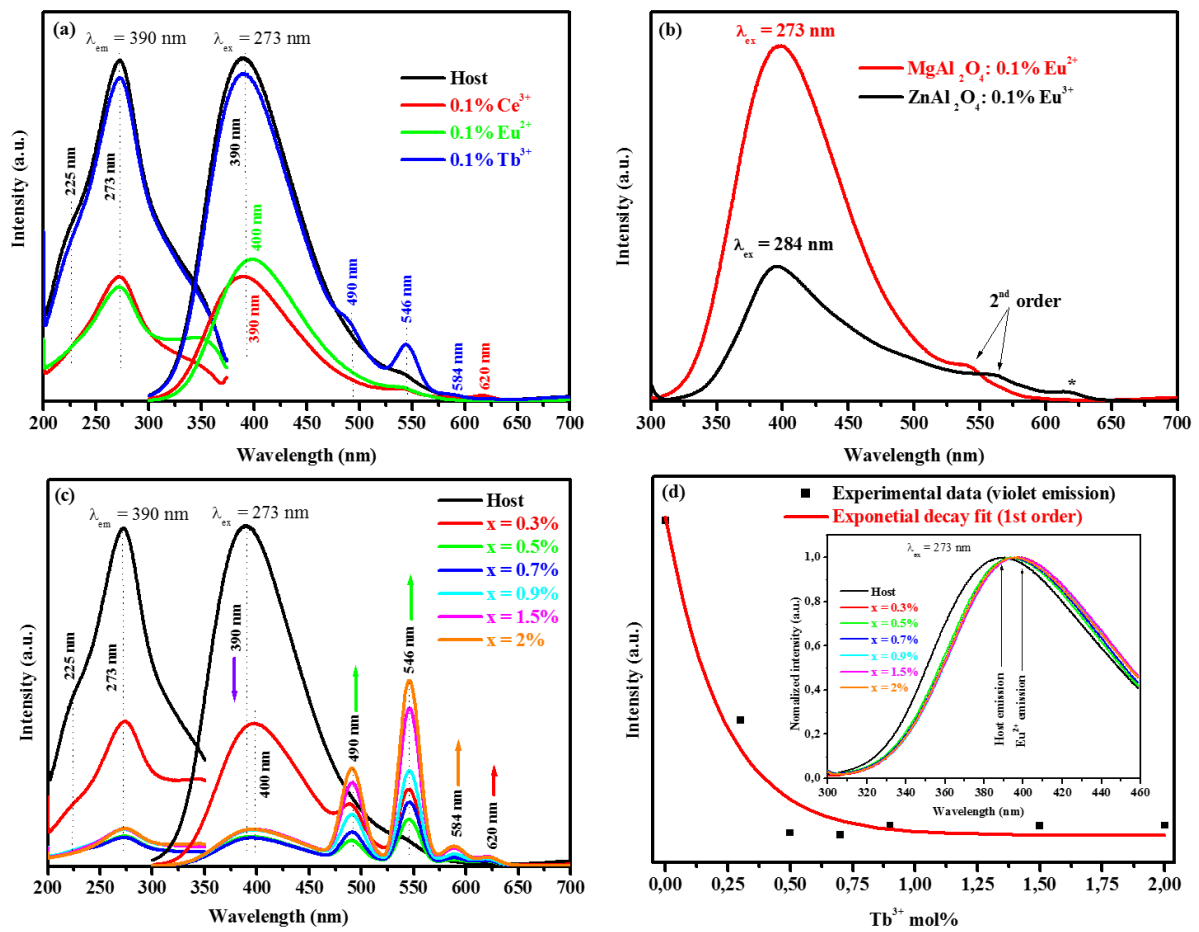


**Figure 7.7.** (a) Excitation and emission spectra of the (a) undoped and singly doped (b) emission spectra of the 0.1%  $Eu^{2+/3+}$  doped in  $ZnAl_2O_4$  and  $MgAl_2O_4$  spinels (c) triply doped at varying  $Tb^{3+}$  mol% and (d) PL intensity as a function of x%  $Tb^{3+}$  for the violet emission (insert: normalized PL intensity as function of x%  $Tb^{3+}$ ).

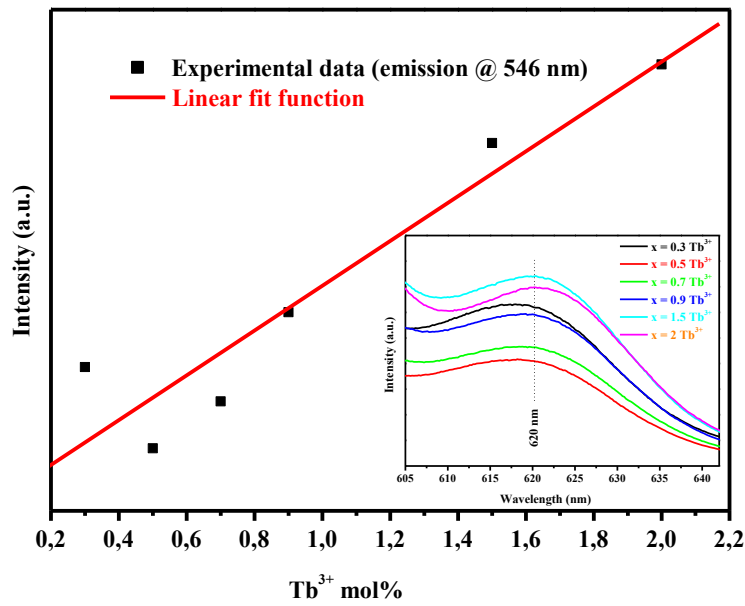


**Figure 7.8.** PL intensity as function of  $x\%$   $\text{Tb}^{3+}$  for the 546 nm emission (insert: magnified version of emission peak at 620 nm).

The Kubelka–Munk function  $K = (1 - R)^2/(2R)$  was used to transform the reflectance to the values proportional to absorbance, and the Tauc plot of  $(Kxh\nu)^n$  against  $h\nu$  [22] (with  $n = 2$ , which is appropriate for a direct band gap material such as  $\text{MgAl}_2\text{O}_4$ ) is presented in figure 7.6 (c) and (d) for the host, single and triple doped samples, respectively. As shown in figure 7.6 (c) and (d), the results indicates that the band gap of the host depends on the dopant type and  $x\%$   $\text{Tb}^{3+}$  ions. Moreover, the results suggests that the optical band gap of  $\text{MgAl}_2\text{O}_4$  can be engineered or tuned between 2.77 - 3.50 eV by varying the  $\text{Tb}^{3+}$  mol% at the range of ( $0 \leq x \leq 2\%$ ). Comparing the UV-Vis and XRD results, it can generally be concluded that the energy gap value depends on the crystallite size of the prepared samples and the largest crystallite size results in the smallest energy gap value and vice versa, which indirectly, means that the dopant type and  $\text{Tb}^{3+}$  mol% influences the energy gap value. Similar behaviour to our results has been observed recently by Nassar et al. [25] in  $\text{MgAl}_2\text{O}_4$ . Remarkably, the XRD (see figure 7.3 (a) and (b)), SEM (see figure 7.4 (a) - (d)) and UV (see figure 7.6 (a)) results for the host and 0.1%  $\text{Tb}^{3+}$  as well as 0.1%  $\text{Ce}^{3+}$  and 0.1%  $\text{Eu}^{2+}$  are found to resembles each other traits. For instances, the features of the XRD in figure 7.3 (a) (e.g. peak shifts), figure 7.3 (b) (e.g. lattice parameter), SEM images and UV-Vis spectrums

for the host and 0.1%  $\text{Tb}^{3+}$  doped samples appears to have the common-like-traits to each other, while on the other hand, the 0.1%  $\text{Ce}^{3+}$  and 0.1%  $\text{Eu}^{2+}$  singly doped are also showing common or similar-like-trends.

#### 7.3.4 PL analysis

The excitation and emission spectra of the host, singly doped and triple doped are shown in figure 7.7 (a) and (c), respectively. Figure 7.7 (a) and (c) shows that the main peaks of excitation when monitoring the emission at 390 nm are at 225 and 273 nm. Note that these results are consistent with the UV-Vis results shown in figure 7.6 (a), which indicated that the absorption band is expected to be below 317 nm. The absorption bands at 225 nm might possibly be due to the band-to-band, while the absorption band at 273 nm might possibly be due to defects within the host. From figure 7.7 (a), it can be deduced that the emission at 390 nm for all samples (e.g. host,  $\text{Tb}^{3+}$  and  $\text{Ce}^{3+}$  singly doped) arises from the defects level (DL) within the host material. When considering the 0.1%  $\text{Eu}^{2+}$  singly doped sample in figure 7.7 (a), it can clearly be noticed that the broad emission peak is located at 400 nm, which is surely attributed to the usual near UV emission of  $\text{Eu}^{2+}$  ion specifically from the  $4f^65d^1 \rightarrow 4f^7(^8S_{7/2})$  transition [26]. Detailed reasons as to why 400 nm peak in this study is not attributed to  $\text{Eu}^{3+}$  have been explained quite well in Xia et al. [24] report. In addition to this, Maia et al. [27] have observed the existence of  $\text{Eu}^{2+}$  in  $\text{MgAl}_2\text{O}_4$ : Eu, Dy. In their results [27] it was observed that the trivalent europium ion ( $\text{Eu}^{3+}$ ) is partially reduced to the divalent state ( $\text{Eu}^{2+}$ ) at 700 and 800  $^\circ\text{C}$ , which is in good agreement with our results when considering the fact that the powder samples were fired at 800  $^\circ\text{C}$ . Thus, our results might serve as the first confirmation of the Maia et al. [27] results. To further proof that the europium exists in a  $\text{Eu}^{2+}$  states in our results, the 0.1% europium was doped in  $\text{MgAl}_2\text{O}_4$  and  $\text{ZnAl}_2\text{O}_4$  spinels and the emission peak for both spinels were compared as shown in figure 7.7 (b). It is important to note that both samples were fired at 800  $^\circ\text{C}$ . As it can be seen in figure 7.7 (b) that in the wavelength range of 600 - 650 nm there is an extra emission peak for the  $\text{ZnAl}_2\text{O}_4$ : Eu, (marked with \*) which is not observed in the case of  $\text{MgAl}_2\text{O}_4$ : Eu phosphor. This behaviour might be indicating different states of europium ion in these hosts. That is;  $\text{Eu}^{3+}$  in  $\text{ZnAl}_2\text{O}_4$  and  $\text{Eu}^{2+}$  in  $\text{MgAl}_2\text{O}_4$ . Based on these observations in our results and the explanations presented in [24,26,27], it is reasonable to propose that the europium ion exists in  $\text{Eu}^{2+}$  state in this results.

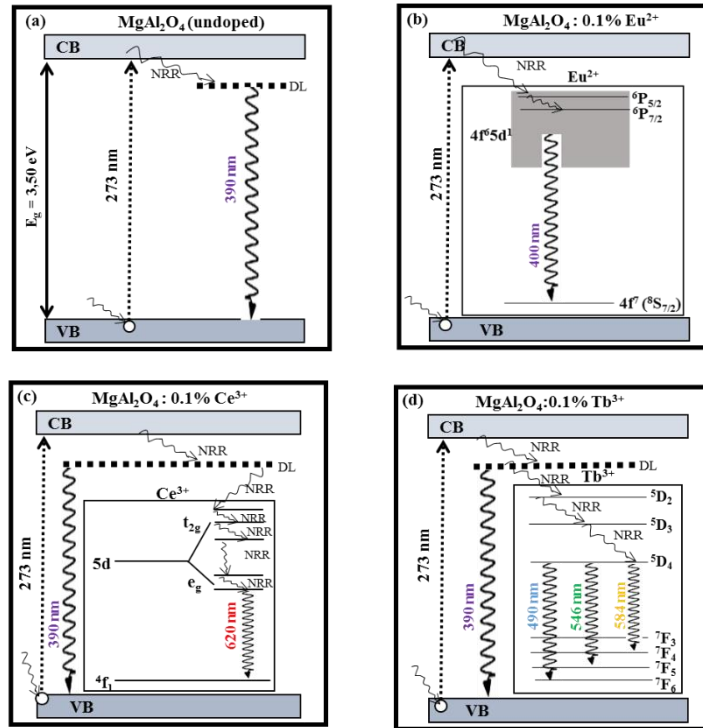


**Figure 7.9.** Proposed energy levels scheme for emission from the (a) host (b) MgAl<sub>2</sub>O<sub>4</sub>:0.1% Eu<sup>2+</sup> (c) MgAl<sub>2</sub>O<sub>4</sub>:0.1% Ce<sup>3+</sup> and (d) MgAl<sub>2</sub>O<sub>4</sub>:0.1% Tb<sup>3+</sup>.

A small emission peak emerging at 620 nm in figure 7.7 (a) is obviously originating from the Ce<sup>3+</sup>, which is attributed to the unfamiliar red emission from 5d (e<sub>g</sub>) → 4f<sup>1</sup> transition in Ce<sup>3+</sup> ion [28]. Le Toquin et al. [28] explained the existence of this emission to be the consequences of successful adjustment of the crystal field splitting by lowering the lowest 5d level in order to decrease the 5d-5f energy band gap, which shifts the phosphor emission towards higher wavelengths. Hence, it is important to point it out that the red emission is observed for the first time in Ce<sup>3+</sup> doped MgAl<sub>2</sub>O<sub>4</sub> system. The emission from Tb<sup>3+</sup> single doped sample is also presented in figure 7.7 (a). It can be noticed that there are four emission peaks observed in Tb<sup>3+</sup> doped MgAl<sub>2</sub>O<sub>4</sub> samples, which are located at 390, 490, 546 and 584 nm. As discussed above, the emission peak at 390 nm originates from the host. The Tb<sup>3+</sup> emission peak at 490 nm is attributed to <sup>5</sup>D<sub>4</sub> → <sup>7</sup>F<sub>6</sub> transition in Tb<sup>3+</sup> ion [13]. The emission peak at 546 nm in all samples is attributed to the second detection of the excitation light wavelength 273 nm (from Xenon lamp).

However, in the case of  $Tb^{3+}$  single doped sample, it is reasonable to attribute it to both the contributions from both the second order emission and  $^5D_4 \rightarrow ^7F_5$  transition in  $Tb^{3+}$  ion [13]. The motive being the fact that it is not easy to differentiate the second order emission and  $^5D_4 \rightarrow ^7F_5$  transition in  $Tb^{3+}$  ion at 564 nm. Lastly, the  $Tb^{3+}$  peak at 584 nm is attributed to the  $^5D_4 \rightarrow ^7F_4$  transition [29]. All the emission mechanisms from the host, and singly doped systems are illustrated in figure 7.9 (a) – (d).

The emission spectra for the triply doped samples at the varying  $Tb^{3+}$  mol% is shown in figure 7.7 (c) and all the emission peak positions are similar as in figure 7.7 (a). Emission intensity as a function of the x%  $Tb^{3+}$  ions on the triply doped systems for the violet emission and 546 nm are presented in figure 7.7 (d) and figure 7.8, respectively. For the violet emission peak, the exponential decay behaviour is observed, which could be attributed to the concentration quenching [30] as the host is triply doped with 0.1%  $Ce^{3+}$ , 0.1%  $Eu^{2+}$ , x%  $Tb^{3+}$ . The luminescence quenching is attributed to the new defect sites that enhance non-radiative (NRR) recombination of the excited electrons. Similar quenching in luminescence intensity has been observed in  $TiO_2$  doped with In- and Ce- by Tang et al. [30]. In order to differentiate the emission from the host at 390 nm and the emission from  $Eu^{2+}$  at 400 nm on the triply doped samples, the normalized emission intensity as a function of the emission wavelength is shown on the insert in figure 7.7 (d). The insert in figure 7.7 (d) clearly proves that for the triple doped samples there is no emission from the host. The emission intensity at 546 nm as function of  $Tb^{3+}$  mol% is shown in figure 7.8, which clearly shows the luminescence enhancement. Note that similar behaviour as in 564 nm is observed for the 490 and 620 nm peak. The magnified version of the emission peak at 620 nm is shown on the figure 7.8 (insert). The luminescence enhancement is attributed to the modification of the defect levels or local environment of the dopant ions [31], which seems to be highly dependent on the  $Tb^{3+}$  mol%.

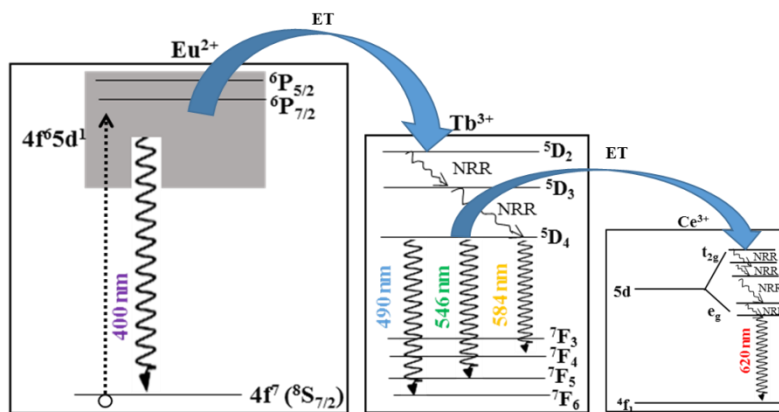


**Figure 7.10.** Schematic diagram of energy transfer mechanism from  $\text{Eu}^{2+} \rightarrow \text{Tb}^{3+} \rightarrow \text{Ce}^{3+}$  in  $\text{MgAl}_2\text{O}_4:0.1\% \text{Eu}^{2+}, 0.1\% \text{Ce}^{3+}, x\% \text{Tb}^{3+}$ .

The decrease in  $\text{Eu}^{2+}$  peak at 400 nm and increase in  $\text{Tb}^{3+}$  peaks at 490, 546, 584 nm and emerging of  $\text{Ce}^{3+}$  peak at 620 nm (shown by the arrows in figure 7.7 (c)) as the  $\text{Tb}^{3+}$  mol% is increase confirms the energy transfer from  $\text{Eu}^{2+} \rightarrow \text{Tb}^{3+} \rightarrow \text{Ce}^{3+}$  in  $\text{MgAl}_2\text{O}_4:0.1\% \text{Eu}^{2+}, 0.1\% \text{Ce}^{3+}, x\% \text{Tb}^{3+}$  as shown in figure 10. Zang et al. [13] has reported the energy transfer  $\text{Ce}^{3+} \rightarrow \text{Tb}^{3+} \rightarrow \text{Eu}^{3+}$  in the triply doped  $\text{CaO-B}_2\text{O}_3\text{-SiO}_2$  glasses synthesized by the melt quenching method. Unlike in the Zang et al. [13] report, the energy transfer in this report is confirmed to be in the following order  $\text{Eu}^{2+} \rightarrow \text{Tb}^{3+} \rightarrow \text{Ce}^{3+}$ . The difference in the energy transfer trend is attributed to the crystal field and oxidation state of the europium ion [13]. Furthermore, Xia et al. [24] have showed that both  $\text{Eu}^{2+}$  and  $\text{Eu}^{3+}$  ion can coexist on the green emitting  $\text{Ba}_2\text{Lu}(\text{BO}_3)_2\text{Cl:Eu}^{2+}/\text{Eu}^{3+}, \text{Tb}^{3+}$  phosphors synthesized via a solid-state reaction. Their results [24] also proved that the presence of  $\text{Eu}^{2+}$  leads to the energy transfer from  $\text{Eu}^{2+} \rightarrow \text{Tb}^{3+}$ , which is in good agreement with this report. Thus, we infer that the oxidation state of europium is dependent on the host material, which was further proven by figure 7.7 (b).

In order to see the dependance of the emission wavelength to the excitation wavelength, the triple doped sample  $\text{MgAl}_2\text{O}_4:0.1\% \text{Eu}^{2+}, 0.1\% \text{Ce}^{3+}, 0.3\% \text{Tb}^{3+}$  was excited at 225, 250, 260, 265 and 273 nm, respectively. The excitation and emission spectra for different excitation wavelength is shown in figure 11 (a). All the peak positions are similar as in figure 7.7 (a) and (c) and, thus, they are attributed to originate from the same notions as discussed above. The emission peak at 546 nm as a fuction of the excitation wavelength is presented in figure 7.11 (b) and the insert in figure 7.11 (b) is the emission intensity of 400 nm as a function of the excitation wavelength. It is interesting to see that when the excitation wavelength is

increased, the 546 nm peak is decreased, while on the other hand the emission peak at 400 nm is observed to increase. These results suggest that the emission centres can be controlled by changing the excitation wavelength. That is; at the lower exciting wavelengths the emission centers are more likely to be  $Tb^{3+}$  ions, whereas at the higher wavelength the emission centers are  $Eu^{2+}$  ions. Zhang et al. [32] showed that the appearance and vanishing of the emission peak position depends on the photo-energy of excitation light for the ZnO films deposited by rf sputtering on various substrates. Their results also showed that the wideness and photoemission intensity depends on the excitation wavelength, which agrees very well with our current findings.

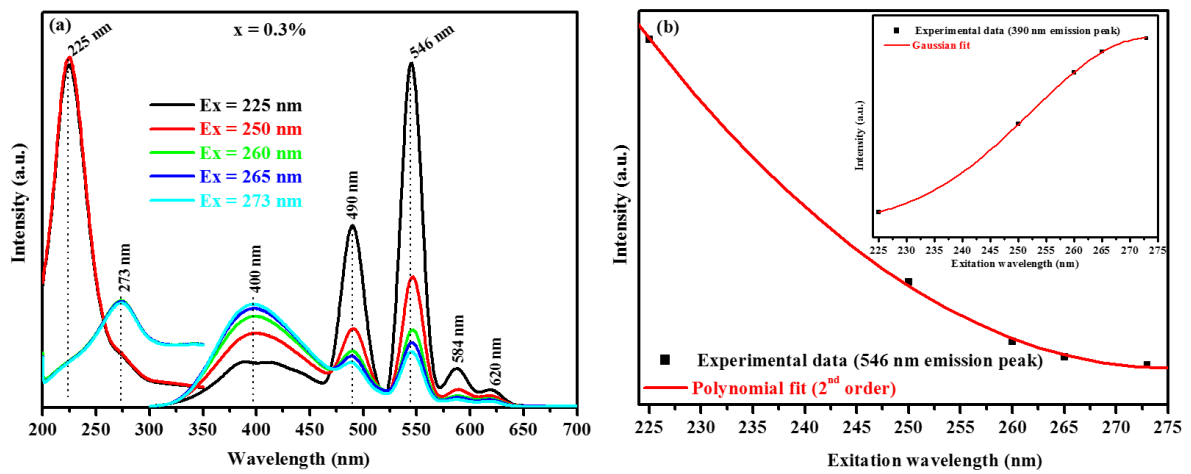


**Figure 7.11.** (a) Emission spectra of  $MgAl_2O_4:0.1\% Eu^{2+}, 0.1\% Ce^{3+}, 0.3\% Tb^{3+}$  excited by 225, 250, 260, 265 and 273 nm, (b) 546 nm emission peak intensity as a function of excitation wavelength (insert: 390 nm emission peak intensity as a function of excitation wavelength).

The phosphor lifetime is presented in figure 7.12 (a), (b) and (c) for the host, singly doped and triply doped samples at the varying  $Tb^{3+}$  mol% and for changing the excitation wavelength. It was found that all the curves followed the single-exponential decay. The decay time is obtained by fitting the decay curve to the equation as [13]:

$$I_t = I_0 \exp\left(-\frac{t}{\tau}\right) \quad (7.1)$$

where  $I_t$  and  $I_0$  are the intensities at times  $t$  and  $0$ , respectively, and  $\tau$  is defined as the luminescence lifetime. Based on Eq. (7.1) and decay curves, the values for the decay lifetime are presented in table 7.1 for each sample.

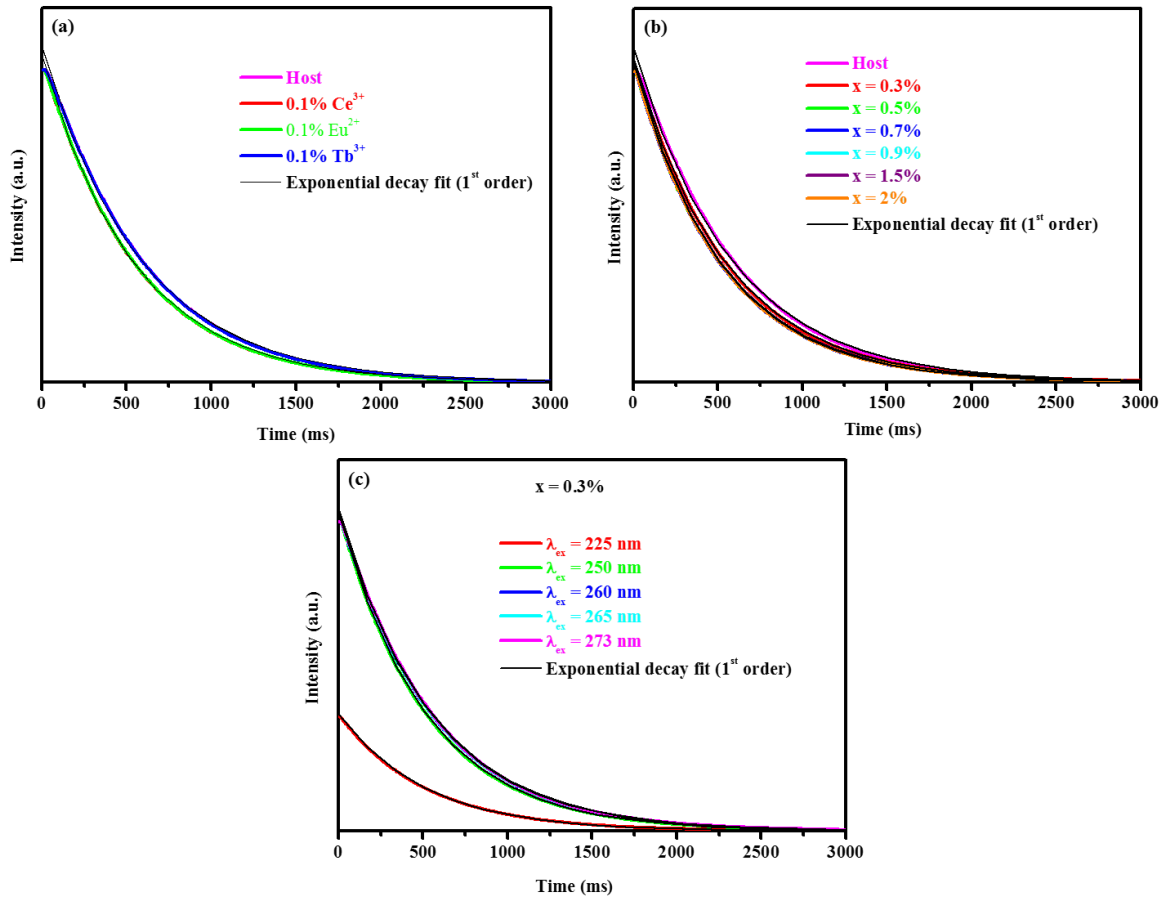


**Figure 7.12.** (a) Decay curves of (a) MgAl<sub>2</sub>O<sub>4</sub> and singly doped MgAl<sub>2</sub>O<sub>4</sub> with 0.1% Eu<sup>2+</sup>, 0.1% Ce<sup>3+</sup> and 0.1% Tb<sup>3+</sup> (b) MgAl<sub>2</sub>O<sub>4</sub>: 0.1% Eu<sup>2+</sup>, 0.1% Ce<sup>3+</sup>, x% Tb<sup>3+</sup> at  $0 \leq x \leq 2\%$  and (c) MgAl<sub>2</sub>O<sub>4</sub>: 0.1% Eu<sup>2+</sup>, 0.1% Ce<sup>3+</sup>, 0.3% Tb<sup>3+</sup> at different excitation wavelength.

The International Commission on Illumination (CIE) chromaticity diagram and coordinates for the MgAl<sub>2</sub>O<sub>4</sub>, singly doped with 0.1% Eu<sup>2+</sup>, 0.1% Ce<sup>3+</sup>, 0.1% Tb<sup>3+</sup> and triply doped with 0.1% Eu<sup>2+</sup>, 0.1% Ce<sup>3+</sup>, x% Tb<sup>3+</sup> at  $0 \leq x \leq 2\%$  is shown in figure 7.13 (a). The triply doped 0.1% Eu<sup>2+</sup>, 0.1% Ce<sup>3+</sup>, 0.3% Tb<sup>3+</sup> phosphor at different excitation wavelength is illustrated in figure 7.13 (b). The corresponding chromaticity coordinates ( $x$ ,  $y$ ) are presented in table 7.1.

As seen in figure 7.13 (a) that the host and singly doped samples emits the bluish colour. Increasing  $Tb^{3+}$  mol% tune the emission colour from bluish  $\rightarrow$  greenish. More interestingly, when the excitation wavelength is increased, the emission colour is tuned from greenish  $\rightarrow$  bluish. Generally, the emission colour of the triply doped phosphor can be tuned by changing the  $Tb^{3+}$  mol% and excitation wavelength, which suggests that this kind of novel phosphor can meet the wide range of application requirements such in blue  $\rightarrow$  green LEDs.

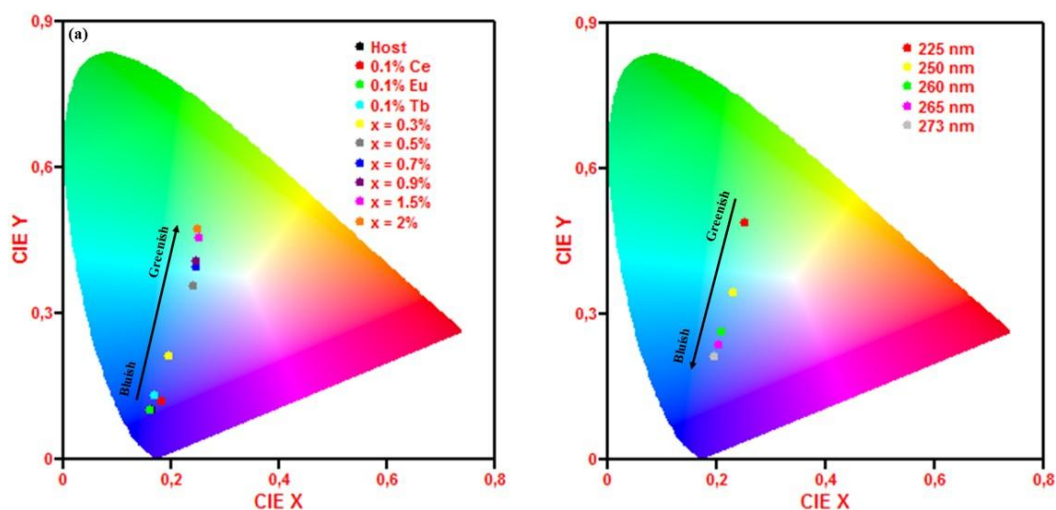


**Figure 7.13.** CIE chromaticity co-ordinates for the (a) host, singly and triply doped samples (b)  $MgAl_2O_4: 0.1\% Eu^{2+}, 0.1\% Ce^{3+}, 0.3\% Tb^{3+}$  at different excitation wavelength.

#### 7.4 Conclusion

In summary, a novel bluish-greenish emitting phosphor  $MgAl_2O_4: 0.1\% Eu^{2+}, 0.1\% Ce^{3+}, 0.3\% Tb^{3+}$  was prepared by a sol-gel technique. XRD analysis confirmed that all of the nanopowders consisted of the pure cubic structures. Crystallites sizes, degree of crystallinity and the morphology of the phosphor were influenced by the type of the dopand and the  $Tb^{3+}$  mol%. HR-TEM revealed the nano-structure of the prepared powder samples. The band gab of the phosphor can be engineered by the type of the dopant and  $Tb^{3+}$  mol% in the triply doped systems. PL results confirmed the existence of the energy transfer from  $Eu^{2+} \rightarrow Tb^{3+} \rightarrow Ce^{3+}$ . CIE colour chromaticity showed that the colour can be tuned from bluish  $\rightarrow$  greenish by changing the  $Tb^{3+}$  mol% and the excitation wavelength.

## References

1. V. Singh, M. D. M. Haque, D-K. Kim, Bull Korean Chem. Soc. **28** (2007) 2477.
2. R. C. Peterson, G. A. Lager, R. L. Hitterman, American Mineralogist **76** (1991) 1455.
3. E. A. Raja, B. Dhabekar, S. Menon, S. P. More, D. K. G. Rao, R. K. Kher, Indian Journal of Pure & Applied Physics **47** (2009) 420.
4. D. Jia, W. M. Yen, J. Lumin. **101** (2003) 115.
5. A. Ibarra, F. J. Lopez, M. de Castro, J. Phys. Rev. B **44** (14) (1999) 7256.
6. K. Izumi, S. Miyazaki, S. Yoshida, T. Mizokawa, E. Hanamura, Phys. Rev. B **76** (2007) 075111.
7. Q. Sai, C. Xia, H. Rao, X. Xu, G. Zhou, P. Xu, J. Lumin. **131** (2011) 2359.
8. V. Singh, V. K. Rai, S. Watanabe, T. K. G. Rao, L. Badie, I. Ledoux-Rak, Y-D. Jho, Appl. Phys. B **108** (2012) 437.
9. S. Saha, S. Das, U. K. Ghorai, N. Mazumder, B. K. Gupta, K. K. Chattopadhyay, Dalton Trans. **42** (2013) 12965.
10. X. Zhang, L. Zhou, Q. Pang, J. Shi, M. Gong, J. Phys. Chem. C **118** (2014) 7591.
11. C. Lorbeer, A-V. Mudring, J. Phys. Chem. C **117** (2013) 12229.
12. M. Jiao, N. Guo, W. Lü, Y. Jia, W. Lv, Q. Zhao, B. Shao, H. You, Dalton Trans. **42** (2013) 12395.
13. Y. Zhang, Z. Zhu, Y. Qiao, Mat. Lett. **93** (2013) 9.
14. A. A. Da Silva, A. de Souza Goncalves, M. R. Davolos, J. Sol-Gel Sci. Technol. **49** (2009) 101.
15. L. F. Koao, F. B. Dejene, R. E. Kroon, H. C. Swart, J. Lumin. **147** (2014) 85.
16. Y-C. Chiu, W-R. Liu, C-K. Chang, C-C. Liao, Y-T. Yeh, S-M. Jang, T-M. Chen, J. Mat. Chem. **20** (2010) 1755.
17. V. A. Lumbarda, Mech. Mater **35** (2003) 53.
18. S. V. Motloun, F. B. Dejene, H. C. Swart, O. M. Ntwaeaborwa, J. Sol-Gel Sci. Technol. **70** (2014) 422.
19. Q. Hou, F. Meng, J. Sun, Nano Res. Lett. **8** (2013) 144.
20. B. D. Cullity, 1956 Elements of X-ray Diffraction, 2nd Ed, Addison Wesley (1978 ) 285.
21. H. M. Rietveld, J. Appl. Crst. **2** (1969) 65.
22. W. A. I. Tabaza, H. C. Swart, R. E. Kroon, J. Lumin. **148** (2014) 192.
23. R. Zhong, J. Zhang, H. Wei, X. Qi, M. Li, X. Han, Chem. Phys. Lett. **508** (2011) 207.

24. Z. Xia, J. Zhuang, H. Liu, L. Liao, *J. Phys. D: Appl. Phys.* **45** (2012) 015302 (7pp).
25. M. Y. Nassar, I. S. Ahmed, I. Samir, *Spectrochimica Acta Part A: Molecular and Biomolecular Spectroscopy* **131** (2014) 329.
26. A. Baran, S. Mahlik, M. Grinberg, E. Zych, *J. Phys: Condens Matter* **25** (2013) 025603 (10pp).
27. A. S. Maia, R. Stefani, C. A. Kodaira, M. C. F. C. Felinto, E. E. S. Teotonio, H. F. Brito, *Opt. Mat.* **31** (2008) 440.
28. R. Le Toquin, A. K. Cheetham, *Chem. Phys. Lett.* **423** (2006) 352.
29. E. A. Raja, B. Dhabekar, S. Menon, S. P. More, T. K. G. Rao, R. K. Kher, *Indian Journal of Pure and Applied Physics* **47** (2009) 420.
30. H. Tang, H. Berger, P. E. Schmid, F. Levy, G. Burri, *Solid State Commun.* **87** (1993) 847.
31. D. Gao, H. Zheng, X. Zhang, W. Gao, Y. Tian, J. Li, M. Cui, *Nanotechnology* **22** (2011) 175702 (5pp).
32. D. H. Zhang, Q. P. Wang, Z. Y. Xue, *Applied Surface Science* **207** (2003) 20.

## Chapter 8: Effects of Zn/Catalyst mole fraction on the Structure and Luminescence Properties of the un-doped and 1.5% Pb<sup>2+</sup> doped ZnAl<sub>2</sub>O<sub>4</sub> powders synthesized by citrate sol-gel method

*“If we knew what it was we were doing, it would not be called research, would it?”*

*~ Albert Einstein*

### 8.1 Introduction

Semiconductor nanoparticles are currently being extensively studied in the context of their size dependent photophysical and photochemical properties [1]. ZnAl<sub>2</sub>O<sub>4</sub> is one of the well-known wide-bandgap (~3.8 eV) semiconductor with a spinel structure [2,3]. ZnAl<sub>2</sub>O<sub>4</sub> has many advantages such as thermal and chemical stability, hydrophobic behavior, high mechanical resistance, low sintering temperature and high quantum yields [4]. ZnAl<sub>2</sub>O<sub>4</sub> and other spinels are known to be an appropriate host lattice for various dopants or activator atoms [5]. Rare earth and transition metals doped ZnAl<sub>2</sub>O<sub>4</sub> systems have been prepared [2]. It is well known that the luminescence properties depends on the particle size, crystal structure, and uniform distribution of activator in the host lattice [3,6]. The other group of dopants called heavy *ns*<sup>2</sup> metals ions such as Tl<sup>+</sup>, Pb<sup>2+</sup> and Bi<sup>3+</sup> are also interesting to the researchers and they have been reported in a considerable number of hosts materials [7,8]. In particular, the luminescence of Pb<sup>2+</sup> is quite diverse and depends strongly on the host lattice [9]. The emissions of Pb<sup>2+</sup> are characteristic of A-band from <sup>3</sup>P<sub>0</sub> → <sup>1</sup>S<sub>0</sub> transition or D-band, which is believed to originate from charge transfer transitions [10]. In our recent reports [11], we successfully showed the possibilities of obtaining two violet emissions from closely different energy levels transitions <sup>3</sup>P<sub>0,1</sub> → <sup>1</sup>S<sub>0</sub> in Pb<sup>2+</sup> ions. Furthermore, in our [11] and Da Silva et al. [12] results, it was shown that the intrinsic intra bandgap defects in ZnAl<sub>2</sub>O<sub>4</sub> (host) due to oxygen vacancies can also result in violet emission. In recent years, numerous methods of fabrication of ZnAl<sub>2</sub>O<sub>4</sub> such as solid state reaction [13], co-precipitation method [14], hydrothermal [15], combustion [16] and sol-gel [6] have been developed. Compared with the traditional techniques, the sol-gel route is a versatile and attractive technique for the fabrication of nanocrystalline powders because of its advantage of producing pure and

S.V. Motloung et al. / J. Lumin. **163** (2015) 8-16.

ultrafine powders at a very low temperature [6,12]. One of the basic components in the sol-gel process is the citric acid (CA). CA provides two main purposes in sol-gel methods, which are; to stabilize the sol-gel method [17] and to adjust the pH [18] and hence increases the magnitude of zeta potential or particle surface modifier. Chew et al. [17] showed that the addition of citric acid as a stabilizer re-sulted in the formation of  $\text{Ba}_2\text{NiTi}_5\text{O}_{13}$  particles with various morphology (i.e. sphere, cube, rod), which were deduced to be caused by citric acid that tends to absorbed on certain dimension of the  $\text{Ba}_2\text{NiTi}_5\text{O}_{13}$  particles as the CA was added. Abreu Jr et al [18] showed that in the sol-gel method, which is commonly known as the Pechini method, are practiced by using citrate salts or mixtures of common salts with CA as precursor. They further showed that the citrate will form complexations via its carboxylate groups with empty orbitals of metals [18]. As a matter of fact from literature [17,18] it can be seen that CA plays significant roles in the particle morphology. Asakura et al. [19] reported the decrease in particle diameter from 10.2 to 4.0 nm with an increase in CA. They further [19] showed that the internal quantum efficiency of the photoluminescence (PL) due to the 4f–5d transition of  $\text{Ce}^{3+}$  increases from 22.0% to 40.1% with increasing amount of CA. Motivated by the [17-19] and since there has not been a report on the effects of CA in the  $\text{ZnAl}_2\text{O}_4$  doped and co-doped phosphors, in this study, we mainly focus on the effect of Zn/CA mole fraction 0.083 – 1.3 during sol-gel synthesis of the undoped and 1.5%  $\text{Pb}^{2+}$  doped  $\text{ZnAl}_2\text{O}_4$  phosphors. Specifically, we report these effects based on the structure, morphology and photoluminescence properties. In addition, there are scarce reports on the sol-gel synthesis of  $\text{ZnAl}_2\text{O}_4$ :  $\text{Pb}^{2+}$  in literature to date. The main aim is to produce phosphor material that can be used for blue light emitting devices.

## 8.2 Experimental

The  $\text{ZnAl}_2\text{O}_4$ :1.5%  $\text{Pb}^{2+}$  nanoparticles were synthesized using a well-known sol-gel technique [6,11], which is summarized in figure 8.1.  $\text{Zn}(\text{NO}_3)_2 \cdot 6\text{H}_2\text{O}$  (98%),  $\text{Al}(\text{NO}_3)_3 \cdot 9\text{H}_2\text{O}$  (98.5%) and CA,  $\text{C}_8\text{H}_8\text{O}_7 \cdot \text{H}_2\text{O}$  (99%) were dissolved in deionized water. CA was used as a chelating agent. The sols stoichiometric molar ratio of Zn:Al was 1:2 mole fraction. Specified amount of  $\text{Pb}(\text{NO}_3)_2$  was added in the solution to dope with 1.5%  $\text{Pb}^{2+}$  ions. The mol% of 1.5%  $\text{Pb}^{2+}$  was chosen because it was the optimum concentration in our previous results [11]. The Zn/CA mole fractions were varied between 0.083 – 1.3 by keeping the moles of  $\text{Zn}(\text{NO}_3)_2 \cdot 6\text{H}_2\text{O}$  constant at 1 mol and varying the CA moles as shown in table 8.1. For all samples, the temperature was kept at ~ 80 °C while constantly stirring using a magnetic

stirrer until the solution forms gels. The gels were dried in an oven at 140 °C, and ground to get powders. The powder samples were ground further and subsequently annealed at 800 °C in a furnace for an hour.

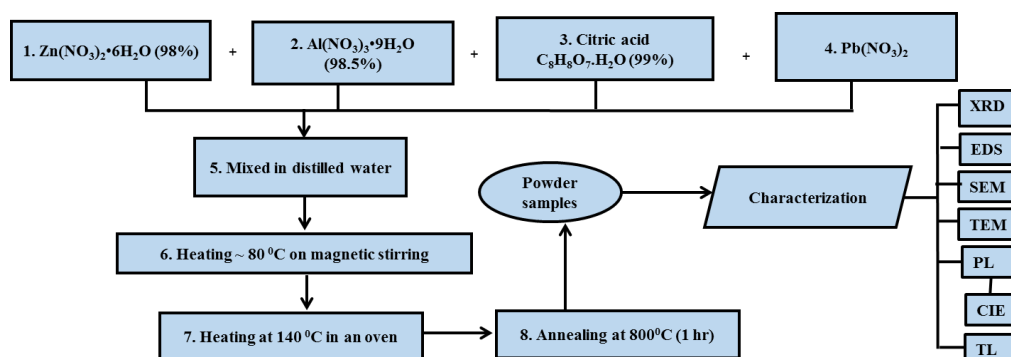


**Figure 8.1.** Summarised scheme for sol–gel synthesis of  $\text{ZnAl}_2\text{O}_4:1.5\% \text{Pb}^{2+}$ .

The crystal structure of the samples was characterized by powder X-ray diffraction (XRD) (Bruker AXS Discover diffractometer) with  $\text{CuK}\alpha$  ( $1.5418\text{\AA}$ ) radiation). The surface morphology and elemental composition of the phosphor powder were investigated using a Shimadzu Superscan ZU SSX-550 electron microscope (SEM) coupled with an energy dispersive X-ray spectroscope (EDS). Transmission Electron microscopy (TEM) was performed with a JEOL JEM 2100 containing a  $\text{LaB}_6$  filament. Photoluminescent (PL) spectra were recorded at room temperature using a Hitachi F-7000 fluorescence spectrophotometer. Thermo luminescence (TL) analyses were done above room temperature by using Nucleonix 1009I TL reader to investigate traps and defects in the solid  $\text{ZnAl}_2\text{O}_4:1.5\% \text{Pb}^{2+}$ .

**Table 8.1** Summary of the samples identification, crystallites size, d spacing and decay times.

Zn/CA	Crystallites size (nm)	d spacing ( $\text{\AA}$ )	Decay Times (ms)	
			$\tau_1$	$\tau_2$
1.3	33.5	2.4346	$1028.2 \pm 0.2$	$4450.1 \pm 567.9$
0.67	27.0	2.4345	$1031.4 \pm 0.3$	$4080.8 \pm 234.8$
0.33	10.2	2.4397	$1050.1 \pm 3.3$	$1473.0 \pm 92.8$
0.11	10.1	2.4507	$1037.7 \pm 1.3$	$1724.5 \pm 137.0$
0.083	10.7	2.4519	$1030.2 \pm 0.1$	$142.6 \pm 3.1$
0.33*	10.9	2.4402	$1028.2 \pm 0.1$	$165.8 \pm 3.2$

\*Un-doped sample

## 8.3 Results and discussion

### 8.3.1 XRD

The crystallinity and purity of the annealed samples prepared by the sol-gel method determined by means of XRD are presented in figure 8.2 (a). The observed diffraction peaks showed broad reflections indicating a fine crystallite nature of the obtained material. The dominant XRD patterns in most of the samples are in agreement with the standard data provided by the International Center for Diffraction Data (JCDPS: 82-1043) for the cubic  $\text{ZnAl}_2\text{O}_4$  spinel phase. These peaks were indexed as (220), (311), (400), (331), (422), (511), (440), (620) and (533) diffraction lines. However, as the CA content was increased (see table 8.1), extra and less intense diffraction peaks of impurities were detected. The diffraction peaks due to the impurities are assigned to be the presence of zincite (hexagonal  $\text{ZnO}$  JCPDS: 36-1451) in the nanocrystals. Yang et al. [20] reported extremely similar crystal structure.

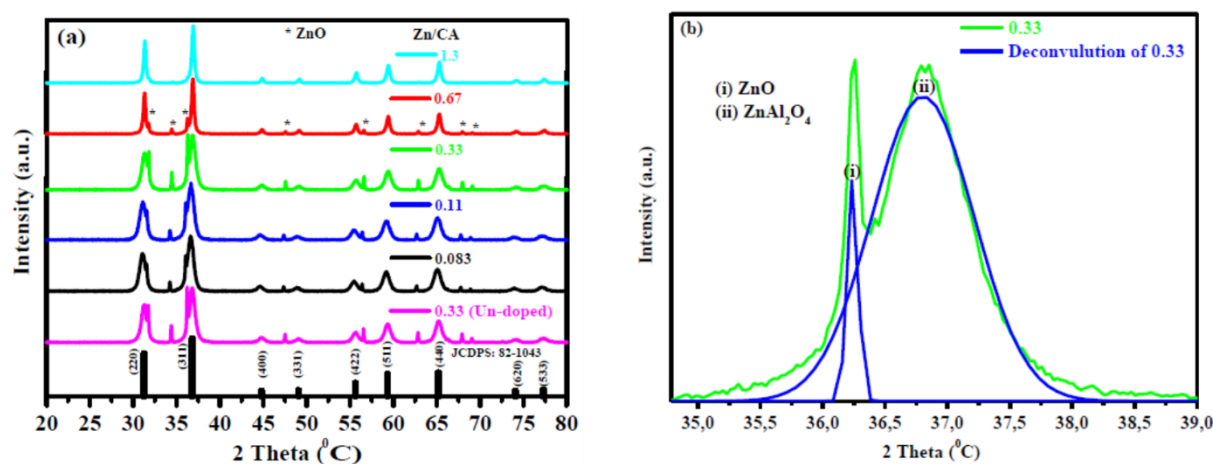


**Figure 8.2.** (a) X-ray patterns of the un-doped and  $\text{ZnAl}_2\text{O}_4:1.5\% \text{Pb}^{2+}$  doped phosphors (b) deconvolution of the Zn/CA mole fraction is equal to 0.33.

The results suggest that increasing the CA content in the precursors is accompanied by ZnO impurities while the diffraction peaks of the  $\text{Al}_2\text{O}_3$  phase could not be detected by XRD because  $\text{Al}_2\text{O}_3$  is amorphous and spreading in the ZnO phase [21]. We propose that the presence of ZnO at lower mole fraction can be attributed to the increase in  $\text{O}^{2-}$  ions (see experimental section above) as the CA content was increased or mole fraction was decreased. Due to equal charge magnitudes,  $\text{O}^{2-}$  is more likely to bond with  $\text{Zn}^{2+}$  than any other ions with different charge magnitude (e.g.  $\text{Al}^{3+}$ ). The fact that  $\text{Pb}^{2+}$  has the same charge magnitude as  $\text{Zn}^{2+}$  one might expect to also have residue of PbO impurities. The reason why there is no PbO impurity in the XRD is because  $\text{Pb}^{2+}$  is much bigger than  $\text{Zn}^{2+}$  and so the charge is less

localized. Thus, the ZnO impurities traces are expected to exist when the Zn/CA mole fraction is decreased. The crystallites sizes shown in table 8.1 were estimated by Scherrer's equation [22] using the most intense peak (311). As it can be seen in table 8.1 and figure 8.1 (a) that the presence of ZnO impurities decreased the crystallites sizes of the nanopowders. Generally, when the Zn/CA mole fraction is increased, the crystallites size is observed to increase too and this is attributed to the aggregation of primary particles, which is induced by the addition of CA [19]. Similar behaviour has been previously reported by Asakura et al. [19]. For all samples the (311) diffraction peak was deconvoluted, as shown in figure 8.2 (b), for an example, in order to distinguish the ZnO and ZnAl<sub>2</sub>O<sub>4</sub> spinel from each other. The peaks at the lower (i) and higher angle (ii) were taken as the ZnO and ZnAl<sub>2</sub>O<sub>4</sub> spinel peaks, respectively. Thus, the Zn/CA mole fractions influence the crystallites sizes. When comparing the doped and un-doped ZnAl<sub>2</sub>O<sub>4</sub> (indicated by the star in table 8.1) for the 0.33 Zn/CA mole fraction, the results suggest that doping with 1.5% Pb<sup>2+</sup> influences the crystallites size.

The analysis of the main diffraction peak (311) shifts and intensity are shown in figure 8.3 (a) and (b). In figure 8.3 (a) the positions of the main diffraction peak evidently shifts to the smaller angle side with the decrease in Zn/CA mole fraction. Such shifting phenomena have been reported in the literature [23], and were explained to result from successful substitutional defects by replacing the bigger dopant ionic radius Eu<sup>3+</sup> (0.96 Å) [23], and Ce<sup>3+</sup> (1.03 Å) [24], with the smaller ionic radius Zn<sup>2+</sup> (0.74 Å) in the ZnO crystal lattice. Thus, the (311) peak shift of ZnAl<sub>2</sub>O<sub>4</sub> in this study shows the same substitutional effects as was reported for ZnO [23]. When considering the un-doped and Pb<sup>2+</sup> doped of 0.33 Zn/CA mole fractions, it is evident that when incorporating the 1.5% Pb<sup>2+</sup> ions into the host lattice there is no noticeable influence on the diffraction peak position. The reason for this might be the less dopant concentration used in this study as reported by Zhong et al. [23] that the effects are only expected at the higher dopant concentration. Therefore, the diffraction peak shifts to the lower diffraction angle must be the result of varying the Zn/CA mole fraction. However, our previous results [11] on ZnAl<sub>2</sub>O<sub>4</sub>:x% Pb<sup>2+</sup> have shown that the peak shift to the higher diffraction angle is due to the increase in Pb<sup>2+</sup> mol% and the possible reasons for such behaviour are outlined therein. Note that the Zn/CA mole fraction used in our previous study [11] was 1.3.

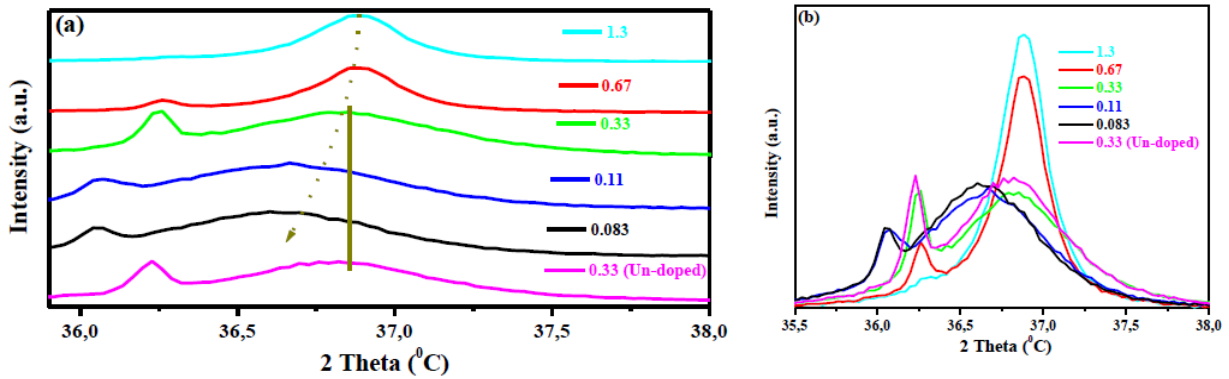


**Figure 8.3.** Analysis of (311) diffraction peak (a) shift and (b) intensity.

It is possible that the increase in Zn/CA mole fraction originates less knocking-off  $\text{Zn}^{2+}$  ions (ionic radius  $0.74 \text{ \AA}$ , [25]) from the lattice sites and the crystal field interaction of the neighbouring  $\text{Zn}^{2+}$  ions with lesser substituted  $\text{Pb}^{2+}$  (ionic radius  $1.01 \sim 1.40 \text{ \AA}$ , [26]) makes it shrink and become smaller than  $\text{Zn}^{2+}$  ions [27], and that serves as a reason why there is an exponential decrease in lattice spacing as a function of Zn/CA mole fraction shown in figure 8.4. This also serves as a reason why there is a slight decrease in d spacing for the Zn/CA = 0.33 doped compared to the un-doped sample (see table 8.1 and figure 8.4). Lumbarda et al. [27] has also reported similar type of behaviour. As shown in figure 8.3 (b) that the diffraction peak widths decreased and the intensity of the diffraction peaks increased with an increase in Zn/CA mole fractions, which is what is associated with an increase in the degree of crystallite size and crystallinity, respectively [24]. In addition, the (311) peak exhibits significant broadening with a decrease in Zn/CA mole fraction, which may be attributed to the loss of crystalline quality in the nanocrystals [25]. Thus, the increase in CA content destroys the crystallinity of the samples. The average lattice spacing was estimated to be  $2.44 \text{ \AA}$ , which corresponds to the (311) lattice spacing of the  $\text{ZnAl}_2\text{O}_4$  reported by Zawadzki et al. [4]. It is, therefore, concluded that the crystal structure of the final product can be controlled by varying the Zn/CA mole fractions.

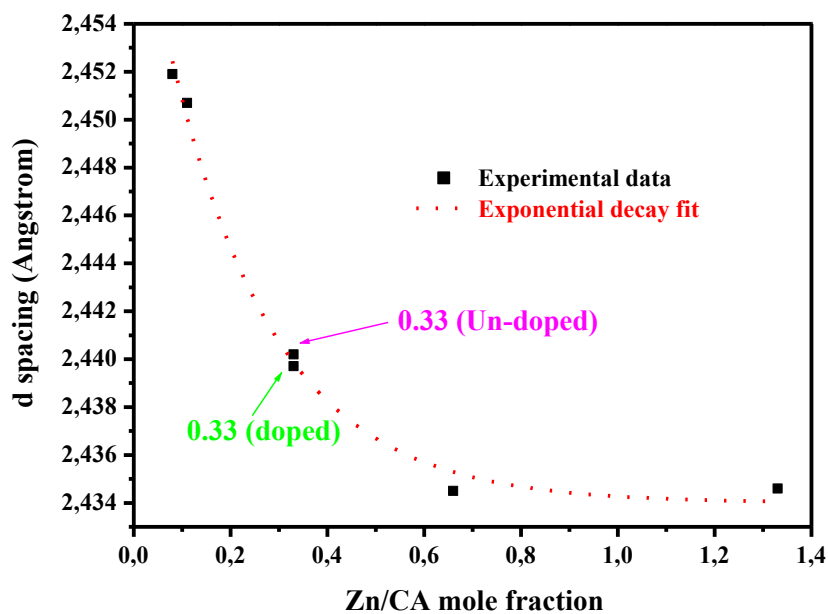


**Figure 8.4.** Lattice spacing as a function of Zn/CA mole fraction.

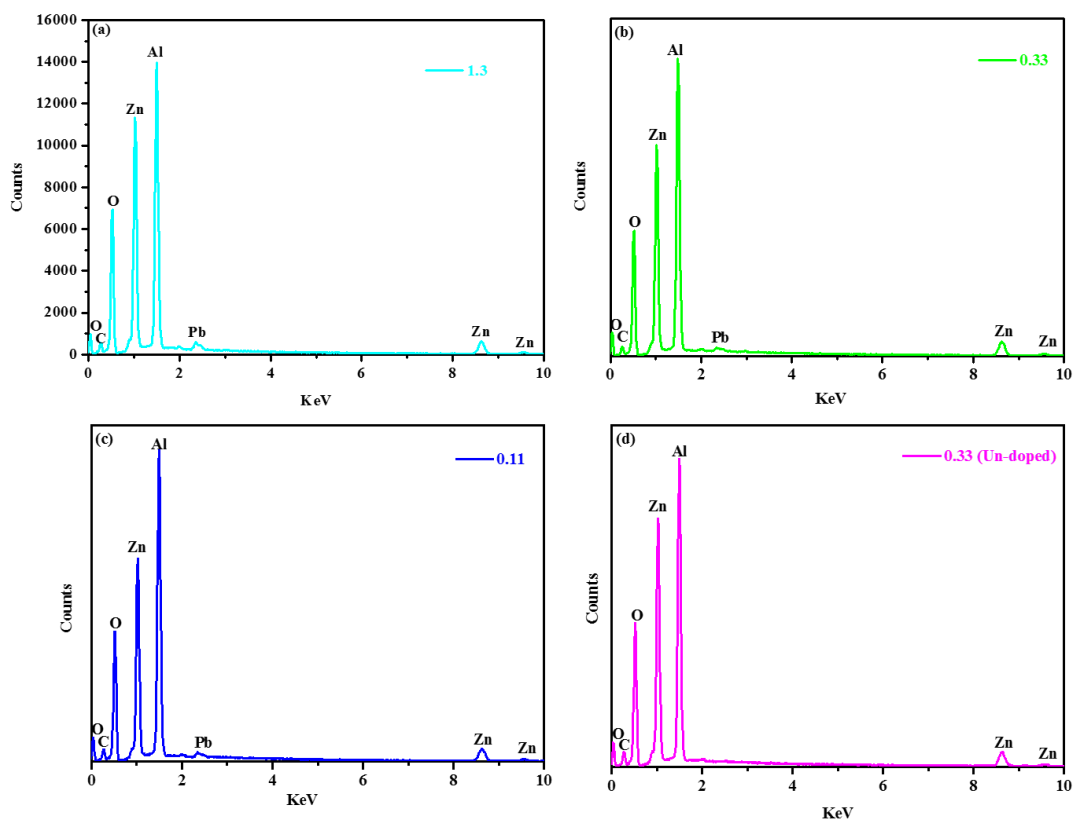


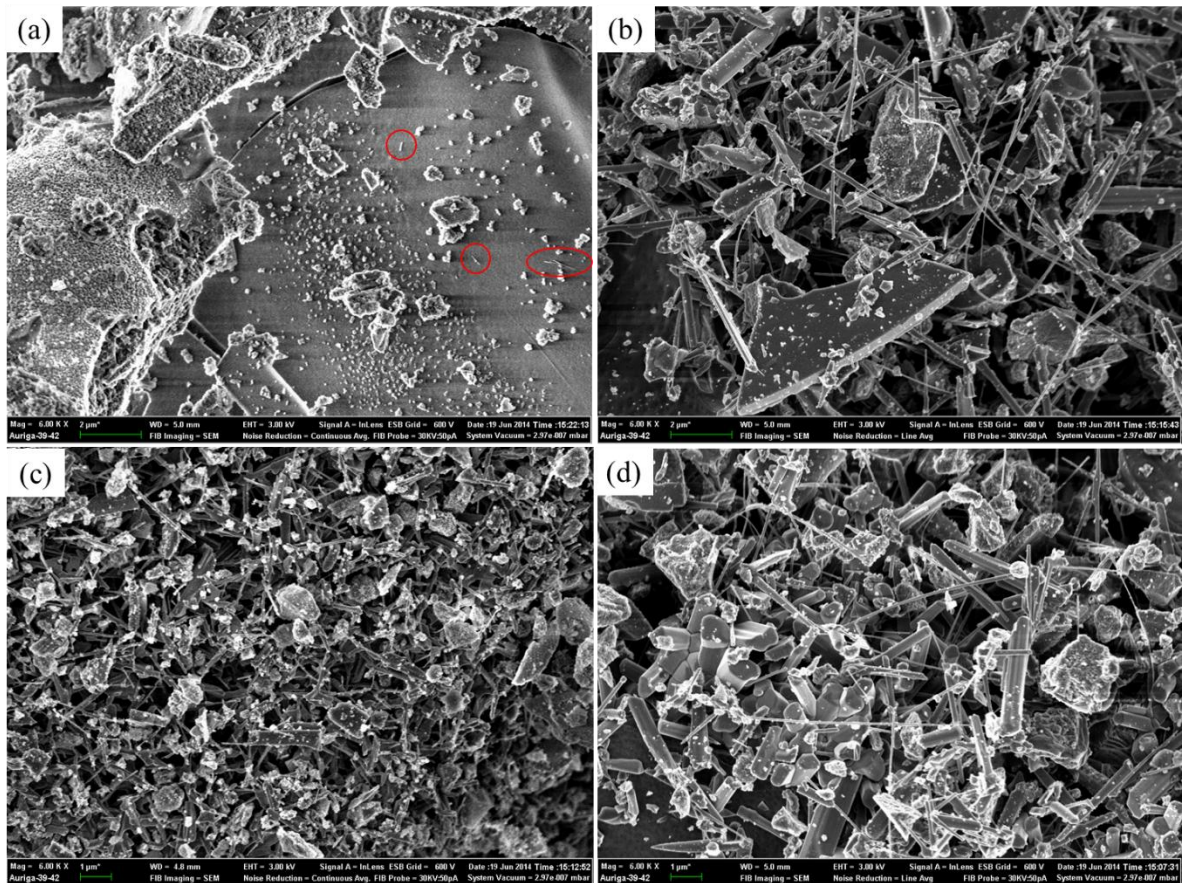
**Figure 8.5.** The raw EDS spectrum for various Zn/CA mole fraction (a) 1.3, (b) 0.33 and (c) 0.11 and (d) 0.33 (un-doped).

### 8.3.2 EDS

The EDS spectrum of the  $\text{ZnAl}_2\text{O}_4:1.5\% \text{Pb}^{2+}$  and un-doped samples are illustrated in figure 8.5. All of the as-designed elements Zn, Al, O and Pb are evidently noticed in the spectrums shown in figure 8.5 (a) – (c). Figure 8.5 (d) presents the EDS spectra of the un-doped sample. The existence of the C peak in all the spectrums is due to the conductive carbon (C) films coated on the samples during the course of EDS measurement and adventitious C from the environment.

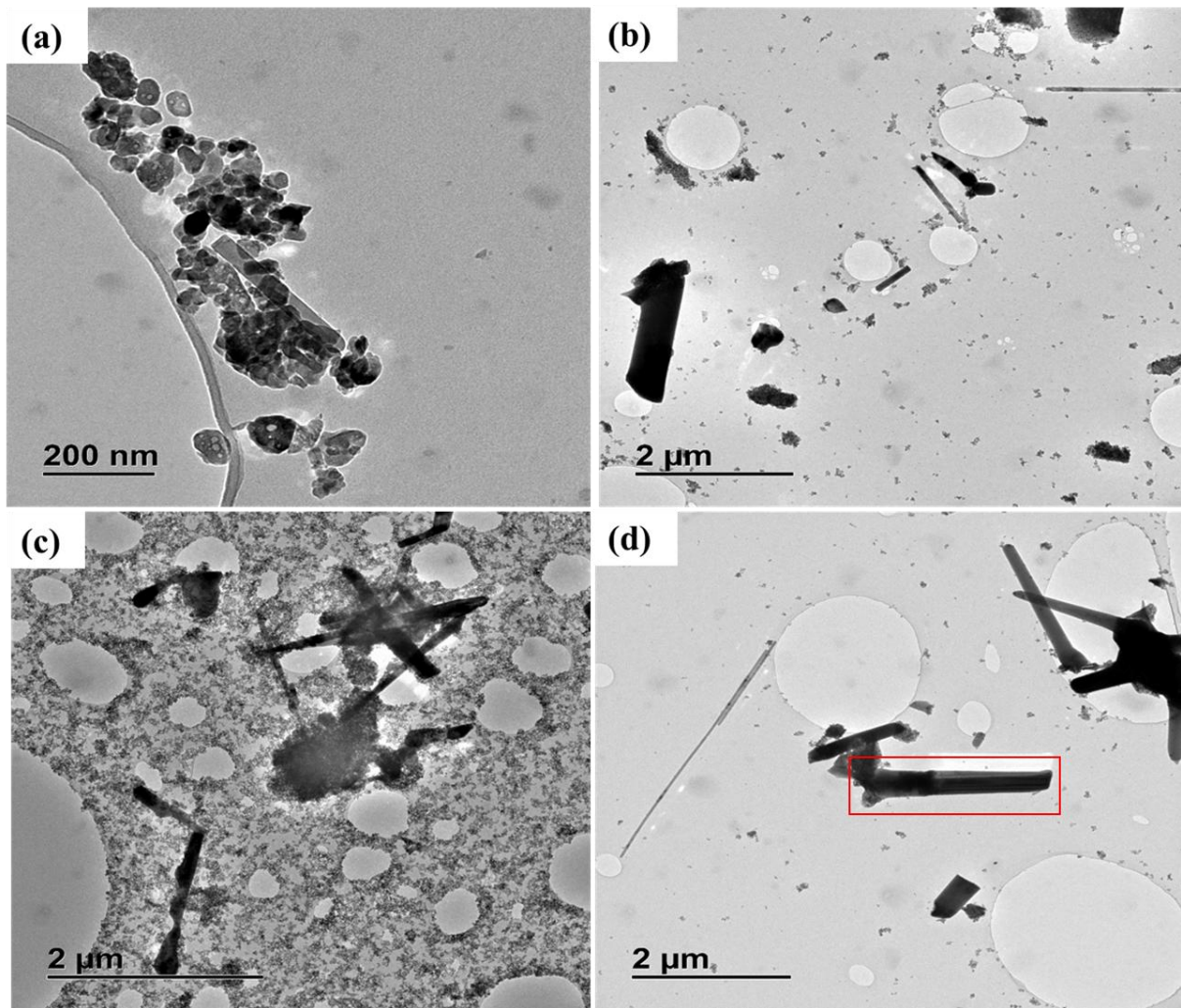
### 8.3.3 SEM and TEM

Figure 8.6 shows the SEM micrographs for the un-doped and 1.5%  $\text{Pb}^{2+}$  doped  $\text{ZnAl}_2\text{O}_4$  at various Zn/CA mole fractions. The morphology at the high Zn/CA mole fraction shown in figure 8.6 (a) consisted of the irregular agglomerated and dispersed particles over the surface and pores. The higher crystallite size corresponds to lower sized particles and more spherical-like structures. Few rods-like morphology (indicated by red circle and ellipse) are also observed at the higher Zn/CA mole fraction. As the Zn/CA mole fraction was decreased (figure 8.6 (b)), there is a morphological evolution from irregular particles with low degree of rods-like structures to the higher degree of rod-like-needles morphologies. Apart from Chew et al. [17] report, we have recently observed [28] similar morphological evolution in  $\text{ZnAl}_2\text{O}_4:0.01\% \text{Cr}^{3+}$  nanocrystals and that was attributed to the different CA contents, which tends to absorb on certain dimension. As the Zn/CA mole fraction is decreased further (see figure 8.6 (c)) it can be seen that a high yield of non-uniform rod-like nanostructures, with a mixture of different particle shapes were formed. These particles of different shapes are also seen over the rod surface. When considering the un-doped samples shown in figure 8.6 (d), it can be seen that there is similarities in the high degree of rod-like-needles morphologies as in doped samples shown in figure 8.6 (b). In addition to this, the rods for the un-doped samples are agglomerated and their sizes are non-uniform. The cubic-like rods structures can evidently be seen in figure 8.6 (d), which is corresponding to the XRD results (JCDPS: 82-1043 for the cubic  $\text{ZnAl}_2\text{O}_4$  spinel phase) shown in figure 8.2. It is therefore evident that the Zn/CA mole fraction influences the phosphor morphology.



**Figure 8.6.** SEM photographs of  $\text{ZnAl}_2\text{O}_4: 1.5\% \text{Pb}^{2+}$  powders annealed at  $800^\circ\text{C}$  for various Zn/CA mole fraction (a) 1.3, (b) 0.33 and (c) 0.11 and (d) 0.33 (un-doped).

The product was further characterised by high-resolution transmission electron microscope (HR-TEM) shown in figure 8.7. As it can be seen that at the higher and lower Zn/CA mole fraction, the degree of rods-like morphologies appears to agree with what has been observed in SEM results in figure 8.6. When considering the un-doped sample shown in figure 8.7 (d), it is reasonable to state that the rod-like particle (indicated by the red rectangle) is cubic, which is in good agreement with the SEM (figure 8.6 (d)) and XRD (JCDPS: 82-1043 for the cubic  $\text{ZnAl}_2\text{O}_4$  spinel phase) shown in figure 8.2. Generally, TEM analysis confirmed the SEM and XRD results.



**Figure 8.7.** TEM photographs of  $\text{ZnAl}_2\text{O}_4: 1.5\% \text{Pb}^{2+}$  powders annealed at  $800\text{ }^\circ\text{C}$  for various Zn/CA mole fraction (a) 1.3, (b) 0.33 and (c) 0.11 and (d) 0.33 (un-doped).

#### 8.3.4 PL analysis

Figure 8.8 (a) presents PL excitation and emission spectra of the un-doped and  $1.5\% \text{Pb}^{2+}$  doped  $\text{ZnAl}_2\text{O}_4$  at various Zn/CA mole fractions. The PL excitation spectra taken when monitoring the violet emission at  $400\text{ nm}$  revealed that there are two absorption bands located at  $276$  and  $328\text{ nm}$ . Both absorptions bands are attributed to the host [29-31]. The emission spectra of these samples, taken under the same excitation of the  $276\text{ nm}$  line are also displayed in figure 8.8 (a). Interestingly, two distinct violet emissions are observed at  $400$  and  $410\text{ nm}$ . The normalized emission spectra shown in figure 8.9 (insert) clearly shows the peak shifts from  $400$  to  $410\text{ nm}$  at the mole fraction of  $0.11$ . Hence, we infer that the violet emission can either originates from the host,  $\text{Pb}^{2+}$  ions or  $\text{ZnO}$  impurities [32]. The

phenomena of the maximum shifts to 410 nm at 0.11 and shifts back to 400 nm at 0.083 is currently not understood, which certainly require further investigation. The emission peak at 400 nm is attributed to arise from the intrinsic intra bandgap defects, such as oxygen vacancies ( $V_0^*$ ) [29]. Da Silva et al. [20] suggested that these defects provide donor levels near the conduction band edge of the oxide. The emission peak at 410 nm is attributed to the  $^3P_1 \rightarrow ^1S_0$  transition induced by  $Pb^{2+}$  ion [11]. We have recently reported [11] very close emissions and their pathways in the un-doped and  $Pb^{2+}$ -doped  $ZnAl_2O_4$  system. In the current study, we propose that the energy levels (as shown in ref [11] figure 8.6 (a)) have been adjusted slightly downwards. The deconvolution of the 0.11 Zn/CA mole fraction (see figure 8.8 (b)) shows that there are three emission peaks labelled (i), (ii) and (iii). As it can be seen in figure 8.8 (a) that the origin of the peak labelled (i) is the same as the 400 nm peak. We propose here that the Zn/CA mole fraction for the investigated range is regulating the defects level in the host. It is proposed that the peak labelled (ii) at 456 nm in figure 8.8 (b) is due to the defect level induced by the ZnO impurities [32]. This can be verified by the absence of ZnO peak (ii) for the 1.3 and 0.67 Zn/CA mole fractions as shown in figure 8.8 (a), which agrees very well with the XRD results in figure 8.2 (a) in terms of the quantity of ZnO impurities. The peak labelled (iii) at 552 nm in figure 8.8 (b) is attributed to the second order emission of the excitation wavelength. When considering the Zn/CA mole fraction 0.33 un-doped and 1.5%  $Pb^{2+}$  doped  $ZnAl_2O_4$ , it can be seen that the  $Pb^{2+}$  ions slightly enhanced the emission intensity, which is certainly expected at this lower mol% of the dopant [33]. In addition, un-doping with  $Pb^{2+}$  ions broadens the excitation spectra and this is attributed to the bigger crystallites sizes for the un-doped compared to doped sample as shown in table 8.1 [1]. Gupta et al. [1], showed on the CdSe nanoparticles that the increase in FWHM of PL peak for higher capping agent concentration is due to the increase in the range of sizes, which result in a broader PL peak. Although in Gupta et al. [1] report they have used mercaptoacetic acid as a capping agent, it was found that the size of CdSe nanoparticles decreases, as the concentration of capping agent is increased, which agrees very well with our current results. Generally, by comparing the XRD and PL results it can be seen that the higher the emission intensity the smaller the crystallites size, which is in agreement with Gupta et al. [1] results on the CdSe nanoparticles. Their results [34] showed that the PL intensity increases and the peak shift towards blue region as the particle size is reduced. It is, therefore, proposed here that the Zn/CA mole fraction controls or regulates the defects level in the host bandgap.

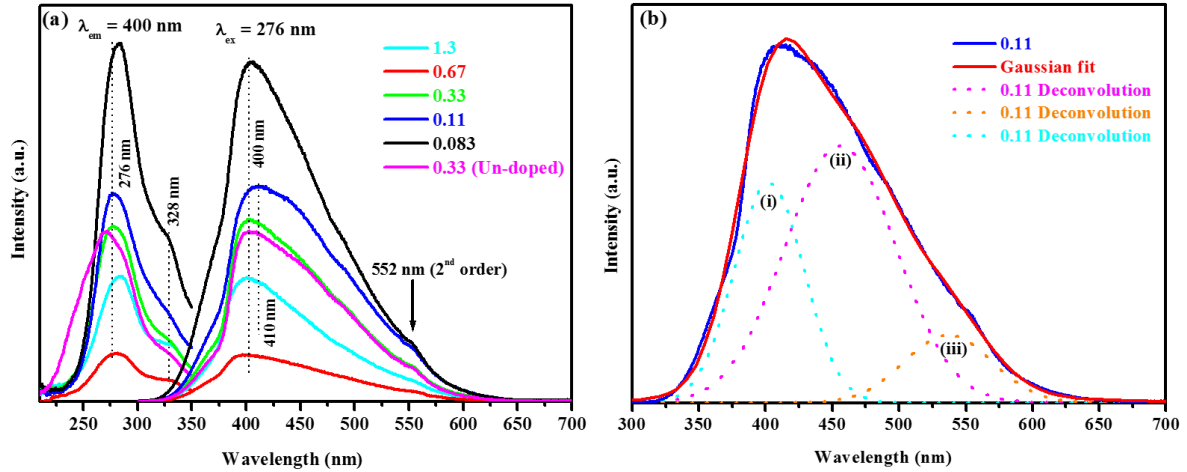


**Figure 8.8.** (a) The excitation and emission spectra of the un-doped and 1.5%  $\text{Pb}^{2+}$  doped  $\text{ZnAl}_2\text{O}_4$  nanophosphors for various Zn/CA mole fractions and (b) Deconvolution of 0.11 Zn/CA mole fraction.

The peaks intensity presented in figure 8.9 showed a parabolic behaviour with a drastic drop to a minimum intensity point at Zn/CA mole fraction equal to 0.9. As shown in figure 8.9 that the emission intensity as the function of the Zn/CA mole fraction revealed the parabolic behaviour. Quenching in the luminescence is attributed to the CA induced point defects, which might be introducing the new trap sites that enhance non-radiative recombination of the excited electrons. The luminescence enhancement is attributed to the modification of the defect levels or local environment of the dopant ions [34], which seems to be controlled by the CA contents. Asakura et al. [19] showed that the PL emission intensity of the  $\text{YAG}:\text{Ce}^{3+}$  due to the 4f–5d transition of  $\text{Ce}^{3+}$  is influenced by the amount of CA. Their report [19], also showed that the particle diameter decreases from 10.2 to 4.0 nm with an increase in CA, which is in good agreement with our results that is; the CA content affects the emission intensity. Unlike most known studies of the effects of the dopant concentration on the emission intensity, for example [6,11,32], which showed a Gaussian behaviour that starts with luminescence enhancement to a certain optimum concentration and then quenching, the variation of Zn/CA mole fraction, for the investigated range, first originates luminescence quenching that is subsequently followed by enhancement [6,11,33]. Possible reason why the emission intensity for 0.67 molar ratio is lower than the 1.3 might be the fact that in 0.67

there is presence of ZnO impurities, which are enhancing the non-radiative of the excited electron, while in the case of 1.3, there is no ZnO impurities (see Fig. 2 (a)).

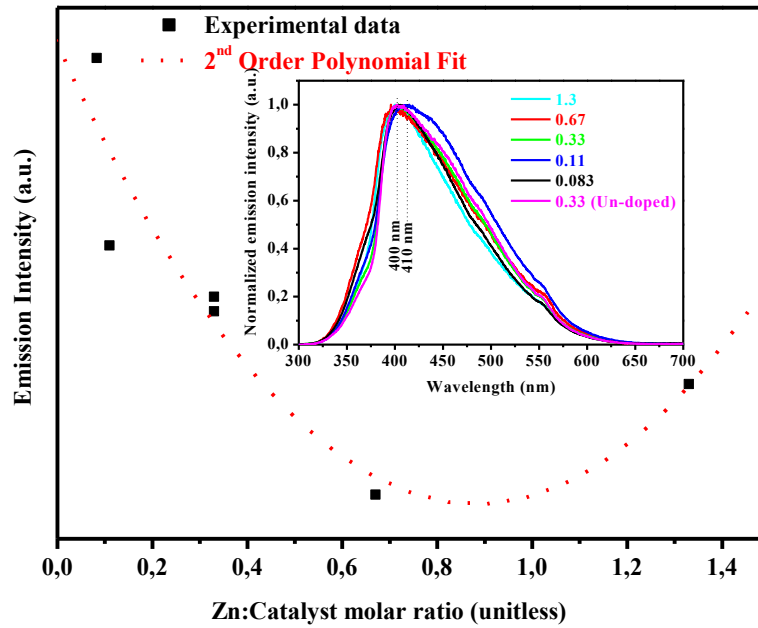


**Figure 8.9.** Emission intensity as a function of Zn/CA mole fractions (insert: normalized emission intensity).

Phosphorescence decay time studies of all powder samples were carried out to investigate the luminescence properties. Figure 8.10 (a) shows the decay curves of the un-doped (0.33 mole fraction) and the  $\text{ZnAl}_2\text{O}_4:1.5\% \text{Pb}^{2+}$  at various Zn/CA mole fractions for the 400 nm emission peak with  $\lambda_{\text{ex}} = 276 \text{ nm}$ . When comparing all the decay curves shapes, it was found that the decay characteristics of this phosphor are similar indicating that all the samples have the same afterglow decay mechanism. The second order exponential decay given in equation 1 was used for fitting all the decay curves.

$$I(t) = I_0 + A_1 e^{-t/\tau_1} + A_2 e^{-t/\tau_2} \quad (1)$$

Where  $I$  represents the phosphorescent intensity,  $I_0$  is the luminescence intensity initially,  $A_1$ ,  $A_2$  are constants,  $t$  is the time of measurement, and  $\tau_1$ ,  $\tau_2$  are the decay time values [35], which are presented in table 8.1. We propose that the huge variation in the second component

( $\tau_2$ ) indicates that an increase in Zn/CA improves the slow decay component of the phosphor lifetime [36]. Thus, it is clear from this observation that the Zn/CA introducing the new trap sites in  $\text{ZnAl}_2\text{O}_4:1.5\% \text{Pb}^{2+}$ . These results indicate that the CA content is vital in the production of the radiative defects, which is also consistent with the observations in Asakura et al. [19]. Figure 8.10 (b) represents the chromaticity co-ordinates of all the samples. The CIE Coordinate Calculator software [37] was used to determine the  $x$  and  $y$  co-ordinates. The software also shows the position of the co-ordinates in the chromaticity diagram and the expected color of the material. As shown in figure 8.10 (b) that there was a small difference in color and some points are on top of each other. Generally, this is in good agreement with the PL results, which showed that the emission position wavelength is the same for all samples. Hence, for the investigated Zn/CA range, it is concluded that the emission color is in the blue region of the CIE chromaticity chart.

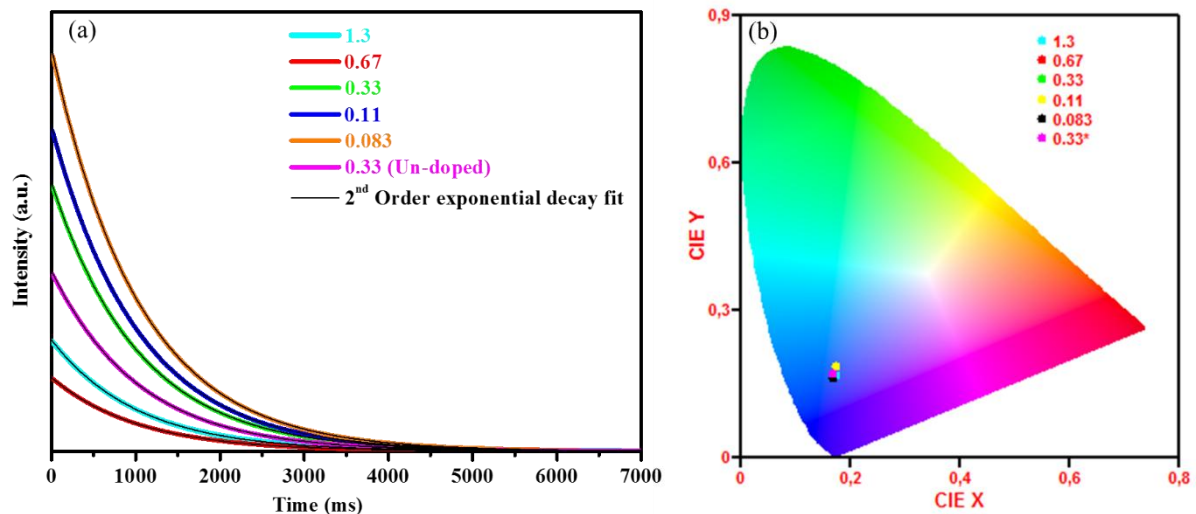


**Figure 8.10.** (a) Decay curves and (b) CIE chromaticity co-ordinates of the un-doped and 1.5%  $\text{Pb}^{2+}$ -doped  $\text{ZnAl}_2\text{O}_4$  nanopowders at the varying Zn/CA mole fraction (star indicates the un-doped sample).

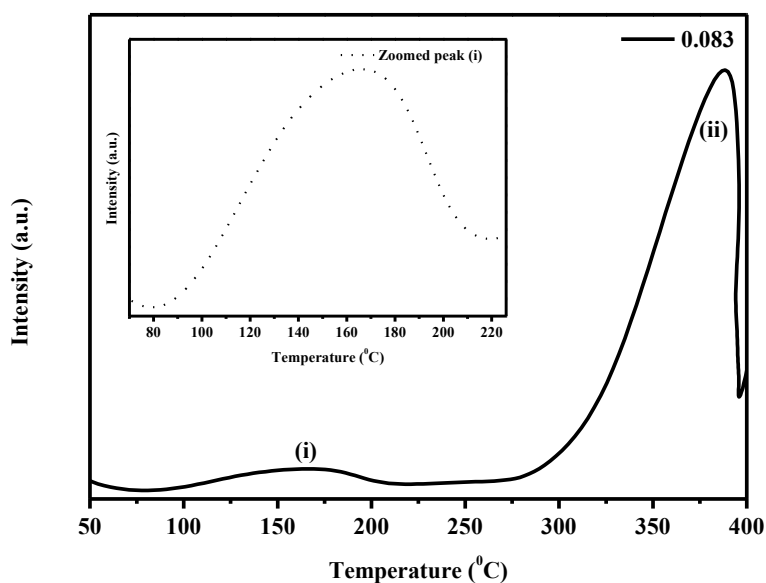


**Figure 8.11.** Glow curve of the UV-irradiated  $\text{ZnAl}_2\text{O}_4$ : 1.5%  $\text{Pb}^{2+}$  nanopowder for Zn/CA mole fraction is 0.083 at a heating rate of  $1\text{ }^\circ\text{C}\cdot\text{s}^{-1}$ .

In order to reveal the presence of defects on the prepared powders, a sample with highest emission intensity (i.e. Zn/CA = 0.083) was analysed for the thermo stimulated luminescence (TSL). As shown in figure 8.11 that the TSL glow curves exhibits two distinct peaks at around (i) 160 and (ii) 387 °C. It is noted that the high temperature peak is found to be more intense than the lower temperature peak, which suggest deep traps. Singh et al. [38] observed similar kind of behaviour. Certainly, each and every peak on the TSL glow curve represent one type of trap present in the lattice [38,39]. From [38,39] it is known that in  $\text{ZnAl}_2\text{O}_4$ , the most probable centres which can be observed are the  $V_0^*$  (as stated in PL results) centres (a hole trapped at a cation vacancy) and F centres (an electron trapped at an anion vacancy). In addition to this, it is known that the cation disorder and non-stoichiometric of aluminates like  $\text{ZnAl}_2\text{O}_4$  provide a large number of lattice defects, which may serve as trapping centres. Therefore, it is with this reasons why the origin of the PL emission in section 8.4 are attributed to the defects emission.

#### 8.4 Conclusion

The X-ray diffraction data revealed that the annealed samples at low CA content consist of highly crystalline cubic  $\text{ZnAl}_2\text{O}_4$  and extra diffraction peaks of impurities have immersed

when the CA content was increased. The shifting of the peaks to higher angles as the Zn/CA mole fraction was increased is attributed to the decrease in the lattice spacing. With the Zn/CA mole fraction variation, there is a morphological evolution from small particles to rod-like-needles particles. Thus, the Zn/CA influenced the morphology. The PL results demonstrated that the violet emission can either be from the host,  $\text{Pb}^{2+}$  or ZnO impurities. The incorporation of 1.5%  $\text{Pb}^{2+}$  ions slightly enhanced the emission intensity. Controlling the Zn/CA mole fraction could quench and enhance the bluish brightness of the  $\text{ZnAl}_2\text{O}_4:1.5\% \text{Pb}^{2+}$  phosphor. The CIE color coordinates of all samples is situated in the blue region of the chart. TSL glow curves exhibits two distinct peaks.

## References

1. P. Gupta, M. Ramrakhiani, *The Open Nanoscience Journal* **3** (2009) 15.
2. D. Zhang, C. Wang, Y. Liu, Q. Shi, W. Wang, Y. Zhai, *J. Lumin.* **132** (2012) 1529.
3. S. K. Sampath, D. G. Kanhere, R. Pandey, *J. Phys.: Condens. Mat.* **11** (1999) 3635.
4. M. Zawadzki, *Solid State Science* **8** (2006) 14.
5. V. Singh, R. P. S. Chakradhar, J. Rao, D. K. Kim, *J. Lumin.* **128** (2008) 394.
6. M. Tsai, Y. Chen, P. Tsai, Y. Wang, *Thin Solid Films* **518** (201) e9.
7. M. Nikl, A. Novoselov, E. Mihokova, K. Polak, M. Dusek, B. McClune, A. Yoshikawa, T. Fukuda, *J. Phys. Condens. Mat.* **17** (2005) 3367.
8. A. A. Seltur, A. M. Srivastava, *Opt. Mat.* **29** (2006) 410.
9. H. F. Folkerts, A. van Dijken, G. Blasse, *J. Phys.: Condens. Mat.* **7** (1995) 10049.
10. A. A. Bol, A. Meijerink, *Phys. Chem. Chem. Phys.* **3** (2001) 2105.
11. S. V. Motlounge, F. B. Dejene, H. C. Swart, O. M. Ntwaeaborwa, *J. Sol-Gel Sci. Technol.* **70** (2014) 422.
12. A. A. Da Silva, A. Goncalves, M. R. Davolos, *J. Sol-Gel Sci. Technol.* **49** (2009) 101.
13. N. J. Van de Laag, S. G. Snel, P. C. M. M. Magusin, G. de With G, *J. Eur. Ceram. Soc.* **24** (8) (2004) 2417.
14. F. L. Yuan, P. Hu, C. L. Yin, S. L. Huang, J. L. Li, *J. Mater. Chem.* **13** (2003) 634.
15. Z. Chen, E. Shi, Y. Zheng, W. Li, N. Wu, W. Zhong, *Mater. Lett.* **56** (2002) 601.
16. S. F. Wang, F. Gu, M. K. Lu, X. F. Cheng, W. G. Zou, G. J. Zhou, S. M. Wang, Y. Y. Zhou, *J. Alloys Compd.* **394** (2005) 255.
17. K. Y. Chew, M. Abu Bakar, N. H. H. Abu Bakar, *Modeling and Numerical Simulation of Material Science* **3** (2003) 23.
18. A. Abreu Jr, S. M. Zanetti, M. A. S. Oliveira, G. P. Thim, *Journal of the European Ceramic Society* **25** (2005) 743.
19. R. Asakura, T. Isobe, K. Kurokawa, T. Takagi, H. Aizawa, M. Ohkubo, *J. Lumin.* **127** (2007) 416.
20. M. Yang, S. Li, G. Chen, *Applied Catalysis B: Environmental* **101** (2011) 409.
21. X. Xia, X. An, X. Wang, Z. Wang, *J. Nat. Gas Chem.* **12** (2003) 259.
22. B. D. Cullity, *1956 Elements of X-ray Diffraction (2nd Ed) Addison Wesley* 285 (1978).
23. M. Zhong, G. Shan, Y. Li, G. Wang, Y. Yiu, *Mat. Chem. Phys.* **106** (2007) 305.

24. C. Cheng, Z. Jiang, C. Liu, J. Photochem. Photobio. A: Chem. **195** (2008) 151.
25. Q. Hou, F. Meng, J. Sun, Nanoscale Research Lettter **8** (2013) 144.
26. S. B. Chen, Y. B. Ma, L. Chen, K. Xian, Geochemical Journal **44** (2010) 233.
27. V. A. Lubarda, Mechanics of Materials **35** (2003) 53.
28. S.V. Motlounge, F. B. Dejene, O. M. Ntwaeaborwa, H. C. Swart, Mater. Res. Express **1** (2014) 045029.
29. A. A. Da Silva, A. Goncalves, M. R. Davolos, S. H. Santagneli, J. Nanosci. Nanotechnol. **8** (2008) 5690.
30. R. F. Martins, O. A. Serra, J. Braz, Chem. Soc. **21** No. 7 (2010) 1395.
31. B. Cheng, S. Qu, H. Zhou, Z. Wang, Nanotechnology **17** (2006) 2982.
32. X. Sun, Y. Zhao, Q. Meng, Scientific Journal of Materials Science **3** (2013) 34.
33. Q. Sai, C. Xia, H. Rao, X. Xu, G. Zhou, P. Xu, J. Lumin. **131** (2011) 2359.
34. D. Gao, H. Zheng, X. Zhang, W. Gao, Y. Tian, J. Li, M. Cui, Nanotechnology **22** (2011) 175702 (5pp).
35. Z. Xia, J. Zhuang, H. Liu, L. Liao, J. Phys. D: Appl. Phys. **45** (2012) 015302 (7pp).
36. B. K. Sharma, N. Khare, D. Haranath, Solid State Communications **150** (2010) 2341.
37. <http://www.mathworks.com/matlabcentral/fileexchange/29620-cie-coordinate-calculator> (accessed 21.10.2012).
38. V. Singh, S. Watanabe, T. K. Gundu Rao, J. F. D. Chubaci, I. Ledoux-Rak, H-Y. Kwak, Appl. Phys. B **98** (2010) 165.
39. K. K. Satapathy, F. Khan, International Journal of Chemical Sciences and Applications **3** (2012) 366.

## Chapter 9: Effects of catalyst/zinc mole fraction on $\text{ZnAl}_2\text{O}_4:0.01\% \text{Cr}^{3+}$ nanocrystals synthesized using sol-gel process

*“Anyone who has never made a mistake has never tried anything new.”*

*~ Albert Einstein*

### 9.1 Introduction

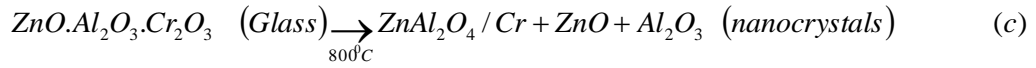
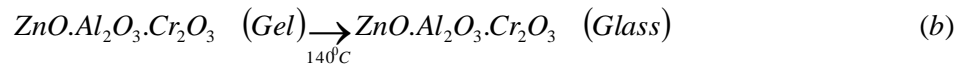
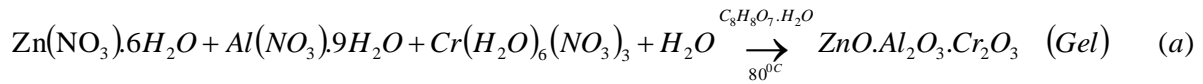
Zinc aluminate ( $\text{ZnAl}_2\text{O}_4$ ) is a wide-band gap ( $\sim 3.8$  eV) semiconductor, which occurs naturally as the mineral known as gahnite and it belongs to the class of inorganic materials called spinels. The reaction between ZnO and  $\text{Al}_2\text{O}_3$  that results into  $\text{ZnAl}_2\text{O}_4$  spinel (closed-packed face-centered-cubic with  $Fd3m$  space group symmetry) follows diffusion mechanism of both Zn and O and an effective unilateral transfer of ZnO into the spinels [1-4].  $\text{Zn}^{2+}$  and  $\text{Al}^{3+}$  metal cations occupy tetrahedral and octahedral sites, respectively. These sites occupation or substitution depend on various factors such as ionic size, cationic charge, electron distribution and electronic states. Gahnite and other spinels are known to be suitable host lattice for various dopants or activator ions for the preparation of phosphors [5,6]. The luminescence properties of rare-earth doped spinels have been reported [7-9]. This luminescence is depend on the particle size, crystal structure, and distribution of activator ions in the host lattice [1,2,9]. The most interesting ions for  $\text{ZnAl}_2\text{O}_4$  doping are transition metal ions. For example,  $\text{Cr}^{3+}$  ion gives either pink or green emission in coloured pigments depending on the strength of the  $\text{ZnAl}_2\text{O}_4$  crystal field.  $\text{Cr}^{3+}$  doped spinels are stable at high temperatures thus they can be used in ceramic applications [11,12]. Numerous methods of preparation of  $\text{ZnAl}_2\text{O}_4$  such as solid state reaction [13], co-precipitation [14], hydrothermal [15], combustion [16] and sol-gel [17] have been developed. Among them, the sol-gel route has been found to be an effective and attractive technique for the synthesis of especially nanoparticulate phosphor materials. The sol-gel technique offers several advantages such as good mixing of starting materials at a very low temperature, it yields materials with low density and low coefficient of thermal expansion [1,18]. One of the fundamental ingredients in the synthetic technique such as sol-gel is a catalyst. Catalytic experiments are known to

S.V. Motlounq et al. / Mater. Res. Express **1** (2014) 045029.

produce the products at the lower activation energy compared to the non-catalytic reactions. Catalysis plays a prominent role in the chemical industry and societies. For example, the majority of chemicals and fuels produced in the chemical industry have been produced using one or more catalysts [19]. Without any doubt, it is therefore clear that catalysis plays a prominent role in society today and will be a critical technology for advancing our life. On the other hand, researchers in the green and sustainable chemistry are focusing on the development of economic and eco-friendly methodologies that are free from the use of any catalyst, reagent, promoter or surfactant in aqueous media [20]. Accordingly, we have devoted our efforts towards investigating the effects of the catalysed and non-catalysed chemical reactions during the synthesis of the  $\text{ZnAl}_2\text{O}_4:0.01\% \text{Cr}^{3+}$  phosphor. In this work, the effects of varying the catalyst/Zn mole fraction (in the range of 0 – 3) on the structure, morphology, band-gap and luminescence properties of  $\text{ZnAl}_2\text{O}_4:0.01\% \text{Cr}^{3+}$  phosphors are reported. The colour tuning by varying the catalyst/Zn mole fraction is investigated. The corresponding luminescence mechanisms are proposed. The objective of this study is to produce phosphor material that can be used for the blue-light emitting devices such as light-emitting diodes (LEDs).

## 9.2 Experimental

The  $\text{ZnAl}_2\text{O}_4:0.01\% \text{Cr}^{3+}$  nanoparticles were synthesized using a well-known sol-gel technique.  $\text{Zn}(\text{NO}_3)_2 \cdot 6\text{H}_2\text{O}$  (98%),  $\text{Al}(\text{NO}_3)_3 \cdot 9\text{H}_2\text{O}$  (98.5%) and citric acid (catalyst),  $\text{C}_8\text{H}_8\text{O}_7 \cdot \text{H}_2\text{O}$  (99%) were dissolved in deionized water. The stoichiometric molar ratio of Zn:Al was 1:2.  $1.5 \times 10^{-6}$  moles of  $\text{Cr}(\text{H}_2\text{O})_6(\text{NO}_3)_3 \cdot 3\text{H}_2\text{O}$  (98%) was added to dope with 0.01%  $\text{Cr}^{3+}$ . The 0.01 mol% of  $\text{Cr}^{3+}$  was chosen because it was found to give maximum luminescent intensity [21]. The catalyst/Zn mole fractions were varied between 0 – 3. For all samples, the temperature was kept at  $\sim 80$  °C while stirring constantly using a magnetic stirrer until the gels were formed. The gels were dried in an oven at 140 °C, and ground to get powders. The powders were annealed at 800 °C in a furnace for one hour. The proposed mechanism for the formation of  $\text{ZnAl}_2\text{O}_4:\text{Cr}^{3+}$  is given by the following reaction equations:



The crystal structure of the samples was analyzed by powder X-ray diffraction (XRD) (Bruker AXS Discover diffractometer) with  $\text{CuK}\alpha$  ( $1.5418\text{\AA}$ ) radiation). The surface morphology of the phosphor powder was investigated using a Shimadzu Superscan ZU SSX-550 electron microscope (SEM). All the TOF-SIMS were performed using the Iontof SIMS<sup>5</sup>. A pulsed 30 kV  $\text{Bi}^+$  primary ion beam, pulsed at 100  $\mu\text{s}$  and operated at 1 pA, was used to acquire chemical images of the phosphor in both the positive and the negative polarities. The powder sample was sputtered on an area of 300 x 300  $\mu\text{m}$  at the sputtering time of 26.21 s/scan. The elemental mapping was rastered over an area of 100 x 100  $\mu\text{m}$  on the surface. The surface images were recorded with a resolution of 512 x 512 pixels. The measurements were performed in a chamber maintained at the base pressure of  $9.4 \times 10^{-9}$  mbar. Diffuse reflectance spectra were recorded using a Lambda 950 UV–vis spectrophotometer with an integrating sphere using spectralon as a reflectance standard. Room temperature photoluminescence (PL) measurements were done using a Hitachi F-7000 fluorescence spectrophotometer.

### 9.3 Results and discussion

#### 9.3.1 Structure and morphology analysis

Figure 9.1 (a) shows the diffraction patterns of the annealed (at 800 °C)  $\text{ZnAl}_2\text{O}_4$  nanostructures for the un-doped and 0.01%  $\text{Cr}^{3+}$ -doped at the various catalyst/Zn mole fractions. The diffraction peaks were relative broad due to smaller particle sizes. The XRD patterns are consistent with the cubic spinel phase of  $\text{ZnAl}_2\text{O}_4$  referenced in the standard JCPDS file number 82-1043. The most prominent peak corresponds to the (311) plane. However, it was noted that as the catalyst content was increased, additional diffraction peaks associated with secondary phases were detected as shown in chemical reaction c. The secondary phase peaks are assigned to be the signatures of the ZnO as reported previously [9,22]. Based on the proposed chemical reaction the final products (reaction c), one can anticipate the presence of  $\text{Al}_2\text{O}_3$  from the XRD results. The reason why  $\text{Al}_2\text{O}_3$  is not present

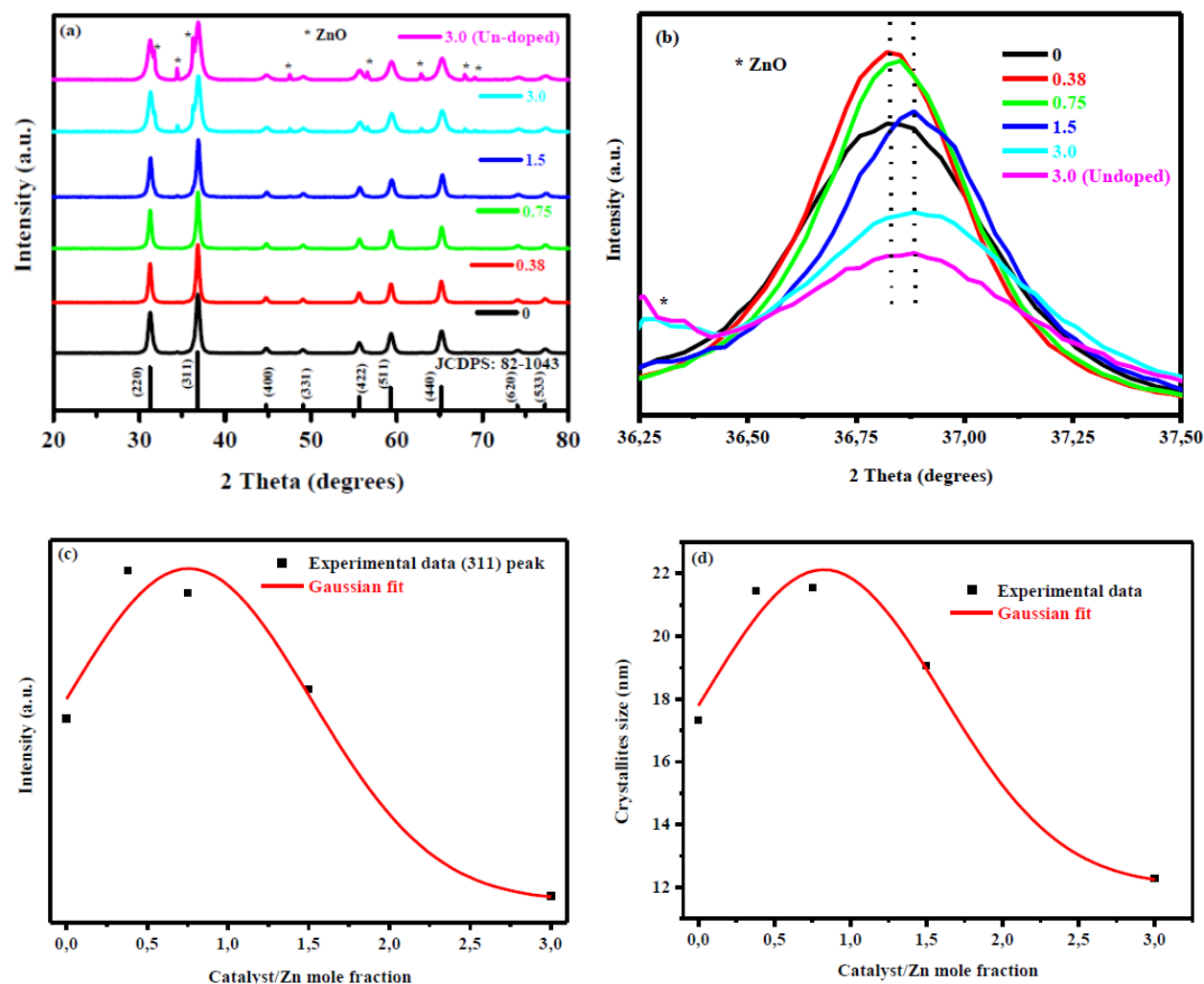
in the XRD patterns might be that  $\text{Al}_2\text{O}_3$  is present in a very small amounts, which makes it below the detection limit of the XRD instrument used [21,23]. In addition to our results, similar crystal structure have been previously observed by Dong et al. [21] and the impurities present therein were attributed to the ZnO. The presence of ZnO at higher mole fraction can be attributed to the reaction between  $\text{Zn}^{2+}$  and  $\text{O}^{2-}$  ions, which are induced by an increase in catalyst content as the mole fraction is increased (see chemical reaction (a)). Due to equal charge magnitudes,  $\text{O}^{2-}$  is more likely to bond with  $\text{Zn}^{2+}$  than other ions with different charge magnitude (e.g.  $\text{Al}^{3+}$  or  $\text{Cr}^{3+}$ ). It is therefore reasonable that there are traces of ZnO impurities especially when the catalyst mole fraction was increased.

**Table 9.1.** Sample identification with related crystallites sizes, decay time and CIE colour coordinates.

catalyst/Zn mole fraction	Crystallites size (nm)	Decay times (ms)	CIE coordinates	
			X	Y
0	17	$513.09 \pm 0.08$	0.393	0.576
0.38	21	$513.91 \pm 0.09$	0.261	0.314
0.75	22	$515.43 \pm 0.10$	0.181	0.171
1.5	19	$515.53 \pm 0.09$	0.192	0.207
3.0	12	$515.28 \pm 0.09$	0.204	0.241
3.0 (un-doped)	10	$514.02 \pm 0.10$	0.204	0.241

When considering the mole fraction of 3 in both the un-doped and doped sample, it can be seen that doping does not influence the crystal structure of  $\text{ZnAl}_2\text{O}_4$ . On the other hand, pure cubic structure is observed for non-catalysed samples as shown in Figure 9.1 (a). The analysis of the most prominent diffraction peak (311) is shown in Figure 9.1 (b). In the case of mole fraction of 3 for both doped and un-doped samples, it can be seen that the doping increases the crystallization without shifting the peak position. In Figure 9.1 (b), it can also be noticed that the increase in the mole fraction decreases the (311) peak intensity, which could be due to the reduced crystallinity [24]. Figure 9.1 (c) shows the variation of (311) peak intensity as a function of the mole fraction, which is showing the Gaussian shape behaviour. The crystallite size of the annealed nanocrystals was estimated from the main diffraction peak (311) by using the Scherrer equation [25] and the associated crystallites sizes are presented in table 9.1. It can also be noted in figure 9.1 (d) that the crystallites sizes as a function of mole

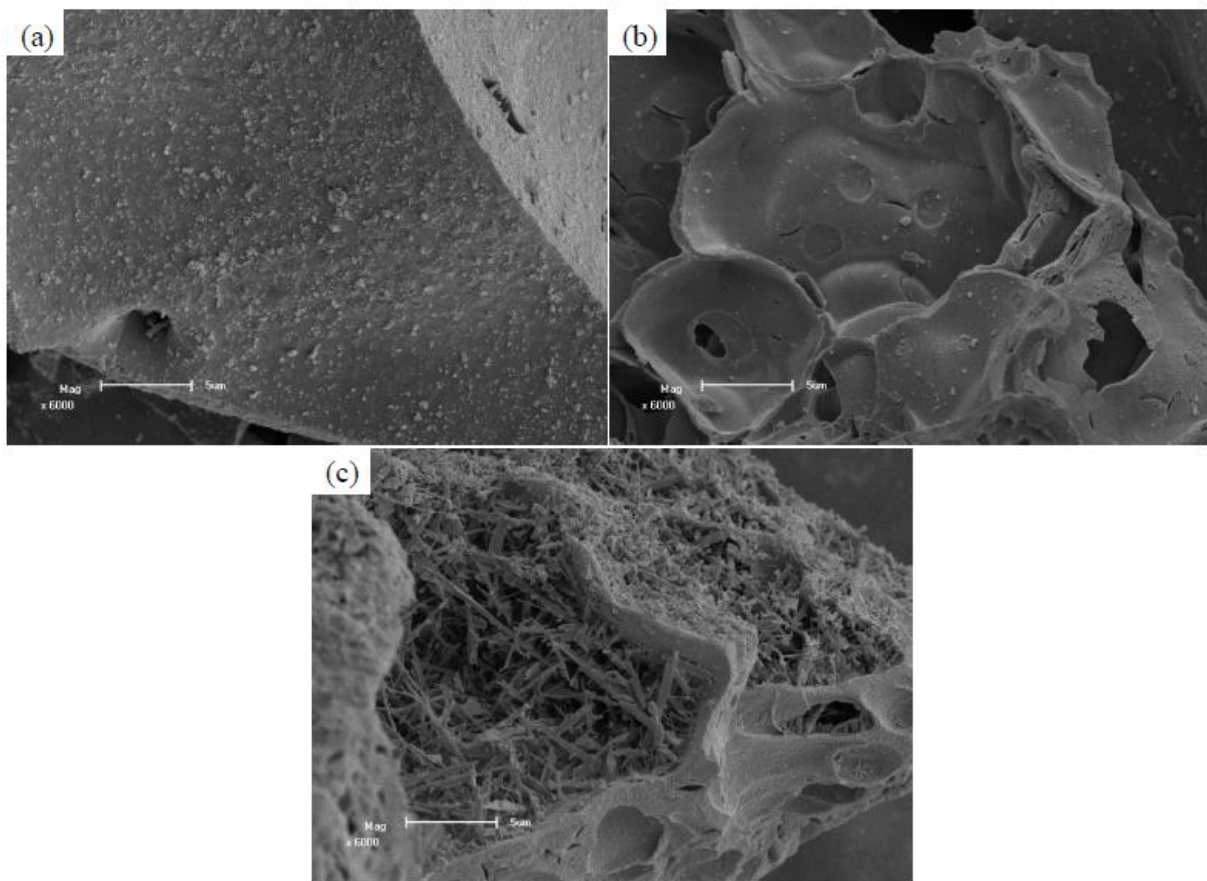
fraction has similar Gaussian shape-type behaviour as in figure 9.1 (c). Note that the undoped sample is not shown in both figure 9.1 (c) and (d). These results suggest that the mole fraction influences the crystallites sizes and crystalline quality of the nanopowder.



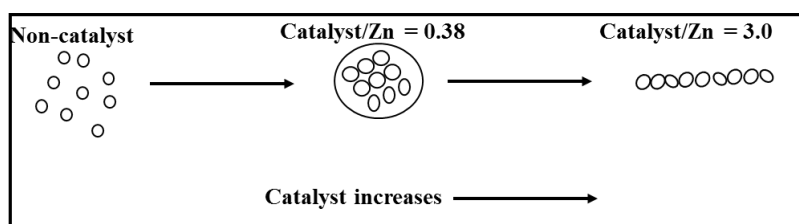
**Figure 9.1.** X-ray patterns of the (a) un-doped, 0.01% Cr<sup>3+</sup>-doped catalysed and non-catalysed ZnAl<sub>2</sub>O<sub>4</sub> phosphors. (b) The analysis of the (311) peak shifts. (c) XRD intensity as a function of mole fraction and (d) Crystallites sizes as a function of mole fraction.

Figure 9.2 presents the SEM images of the ZnAl<sub>2</sub>O<sub>4</sub>:0.01% Cr<sup>3+</sup> powders annealed at 800 °C for various catalyst/Zn mole fractions. The morphology of the non-catalysed sample shown in Figure 9.2 (a) consists of the smaller spherical particles encrusted on the platelet-like structures. There were also some pores and voids on the surface. When the reaction is catalysed at the lower mole fraction, shown in Figure 9.2 (b), the plate like crystal structures,

with pores and smaller particles were observed. All the pores in the surface morphology can be attributed to the evolution of a great quantity of gas during annealing process. At the higher mole fractions, the morphological transformation from plates to rods-like-structures was observed. These morphological evolution as illustrated in Figure 9.2 and 9.3 is caused by citric acid that tends to absorb on certain dimension of the  $\text{ZnAl}_2\text{O}_4:0.01\% \text{Cr}^{3+}$  particles when different concentration of citric acid was added [26]. Comparable to our findings, Chew et al. [26] have reported that the addition of citric acid as a stabilizer (mole ratio of 0.5, 1.0, 2.0, 4.0) resulted in the formation of  $\text{Ba}_2\text{NiTi}_5\text{O}_{13}$  particles with various morphology (i.e. sphere, cube, rod). Therefore, in addition to [26], these results prove that citric acid is not only able to control the size of  $\text{ZnAl}_2\text{O}_4:0.01\% \text{Cr}^{3+}$  particles, but it is also able to control the morphology of particles.



**Figure 9.2.** SEM images of the  $\text{ZnAl}_2\text{O}_4:0.01\% \text{Cr}^{3+}$  powders annealed at  $800\text{ }^\circ\text{C}$  using various catalyst/Zn mole fractions (a) 0 (non-catalysed), (b) 0.38 and (c) 3.0.



**Figure 9.3.** Schematic diagram for morphological evolution of  $\text{ZnAl}_2\text{O}_4:0.01\% \text{Cr}^{3+}$  nanoparticles.

### 9.3.2 Optical properties

The diffuse UV–vis reflectance spectra of the powder samples are shown in figure 9.4 (a). For the 3.0 (un-doped), 0.75, 1.5 and 3.0 mole fractions, the spectra revealed more than 90% reflectance in the visible range from 400 - 800 nm. When considering the un-doped and doped samples for the mole fraction of 3.0, it is noted that doping with 0.01%  $\text{Cr}^{3+}$  ions does not affect the absorption edge. Furthermore, when considering the non-catalysed and catalysed powders, an obvious shift to the lower wavelength is observed, which suggests that the bandgap of the  $\text{ZnAl}_2\text{O}_4$  can be engineered by varying the mole fraction of catalyst/Zn. For the catalyzed samples, it can also be seen from figure 9.4 (a) that the increase in the mole fraction resulted in the decrease in the reflectance. The spectra revealed that there are four (283, 383, 426 and 572 nm) possible absorption bands from the non-catalysed and catalysed (0.38) samples. The absorption band at 283 nm is attributed to the charge transfer (CT) transitions of chromium ion [25]. In addition to the Weckhuysen et al. report [27], it is clear from our results that the absence of 283 nm absorption band from the un-doped sample indicates clearly that the absorption band originates from the chromium ion/s. The absorption band at 383 nm can either be attributed to the band-to-band of the  $\text{ZnAl}_2\text{O}_4$  host structure or the ZnO impurities. This is supported by the fact that for 0.38 and 0.75 mole fractions, for an example, there were no impurities associated with ZnO from the XRD results in figure 9.1 (a) and when looking at the reflectance results in figure 9.4 (a) for the same samples (0.38 and 0.75 mole fractions), it can be seen that the 383 nm absorption band is still present.

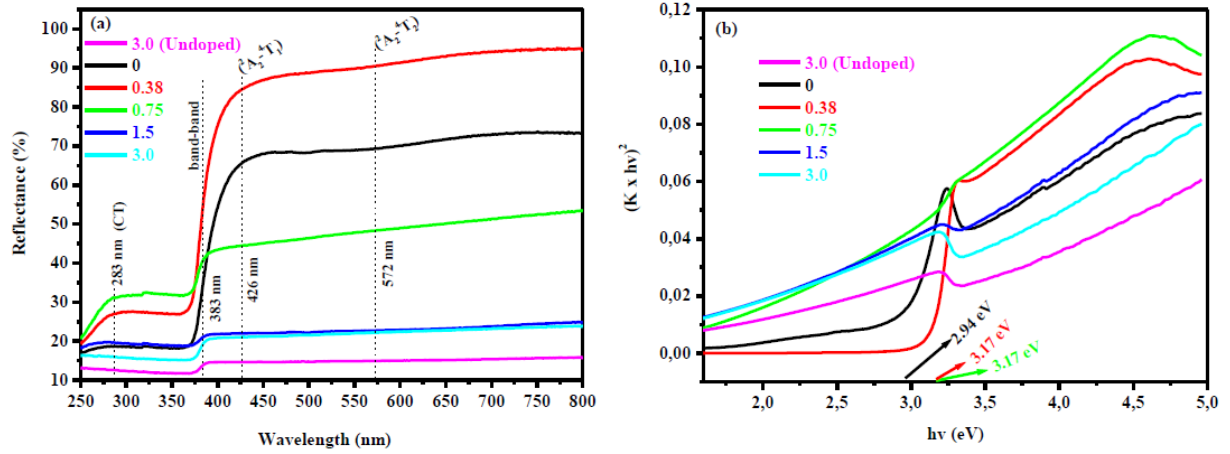


**Figure 9.4.** (a) The reflectance spectra of the un-doped and 0.01%  $\text{Cr}^{3+}$  doped  $\text{ZnAl}_2\text{O}_4$  samples at the varying catalyst/Zn mole fraction (b) Plot of  $(K \times hv)^2$  versus  $(hv)$  photon energy to determine the band gap energy of the nano-powder samples.

Thus, it is for this reason that we attribute the absorption band at 383 nm to the band-band transition in  $\text{ZnAl}_2\text{O}_4$  host. Two absorption bands observed at 426 and 572 nm are respectively assigned to the  ${}^4\text{A}_2 \rightarrow {}^4\text{T}_1$  and  ${}^4\text{A}_2 \rightarrow {}^4\text{T}_2$  spin-allowed transitions of 3d–3d configuration of  $\text{Cr}^{3+}$  ions [12]. Similarly, apart from the Dong et al. [21] and Miron et al. [12] reports, the absence of these absorption bands from the un-doped samples in our results signifies that both absorption bands are not originating from the  $\text{ZnAl}_2\text{O}_4$ . All of these absorptions bands are also shown in the proposed absorptions and emissions mechanism in figure 9.6. Thus, the variation in mole fractions influences the absorption of the  $\text{ZnAl}_2\text{O}_4:0.01\% \text{Cr}^{3+}$  phosphor.

The Kubelka–Munk theory was used to transform the reflectance to values proportional to absorbance. Kubelka-Munk function can be determined by the following relation  $K = (1 - R)^2 / 2R$  [28]. Where  $K$  is the Kubelka-Munk function corresponding to absorbance and  $R$  is the reflectance. The energy bandgap ( $E_g$ ) was estimated from the plots of  $(K \times hv)^n$  versus  $(hv)$ , as shown in figure 9.4 (b) where  $(hv)$  is the photon energy using  $n = 2$  which is appropriate for indirect allowed transition [28]. As shown in figure 9.4 (b), the estimated  $E_g$  values for the non-catalysed (0) was found to be 2.94 eV, while for the 0.38 and 0.75 mole fractions were both found to be 3.17 eV, which suggests that the bandgap of  $\text{ZnAl}_2\text{O}_4$  host

was dependent on the catalyst content. Note that the  $E_g$  for the 3.0 (un-doped), 3.0 and 1.5 mole fractions could not be determined from figure 9.4 (b) as it is not easy to extrapolate the straight lines as required by the Kubelka–Munk theory. Therefore, doping with 0.01%  $\text{Cr}^{3+}$  ions does not affect the  $E_g$  of the host, while varying the catalyst/Zn mole fraction certainly influenced the  $E_g$  of the host.

The PL excitation and emission spectra of the un-doped and 0.01%  $\text{Cr}^{3+}$ -doped  $\text{ZnAl}_2\text{O}_4$  at various catalyst/Zn mole fractions are shown in figure 9.5 (a). The excitation and emission spectra of the un-doped and 0.01%  $\text{Cr}^{3+}$ -doped  $\text{ZnAl}_2\text{O}_4$  samples are compared in figure 9.5 (b). Figure 9.5 (a) and (b), show that the main peaks of excitation when monitoring the emission at 395 nm are at 276, 283 and 331 nm. The absorption band at 276 nm is most likely coming from the absorption of the host lattice, namely, the band-to-band transition of  $\text{AlO}_6$  anion grouping in  $\text{ZnAl}_2\text{O}_4$  [7, 29]. In comparison with Cheng et al. report [7], we propose that the other absorption band at 331 nm must arise from the charge-transfer (CT) transition. The absorption band at 283 nm in figure 9.4 (a) is assigned to the CT transitions of chromate  $\text{Cr}^{3+}$  ion [27]. It is clear from both the UV (figure 9.4 (a)) and PL (figure 9.5 (a) and (b)) that the host does not have the absorption band at 283 nm. Thus, it is reasonable to assign the absorption band at 283 nm to the  $\text{Cr}^{3+}$  ion. The emission spectra reveal that both un-doped and 0.01%  $\text{Cr}^{3+}$ -doped  $\text{ZnAl}_2\text{O}_4$  powders exhibit violet emission at the same wavelength position with maxima at 401 nm, which proves that the emission is originating from the host. This emission from the host at 401 nm is ascribed to the intrinsic intrabandgap defects, such as oxygen vacancies ( $\text{V}_\text{o}^*$ ) [29,30]. Da Silva et al. [30] suggested that these defects provide donor levels (DL), near the conduction band edge of the oxide as shown in figure 9.6 (a). Figure 9.5 (b) suggest that doping with 0.01%  $\text{Cr}^{3+}$  improves the emission intensity of the host, which is certainly expected at this lower concentration of the dopant [31].

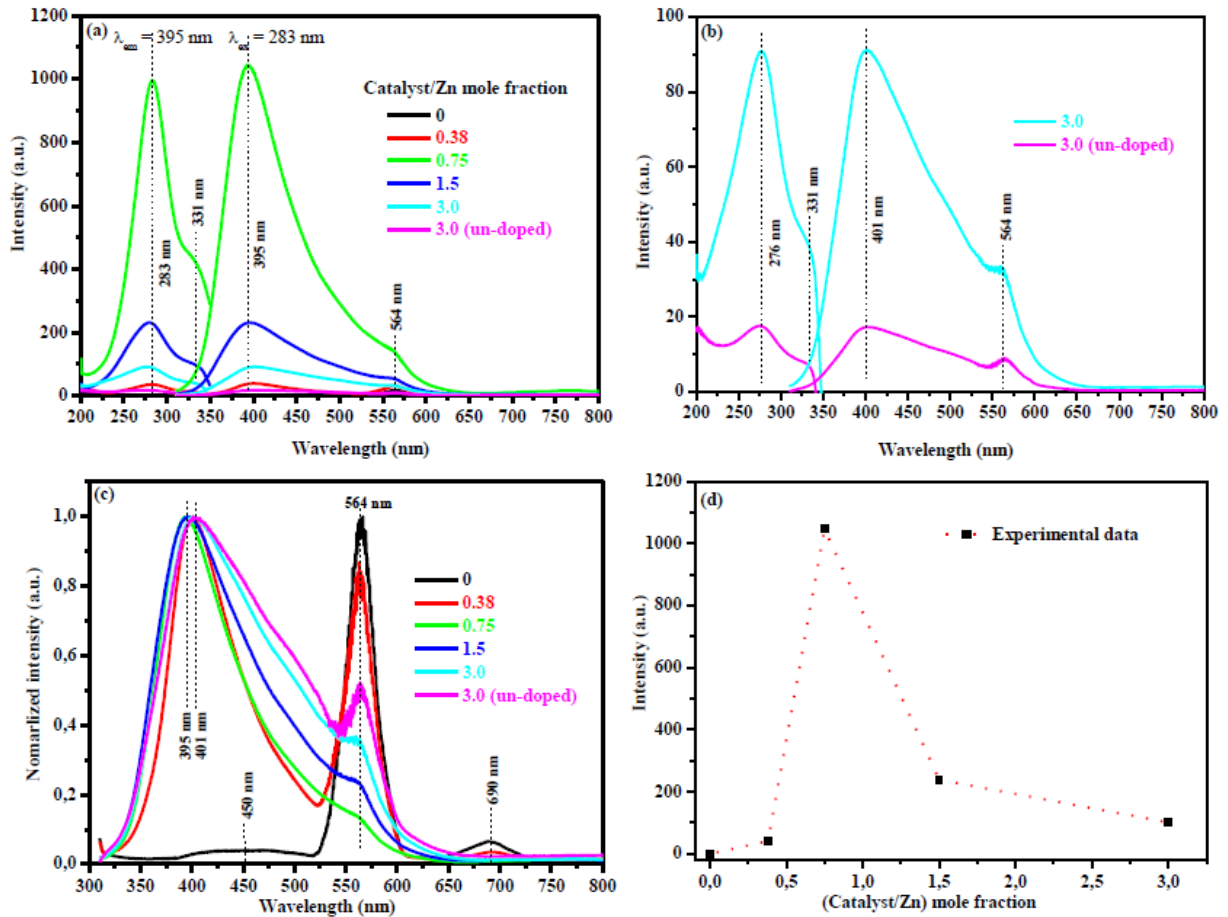


**Figure 9.5.** (a) Excitation and emission spectra of the un-doped and 0.01% Cr<sup>3+</sup>-doped ZnAl<sub>2</sub>O<sub>4</sub> at different catalyst/Zn mole fractions (b) Comparison of the un-doped and 0.01% Cr<sup>3+</sup>-doped ZnAl<sub>2</sub>O<sub>4</sub> samples. (c) Normalized emission intensity versus wavelength (d) PL intensity as a function of catalyst/Zn mole fractions.

When varying the catalyst/Zn mole fraction, it was found that the mole fraction of catalyst/Zn of 0.75 had the highest PL intensity centered at 395 nm, which is attributed to the Cr<sup>3+</sup> ion corresponding to the  $^4T_1 \rightarrow ^4A_2$  transition [12] as shown in figure 9.6 (b). In order to establish if there was any peak shift, the normalized PL emission intensity versus wavelength is presented in figure 9.5 (c). As shown in the figure 9.5 (c), there is a peak shift centered at 395 nm and 401 nm. As discussed above, these peaks are attributed to the Cr<sup>3+</sup> ion and the defects level in the host, respectively. The emission peak at 564 nm is assigned to either the second order emission or  $^4T_2 \rightarrow ^4A_2$  transition from Cr<sup>3+</sup> [12]. In addition, it can also be due to the host as it was reported by Da Silva et al. [30]. We infer that the 564 nm peak might possibly be due to the second order emission based on the following arguments. When considering the un-doped sample in figure 9.5 (b), the existence of 564 nm serves as the good reason to not

assign it to the  $\text{Cr}^{3+}$  ion. Furthermore, since there is no peak shift in all samples for the 564 nm in figure 9.5 (c), it is reasonable to attribute this peak to the second order emission. An appearance of additional peak at 690 nm is observed in figure 9.5 (c) and is assigned to so-called R lines (as described in ref [32]) of the  ${}^2\text{E} \rightarrow {}^4\text{A}_2$  transition in  $\text{Cr}^{3+}$  ion. These results indicate that the  $\text{Cr}^{3+}$  ions occupy multiple sites in  $\text{ZnAl}_2\text{O}_4$ , as previously suggested [33]. The emission intensity as a function of wavelength is shown in figure 9.5 (d), which shows both the luminescence enhancement and quenching phenomena. Quenching of luminescence is attributed to the catalyst induced point defects [34], which might be introducing the new defect sites due to the impurities such as ZnO, as shown in figure 9.1 (a) and (b), that enhance non-radiative recombination. The luminescence enhancement is attributed to the modification of the defect levels or local environment of the dopant ions [35], which seems to be highly dependent on the catalyst contents. Hafeez et al. [34] reported that the type and size of catalysts can regulate the intrinsic defects caused by Zn and S vacancies in the ZnS host. This is in good agreement with our results, that is; the catalyst content influences the emission intensity. We therefore propose that the catalyst/Zn mole fraction for the investigated range is indeed regulating the defects population in the host.

All transitions discussed from the UV and PL are summarized in the proposed energy level diagram shown in figure 9.6. Figure 9.6 (a) presents the absorption and emission taking place in the host, while figure 9.6 (b) presents the mechanism taking place when the  $\text{Cr}^{3+}$  absorbs the excitation energy and emits the visible light. It is important to mention that the excitation of 283 nm was kept constant for all samples. In case of the host (see figure 9.6 (a)), the electrons in the valence band (VB) are excited to the conduction band and de-excited by non-radiative relaxation (NRR) and trapped on the defect levels (DL) such as oxygen vacancies ( $\text{V}_\text{o}^*$ ), and then de-excited to the valence band by radiative decay. The mechanism taking place in the case of the emission from the  $\text{Cr}^{3+}$  can be interpreted as follows: Firstly, after the excitation, the electrons in the ground state ( ${}^4\text{A}_2$ ) are excited to the  ${}^4\text{T}_1$  or  ${}^4\text{T}_2$  levels and they may directly be de-excited to the  ${}^4\text{A}_2$  by emitting visible photons but this depends on the energy gap. Secondly, the excited electrons may phonon decay to the  ${}^4\text{T}_2$  or  ${}^4\text{T}_2$  or  ${}^2\text{E}$ , as indicated in figure 9.6 (b), and will then be de-excited to the  ${}^4\text{A}_2$  level. Since the gap between the  ${}^2\text{E}$  and the  ${}^4\text{A}_2$  levels is large, so the electrons in the  ${}^2\text{E}$  level or one of the T levels go back to the ground state  ${}^4\text{A}_2$  by radiative relaxation. The emission colours are also shown in figure 9.6 (b).

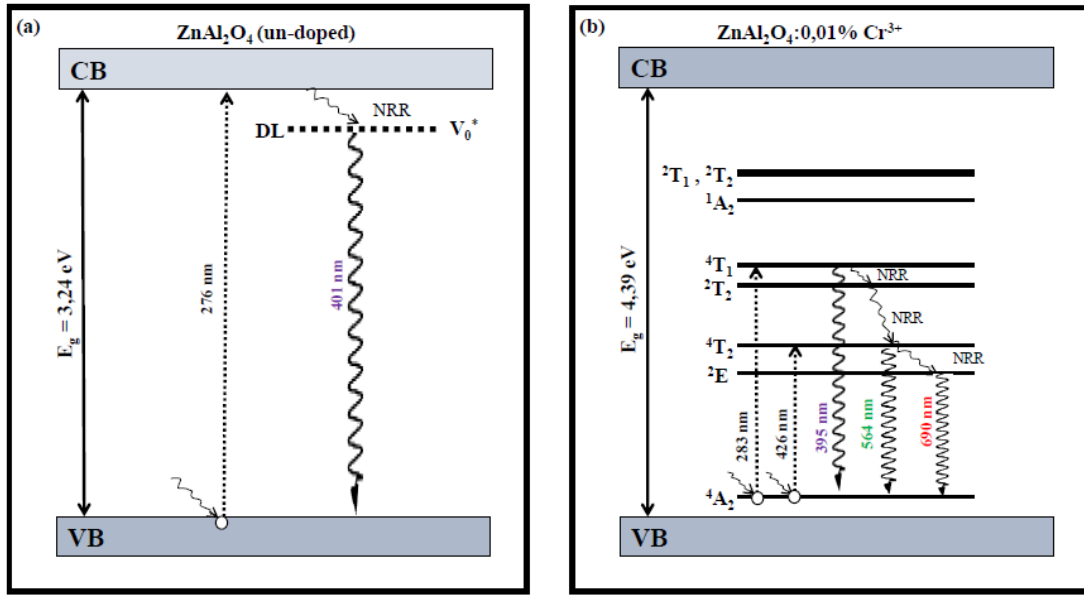


**Figure 9.6.** The proposed absorption and emission mechanism in (a) un-doped and (b) 0.01%  $\text{Cr}^{3+}$   $\text{ZnAl}_2\text{O}_4$  prepared by the sol-gel technique.

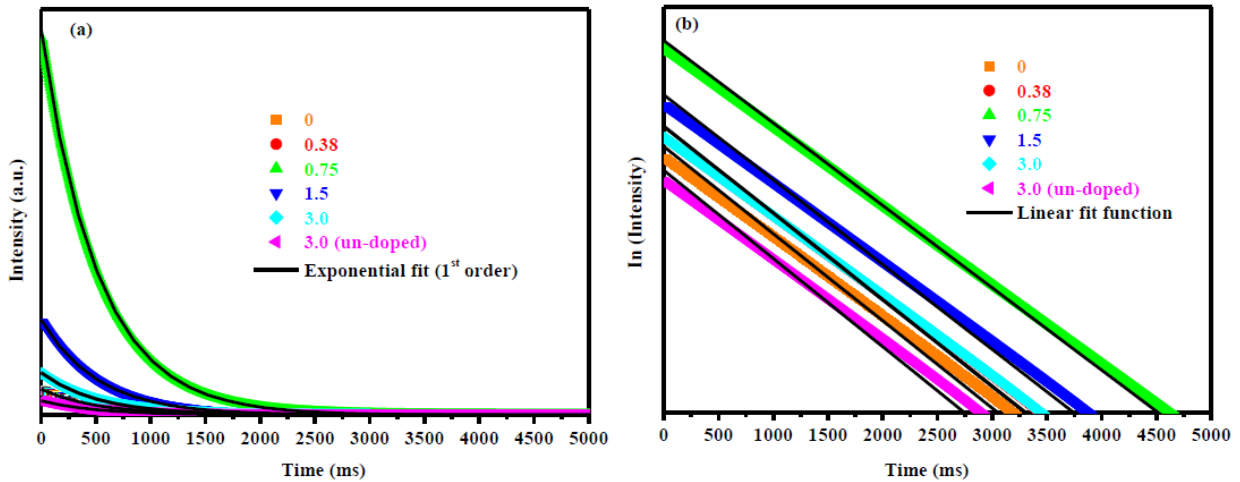


**Figure 9.7.** (a) The decay curves and (b) natural logarithm as a function of time for the un-doped and 0.01%  $\text{Cr}^{3+}$ -doped  $\text{ZnAl}_2\text{O}_4$  nanopowders at the varying catalyst/Zn mole fraction.

Figure 9.7 (a) shows the decay curves for the un-doped and 0.01%  $\text{Cr}^{3+}$   $\text{ZnAl}_2\text{O}_4$  nanopowders for the different catalyst/Zn mole fractions. Comparing all the decay curves shapes, it was found that the decay characteristics of this phosphor are similar indicating that all the samples have the same afterglow decay mechanism. The decay times are presented in table 9.1. In order to illustrate and compare the afterglow behaviour of the samples, the

natural logarithm as a function of time is plotted in figure 9.7 (b). The results are consistent with the measurements of the PL emissions in figure 9.5 (a), where the 0.75 sample is observed with the highest emission intensity, indicating that the catalysed chemical reaction regulates the defects population. The non-catalysed sample has the lowest initial luminescent intensity and also the shortest afterglow, which indicates that the catalyst is vital for the production of the radiative defects. This is also consistent with the observations in ref [34].

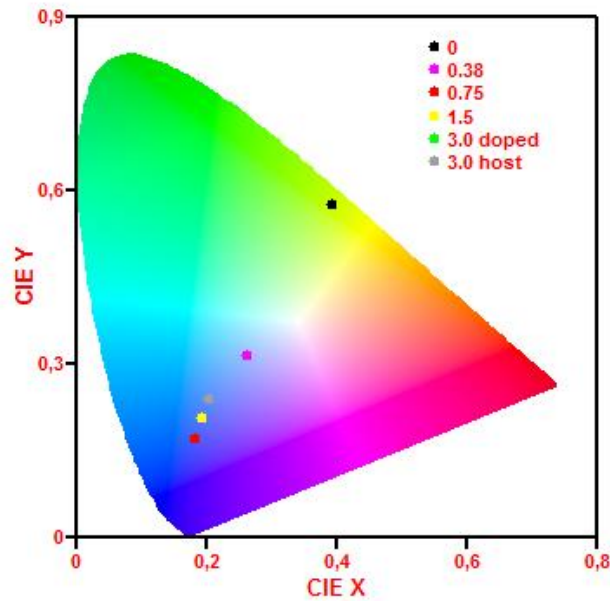


**Figure 9.4.** CIE colour tuning by varying the catalyst/Zn mole fraction as indicated.

Figure 9.8 represent the chromaticity co-ordinates of all the samples on the PL spectra in figure 9.5 (a), which were determined using the CIE Coordinate Calculator software [36]. The software also shows the position of the co-ordinates in the chromaticity diagram and the expected colour of the material. As shown in figure 9.8 there is a huge difference in colour between catalysed and non-catalysed samples in the CIE. For the doped and un-doped samples there is no shift in CIE colour coordinated (grey on top of green colour) as it can also be confirmed in table 9.1. Hence, it is concluded that the emission colour can be tuned by varying the catalyst/Zn mole fraction.

#### 9.4 Conclusion

The un-doped and  $\text{ZnAl}_2\text{O}_4:0.01\% \text{Cr}^{3+}$  nanopowders were successfully synthesised at a relatively low temperature ( $\sim 80^\circ\text{C}$ ). The XRD data revealed that the annealed samples consisted of pure cubic crystalline structures at the lower catalyst/Zn mole fractions, while the presence of ZnO is shown to exist at the higher mole fractions. The crystallinity is also influenced by the mole fraction. The required morphology could simply be obtained or tuned by varying the mole fraction. The results showed that the bandgap of the phosphor can be tuned by varying the catalytic mole fraction. PL spectra indicated that the emission can either originate from the host or from transitions in the  $\text{Cr}^{3+}$  ion itself. It was also noted that the catalyst/Zn mole fraction regulated the defects population and as a result influenced the emission intensity. The colour chromaticity showed that the emission colour of  $\text{ZnAl}_2\text{O}_4:0.01\% \text{Cr}^{3+}$  phosphor could be tuned for the first time by varying the mole fraction of the catalyst/Zn.

## References

1. M. Tsai, Y. Chen, P. Tsai, Y. Wang, *Thin Solid Films* **518** (2010) e9.
2. S. K. Sampath, J. F. Cordaro, *J. Am. Ceram. Soc.* **81** (1998) 649.
3. E. M. A. Jamal, D. S. Kumar, M. R. Anantharaman, *Bull. Mater. Sci.* **34** (2011) 251.
4. H. J. Fan, A. Lotnyk, R. Scholz, Y. Yang, D. S. Kim, E. Pippel, S. Senz, D. Hesse, M. Zacharias, *J. Phys. Chem. C.* **112** (2008) 6770.
5. V. Singh, R. P. S. Chakradhar, J. Rao, D. K. Kim, *J. Lumin.* **128** (2008) 394.
6. G. Lakshminarayana, L. Wondraczek, *J. Solid State Chem.* **184** (2011) 1931.
7. B. Cheng, S. Qu, H. Zhou, Z. Wang, *Nanotechnology* **17** (2006) 2982.
8. X. Y. Chen, C. Ma, S. P. Bao, Z. Li, *J. Colloid Interface.* **346** (2010) 8.
9. K. G. Tshabalala, S. Cho, J. K. Park, S. Pitale, I. M. Nagpure, R. E. Kroon, H. C. Swart, O. M. Ntwaeaborwa, *J. of Alloys and Compd.* **509** (2011) 10115.
10. E. Martinez-Sanchez, M. Garcacia-Hipolito, J. Guzman, F. Ramos-Brito, J. Santoyo-Salazar, R. Martinez-Martinez, O. Alvarez-Fregoso, M. I. Ramos-Cortes, J. J. Mendez-Delgado, C. Falcony, *Phys. Status Solidi a.* **202** (2005) 102.
11. Cz. Koepke, K. Wisniewski, M. Grinberg, G. H. Beall, *Spectrochimica Acta Part A* **54** (1998) 1725.
12. I. Miron, I. Grozescu, *Optoelectronics and Advance Materials – Rapid Communications* **6** (2012) 673.
13. N. J. Van de Laag, S. G. Snel, P. C. M. M. Magusin, G. de With, *J. Eur. Ceram. Soc.* **4** (8) (2004) 2417.
14. F. L. Yuan, P. Hu, C. L. Yin, S. L. Huang, J. L. Li, *J. Mater. Chem.* **13** (2003) 634.
15. Z. Chen, E. Shi, Y. Zheng, W. Li, N. Wu, W. Zhong, *Mater. Lett.* **56** (2002) 601.
16. A. K. Adak, A. Pathak, P. Pramanik, *J. Mater. Sci. Lett.* **17** (1998) 559.
17. M. Nikl, A. Novoselov, E. Mihokova, K. Polak, M. Dusek, B. McClune, A. Yoshikawa, T. Fukuda, *J. Phys. Condens. Mat.* **17** (2005) 3367.
18. O. M. Ntwaeaborwa, H. C. Swart, R. E. Kroon, P. H. Holloway, J. R. Botha, *Surf. Interface Anal.* **38** (2007) 458.
19. D. Duzenli, PhD thesis Middle East Technical University (2010).
20. R. G. Chary, G. R. Reddy, Y. S. S. Ganesh, K. V. Prasad, A. Raghunadh, T. Krishna, S. Mukherjee, M. Pal, *Adv. Synth. Catal.* **356** (201)160.
21. G. Dong, X. Xiao, M. Peng, Z. Ma, S. Ye, D. Chen, H. Qin, G. Deng, Q. Liang, J. Qiu, *RSC Advances* **2** (2012) 2773.

22. M. Yang, S. Li, G. Chena, *Applied Catalysis B: Environmental* **101** (2011) 409.
23. X. Xia, X. An, X. Wang, Z. Wang, *J. Nat. Gas Chem.* **12** (2013) 259.
24. Q. Hou, F. Meng, J. Sun, *Nanoscale Res. Lett.* **8** (2013) 144.
25. B. D. Cullity, 1956 *Elements of X-ray Diffraction* 2nd Ed Addison Wesley 285 (1978).
26. K. Y. Chew, M. Abu Bakar, N. H. H. Abu Bakar, *Modeling and Numerical Simulation of Material Science* **3** (2013) 23.
27. B. M. Weckhuysen, A. A. Verberckmoes, A. R. De Baets, R.A. Schoonheydt, *J. Catal.* **166** (1997) 160.
28. C. Aydin, M. Benhaliliba, A. A. Al-Ghamdi, Z. H. Gafer, F. El-Tantawy, F. Yakuphanoglu, *J. Electroceram.* **31** (2013) 265.
29. A. A. Da Silva, A. Goncalves, M. R. Davolos, S. H. Santagneli, *J. Nanosci. Nanotechnol.* **8** (2008) 5690.
30. A. A. Da Silva, A. Goncalves, M. R. Davolos, *J. Sol-Gel Sci. Technol.* **49** (2009) 101.
31. Q. Sai, C. Xia, H. Rao, X. Xu, G. Zhou, P. Xu, *J. Lumin.* **131** (2011) 2359.
32. D. Jia, L. A. Lewis, X-j. Wang, *Electrochem. Solid-State Lett.* **13** (4) (2010) J32.
33. M. Casalboni, A. Luci, U. M. Grassano, B. V. Mill, A. A. Kaminskii, *Phys. Rev. B.* **49** (1994) 3781.
34. M. Hafeez, S. Rehman, U. Manzoor, M. A. Khan, A. S. Bhatti, *Phys. Chem. Chem. Phys.* **15** (2013) 9726.
35. D. Gao, H. Zheng, X. Zhang, W. Gao, Y. Tian, J. Li, M. Cui, *Nanotechnology* **22** (2011) 175702 (5pp).
36. <http://www.mathworks.com/matlabcentral/fileexchange/29620-cie-coordinate-calculator> (accessed 21.10.2012).

## Chapter 10: Summary and conclusion

*“The content of physics is the concern of physicist, its effect the concern of all men.”*

*~ Friedrich Durrenmatt*

The  $\text{MAl}_2\text{O}_4$  ( $\text{M} = \text{Zn}$  or  $\text{Mg}$ ) doped and co-doped phosphors were successfully prepared by sol-gel technique at a relatively low temperature ( $\sim 80$  °C). The XRD data in the case of varying the  $x$  mol% in the singly ( $x\% \text{Pb}^{2+}$ ), doubly ( $\text{Ce}^{3+}$ ,  $x\% \text{Eu}^{3+}$ ) and triply ( $\text{Eu}^{3+}$ ,  $\text{Ce}^{3+}$ ,  $x\% \text{Tb}^{3+}$ ) doped  $\text{ZnAl}_2\text{O}_4$  and  $\text{MgAl}_2\text{O}_4$  crystal lattice, respectively, revealed that the annealed samples consist of highly crystalline cubic structures. That is; varying the  $x$  mol% does not affect the crystal structure of the phosphors. However, in the case of  $\text{ZnAl}_2\text{O}_4$   $x\% \text{Cr}^{3+}$ , the  $\text{Cr}^{3+}$  ions (depending on the mol%) can occupy both the octahedral and tetrahedral sites in the host matrix, which suggest that varying the  $\text{Cr}^{3+}$  mol% alters the crystal structure. In the case of varying the CA content in singly doped  $\text{ZnAl}_2\text{O}_4$  with 1.5%  $\text{Pb}^{2+}$  and 0.01%  $\text{Cr}^{3+}$  studies, the XRD data revealed that the annealed samples at low CA content consist of pure and highly crystalline cubic  $\text{ZnAl}_2\text{O}_4$  with an extra diffraction peaks at the higher CA content. Impurities peaks are attributed to the CA induced impurities.

In the study of  $\text{ZnAl}_2\text{O}_4$  singly doped with 1.5%  $\text{Pb}^{2+}$  and 0.01%  $\text{Cr}^{3+}$  systems, the positive and negative deviation from the Virgard's law was observed. In the study of  $\text{ZnAl}_2\text{O}_4$ :  $x\% \text{Pb}^{2+}$  the SEM results also suggest that the good particle agglomeration and voids leads to an easy escape routes to the emitted light with the consequent of enhancing the luminescence of a phosphor. The PL results demonstrated that undoped and  $\text{Pb}^{2+}$  impurities activated  $\text{ZnAl}_2\text{O}_4$  emits at slightly different UV positions, which suggests that the emission can be from either the host or  $\text{Pb}^{2+}$  ions. At the higher  $\text{Pb}^{2+}$  mol%, the luminescence quenching behaviour occurs due to the introduction of more new defect sites that enhance non-radiative recombination of the excited electrons.

In the study of  $\text{ZnAl}_2\text{O}_4$  singly doped with  $x\% \text{Cr}^{3+}$  the TOF-SIMS analysis revealed the presence of all as-designed elements. Varying  $\text{Cr}^{3+}$  influences the morphology of the phosphor. UV-Vis results showed that the band gap of the phosphor can be engineered or tuned. The PL results demonstrated that the violet emission can be due to the host or  $\text{Cr}^{3+}$

ions. The critical energy transfer distance of  $\text{Cr}^{3+}$  in  $\text{ZnAl}_2\text{O}_4$  host is calculated to be 23 Å. CIE colour coordinate showed no significant shifts on the violet emission colour.

In the study of  $\text{ZnAl}_2\text{O}_4: 0.1\% \text{Ce}^{3+}, x\% \text{Eu}^{3+}$  system the FWHM, strain, crystallites sizes, degree of crystallinity and lattice fringes were influenced by the type of the dopand and co-doping. PL results confirmed the existence of the radiative energy transfer from  $\text{Ce}^{3+} \rightarrow \text{Eu}^{3+}$ . CIE colour chromaticity showed that the colour can be tuned from bluish  $\rightarrow$  reddish by changing the  $\text{Eu}^{3+}$  mol%.

In the study of the triply doped  $\text{MgAl}_2\text{O}_4: 0.1\% \text{Eu}^{3+}, 0.1\% \text{Ce}^{3+}, x\% \text{Tb}^{3+}$  the crystallites sizes, degree of crystallinity and the morphology of the phosphor were influenced by the type of the dopand and the  $\text{Tb}^{3+}$  mol%. The band gab of the phosphor can be engineered by the type of the dopant and  $x\% \text{Tb}^{3+}$  in the triply doped systems. PL results confirmed the existence of the energy transfer from  $\text{Eu}^{2+} \rightarrow \text{Tb}^{3+} \rightarrow \text{Ce}^{3+}$ . CIE colour chromaticity showed that the colour can be tuned from bluish  $\rightarrow$  greenish by changing the  $\text{Tb}^{3+}$  mol% and the excitation wavelength.

In the study of the effects of CA content in  $\text{ZnAl}_2\text{O}_4:1.5\% \text{Pb}^{2+}$  phosphor, the results showed that with the Zn/CA mole fraction variation, there is a morphological evolution from small particles to rod-like-needles particles. The PL results demonstrated that the violet emission can either be from the host,  $\text{Pb}^{2+}$  or ZnO impurities. The incorporation of 1.5%  $\text{Pb}^{2+}$  ions slightly enhanced the emission intensity. Controlling the Zn/CA mole fraction could quench and enhance the bluish brightness of the  $\text{ZnAl}_2\text{O}_4:1.5\% \text{Pb}^{2+}$  phosphor. The CIE color coordinates of all samples is situated in the blue region of the chart. TSL glow curves exhibits two distinct peaks.

Lastly, but not least, in the study of the effects of CA content in  $\text{ZnAl}_2\text{O}_4:0.01\% \text{Cr}^{3+}$ , the XRD results showed that the crystallinity is also influenced by the CA content. SEM result showed that the required morphology could simply be obtained or tuned by varying the mole fraction. The results showed that the band gap of the phosphor can be tuned by varying the catalytic mole fraction. PL spectra indicated that the emission can either originate from the host or from transitions in the  $\text{Cr}^{3+}$  ion itself. It was also noted that the catalyst/Zn mole fraction regulated the defects population and as a results influenced the emission intensity. The colour chromaticity showed that the emission colour of  $\text{ZnAl}_2\text{O}_4:0.01\% \text{Cr}^{3+}$  phosphor was tuned for the first time by varying the mole fraction of the catalyst/Zn.

As far as the current study is concern and for future prospects, it is recommended that the following aspects are investigated:

- ✓ To study the effects of annealing temperature and gas atmosphere in the  $\text{ZnAl}_2\text{O}_4$  singly doped with 1.5%  $\text{Pb}^{2+}$  and 0.01%  $\text{Cr}^{3+}$  systems;
- ✓ To study the effects of the CA content in the co-doped and triply doped  $\text{MAl}_2\text{O}_4$  (M = Zn or Mg);
- ✓ To study the effects of M, Al and O moles in the doped  $\text{M}_x\text{Al}_y\text{O}_z$  (M = Zn or Mg) phosphor;
- ✓ To study the effects of Cd mol% in x% Cd doped  $\text{MgAl}_2\text{O}_4$ ;
- ✓ To study the effects of Cu mol% in x% Cu doped  $\text{ZnAl}_2\text{O}_4$ ;
- ✓ To study the effects of In mol% in x% In doped  $\text{MgAl}_2\text{O}_4$ ;
- ✓ To study the influence of varying  $\text{Cr}^{3+}$  mol% in  $\text{MgAl}_2\text{O}_4:0.1\% \text{Eu}^{2+}$ , x%  $\text{Cr}^{3+}$  nanophosphor; and
- ✓ To study the effects of CA content in all of the above mentioned possible suggestions.

## Publications

1. **S.V. Motlounq**, B. F. Dejene, H. C. Swart, O. M. Ntwaeaborwa, J. Sol-gel Sci. technol. **70** (2014) 422.
2. **S.V. Motlounq**, F. B. Dejene, O. M. Ntwaeaborwa, H. C. Swart, Mater. Res. Express **1** (2014) 045029.
3. **S.V. Motlounq**, F. B. Dejene, O. M. Ntwaeaborwa, H. C. Swart, “*Colour tuning and energy transfer pathways in MgAl<sub>2</sub>O<sub>4</sub> triply doped with 0.1% Ce<sup>3+</sup>, 0.1% Eu<sup>2+</sup>, x% Tb<sup>3+</sup> nanocrystals synthesized using sol-gel process*” J. Lumin. (2015) revised article submitted.
4. **S.V. Motlounq**, F. B. Dejene, O. M. Ntwaeaborwa, H. C. Swart, “*Effects of Zn/citric acid mole fraction on the Structure and Luminescence Properties of the un-doped and 1.5% Pb<sup>2+</sup> doped ZnAl<sub>2</sub>O<sub>4</sub> powders synthesized by citrate sol-gel method*” J. Lumin. **163** (2015) 8-16 (DOI: 10.1016/j.jlumin.2015.02.027).
5. **S.V. Motlounq**, F. B. Dejene, O. M. Ntwaeaborwa, H. C. Swart, “*Effects of Cr<sup>3+</sup> mol% on the structure and optical properties of the ZnAl<sub>2</sub>O<sub>4</sub>:Cr<sup>3+</sup> nanocrystals synthesized using sol-gel process*” Ceramics International **41** (2015) 6776-6783 (DOI: 10.1016/j.ceramint.2015.01.124).
6. **S.V. Motlounq**, F. B. Dejene, O. M. Ntwaeaborwa, H. C. Swart, “*Radiative energy transfer in ZnAl<sub>2</sub>O<sub>4</sub>:0.1% Ce<sup>3+</sup>, x% Eu<sup>3+</sup> nanophosphor synthesized by sol-gel process*” Physica B (accepted).

## International conferences

1. XVII International Sol-Gel Conference, Spain (Madrid), 25 – 30 August 2013.  
Effects of Pb<sup>2+</sup> ions concentration on the structure and PL intensity of Pb-doped ZnAl<sub>2</sub>O<sub>4</sub> nanocrystals synthesized using sol-gel process,  
**S.V. Motlounq**, F. B. Dejene, O. M. Ntwaeaborwa, H. C. Swart
2. 17<sup>th</sup> International conference on Luminescence and Optical Spectroscopy of Condensed Matter, Poland (Wroclaw), 13 – 18 July 2014.  
Energy transfer in ZnAl<sub>2</sub>O<sub>4</sub>:0.1% Ce<sup>3+</sup>, x% Eu<sup>3+</sup> (0 ≤ x ≤ 2%) nanophosphor synthesized by sol-gel process,  
**S.V. Motlounq**, F. B. Dejene, O. M. Ntwaeaborwa, H. C. Swart
3. 5th International Conference on Luminescence and Applications (ICLA 2015), India (Bangalore) 9-12 February 2015 (abstract accepted)

Structural and optical studies of  $\text{ZnAl}_2\text{O}_4: x\% \text{Cu}^{2+}$  ( $0 \leq x \leq 1.25\%$ ) doped nanocrystals synthesized via citrate sol–gel route,

**S.V. Motloug**, F. B. Dejene, O. M. Ntwaeaborwa, H. C. Swart

4. Advanced Materials World Congress, Sweden (Stockholm) 23 – 26 August 2015 (abstract accepted)

Effects of  $\text{In}^{3+}$  doping concentration on the  $\text{MgAl}_2\text{O}_4:x\% \text{In}^{3+}$  nanophosphor,

**S.V. Motloug**, F. B. Dejene, O. M. Ntwaeaborwa, H. C. Swart

#### National conferences

1. The 57<sup>th</sup> Annual Conference of the South African Institute of Physics, University of Pretoria, 9 – 13 July 2012.

Sol-gel synthesis and Characterization of Structural and Luminescence Properties of  $\text{ZnAl}_2\text{O}_4$  doped with  $\text{Mn}^{2+}$  powder phosphor,

**S.V. Motloug**, F. B. Dejene, O. M. Ntwaeaborwa, H. C. Swart

2. 5<sup>th</sup> South African Conference on Photonic Materials, Kariega Game Reserve, 29<sup>th</sup> April – 3<sup>rd</sup> May 2013.

Effects of Zn:catalyst molar ratio on  $\text{ZnAl}_2\text{O}_4:0.05\% \text{Cr}^{3+}$  nanocrystals synthesized using sol-gel process,

**S.V. Motloug**, F. B. Dejene, O. M. Ntwaeaborwa, H. C. Swart

3. The 59<sup>th</sup> Annual Conference of the South African Institute of Physics, University of Johannesburg, 7 – 11 July 2014.

Effects of  $\text{Cr}^{3+}$  mol% on the structure and optical properties of the  $\text{ZnAl}_2\text{O}_4:\text{Cr}^{3+}$  nanocrystals synthesized using sol-gel process,

**S.V. Motloug**, F. B. Dejene, O. M. Ntwaeaborwa, H. C. Swart

## Biography

Setumo Victor Motlounq is the son of Mrs. Thobisile Rose Mbatha and the late Mr. Phutheho Smuts Motlounq. He was born in Qwaqwa Tseseng (Sefikaneng) Village.

**School life:** He started to attend school at Tseseng primary school and he attended the senior primary school at Koos Mota. He then went to Seotlong Agriculture and Hotel School where he studied Agriculture and matriculated in 2000.

**Traditional schooling:** From November 2000 – January 2001 (three months), he attended the traditional school at *Tlokoeng Mophatong wa Ntate Komako Mosanku dihlabeng tsa ha-bohobe*.

**Tertiary life:** He studied his undergraduate degree (in Chemistry) at the University of the Free State (Qwaqwa Campus). He achieved an award of being the best student in senior graduate physics in 2004. In 2005, he went to the University of the Western Cape (UWC) where he graduated for the BScHons (in nuclear and accelerator physics). In 2006, while registered with UWC, he went to Pretoria at NECSA (Radiation Utilization Department) where he did his Masters research (in nuclear and accelerator physics). In 2007, he was a PhD student and worked as a tutor at the Wits University. In 2008, he registered a PhD (Metallurgy Engineering) with the University of Pretoria while doing his research at the Council of Scientific Research (CSIR) at National Laser Center (NLC). In 2009 and 2010, he decided to go back to the nuclear and he was given an internship position at National Nuclear Regulator (NNR) and NECSA (SAFARI1). Due to no fulltime job, near the end of 2010, he decided to go back to school and pursue his PhD degree with University of Johannesburg. In early 2011, he found the full time job (Lecturing position) at the University of the Free State (Qwaqwa Campus).

**Presently:** He is a physics lecturer at the University of the Free State (Qwaqwa Campus). He is teaching at both undergraduate and postgraduate level. He is also supervising, co-supervising and mentoring the Third years, BScHons and Masters students. From his Thuthuka bursary, he is sponsoring or funding 2 third years, 1 BScHons and 1 Masters students.

**Research interest:** His research interest is in semiconductor, nanotechnology, nanomaterials synthesis and characterization as well as nuclear and radiation physics. He is also interested in polymers (i.e. cellulose) research. His research work is recognized by the international

community (e.g. He is a reviewer of the international Journals). Last but not least, he is also interested to pursue MBA.

**Hobby:** He likes to play soccer and interested to play guitar at his free time. He also likes jokes but not good at making them. He is also interested in culture and tradition of Basotho (e.g. he normally serves in a committee for Batlokoa traditional school planning).

*“It’s only via education where a shepherd/cowherd/goatherd can become a Doctor. I am a good sample of this!”*

*~Setumo*